

NORTH ATLANTIC TREATY ORGANIZATION



RESEARCH AND TECHNOLOGY ORGANIZATION

BP 25, 7 RUE ANCELLE, F-92201 NEUILLY-SUR-SEINE CEDEX, FRANCE

## RTO MEETING PROCEEDINGS 9

**Intelligent Processing of High Performance Materials**

(le Traitement sophistiqué de matériaux très performants)

*Papers presented at the Workshop of the RTO Applied Vehicle Technology Panel (AVT)  
(organised by the former AGARD Structures and Materials Panel) held in Brussels, Belgium,  
13-14 May 1998.*

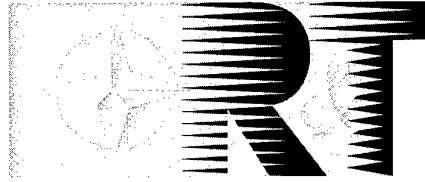
DISTRIBUTION STATEMENT A:  
Approved for Public Release -  
Distribution Unlimited



19981201 109

THIS QUALITY INSPECTED 3

**NORTH ATLANTIC TREATY ORGANIZATION**



**RESEARCH AND TECHNOLOGY ORGANIZATION**

BP 25, 7 RUE ANCELLE, F-92201 NEUILLY-SUR-SEINE CEDEX, FRANCE

---

**RTO MEETING PROCEEDINGS 9**

## **Intelligent Processing of High Performance Materials**

(le Traitement sophistiqué de matériaux très performants)

*Papers presented at the Workshop of the RTO Applied Vehicle Technology Panel (AVT)  
(organised by the former AGARD Structures and Materials Panel) held in Brussels, Belgium,  
13-14 May 1998.*



---

AQF99-03-0289

# The Research and Technology Organization (RTO) of NATO

RTO is the single focus in NATO for Defence Research and Technology activities. Its mission is to conduct and promote cooperative research and information exchange. The objective is to support the development and effective use of national defence research and technology and to meet the military needs of the Alliance, to maintain a technological lead, and to provide advice to NATO and national decision makers. The RTO performs its mission with the support of an extensive network of national experts. It also ensures effective coordination with other NATO bodies involved in R&T activities.

RTO reports both to the Military Committee of NATO and to the Conference of National Armament Directors. It comprises a Research and Technology Board (RTB) as the highest level of national representation and the Research and Technology Agency (RTA), a dedicated staff with its headquarters in Neuilly, near Paris, France. In order to facilitate contacts with the military users and other NATO activities, a small part of the RTA staff is located in NATO Headquarters in Brussels. The Brussels staff also coordinates RTO's cooperation with nations in Middle and Eastern Europe, to which RTO attaches particular importance especially as working together in the field of research is one of the more promising areas of initial cooperation.

The total spectrum of R&T activities is covered by 6 Panels, dealing with:

- SAS Studies, Analysis and Simulation
- SCI Systems Concepts and Integration
- SET Sensors and Electronics Technology
- IST Information Systems Technology
- AVT Applied Vehicle Technology
- HFM Human Factors and Medicine

These Panels are made up of national representatives as well as generally recognised 'world class' scientists. The Panels also provide a communication link to military users and other NATO bodies. RTO's scientific and technological work is carried out by Technical Teams, created for specific activities and with a specific duration. Such Technical Teams can organise workshops, symposia, field trials, lecture series and training courses. An important function of these Technical Teams is to ensure the continuity of the expert networks.

RTO builds upon earlier cooperation in defence research and technology as set-up under the Advisory Group for Aerospace Research and Development (AGARD) and the Defence Research Group (DRG). AGARD and the DRG share common roots in that they were both established at the initiative of Dr Theodore von Kármán, a leading aerospace scientist, who early on recognised the importance of scientific support for the Allied Armed Forces. RTO is capitalising on these common roots in order to provide the Alliance and the NATO nations with a strong scientific and technological basis that will guarantee a solid base for the future.

The content of this publication has been reproduced directly from material supplied by RTO or the authors.



*Printed on recycled paper*

Published November 1998

Copyright © RTO/NATO 1998  
All Rights Reserved

ISBN 92-837-1004-5



*Printed by Canada Communication Group Inc.  
(A St. Joseph Corporation Company)  
45 Sacré-Cœur Blvd., Hull (Québec), Canada K1A 0S7*



North Atlantic Treaty Organization

## *Research and Technology Agency*

*RTA Headquarters: 7, rue Ancelle - 92200 Neuilly-sur-Seine, France*

ST/60/4

19 August, 1998

TO: Recipients of RTO Publications  
FROM: Scientific Publications Executive  
SUBJECT: **RTO Technical Publications**

As you probably know, NATO formed the Research and Technology Organization (RTO) on 1 January 1998, by merging the former AGARD (Advisory Group for Aerospace Research and Development) and DRG (Defence Research Group). There is a brief description of RTO on page ii of this publication.

This new organization will continue to publish high-class technical reports, as did the constituent bodies. There will be five series of publications:

- AG** **AGARDographs** (Advanced Guidance for Alliance Research and Development), a successor to the former AGARD AGARDograph series of monographs, and containing material of the same long-lasting value.
- MP** **Meeting Proceedings**: the papers presented at non-educational meetings at which the attendance is not limited to members of RTO bodies. This will include symposia, specialists' meetings and workshops. Some of these publications will include a Technical Evaluation Report of the meeting and edited transcripts of any discussions following the presentations.
- EN** **Educational Notes**: the papers presented at lecture series or courses.
- TR** **Technical Reports**: other technical publications given a full distribution throughout the NATO nations (within any limitations due to their classification).
- TM** **Technical Memoranda**: other technical publications not given a full distribution, for example because they are of ephemeral value only or because the results of the study that produced them may be released only to the nations that participated in it.

The first series (AG) will continue numbering from the AGARD series of the same name, although the publications will now relate to all aspects of defence research and technology and not only aerospace as formerly. The other series will start numbering at 1, although (as in the past) the numbers may not appear consecutively because they are generally allocated about a year before the publication is expected.

All publications, like this one, will also have an 'AC/323' number printed on the cover. This is mainly for use by the NATO authorities.

Please write to me (do not telephone) if you want any further information.

G.W.Hart



# **Intelligent Processing of High Performance Materials**

## **(RTO MP-9)**

### **Executive Summary**

Intelligent Processing of High Performance Materials (IPM) is an emerging methodology for simulating and controlling the processing and manufacture of materials. The main driver for this methodology is to improve quality and reduce the costs associated with advanced materials. The increasing focus on affordability has resulted in a shift from product technology development, which in the past has led to increasingly expensive military systems, to development of process technologies which offer the promise of achieving technology affordability while maintaining or improving product quality. The growing interest in affordable process technologies is exhibited by the proliferation of programs addressing "flexible," "agile," and "intelligent" manufacturing, concurrent engineering, integrated product and process development, and "lean" aircraft production. In addition to its role in intelligent manufacturing systems of the future, IPM offers significant near-term advantages in the production of higher quality, more affordable military systems.

A very successful Workshop on Intelligent Processing of High Performance Materials was held by the former AGARD Structures and Materials Panel on 13 and 14 May 1998 in Brussels, Belgium. A total of sixteen papers were presented on a wide range of subjects related to IPM. These included an overview of the topic, analytical techniques associated with IPM, and applications of IPM to both metallic and non-metallic materials. In the Round Table Discussion at the end of the Workshop, recommendations for current needs and future developments were discussed. It was suggested that a Working Group be formed to develop and exchange "bench-mark" properties to be used for IPM since one major road block in its implementation is the lack of data available for the dynamic process involved in IPM. This could be accomplished by the use of the Internet to exchange information, properties, and testing techniques.

# **Le traitement sophistiqué de matériaux très performants**

**(RTO MP-9)**

## **Synthèse**

Le traitement sophistiqué de matériaux très performants (IPM) est une méthodologie naissante pour la simulation et le contrôle de la fabrication et du traitement des matériaux. L'objectif principal de cette méthodologie est d'améliorer la qualité des matériaux avancés et de réduire les coûts associés. La pression croissante sur les coûts a entraîné un changement d'orientation. Auparavant basé sur les technologies des matériaux, responsables de la flambée des prix des systèmes militaires, le développement s'appuie maintenant sur les technologies des procédés, plus abordables sur le plan financier et garantant le maintien voire de l'amélioration de la qualité des produits. L'intérêt grandissant manifesté pour les technologies de système est démontré par la prolifération de programmes visant la fabrication "souple", "agile" et "intelligente", l'ingénierie concurrente, le développement simultané du concept et des produits et la production aéronautique à moindre coût. En plus du rôle qu'il jouera dans les systèmes de fabrication intelligents à l'avenir, l'IPM offre des avantages considérables dans le court terme, en ce qui concerne la production de systèmes militaires de meilleure qualité à des coûts d'acquisition plus acceptables.

L'atelier sur le traitement sophistiqué des matériaux très performants organisé du 13 au 14 mai 1998 à Bruxelles par l'ancien Panel AGARD des structures et matériaux a connu un franc succès. En tout, seize communications ont été présentées sur des sujets se rapportant à l'IPM et notamment un exposé général de la question, les techniques analytiques associées à l'IPM, et les applications de l'IPM aux matériaux métalliques et non métalliques. Un certain nombre de recommandations concernant les besoins actuels et les développements futurs ont été faites lors de la table ronde qui a clôturé la séance. Il a été proposé de créer un groupe de travail afin de développer et d'échanger les caractéristiques de référence à utiliser pour l'IPM puisque l'un des principaux obstacles à sa mise en œuvre s'avère être le manque de données relatives aux processus dynamiques de l'IPM. Ceci pourrait être accompli en se servant d'Internet pour l'échange d'informations, de caractéristiques et de techniques d'essais.

# Contents

	Page
Executive Summary	iii
Synthèse	iv
Preface	vii
Committee Members	viii
	Reference
Technical Evaluation Report by J. Waldman and H.G.N. Wadley	T
<b>SESSION I: OVERVIEW AND ANALYTICAL TECHNIQUES</b>	
A Review of the Intelligent Processing of Materials and a Case Study of Titanium Matrix Composite Consolidation by H.N.G. Wadley and R. Vancheeswaran	1
Process-Structure-Property Relationships Obtained with Natural Computation by T. de Weijer	2
Intelligent Process Control With Evolution Strategy by H. Offergeld	3
Establishing Best Practice in the Design and Manufacture of Hollow Titanium Fan Blades by G.A. Fitzpatrick and A.D. Lloyd	4
Guaranteeing 100% Quality Through Closed Loop Process Control by O. Schnerr and W. Michaeli	5
<b>SESSION II: METALLIC MATERIALS APPLICATIONS I</b>	
Intelligent Processing in a Hot Rolling Mill for Structural Steels by P.J. van der Wolk, C. Dorrepaal, J. Sietsma and S. van der Zwaag	6
Intelligent Control Strategies for Metal Forging Processes by J.C. Malas and W.G. Frazier	7
Intelligent Processing of P/M Materials by W.E. Frazier, J. Waldman and P.A. Parrish	8
Process Modelling and Control for Cold Hearth Refining of Intermetallic Alloys by R.M. Ward, T.P. Johnson and J.M. Young	9
Paper 10 withdrawn	

### **SESSION III: METALLIC MATERIALS APPLICATIONS II**

- Laser Ultrasonic Measurement of Microstructure Evolution During Metals Processing** 11  
by M. Dubois, A. Moreau, A. Dawson, M. Militzer and J.F. Bussière
- Modelling of Ti Alloy Melting by EBCHM: Impact of Process Parameters for Hard-Alpha Dissolution** 12  
by J.P. Bellot, A. Jardy, S. Bourguignon and D. Ablitzer

**Paper 13 withdrawn**

### **SESSION IV: NON-METALLIC MATERIALS APPLICATIONS**

- Automated Fabrication Technologies For High Performance Polymer Composites** 14  
by M.J. Shuart, N.J. Johnston, H.B. Dexter, J.M. Marchello and R.W. Grenoble
- Remote Cure Sensing of Polymer Composites** 15  
by D.A. Pullen, D. Attwood, I. Partridge, M. Batchelor and G. Cracknell
- Process Control of Deposition Profiles in the Manufacture of EB-PVD Thermal Barrier Coatings** 16  
by J.R. Nicholls, V. Pereira, K.J. Lawson and D.S. Rickerby
- Laser Heated Oxide Fiber Growth Using Melt Modulation Technique** 17  
by A. Sayir, S.C. Farmer, P. Dickerson and A. Chait

**Paper 18 withdrawn**

- Smart Curing of Composite Materials in Autoclave** 19  
by P. Dublineau and J. Cinquin

# Preface

Intelligent Processing of High Performance Materials (IPM) is an emerging methodology for simulating and controlling the processing and manufacture of materials. It is finding widespread application during the manufacture of electronic, photonic and composite (i.e. high performance) materials, as well as primary metals such as steel and aluminum. IPM simulation tools seek to create, at the level of an engineering workstation, a "virtual" version of a process. They combine process models for a material's response to processing stimuli (e.g. pressure, temperature, and environmental conditions) with characteristics of the process equipment to predict the material's performance defining attributes at the completion of the process. Thus, they provide a methodology for the process engineer to conduct "what if..." trials in minutes or hours compared to weeks or months of practical experimentation, and for near optimal processing approaches to be identified. IPM controllers are an innovative extension of today's state-of-the-art in control technology. They exploit the recent availability of non-invasive sensors that sense critical product variables during the process. This new knowledge about the state of the process, together with process models, can be used to plan and execute feedback control schemes leading to products with "goal state" combinations of performance defining property attributes. This radically new approach to process control enables the processing of high performance materials hitherto considered too unstable for commercialization and significantly improves the yield/quality of those already being manufactured today.

The objectives of the NATO RTO Workshop were to examine state-of-the-art analytical techniques and application of these techniques to metallic and non-metallic materials. An additional objective was to identify research and development needs for further implementation of IPM methods for cost reduction and quality improvement.

Edgar A. Starke, Jr.  
Co-Chairman of the  
Sub-Committee on IPM

# Sub-Committee Members

## Chairmen

Dr E.A. STARKE  
Oglesby Professor of Materials Science  
UVA Light Metals Center  
Thornton Hall  
Charlottesville, VA 22903-2442

Mr. S. MORAN  
Aviation Systems Technology Div.  
Office of Aeronautics, Code R  
NASA HQ Research Div. Code RH  
Washington, DC 20546

E. Campo	-	IT	R. Potter	-	UK
D. Chaumette	-	FR	T. Ronald	-	US
P. Costa	-	FR	A. Salvetti	-	IT
E.E. Gdoutos	-	GR	S. Sampath	-	US
P. Heuler	-	GE	E. Selcuk	-	TU
J.P. Immarigeon	-	CA	D. Simpson	-	CA
R. Kochendörfer	-	GE	W. Van der Hoeven	-	NE
L. Kompotiatis	-	GR	D. Viechnicki	-	US
S. Moran	-	US	J. Waldman	-	US
C. Moura Branco	-	PO	S. Welburn	-	UK
C. Perron	-	CA	M. Winstone	-	UK

## Panel Executive

Dr. J.M. CARBALLAL, SP

Mail from Europe:

RTA-OTAN/AVT  
BP 25  
7, rue Ancelle  
F-92201 Neuilly-sur-Seine Cedex  
France

Mail from US and Canada:

RTA-NATO/AVT  
PSC 116  
APO AE 09777

Tel. 33(0)1 55 61 22 90 & 92  
Telefax 33(0)1 55 61 22 99 & 98

## TECHNICAL EVALUATION REPORT

By

**Dr. J. Waldman**  
**Drexel University**  
**32nd and Chestnut Streets**  
**Philadelphia, PA 19104, USA**

**Prof. H.N.G. Wadley**  
**University of Virginia**  
**School of Eng. and Applied Sciences**  
**Charlottesville, VA 22903-2442, USA**

Intelligent processing of Materials (IPM) is a methodology for simulating and controlling the processing and manufacture of materials. It is finding widespread application during the manufacture of functional electronic, photonic and composite materials as well as primary metals such as steel and aluminum. The knowledge about the state of the manufacturing process determined in real time from sensors can be used together with process models to plan and execute feedback control schemes to control materials processing and manufacturing thereby reducing cost and improving the quality of the product.

The workshop was conducted in 4 sessions followed by a round table discussion.

### Session I - Overview and Analytical Techniques

Paper 1 by H.N.G. Wadley gave an overview of IPM followed by a specific case study on the IPM of titanium matrix composites. Wadley indicated that IPM combines mathematical modeling of processes, sensing of material composition and microstructure and model predictive control for synthesizing materials. Wadley indicates that the motivation for the development of IPM is that successful high performance materials are engineered products with an optimum balance of cost and properties that make them best suited for a particular application. This balance of properties results in need for a "goal-state microstructure" because most properties are composition and structure sensitive. Since a combination of microstructural parameters must be optimized to achieve the best performance while at the same time keeping manufacturing costs at a minimum, the use of IPM is crucial to develop new process design methodologies. By using IPM, process design can be developed that incorporates the use of "microstructure sensors" that are used to directly sense the quality of the product being formed or processed. Using this sensor technology it can then be possible to attempt feedback control of the product's microstructure to attempt to control the problem of product performance variability. However, since there is no direct way to control microstructure or composition, this control is usually done using a model-based control approach. Thus, process modeling is a very important aspect of IPM. In those cases where the models are difficult to develop or very complex, various heuristic approaches are being used. Wadley then discussed the specific case of titanium matrix composite manufacture with emphasis on modeling the

consolidation step. He also discussed model-based process design of the variability of material properties due to consolidation. Finally, Wadley presented a discussion on methods of sensing microstructure, which involve both density sensors and fiber fracture sensors and feedback control during consolidation of the composites. Paper 2 by de Weijer discussed the use of artificial neural networks (ANN) to describe the relationships between the process-structure-property relationships in polyethylene terephthalate (PET) fibers. Paper 3 by Offergeld presented the practical results obtained during on-line optimization of injection molding processes. Their results showed that by using on-line optimization the productivity is increased by up to 20%. Paper 4 by Fitzpatrick and Lloyd was an overview of the work being done by Rolls Royce on electronically integrating engineering and manufacturing activities and incorporating process modeling to optimize the design and manufacture of hollow titanium fan blades. Paper 5 by Schnerr and Michaeli described a new method they developed that permits the prediction of the quality of injection molded plastic components from the knowledge of the process variables. The correlation can then be used to correlate the quality of the molded parts and the processing conditions used. With this technique for on-line quality control scrap production can be reduced

#### Session II and Session III - Metallic Materials Applications

Paper 6 by van der Wolk, Dorrepaal, Sietsma and van der Zwaag described a statistical model that has been developed to predict continuous cooling transformation (CCT) diagrams over a wide range of steel compositions. Both the position and the size of the phase fields in which phase transformations occur are well predicted. The CCT diagrams have been modeled using neural networks. This model reproduces the original CCT diagrams as well as predicts CCT diagrams for new steel compositions. Paper 7 by Malas and Frazier described the application of IPM for metal forging processes. This IPM system for forging consists of open-loop process design, feedback compensation, feedforward compensation and learning and adaptation systems. They pointed out that the nature of metalworking operations such as forging do not permit the straightforward application of IPM methods because of the difficulties associated with dynamic actuation and sensing capabilities. Malas and Frazier suggested that these restrictions can be overcome by designing the forming and heating operations for optimized sequential actuation and using process models and existent measurements for feedforward and feedback control. This paper described in some detail emerging design tools for forging process design. These tools include material processing maps, microstructural trajectory optimization, shape change optimization, equipment modeling and discrete event optimization. Finally Malas and Frazier described the current implementation challenges to IPM for forging. These challenges are development of in-situ sensors to measure grain flow pattern, residual stresses, microstructural characteristics and process parameters and the development of dynamic material behavior models. Paper 8 by Frazier, Waldman and Parrish described the development of an intelligent hot isostatic press (HIP) for processing powder materials. The intelligent HIP consisted of in-situ sensors, constitutive models and an intelligent control system. Eddy current sensors were developed to measure dimensional changes thus enabling the calculation of density changes. An



acoustic sensor was developed to measure grain size. The constitutive models were based on micromechanics principles and built upon Ashby's methodology of dividing HIP consolidation into two stages. The intelligent control system integrated process modeling and prediction, intelligent control algorithms and the in-situ sensors. It utilized a process design tool to assist in the design of HIP process schedules and to predict the density of the material following processing. Paper 9 by Ward, Johnson and Young described the use of process modeling and control for cold hearth refining of Ti-base intermetallic alloys. The process model was a 1-D qualitative model based on the empirical experience accumulated from much work on cold hearth melting of these materials. Paper 11 by Dubois, Moreau, Dawson, Militzer and Bussiere described the use of laser ultrasonics to measure the microstructure and phase changes in steels and also the sintering of powder metal iron compacts. This work established the capabilities laser ultrasonics for characterizing the microstructure in real-time during high temperature processing. Paper 12 by Bellot, Jardy, Bourguignon and Ablitzer described a model of titanium alloy melting by electron beam cold hearth melting (EBCHM) in order to eliminate hard alpha inclusions by dissolution or settling.

#### Session IV - Non-Metallic Materials Applications

Paper 14 by Shaurt, Johnston, Dexter, Marchello and Grenoble described automated fabrication technologies for producing high performance graphite-fiber reinforced polymer composite structures. The processes discussed were the fabrication of textile preforms by weaving and braiding in combination with vacuum assisted resin transfer molding (VARTM) and resin film infusion (RFI) as well as new developments involving automated tow/tape placement (ATP). Paper 15 by Pullen, Attwood, Partridge, Batchelor and Cracknell described work being done on real-time cure monitoring of polymer composites. The specific aspects of the work presented involved the relationship between cure cycle and mechanical properties, evaluation of the dielectric cure monitoring method and developing models for predicting and optimizing the cure cycle. Paper 16 by Nicholls, Pereira, Lawson and Rickerby described the development of process control models capable of predicting both the deposition rate and column inclination during the deposition of electron beam physical vapor deposition (EB-PVD) thermal barrier coatings. Paper 17 by Sayir and Farmer discussed laser heated oxide fiber growth using an innovative melt modulation technique. Paper 19 by Dublineau and Cinquin discussed work on the smart curing of composite materials using an autoclave.

#### Round Table Discussion

The discussion focused on the status of the various components of intelligent processing, e.g. modeling, sensors, etc. and the challenges and issues associated with commercializing IPM. Of particular note was the need to evaluate the dynamic effects on materials, to address the issues of scale-up, to evaluate new algorithms and to validate and evaluate novel low cost materials processing methods. The unique opportunities for IPM in helping to accelerate the movement of new advanced materials from the laboratory to use in both military and commercial systems was also discussed. Finally,

the issue of the use of IPM in reducing the cost of retrofitting aging systems with new advanced materials was discussed.

### Recommendations

During the Round Table Discussion a number of participants recommended that a Working Group be formed to develop and exchange "bench-mark" properties to be used for IPM. This is a key issue in exploiting and utilizing IPM on a larger scale. For example, one major roadblock to the wider use of IPM is the lack of data available for the dynamic processes involved in IPM. Another recommendation from the Round Table Discussion was that more use should be made of the Internet to exchange information, properties and testing techniques associated with IPM. Further work to couple process models with various optimization methods to be used for process design should be done. Such efforts are likely to lead to new processes that will profoundly improve the yield and quality of aerospace materials processing - particularly those systems that have been difficult to mature (e.g. the chemical and physical vapor deposition of coatings, cure of thick section composites and the isothermal forging/rolling of some titanium and nickel-base superalloys). In the sensor area, many potential non-destructive evaluation (NDE) methods can be adapted to sense important parameters in manufacturing processes. Further work in this area will make important contributions to the processing of aerospace structural materials. Least explored and developed is the coupling of models and sensors with new control concepts based upon nonlinear control theory, fuzzy logic, etc. This coupling has the potential to make revolutionary impact on processing and will enable the successful manufacture of materials hitherto considered too complex for military or commercial applications. They also promise to relax the considerable (post process) inspection cost burden borne by safety critical structural materials today.

# A Review of the Intelligent Processing of Materials and a Case Study of Titanium Matrix Composite Consolidation

Haydn N. G. Wadley and R. Vancheeswaran

Intelligent Processing of Materials Laboratory

University of Virginia,

Charlottesville, VA-22903

## ABSTRACT

The recent emergence of a general Intelligent Processing of Materials (IPM) methodology that combines mathematical modeling of processes, novel material composition/microstructure sensing and model predictive control for synthesizing high performance materials is reviewed. To illustrate its application, the IPM approach is applied to the consolidation of fiber reinforced metal matrix composites. The consolidation process seeks to eliminate matrix porosity while minimizing fiber microbending/fracture and the growth of reaction products at the fiber-matrix interface. By combining a model predictive process path planning concept with time dependent consolidation models, a method could be devised for optimal design of process schedules that evolve performance defining microstructural parameters of the composite (i.e. relative density, fiber fracture density and fiber-matrix reaction thickness) to pre-determined goal states resulting in composites of a desired mechanical performance. In the real world, the input material parameters used for the model are always stochastically distributed. This variability in the material parameters is shown to significantly affect the final microstructural states resulting in sometimes large reductions in the yield of the goal state material, even when the optimal process is used. By combining in-situ sensors that measure relative density and fiber fracture with model-based predictions of future evolution of the microstructural states, on-line control of the process inputs to drive the uncertain plant's microstructure to the desired goal state is shown to be possible. This increases process yield and can force process failures to only occur in ways that are easily inspected for after processing.

## 1. INTRODUCTION TO IPM

Intelligent Processing of Materials (IPM) has emerged as a new technology for designing and controlling the synthesis and processing of materials[1]. It is beginning to impact the design and manufacture of many of today's advanced materials; especially those whose performance is sensitively linked to their structure and composition. For example, it is used during (i) the forging/forming of aerospace alloys [2-5], (ii) the growth of ceramic fibers for high performance composites[6], (iii) the production of alloy powders used in aircraft engines[7-9], (iv) the manufacture of metal and ceramic matrix composites[10,11], (v) the deposition of coatings for oxidation protection[12], and (vi) the synthesis of high thermal conductivity substrates for the thermal management of multichip modules[13]. It is also being explored by the defense electronics community to improve the yield and performance of infrared imaging sensors[14] and to speed the development of new

device technologies based upon quantum well structures[15]. The primary metals industry also vigorously pursue its application.

Motivation for IPM's development has come from a dawning realization that successful high performance materials are engineered products with an optimum balance of properties (including cost) that make them best suited for a particular type of application. This balance of properties leads to a need for a "goal-state microstructure" because for the most part, properties are composition and structure sensitive. For instance, the high strength of Nextel 610<sup>TM</sup> fibers (manufactured by 3M Inc.) is derived from their fine grain size and small size of the flaw population. The spectral sensitivity of a  $\text{Hg}_{(1-x)}\text{Cd}_x\text{Te}$  infrared detector depends critically on controlling the value of  $x$  (the composition) and keeping second phase Te precipitates and dislocation contents low[16]. Likewise, a critical grain size is needed for  $\text{Si}_3\text{N}_4$  protective coatings since the oxidation rate varies by orders of magnitude when the grain size is changed[12], while the damage tolerance of metal matrix composites is lost when the fiber-matrix interface is allowed to form thick reaction products or the fibers are broken during processing[17].

Usually, a combination of microstructural parameters must be optimized to achieve best performance. As a result, today's successful high performance materials have to be processed so they always have the "engineered" composition and microstructure which give the properties that meet a design's specification. Ideally, they should do this within the smallest possible tolerances so that conservative "design factors" can be reduced or eliminated, and the material's performance fully exploited even in safety critical applications. Reducing or eliminating the need for preservice nondestructive inspection can also significantly reduce manufacturing costs.

Process design using Intelligent Processing of Materials concepts is one of several approaches used today to develop tomorrow's engineering materials base[1,18,19]. As a feedback control methodology, it is predicated upon the development of "microstructure sensors", Fig. 1. Many of the new microstructure sensor technologies were originally developed by the nondestructive evaluation community. Today, they are used to directly sense the product being formed and allow inference of its quality defining attributes[20]. For example, eddy current (proximity) sensors can be used during hot isostatic pressing [21,22] to measure the relative density of an initially porous body. Other sensors have been developed for detecting fiber fracture in composites [75], measuring liquid-solid interface velocities during the solidification of metals[23]

solid interface velocities during the solidification of metals[23] and semiconductors[24,25], deducing texture in rolled steel/aluminum alloys[26,27], characterizing grain size during recrystallization[28], and determining fiber diameter[29] and crystallographic orientation [30] during single crystal sapphire growth. When the appropriate sensor technology exists (or can be developed at a reasonable cost), it becomes possible to attempt feedback control of the product's microstructure and to therefore directly attack the problem of performance variability.

#### Intelligent Composite Consolidation Processing:

Robust interactive sensor-based guidance of material microstructure (properties) evolution toward a user-defined goal state

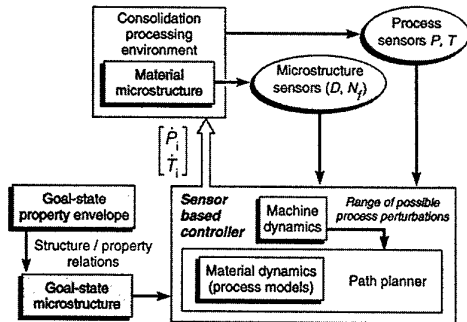


Fig. 1 The IPM loop for the consolidation processing of fiber reinforced MMC's.

However, this approach is not as simple as implementing feedback control of process variables (e.g. the temperature in a furnace). For one thing, there is no direct way to control microstructure or composition - the only variables available for direct actuation are the process conditions, i.e. heat flux distributions, gas/liquid flow rates, pressures, and so on. If the materials response to the change of process conditions (i.e. the material dynamics) can be sensed, the new sensor measurements can then be used for feedback control using a model based control approach.

Material dynamics are a (usually greatly simplified) mathematical description of the process. They capture the relationships between the variables one can directly actuate, the initial material condition and the microstructural quantities of interest. This process modeling has been an area of intense study during the past two decades and excellent models for many of the phenomena encountered in processing now exist. For example, the density of alloy powder preforms during hot isostatic processing (HIPing) or sintering can be predicted with models developed by Ashby and his coworkers[31]. The software for doing this on a personal computer is now widely available[32] and other software products are being introduced for handling more complex near net shape problems[33]. By numerically integrating these models, one can simulate the evolution of the process over time and so predict the materials dynamic response to processing. Knowledge of the machine's dynamic response (i.e. its heating and pressurization rate limits in the HIP case) then allows the prediction of the outcome of

any realizable process, and the possibility of implementing either of IPM's two modalities: (i) designing optimal process schedules via process simulation and/or (ii) using model-based feedback control to achieve goal-state microstructures[34].

In cases where the models are difficult to develop, or are too complex for treatment by the more formal methods alluded to above, other more heuristic approaches are being developed using neural nets[35], fuzzy-logic[36] and expert systems[37-39] and genetic algorithms. Indeed, it was an early reliance upon these artificial intelligence techniques for feedback control that led to the coining of the term Intelligent Processing of Materials.

## 2. TITANIUM MATRIX COMPOSITE MANUFACTURE

The designs of future high speed aircraft, missiles and propulsion systems have generated a need for stiff, strong, light, oxidation, and creep-resistant materials that can be used at high temperatures[40,41]. These needs cannot be satisfied by materials available today, and researchers are developing a variety of advanced composite materials composed of light metal/intermetallic matrices reinforced with silicon carbide or aluminum oxide fibers. The matrices of interest include conventional titanium (e.g. Ti-6Al-4V) or nickel alloys, as well as intermetallics.

Metal and intermetallic matrix composites are difficult to process. Contact between molten titanium alloys and ceramic fibers for more than a second or two results in aggressive chemical reactions, fiber dissolution, and a loss of critical matrix/fiber properties[42-45]. The result is a serious reduction of composite strength[46]. A variety of novel processing approaches are being developed to bypass this. They include foil-fiber-foil[47], vapor phase fiber coating[48-50], powder cloth[51], and molten droplet spray deposition[19]. Each reduces or even eliminates liquid matrix-fiber contact, but all require additional lay-up and consolidation process steps to achieve a near net shape composite.

The use of molten droplet spray deposition methods has shown significant early promise for the deposition of conventional and intermetallic titanium alloys on prealigned ceramic fiber arrays[19]. The result is typically a 200 $\mu$ m thick monolayer containing parallel, evenly spaced 140 $\mu$ m diameter SCS-6 silicon carbide fibers in a porous matrix, Fig. 2. The monolayers are layed-up to create a preform with the desired fiber architecture and they are then either hot isostatically or vacuum hot pressed to near net shape[52,53]. The mechanical properties of the composites formed in this way are determined by the initial properties of the constituent materials, i.e. those of the matrix, the fiber and the interface, and by the residual stresses/damage induced during processing[56, 57]. In particular, the matrix may not completely densify, extensive chemical reaction of the fiber's coating can occur[60] and the bending or even fracture of the composite's fibers can result in a dramatic loss of strength[61], Fig. 2. Mathematical models have been developed to predict the evolution of all the microstructural states [52-62].

The dependence of microstructural evolution upon processing condition history has now been analyzed and their dynamics captured in new process simulation tools[62]. These

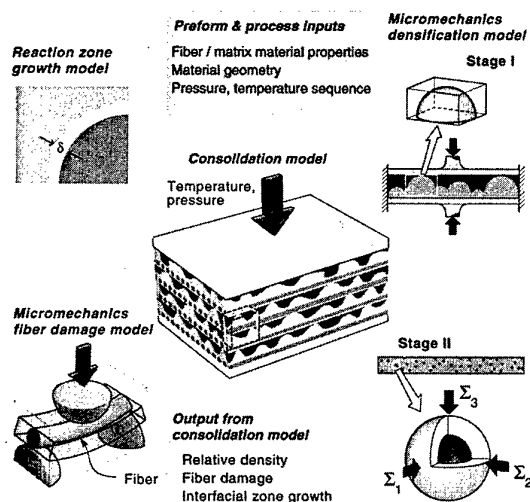


Fig. 2 The consolidation of a monotape lay-up can be modeled and simulated using (i) the properties of the constituent materials, (ii) the geometry of the composite preform and (iii) the input process schedules. Micromechanical models can be used to predict the densification and fiber damage response of the composite while a kinetic model is used to predict the reaction layer's thickness.

have been used to explore the processability of different composite systems, to identify optimum process schedules, and, in conjunction with microstructure sensors, they can now be used for model-based feedback control. Each is now reviewed in more detail as one example of the way in which the IPM approach can be applied.

### 3. MODELING THE CONSOLIDATION STEP

#### 3.1 Densification

Prior to consolidation, a plasma spray-deposited TMC monotape layup typically contains 35 to 45% internal porosity. Most of this porosity arises as a consequence of the surface roughness, the remainder is in the form of isolated voids within individual monotapes, Fig. 2. Upon application of an applied stress, the layup densifies by the inelastic flow of material into the internal voids and by deformation of surface asperities at places where adjacent monotapes are pressed into contact. Recently, a model has been developed[53-55] to predict the density of a TMC laminate as a function of the applied stress, temperature and time, given the constituent materials properties and the geometrical parameters of the monotape (e.g. its surface roughness distribution).

The complex internal deformation geometry problem is broken down by visualizing each composite monotape as consisting of two layers, or laminae, Fig. 2. One, referred to as the "r"-lamina (reinforced lamina) contains the array of fibers, has all smooth sides and typically contains about 10% internal porosity in the form of isolated voids (the exact amount depends on how the spray process was performed), the other,

referred to as the "s"-lamina (surface lamina), contains only the surface asperities. Densification of the s-lamina is treated in two stages: at lower relative densities ( $D^s_0 \leq D^s \leq 0.85$ ), where  $D^s_0$  is the initial relative density of the s-lamina), densification occurs by the blunting of asperities[54,55]. This is referred to as "Stage I" by analogy to the situation encountered in powder consolidation[31]. At higher densities ( $0.95 \leq D \leq 1$ ), where  $D$  is the matrix relative density), "Stage II" densification is more accurately described as the shrinkage of internal, closed voids. A smooth interpolation can be used to describe the transition between stages.

The densification of the r-lamina (and of the s-lamina during Stage II) occurs by the shrinkage of internal voids; these are assumed to be spherical, non-interacting and of uniform size. A homogenous stress distributions is assumed to induce their collapse. Potential functions can then be used to describe the density-dependent material response for mechanisms such as plastic yielding, power-law creep and diffusional flow [53]. The components of the deformation strain rate are given by the stress gradient of these potential functions. The total principal stress rate components within each lamina are the sum of the contributions from each of the mechanisms. Expressions have been developed that relate force and density for each of the dominant deformation mechanisms, i.e. plastic yielding, power law creep and diffusional flow. The overall densification response is obtained by integrating the densification components from the two geometric models (asperity blunting and void collapse) for each of the three densification mechanisms.

#### 3.2 Fiber Fracture

A fiber fracture model based upon micromechanical analyses of representative unit cells can be used to predict the overall response of a lay-up by calculating a sum of all the local (unit cell) responses[59]. The general form of the unit cell chosen for analysis consisted of a single fiber undergoing three-point bending due to forces imposed by (three) contacting asperities, Fig. 2. An important parameter that determines the response of a given unit cell is the length of the fiber segment in bending which is governed by the statistically distributed asperity spacing. The deflection of the ceramic fiber, which is regarded as deforming elastically under all conditions, is calculated using simple beam theory. From this deflection, the stress within the fiber can be calculated and, for a fiber of known diameter, elastic modulus and strength distribution, the probability of fracture can be determined.

The fiber deflection of a unit cell is described by a single ODE and is quite easy to compute. But the prediction of the overall rate of fiber fracture is quite complicated because as densification occurs, and monotapes are pressed together, the number of asperities in contact along the length of any given fiber continually increases. As these new contacts are established, existing bend segments become sub-divided into smaller (stiffer) cells. Thus, the statistical distribution of bend segment lengths is density-dependent and to calculate the number of accumulated fractures at any time, the creation, deflection and elimination of bend cells must all be tracked [59].

An important feature of the fiber fracture model is its dependence on densification; since the current density determines the number of bend cells, the distribution of cell lengths and the deformed heights of all unit cells, the density is used as an input to the fiber fracture model (instead of the applied pressure and temperature). This coupling of models is only one-way of satisfying this need; experimental densification data could also be used.

### 3.3 Reaction Zone Growth

At elevated temperatures, titanium alloy matrices always react with reinforcing fibers and their protective coatings. This eventually degrades the strength of the fiber, adversely affecting its properties. For example, it has been shown that in the Ti-24Al-11Nb/SCS-6 system, the sliding resistance of the fiber/matrix interface becomes too great (so that damage tolerance is lost) once the thickness of the reaction zone exceeds a critical value of about a micron [60]. Based on studies of several titanium matrix composite systems, including Ti-24Al-11Nb/SCS-6 and Ti-6Al-4V/SCS-6, the thickness of the reaction zone has been shown to follow a simple parabolic law with respect to time:

$$\delta = kt^{(1/2)}; \quad (1)$$

where  $k = k_0 \exp\left(-\frac{Q}{RT}\right)$ , in which  $k_0$  is the pre-exponential reaction (diffusion) mobility,  $Q$  is the activation energy for the reaction and  $T$  is the absolute processing temperature.

### 3.4 Process Simulation

A simulator of a consolidation process can be thought of as an input/output device which uses models for the microstructural variables (in this case relative density, fiber fracture density and reaction layer thickness), initial monolayer geometry and material parameters, and "admissible" input schedules (i.e. schedules that are constrained by limitations of the hot isostatic press or vacuum hot press) to predict the time-dependent microstructural evolution [62]. The simulations analyze the fundamental micromechanical/chemical problems encountered in consolidation so that the evolution of the material states can be predicted. The evolution of these states for any prescribed process cycle results in a temporal trajectory of the composite's density, fiber fracture and the reaction layer thickness at the fiber-matrix interface.

The simulation requires the input of various material parameters. Several of these are functions of temperature and stress and, therefore depend upon the temporally varying process conditions. Some (e.g. the Dorn constant,  $B$ , and the creep stress exponent,  $n$ ) are also matrix microstructure dependent [53]. Models have been developed to calculate the relevant microstructural features and update the resulting materials constitutive response [59]. A table of a plasma sprayed composite's material and geometric parameters is presented below in Table 1 [66]. The temperature,  $T(t)$ , and applied pressure,  $P(t)$ , schedules are defined as time-dependent functions whose absolute values and slew rates are constrained to lie between upper and lower limits.

**Table 1: Parameters used for Simulation Studies [62]**

Parameter (units)		Ti-6Al-4V
<b>Matrix Material Parameters</b>		
Melting temperature (K)	$T_m$	1941
Atomic volume ( $m^3/\text{atom}$ )	$\Omega$	$1.78 \times 10^{-29}$
Yield stress-temperature relation (MPa)	$\sigma_y$	$884.0 - 0.92T$
Young's Modulus-temperature fn. (GPa)	$E$	$115 - 0.056T$ $172.4 - 0.16T$
Power law creep constant ( $\text{MPa}^{-n}/\text{sec}$ )	$B_0$	$6 \times 10^{-17}$
Power law creep exponent	$n$	4.0
Power law creep activ. energy (KJ/mol)	$Q_c$	280
Pre-exp bound. diffusion mobility ( $m^3/\text{sec}$ )	$D_{\text{dob}}$	$1.015 \times 10^{-14}$
Activ. energy for bound. diffusion (KJ/mol)	$Q_b$	125
Pre-exp volume diffusion mobility ( $m^2/\text{sec}$ )	$D_{\text{ov}}$	$9.54 \times 10^{-8}$
Activ. energy for volume diff. (KJ/mol)	$Q_v$	152
Work-hardening exponent	$p$	0.3
Work-hardening coefficient (MPa)	$k$	3342
<b>Statistical Surface Roughness Parameters</b>		
Initial Density - s-layer	$D_o^s$	0.3
Initial Density - r-layer	$D_o^r$	0.92
Initial height of asperity (m)	$z_o$	$210.52 \times 10^{-6}$
Mean of asperity heights of s-layer (m)	$\bar{h}$	$91.06 \times 10^{-6}$
SD for asperity heights of s-layer (m)	$\sigma_h$	$39.82 \times 10^{-6}$
radius of s-layer (m)	$r$	$70 \times 10^{-6}$
Asperity radii exponential factor ( $\mu m^{-1}$ )	$\lambda$	0.0178
Areal density of asperities ( $\mu m^2$ )	$\gamma$	$5 \times 10^{-5}$
Lineal density of asperities ( $\mu m^{-1}$ )	$\rho$	$3.87 \times 10^{-3}$
<b>Mechanical Properties of the SiC Fiber</b>		
Diameter ( $\mu m$ )	$d_f$	142
Young's Modulus (GPa)	$E_f$	425
Reference Strength (GPa)	$\sigma_{ref}$	4.5
Weibull Modulus	$m$	13.0
<b>Kinetic Parameters for Matrix/Fiber Reactions in TMC</b>		
Activation Energy for the reaction (KJ/mol)	$Q$	209
Activ. Energy Pre-exp. Coeff. ( $m/\text{sec}^{0.5}$ )	$\kappa_0$	$2.27 \times 10^{-4}$

## 4. MODEL BASED PROCESS DESIGN

Simulation tools like the one above enable one to search for an acceptable process by trial and error. However, there is no guarantee that the human intuition that directs the search will lead to the discovery of the best process cycle. One ought to be able to do better by applying formal optimization methods [63]. In an more formal sense, we seek to find the process cycle that, for a given set of initial conditions,

material properties, and machine dynamics results in a user specified material goal state at process completion. This is called path planning and many different approaches have been developed by the controls community to optimally accomplish it [63].

The objective of path planning is the computation of a process schedule (i.e. process trajectory inputs) that transforms (using the input material and machine dynamics together with convex optimization, Fig. 1) a composite's microstructure from an initial state to a predefined (user chosen) "goal" state,  $x_g$ , at the end of the process cycle. We have explored one promising approach known as Model Predictive Planning (MPP)[63] which has the advantage of enabling one to exploit the predictive capabilities of a process model. Consider Fig. 3 which shows a trajectory resulting from the application of a temperature and pressure schedule (not shown). The material starts from an initial condition,  $x_i$ , in the lower left corner of the space at time  $t=0$ . As time elapses, the material structure moves along a trajectory like that shown in Fig. 3. The problem is to find a realizable process schedule,  $[T(t), P(t)]$ , that connects the initial state,  $x_i$ , to the goal state  $x_g$  subject to the limitations of the process equipment and a specified maximum process time.

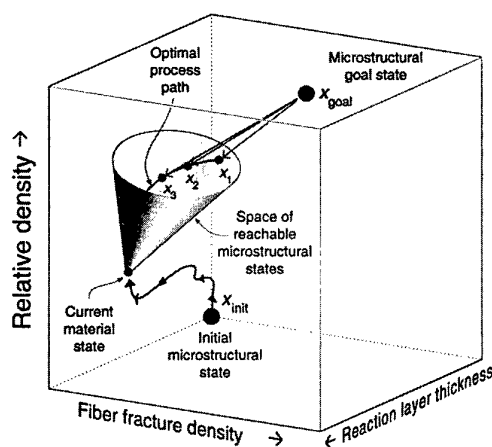


Fig. 3 The process path optimization problem encountered in consolidation processing of metal and intermetallic matrix composite

Suppose at a time  $t=t^c$ , the materials microstructural state is at  $x(t^c)=x^c$ . This point is labeled "current material state" in Fig. 3. Simple physical reasoning indicates that when following the trajectory away from the current point, one can only move toward increasing relative density, fiber fracture density, and reaction product thickness. Since the models mirror this physical reasoning,  $D(t)$ ,  $N_f(t)$ , and  $\delta(t)$  are monotonic, non-decreasing functions of time. This means that all physically feasible paths must lie in a conically shaped region originating from  $x^c$ . We call this the infinite

horizon (or infinite time) reachable set and denote it by  $R(x^c)$ . Approximations to  $R(x^c)$  are used in path-planning. The method we have explored constructs reachable set approximations from convex polytopes based upon local affine approximations of the dynamic equations. As the approximation is local, it can only be extrapolated a short time into the future. The method therefore takes many small steps toward the goal state and recomputes its approximation at each step. It is an example of a receding horizon strategy [34].

To illustrate the method's application, we path plan the process trajectory for a Ti-6Al-4V-matrix/SCS-6-fiber composite. We take as the goal state, a relative density of 0.999 which must be achieved while causing less than 1 fiber fracture/m and accruing less than  $0.5\mu\text{m}$  of reaction product thickness. The Ti-6Al-4V/SCS-6 system is quite processible and many schedules might accomplish it. Here we seek to find the schedule which minimizes the fiber fracture density while not exceeding the reaction layer thickness objective and force the process to terminate within 420 minutes. Placing the material system in a "nominal" HIP machine and applying the path planning method gives the result shown in Fig. 4. For this example, the desired density was reached while the goal states for fiber deflections (and thus the number of fiber breaks/m) and reaction product thickness were held at or below their target values.

Examination of the time plots in Fig. 4 indicates the planner computed a clever process schedule. First the temperature was ramped at the maximum (machine limited) rate until the soak temperature was reached. The planner then began ramping the pressure at the maximum rate. However, as the fiber deflections began to rapidly approach their goals, the planner actively adjusted the pressure. Because of the differing bending dynamics for fibers with varying span lengths, some cells slightly overshoot their deflection goals while many others barely reached them, Fig. 4(g). In trying to keep all the deflections near their goals while still pursuing densification, the planner "hunts" in pressure as it searches forward in time for a near optimal strategy. As densification progresses, the stiffness of the bending cells begins to rapidly increase, fiber fracture becomes less likely, and a "race" then develops between "densification to theoretical density" and "reaction product layer growth to the critical value". Since density depends on pressure while reaction layer thickness does not, the planner ramps the pressure at the maximum rate. It is plausible to assume that the process schedule so constructed is nearly time optimal since the planner keeps a constraint active at all times.

To understand why the MPP method works, one can view consolidation as a process in which fiber fracture and fiber-matrix reactions are failure mechanisms for the densification process. For processes of the type shown in Fig. 4, it is possible to plot surfaces of constant reaction layer thickness and fiber fracture density in a three dimensional ( $P_{rate}$ - $T$ - $t$ ) process space. Fig. 5 shows the projections of this 3-dimensional process space for the processing of a Ti-6Al-4V

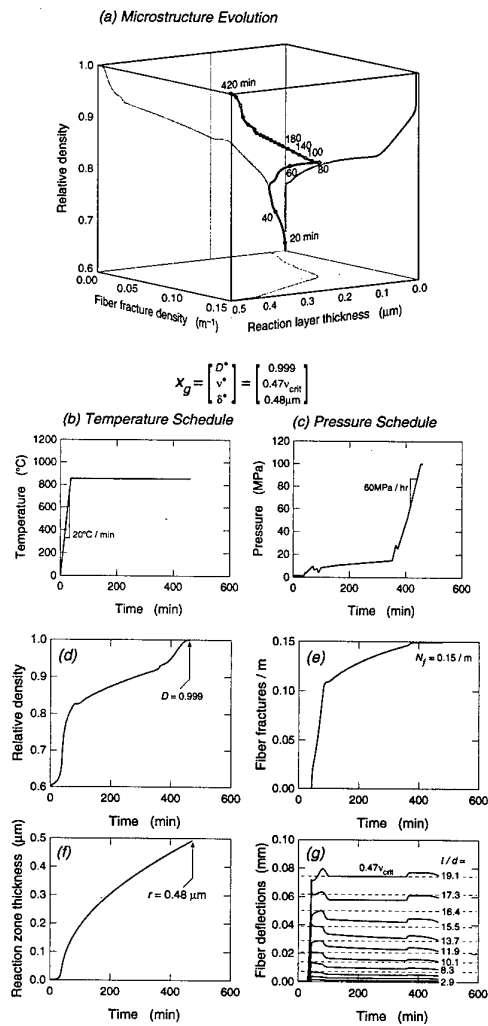


Fig. 4 The process path optimization problem encountered in consolidation processing of metal and intermetallic matrix composite

matrix reinforced with SCS-6 fibers. The failure surfaces shown correspond to  $N_f=1$  fracture/m and  $\delta=0.47\mu m$ .

When the optimal trajectory (shown by the black line) is superimposed on the failure surface of the process, the optimal process is seen to have found a way to avoid the fracture and reaction layer failure surfaces while still densifying the composite completely. In this case the trajectory is initially pressure rate limited by the fracture surface. However, after about 200 minutes of consolidation, the bound on pressurization rate disappears (see Fig. 5a.) and is replaced by the need to avoid reaction layer failure. The relatively low consolidation temperature and reactivity of the Ti-6Al-4V matrix enables this to be accomplished. The lesson to be drawn is that optimal processes hug first one failure surface and then jump to follow a second until the

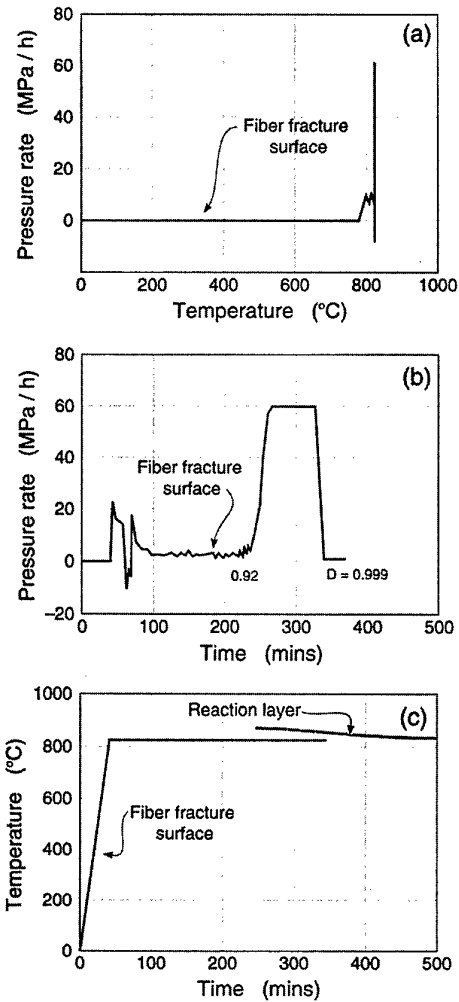


Fig. 5 Microstructure failure surfaces and the individual projections in process space for a Ti-6Al-4V/SCS-6 composite(60).

goal state is reached. The solutions to many optimization problems behave in this way. By mapping the failure surfaces in a process trajectory space, this simple graphical method can be used to estimate a near optimal process. This approach appears to be a useful approach for designing process trajectories for many other processes (e.g. designing a cooling path that avoids precipitation and cracking in tool steels).

## 5. VARIABILITY OF MATERIAL PROPERTIES

The consolidation model mentioned above contains material and geometry parameters that are likely to vary from sample to sample. For example, uncontrolled changes in temperature during the plasma spray process used to manufacture the tapes can cause the matrix grain size and thus the creep exponent to vary. Likewise, changes in the deposition rate of the CVD process used to grow SiC fibers results in vari-



ations in fiber diameter, internal stress and defect populations and therefore the Weibull parameters which characterize its strength. The effect of material parameter variability on the outcome of a process can be examined by stochastic modeling.

### 5.1 Prediction of Yield

To illustrate, a normal distribution was used to represent the variation of a material parameter. The mean of the normal distribution was chosen as the nominal (baseline) value, Table 1, that achieved the goal state using the optimized process designed in the previous section. The distribution's standard deviation,  $\sigma$ , was selected so that the  $\pm 3\sigma$  spread in property values corresponded to the expected level of uncertainty (Table 2) [72-74]. A random number was used to select a material and geometric parameter was made from the distribution, and a simulation was performed to determine the final state reached. This procedure was repeated many times and a distribution of the final material states determined.

**Table 2: Variable Parameters used for Simulation Studies [62,72-74]**

Parameter (units)	Sym.	Variation ( $\pm 3\sigma$ )
<b>Matrix Material Parameters</b>		
Yield stress-temperature relation (MPa)	$\sigma_y$	$884 \pm 20$
Power law creep exponent	$n$	$4 \pm 0.5$
Power law creep activ. energy (KJ/mol)	$Q_c$	$280 \pm 20$
<b>Mechanical Properties of the SiC Fiber</b>		
Diameter (mm)	$d_f$	$142 \pm 7$
Reference Strength (GPa)	$\sigma_{ref}$	$4.5 \pm 0.5$
Weibull Modulus	$m$	$13 \pm 3$
<b>Kinetic Parameters for Matrix/Fiber Reactions in TMC</b>		
Activ. Energy for the reaction (KJ/mol)	$Q$	$209 \pm 20$

The spread of the final microstructural attributes is plotted in Fig. 6. The criterion for an acceptable composite material with a relative density of above 0.995, a fiber fracture density of less than 1.0 break/m and a reaction layer thickness of less than 1.0  $\mu\text{m}$ . The process is assumed to be successful only when all of the microstructural attributes are satisfied. Analysis of the data in Fig. 6 indicates that the yield for this process was a disappointing 60.9%.

### 5.2 Parameter Perturbations

Some material parameters have a large effect upon the process variation. To find the sensitivity of the final microstructure to the individual parameter variations two sets of numerical experiments were conducted. For the first set of numerical experiments, only one material parameter was assumed to be stochastic and a deterministic nominal value was used for all the other parameters (the value in Table 1). The stochastic parameter was again assumed to follow a normal distribution with its mean and standard deviation defined in the same way as above. A Monte Carlo method was then

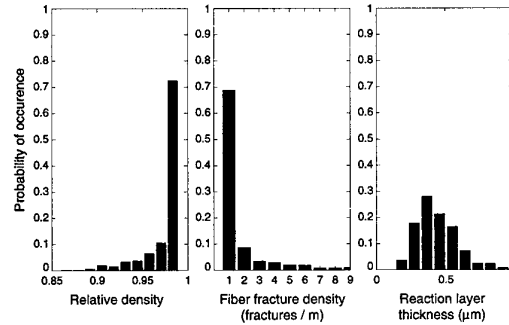


**Fig. 6** The microstructural attributes achieved from a system with stochastic material parameters when the optimal path planned schedule is used. The goal state used by the path planner is  $D_g = 0.999$ ,  $N_{fg} = 0.33/\text{m}$ ,  $\delta_g = 0.42 \mu\text{m}$

used to assign values to the stochastic material parameter and the simulation was re-run using the path planned schedule. The process was then repeated many times and the final state statistics recorded. The estimated material property extremes (i.e.  $\pm 3\sigma$  value of the distribution) for the stochastic material parameter were then changed and the experiment repeated. From the data, the mean and the standard deviation of each of the microstructural attributes was computed along with the yield (i.e. material whose states reached or exceeded  $x_g$ ), Table 3.

The yield was computed using a goal state defined by a density of 0.998 or greater, a fiber fracture density of less than 1.0/m and a reaction layer thickness less than 1  $\mu\text{m}$ . Table 3 shows the yield of the process for changes in each of the above material parameters. The analysis reveals that system was especially sensitive to variations in the matrix creep exponent.

In the second set of experiments, all the parameters listed in Table 2 were assumed to be stochastic and followed a normal distribution with their mean defined as their nominal value (Table 2) and the  $\pm 3\sigma$  values are the estimated material property extremes. This enabled a study of the effect of constraining or relaxing the variability of a single parameter on the final microstructure of a stochastic system. The optimal open loop path planned consolidation schedule was again used. Results are summarized in Table 4.

The yield was computed using a goal state defined by a density of 0.998 or greater, a fiber fracture density of less than 1.0/m and a reaction layer thickness less than 1  $\mu\text{m}$ . Table 3 shows the yield of the process for changes in each of the above material parameters. The analysis reveals that the system was especially sensitive to variations in the matrix creep exponent.

**Table 3: Effect of Single Parameter Variability on Final Microstructural States**

Matl. Par.	$\pm 3\sigma$	Yield	$D_f$	$N_f(m^{-1})$	$\delta_f(\mu m)$
[Units]		(%)	Mean (St. Dev)	Mean (St. Dev)	Mean (St. Dev)
$n_{crp}$	0.25	90.8	0.9987 (0.00028)	0.61 (0.9)	4.19e-7 (1.59e-9)
	0.50	73.0	0.9987 (0.00040)	4.13 (19.17)	4.18e-7 (3.46e-9)
	0.75	68.4	0.9987 (0.00039)	17.72 (54.75)	4.16e-7 (4.48e-9)
	1.00	64.0	0.9987 (0.00039)	44.8 (124.5)	4.14e-7 (7.04e-9)
$Q_c$ [KJ/mol]	5.00	100	0.9987 (0.00039)	0.323 (0.0745)	4.19e-7 (1.4e-9)
	10.0	99.6	0.9984 (0.00080)	0.343 (0.1597)	4.18e-7 (3.9e-9)
	15.0	95.8	0.9981 (0.00136)	0.401 (0.2954)	4.17e-7 (3.96e-9)
	20.0	90.4	0.9977 (0.00225)	0.523 (0.7476)	4.16e-7 (4.91e-9)
$Q_1$ [KJ/mol]	5.00	99.4	0.9989 (0.0)	0.3084 (0.0)	4.3e-7 (0.3e-7)
	10.0	99.6	0.9989 (0.0)	0.3084 (0.0)	4.3e-7 (0.68e-7)
	15.0	100.0	0.9989 (0.0)	0.3084 (0.0)	4.4e-7 (1.1e-7)
	20.0	100.0	0.9989 (0.0)	0.3084 (0.0)	4.5e-7 (1.5e-7)
$d_f$ [m]	1e-6	100.0	0.9989 (0.0)	0.312 (0.06)	4.19e-7 (0.0)
	3e-6	100.0	0.9989 (0.0)	0.3349 (0.135)	4.19e-7 (0.0)
	5e-6	100.0	0.9989 (0.0)	0.3621 (0.2)	4.19e-7 (0.0)
	7e-6	100.0	0.9989 (0.0)	0.42 (0.36)	4.19e-7 (0.0)
$m$	0.75	100.0	0.9989 (0.0)	0.3115 (0.059)	4.19e-7 (0.0)
	1.50	100.0	0.9989 (0.0)	0.335 (0.136)	4.19e-7 (0.0)
	2.25	99.80	0.9989 (0.0)	0.3621 (0.2013)	4.19e-7 (0.0)
	3.00	97.83	0.9989 (0.0)	0.4205 (0.3612)	4.19e-7 (0.0)
$\sigma_{ref}$ [MPa]	125	100	0.9989 (0.0)	0.3111 (0.0337)	4.19e-7 (0.0)
	250	100	0.9989 (0.0)	0.3155 (0.0660)	4.19e-7 (0.0)
	375	100	0.9989 (0.0)	0.326 (0.1104)	4.19e-7 (0.0)
	500	100	0.9989 (0.0)	0.3397 (0.1670)	4.19e-7 (0.0)

It is interesting to note that the combined variability of material parameters results in additional degradation of the predicted yield. Variability of the creep exponent had an especially severe effect on the fiber fracture density. The creep activation energy has a little less severe effect on the fiber fracture density, but was nonetheless important. It is evident that significant numbers of consolidation experiments will be unsuccessful

in reaching the goal state when variability exists in the input material parameters. Several strategies could be tried to overcome this issue. For example, better control of the prior process step would have a significant impact on the yield. In the section below, the alternative use of microstructure sensing and feedback control is explored.

**Table 4: Effect of Multiple Parameter Variability on Final Microstructural States**

Matl. Par.	$\pm 3\sigma$	Yield	$D_f$	$N_f(m^{-1})$	$\delta_f(\mu m)$
[Units]		(%)	Mean (St. Dev)	Mean (St. Dev)	Mean (St. Dev)
$n_{crp}$ [Unit-less]	0.25	77.3	0.998 (0.0002)	1.39 (3.23)	4.33e-7 (1.43e-7)
	0.50	66.3	0.998 (0.0002)	5.83 (21.25)	4.42e-7 (1.47e-7)
	0.75	59.6	0.998 (0.0002)	16.89 (54.47)	4.30e-7 (1.43e-7)
$Q_c$ [KJ/mol]	10	72.2	0.998 (0.0010)	4.91 (17.89)	4.51e-7 (1.47e-7)
	20	66.3	0.998 (0.0021)	5.83 (21.11)	4.41e-7 (1.47e-7)
	30	62.09	0.997 (0.0041)	7.65 (28.15)	4.42e-7 (1.5e-7)

## 6. MICROSTRUCTURE SENSING.

### 6.1 Density Sensor

During consolidation processing, the relative density can be deduced by measuring the volume or shape changes of the component. This can be accomplished during consolidation by using a multifrequency eddy current technique [21, 22, 64]. The probes measure the separation distance between a fixed probe-tip and the (changing) position of the sample surface near the probe tip [22]. Pairs of probes maintained a fixed (or known) distance apart then allow determination of a component's thickness thereby behaving as eddy current calipers. The response of these eddy current probes depends upon the probe's design/operating frequency, the electrical/magnetic properties of the component, and the component's shape in the vicinity of the probe. Relationships between these parameters and the impedance of the probe/test circuit have been investigated to perfect the sensor's design and develop algorithms to analyze multifrequency impedance data so that the component's dimensions may be deduced to the needed level of precision for model verification or feedback control [65-69].

Normally, a two-coil design for each probe is used so that to first order, the measured response is, independent of temperature (this avoids the need for active cooling of the sensor which is impractical in the HIP environment). The primary coil of the sensor, is connected to a variable frequency oscillator with optional power amplification. The current ( $I_p$ ), that flows in the solenoid generates an electromagnetic field, a fraction of which links the sample of interest and the secondary coil. By measuring the voltage drop ( $V_p$ ), across a precision resistor ( $R$ ) to ground, the value of the primary current ( $I_p$ ) can be continuously monitored. The fluctuating electromagnetic field associated with the primary current induces eddy currents in the nearby conducting sample. The eddy cur-

rents, whose magnitude depends upon the rate of change of flux (which increases with frequency), act to oppose the change in field (Lenz's law) and thereby perturb the field of the primary coil. The perturbed field can be conveniently measured with a second coil aligned coaxially with the primary. The voltage induced in the secondary coil ( $V_s$ ), though small can be amplified, and if measured with a high impedance instrument, is independent of the secondary windings resistance, and thus the sensor's temperature. The ratio  $V_s/V_p$  defines a sensor gain ( $G$ ), and the difference in phase between primary and secondary,  $\phi = \phi_s - \phi_p$ , defines the measured phase. Then at any measurement frequency, the complex impedance components can be found from:

$$\begin{aligned} \text{Real}Z &= (G/G_0)\sin(\phi - \phi_0) & ; \\ \text{Imag}Z &= (G/G_0)\cos(\phi - \phi_0) \end{aligned} \quad (2)$$

where the subscript zero refers to the values of an empty coil located far from any conductor.

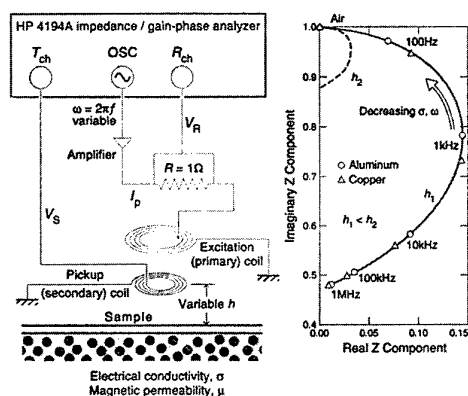


Fig. 7 The eddy current probe sensors measurement principle. If the sensor is at a fixed position, movement of the sample surface normal to the sensor changes  $h$ , and therefore the sensor's response.

The impedance normalized by the empty coil value is plotted on the right in Fig. 7 for two different distances ( $h$ ) above a uniform conductor with the electrical conductivity of copper. At low frequencies, the rate of change of flux is small, and the eddy current density is low, but is distributed deeply within the sample because the skin depth  $\delta$  is large (recall that  $\delta = (2/\omega\sigma\mu)^{1/2}$  where  $\omega$  is the radial frequency,  $\sigma$  the conductivity and  $\mu$  the sample's permeability). At low frequencies there is quite a large change of phase because the flux deeply penetrates the conductor, but almost no eddy current losses occur because the eddy current density is small, so the impedance is almost purely inductive (imaginary). As the frequency is increased, eddy current densities increase resulting in greater losses that are reflected by the increase in the real part of  $Z$ . The imaginary component decreases because the flux does not penetrate as deep into the sample. At very high frequencies,

the skin effect limits the depth of flux penetration severely, and the total eddy current losses also decrease because the volume supporting the eddy currents becomes very small, and overpowers the increase in current density associated with the now very high rate of flux change. In the limit, the eddy current losses go to zero and the impedance curve intersects the imaginary axis at a value determined by the ratio of the flux linking the sample and the secondary coil to the total flux. Thus, as the sample densifies, and its surface moves away from the sensor, fewer flux lines link the sample and the high frequency intercept moves towards the origin at ( $Z=0+1j$ ).

## 6.2 Fiber Fracture Sensor

Fiber fracture during the consolidation of metal matrix composites can be sensed by detecting the acoustic emissions (elastic waves) generated when a stressed fiber fractures [75]. For detection of the fiber breaks that occur during consolidation, a high temperature wave guide was attached to the HIP canister in the "hot" zone of the hot isostatic press (HIP). This waveguide propagated the elastic signal to a relatively cool region ("cold" zone) within the pressure vessel (See Fig. 8) that remained below 35°C. A resonant piezoelectric transducer was then attached to the cold end of the wave guide to measure the acoustic emission signal. The signal was transferred via a thermocouple feedthrough port in the base of the HIP and was then read into a high band pass A/D converter and the signature recorded on a personal computer. Only the acoustic signals that were higher than an experimentally determined magnitude where fiber breaks occur were saved in the computer and at that time the acoustic signal's RMS voltage was calculated and recorded.

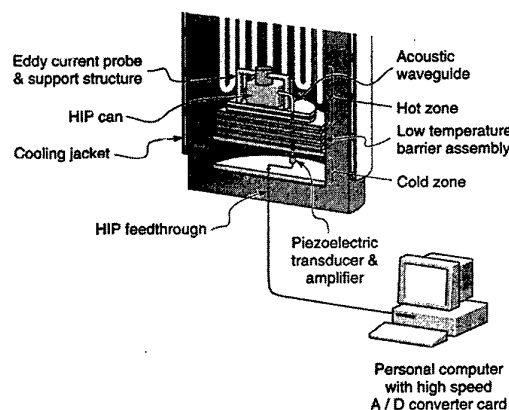


Fig. 8 A schematic of the acoustic emission sensor and its placement in the HIP furnace.

## 7. FEEDBACK CONTROL

During consolidation of composites the dynamics are nonlinear, irreversible, and change as the density increases [62,63]. Since an optimal controller depends on the dynamics it will vary as the process (i.e. density) progresses. This complicates the design of a feedback control algorithm. However,

the dynamics of composite consolidation are fairly slow (i.e. the process requires several hours to complete), and so a relatively small closed-loop bandwidth is required for successful control. As a result, the Nyquist sampling rate of the process by the sensors can be low, and ample time (1-2 minutes) is available for computations (i.e. solving a convex optimization problem) inside the time cycle of the control loop. In view of this, it is logical to consider controller architectures that might normally be too computationally intensive for processes requiring faster sensor sampling rates. For example, sufficient time exists to compute an optimal control for the remainder of the process. A second difficulty arises because direct actuation of the microstructural state is not possible. Instead, microstructure manipulation is achieved by changing the process variables. Since the process models link process variable trajectories to the microstructural states, a model based control approach appears feasible, Fig. 9. In the scheme implemented, a path planner is embedded in the controller [70]. The control architecture seeks to constantly form a local linearization of the material dynamics which is then used to compute an optimal temperature and pressure schedule for the remainder of the process that steers the current material state,  $(x_h)$  to the desired goal state  $x_g$ .

The basic design of the controller is shown in Fig. 9. It uses an estimator to predict the responses of the microstructural attributes including like the reaction layer thickness that cannot be sensed. The estimator uses the process models to estimate future material states given the present estimated states  $\hat{\delta}$ , the sensed process states  $(T, P)$  as well as the current values of the actuator inputs  $(\dot{T}, \dot{P})$ . In this case, the states (both estimated and sensed) are fed back to the controller which then drives the system to the desired goal state. Because the composite's response to consolidation variables evolves during the process, the controller is continuously redesigned (using new local linearizations of the system) as the process progresses through the consolidation cycle.

Six steps are used to construct the model predictive control algorithm [63]:

**Step 1: Normalization** First a change of variables is made to the material model so that the states and process inputs lie in the interval  $[0, 1]$ . This enhances the numerical conditioning of a subsequent convex program (Step 6).

**Step 2: Cascade Connection** The material model is cascaded with the machine model to obtain an overall (plant) model.

**Step 3: Local Affine Approximation** An affine approximate model can be constructed around the current material microstructural state and current process environment by taking a first-order Taylor approximation of the vector field. If  $x^c$  is the current plant state, we can denote deviations from this state as  $(\tilde{x} = x - x^c)$ . A linear approximation can then be written:

$$\frac{d\tilde{x}}{dt} = A\tilde{x} + Bu + C \quad (3)$$

where  $A$  and  $B$  are the partials of the vector field with respect

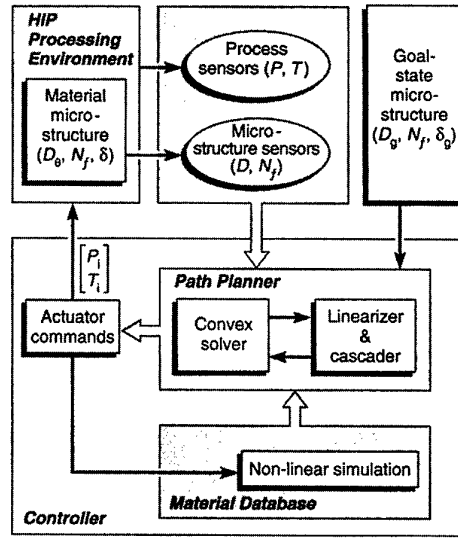


Fig. 9 System after closing loop with a nominal controller. Predictive models for microstructure evolution, sensor response, and actuation dynamics are combined with convex optimization methods to plan process schedules that result in a target microstructure

to the state vector  $(\tilde{x})$  and input vector  $u$  respectively.  $C$  is a drift vector that remains at the operating point,  $C = F(x^c, 0)$  which gives an affine local approximation. The derivatives required to evaluate the matrices  $A$  and  $B$  and the vector  $C$  can be computed once, off-line. Since  $x^c$  cannot be an equilibrium point of the plant model unless the current temperature and pressure are both identically zero,  $C$  appears additively in (3).

**Step 4: Discretization in Time** Discretizing (3) in time by a Forward Euler method gives a recursion equation:

$$\tilde{x}((k+1)T) = (I + TA)\tilde{x}(kT) + TBu(kT) + TC \quad (4)$$

where  $T$  is chosen as the sampling interval. Propagating this discrete equation forward starting from  $\tilde{x}(0) = 0$  yields

$$\tilde{x}(\Delta t) = \sum_{k=0}^{N_t-1} T(I + TA)^{N_t-1-k} (Bu(k) + C) \quad (5)$$

where  $N_t = \frac{\Delta t}{T}$ . At time  $t^c$ , the model state is  $x^c$ , and the HIP machine is commanded for a finite horizon interval  $\Delta t$  with the slow rate control

$$u(t) = u(k) \text{ for } kT \leq t \leq (k+1)T, \quad (6)$$

where  $k=0,1,2,\dots, \frac{\Delta t}{T} - 1$ . Thus the model approximation for state  $x$  will be:

$$x(t^c + \Delta t) \approx x^c + \sum_{k=0}^{N_t-1} T(I + TA)^{N_t-1-k} (Bu(k) + C) \quad (7)$$

The set of states that can be reached using (7) given that the bounds on the inputs (7) and the finite horizon  $\Delta t$ , yields an approximation to the conically shaped region shown in Fig. 3.

**Step 5: Local Planning by Convex Optimization** The approximate reachable set, defined by (3) and (4-7) is a convex polytope, so locally feasible controls can be found by solving a convex feasibility problem. Locally optimal controls can be found by minimizing a convex objective function over this convex polytope. The decision variables in the program are the values of the inputs over the finite horizon as shown in (7). Since we seek to steer  $x_h(t) \rightarrow x_g$ , a logical choice of convex objective is a weighted Euclidean distance between  $x_h(t)$  and  $x_g$  which leads to a quadratic program which can be efficiently solved. The objective presented to the local convex solver is

$$E = \sum_{k=1}^{N_t} \frac{k}{N_t} [x_h(kT) - x_g]^T W [x_h(kT) - x_g] \quad (8)$$

which is a weighted sum of the distance between the goal state and the projected future material states (based on the affine approximation). The factor  $k/N_t$  in the summation of the objective function places higher weight on plant states farther in time from the current state  $x^c$ , and makes the planner more aggressive in reducing the total duration of the process schedule. The planner attempts to densify the layout while not deflecting/fracturing fibers and not accruing unacceptable amounts of reaction product. The weighting matrix  $W$  in the objective function allows a trade-off between the competing goals to be made quantitatively. Necessary and sufficient conditions satisfied by a minimizer of (8) subject to (7) and (4-7) are given by the Kuhn-Tucker equations [71], and the solution can be found using constrained optimization. We mention that sequential quadratic programming (SQP) methods are applicable, and they give superlinear convergence by using a quasi-Newton updating procedure for accumulating second order information. The method described is thus suitably fast for on-line implementation[71].

**Step 6: Local Control Application** Once the optimal values of  $u(k)$  are found, the actuator control  $u(k)$  (6) is applied for the first interval  $T$  to the perturbed plant (nonlinear simulation). This is then integrated forward by a suitable numerical method (e.g. Runge Kutta) to give a new current state,  $x^c$ , and we then return to Step 4. The stopping criterion is a suitably small objective value indicating nearness to the goal  $x_g$ , or the passing into a state from which the goal state  $x_g$  cannot be reached.

To drive the regulated variables ( $D, v, \delta, T, P$ ) to their goal ( $x_g$ ), a convex solver was used to optimally compute the control actions for a finite time look ahead horizon. The convex program was set up to minimize an objective function (in this case a weighted sum of the Euclidean distance between the goal state and the projected future states) to select the "best" control action (locally). Moderately sized convex programs (with 20-50 variables and 40-100 constraints) can be solved easily in the available time. Once the actuation vector ( $u(k)$ ) was found from the optimization, it was applied to the plant (HIP process) until the next sampling of the process, whereupon the process was repeated.

To explore the consequence of implementing feedback control of density and fiber fracture, we first conduct a nonlinear simulation (using the set of nominal parameters in Table 1) to simulate the states. The numerical experiments performed sought to establish the benefit of density and fiber fracture sensor-based control actions when variability existed in the material parameters. An ideal filter was assumed that maps the acoustic emission fiber fracture sensor measurement to fiber deflections.

A random selection of material parameters was made from the distribution defined in Table 2 and a numerical experiment conducted using feedback control to determine the process schedule which is needed to drive the process to the (user defined) goal state. The simulation was allowed to run for a variety of fixed times upto a maximum of 20 hours. This process was then repeated using another sampling of the material distribution. The statistical outcome of the process is displayed in. A large increase in yield (37.4%) resulted from sensing the microstructural states and using the sensor measurements for feedback control when the maximum consolidation time was 20 hours.

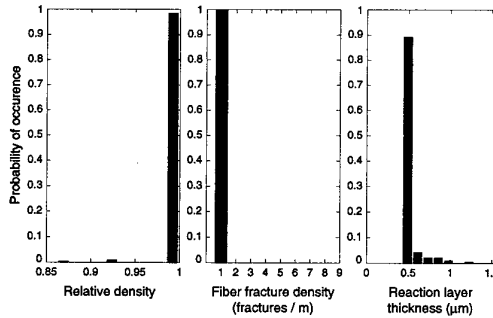


Fig. 10 The microstructural attributes achieved from a system with stochastic material parameters when the density and fiber fracture (and fiber deflections) are sensed and a model based feedback controller is used. The goal state used by the path planner is  $D_g = 0.999$ ,  $N_{fg} = 0.33/\text{m}$ ,  $\delta_g = 0.42 \mu\text{m}$ . The yield achieved after 20 hours of processing is 98.2%

To compare the final microstructure reached with the open loop simulations and closed loop simulations, the deviation of the final microstructural state from the final microstructure of

the nominal material is plotted in Fig. 11. The spread in process end points about the origin is clearly reduced when feedback control is implemented. It is interesting to note that the

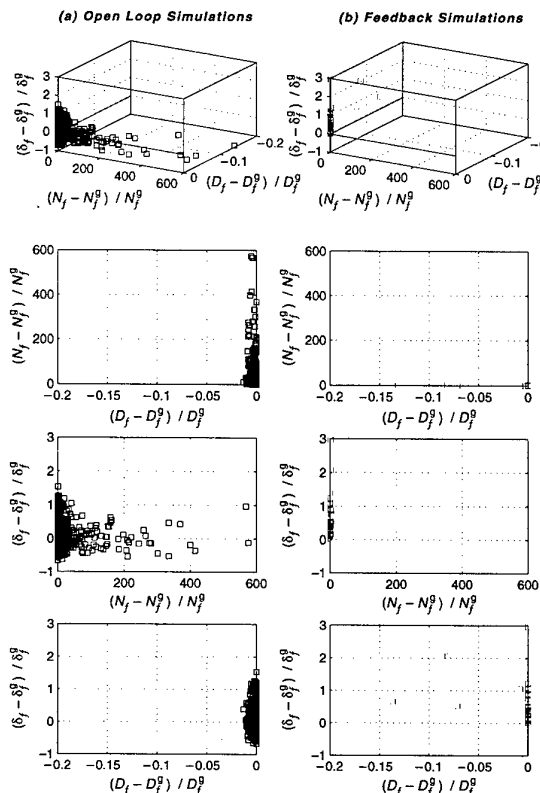


Fig. 11 A comparison of scatter plots showing the deviation of the end point states reached by a Ti-6Al-4V/SCS-6 material system with stochastic material parameters. The open loop simulation used the optimal path planned schedule as an input. The feedback control system used the density and fiber fracture (and deflection data) for sensing and feedback. The goal state was  $D_g = 0.999$ ,  $N_g = 0.33/\text{m}$ ,  $\delta_g = 0.42 \mu\text{m}$

open loop simulations have a large spread in fiber fractures (Fig. 11e). This occurred because the path planner had no way of knowing the inelastic stiffness of the system and blindly followed the path planned schedule. Feedback nearly completely eliminated this effect, and very little fiber fracture density resulted (Fig. 11f). Occasionally, the feedback approach failed to fully densify the composites. This was less rarely encountered in the open loop simulations. The reason for this behavior is that for very creep resistant matrices, the feedback simulation continues to realize that the fiber deflection cells are at or very near their goal state deflections and avoids increasing the pressure (which would cause fiber fracture) to reach the density goal. The problem was compounded when the maximum time for the process was decreased. When the maximum consolidation time was decreased to 600 minutes,

the yield dropped from 98.2% to 80.9%. For the most creep resistant matrices, the time constraint was reached before the composite could be completely consolidated. As the time constraint was relaxed, the spread in final density was reduced. However, this occurred at the expense of the unsensed) growth in interfacial reaction layer thickness. Interestingly, the control design can be used to force process failures that are potentially detectable (i.e. relative density) with non-destructive evaluation techniques. Reaction layer thickness and the many broken fibers of an open loop process scheme are harder to detect than a voided matrix.

## 8. CONCLUSIONS

Intelligent Processing of Materials has been shown to be a new way of designing and controlling materials synthesis and processing. It is beginning to impact a broad spectrum of materials and processes. Predictive process modeling combined with convex optimization techniques allows materials engineers to rapidly design processes that result in the attainment of a goal state microstructure - a key step in the development of a processing technology that enables the high yield manufacture of engineered materials. When microstructure sensors are available, a new type of IPM feedback control methodology becomes feasible. The first steps in this direction have been made and several approaches appear to hold promise. The application of this IPM control approach is paced by the development of microstructure sensors. As the materials community finds ways to exploit non-invasive sensor techniques based on eddy currents, laser ultrasonics, dielectric spectroscopy, microwave reflectivity, ellipsometry, etc. to inexpensively satisfy these microstructural monitoring needs, the extension of IPM as a feedback control method is likely to grow rapidly because of its potential to increase yield, reduce process costs and more rapidly realize the significant benefits of new high performance materials.

## Acknowledgements

We are grateful for support of this work by the Advanced Research Projects Agency (A. Tsao, Program Manager). The helpful comments and discussions of D. M. Elzey (University of Virginia), D. G. Meyer (University of Colorado) and R. L. Kosut (SCSolutions Inc., Sunnyvale, CA) are gratefully acknowledged.

## References

1. H.N.G. Wadley and W.E. Eckhart, JOM, **41**, (10), 1989.
2. W. M. Mullins, R.D. Irwin, J. C. Malas and S. Venugopal, Scripta Mater., Vol. 36, No. 9, pp. 967-974, 1997.
3. S. Venugopal, E. A. Medina, J. C. Malas, S. Medeiros, W. G. Frazier, W.M. Mullins, & R. Srinivasan, Scripta Mater., Vol. 36, No. 3, pp. 347-353, 1997.
4. J.C. Malas, W.G. Frazier, S. Venugopal, E.A. Medina, S. Medeiros, R. Srinivasan, R.D. Irwin, W.M. Mullins, and A.B. Chaudhary, Met. Trans B, *In Press*, 1997.
5. W. G. Frazier, R.D. Irwin, E. A. Medina and J. C. Malas, J. of Mater. Engg. and Perf., Vol 6, No.2, pp. 153-160, 1997.
6. D.G. Backman, D. Wei, L.C. Filler, R. Irwin and J. Collins, in "Advanced Sensing, Modelling and Control of Materials

- Processing," Ed. by E.F. Matthys and B.G. Kushner, TMS (Warrendale), p. 3, 1992.
7. S.D. Ridder, S.A. Osella, P.I. Espina and F.S. Biancaniello, in "Thermal Structures and Materials for High-Speed Flight," Ed. by E.A. Thornton, AIAA (Washington, D.C.), p. 499, 1992.
  8. B.G. Kushner and R.J. Schaefer, in "Intelligent Processing of Materials," Ed. by H.N.G. Wadley and W.E. Eckhart, TMS (Warrendale), p. 55, 1990.
  9. R.J. Schaefer, in "Thermal Structures and Materials for High-Speed Flight," Ed. by E.A. Thornton, AIAA (Washington, D.C.) p. 523, 1992.
  10. D.G. Backman, E.S. Russell, D.Y. Wei and Y. Pang, in "Intelligent Processing of Materials," Ed. by H.N.G. Wadley and W.E. Eckhart, TMS (Warrendale), p. 17, 1990.
  11. H.N.G. Wadley, D.M. Elzey, L.M. Hsiung, Y. Lu and D.G. Meyer, in "Monograph on Flight-Vehicle Materials, Structures and Dynamics Technologies - Assessment and Future Directions," Ed. by A.K. Noor and S.L. Venneri, In Press, 1994.
  12. J.R. Strife, W.Y. Lee, R.D. Veltri, C.F. Sack, R.J. Kee, G.H. Evans, R.S. Larson, D.S. Dandy, M.E. Coltrin, P. Ho and R.J. Buss, in "Thermal Structures and Materials for High-Speed Flight," Ed. by E.A. Thornton, AIAA (Washington, D.C.) p. 485, 1992.
  13. M.E. Coltrin, unpublished work.
  14. D.E. Witter, in "Intelligent Processing of Materials," Ed. by H.N.G. Wadley and W.E. Eckhart, TMS (Warrendale), p. 91, 1990.
  15. Y. Lu, M.V. Moore, D.T. Queheillalt, and H.N.G. Wadley, in "Proceedings of Review of Quantitative Nondestructive Evaluation, Vol 13," Ed. by D.O. Thompson and D.E. Chimenti, (NY), 1994.
  16. R.M. Wood, "Optical Materials," Institute of Materials (London), p. 80, 1993.
  17. P.E. Cantonwine, Master of Science Thesis, University of Virginia, 1993.
  18. P.A. Parrish and W.G. Barker, JOM, 42 (7), p. 14, 1990.
  19. D.G. Backman, JOM, 42 (7) p. 17, 1990.
  20. R. Mehrabian and H.N.G. Wadley, JOM, 37 (2), p. 51, 1985.
  21. A.H. Kahn, M.L. Mester and H.N.G. Wadley, in "Proc. 2nd International Conference on Hot Isostatic Pressing," Ed. by R.J. Schaefer and M. Linzer, ASM (Metals Park), p. 341, 1989.
  22. K.P. Dharmasena and H.N.G. Wadley, in "Review of Progress in Quantitative NDE," Vol 10B, Ed. by D.O. Thompson and D.E. Chimenti, Plenum Press, (NY), p. 1757, 1991.
  23. F.A. Mauer, S.J. Norton, Y. Grinberg, D. Pitchure and H.N.G. Wadley, Met. Trans B, 22B, p. 467, 1991.
  24. K.P. Dharmasena and H.N.G. Wadley, J. Crystal Growth, p. 553, 1993.
  25. K.P. Dharmasena and H.N.G. Wadley, J. Crystal Growth, 1996, In Press.
  26. R.B. Thompson and A.V. Clark, in "Intelligent Processing of Materials," Ed. by H.N.G. Wadley and W.E. Eckhart, TMS (Warrendale), p. 227, 1990.
  27. R.B. Thompson, S.S. Lee and J.F. Smith, Ultrasonics, 25, p. 133, 1987.
  28. C.B. Scruby, Private Communication, 1994.
  29. D.G. Backman, D. Wei, L.C. Filler, R. Irwin, and J. Collins, in "Advanced Sensing, Modelling, and Control of Materials Processing," Ed. by E.F. Matthys and B.G. Kushner, TMS (Warrendale), 1992.
  30. H.N.G. Wadley, Y. Lu and J.A. Goldman, JNDE, In Press, 1994.
  31. W.B. Li, M.F. Ashby and K.E. Easterling, Acta Metallurgica, 35, p. 2831, 1987.
  32. M.F. Ashby, HIP 6.0 Software for HIP Diagrams, Dept. Eng., Univ. of Cambridge, UK, 1990.
  33. L. Christodoulou, BDM Product Sheet, 1993.
  34. D.G. Meyer and H.N.G. Wadley, Met Trans B, 24B, p. 289, 1993.
  35. S.A. Osella, in "Intelligent Processing of Materials," Ed. by H.N.G. Wadley and W.E. Eckhart, TMS (Warrendale), p. 339, 1990.
  36. A.L. Moran and D.R. White, JOM, 42 (7), p. 21, 1990.
  37. V.V. Badami, P. Nielsen and J.B. Comly, in "Intelligent Processing of Materials," Ed. by H.N.G. Wadley and W.E. Eckhardt, TMS (Warrendale), p. 369, 1990.
  38. S.B. Dolins and J.D. Reese, in "Intelligent Processing of Materials," Ed. by H.N.G. Wadley and W.E. Eckhardt, TMS (Warrendale), p. 385, 1990.
  39. M. Makhlof, R. Makhlof, R.K. Heinzmann, J. J. Baush, R.D. Sisson, in "Advanced Sensing, Modelling and Control of Materials Processing," Ed. by E.F. Matthys and B.G. Kushner, TMS (Warrendale), p. 223, 1992.
  40. D.L. Anton and D.H. Shah, in "MRS Symposium Proceedings", 133, Ed. C.T. Liu, A.I. Taub, N.S. Stoloff, and C.C. Koch, MRS (Pittsburgh), p. 361, 1989.
  41. J.R. Stephens, in "Metal and Ceramic Matrix Composites: Processing, Modelling and Mechanical Behavior," Ed. by R.B. Bhagat, A.H. Clauer, P. Kumar, and A.M. Ritter, TMS (Warrendale), p. 3, 1990.
  42. N.A. James, D.J. Lovett, and C.M. Warwick, in "Composites: Design, Manufacture and Application, ICCM VIII," Ed. by S.W. Tsai and G.S. Springer, SAMPE, 2 (19), p. 11, 1992.
  43. M.S. Misra and S.G. Fishman, *ibid*, p. 18A1.
  44. T. Onzawa, A. Suzumura, and J.H. Kim, *ibid*, p. J1.
  45. W.J. Whatley and F.E. Wawner, J. Mater. Science Letters, 4, p. 173, 1985.
  46. S. Ochiai and Y. Murakami, J. Mater. Science, 14, p. 831, 1979.
  47. D.R. Schuyler, M.M. Sohi, and R. Mahapatra, in "Interfaces in Metal-Ceramic Composites," Ed. by R.Y. Lin, R.J. Arsenault, G.P. Martins, and S.G. Fishman, TMS (Warrendale), p. 475, 1989.
  48. D.A. Hartwick and R.C. Cordi, in "Intermetallic Matrix Composites," Ed. by D.L. Anton, P.L. Martin, D.B. Miracle, and R. McMeeking, MRS (Pittsburgh), 194, p. 65, 1990.
  49. P.G. Partridge and C.M. Ward-Close, Int. Mat. Rev., 38, p. 1, 1993.
  50. H.E. Deve, D.M. Elzey, J.M. Warren, and H.N.G. Wadley, in "Proceedings of 8th CIMTEC World Ceramic Congress and Forum on New Materials," Ed. by P. Vincenzi, 1994 (In Press).
  51. P.K. Brindley, in "High Temperature Ordered Intermetallic Alloys II," Ed. by N.S. Stoloff, C.C. Koch, C.T. Liu, and O. Izumi, MRS (Pittsburgh), 81, p. 419, 1987.
  52. D.M. Elzey, J.M. Kunze, J.M. Duva, and H.N.G. Wadley, in "Mechanical Properties of Porous and Cellular Materials," 207, Ed. L. Gibson, D.J. Green, and K. Sieradzki, MRS (Pittsburgh), p. 109, 1991.

53. D.M. Elzey and H.N.G. Wadley, *Acta Metall. et Mater.*, **41** (8), p. 2297, 1993.
54. R.S. Gampala, D.M. Elzey & H.N.G. Wadley, *Acta Metall. Mater.*, **42** (9), pp. 3209-3221, 1994.
55. R. Gampala, D.M. Elzey, H.N.G. Wadley, *Acta Metall. Mater.*, Vol. 44, No. 4, pp.1479-1495, 1996.
56. S.L. Draper, P.K. Brindley, and M.F. Nathal, in "Developments in Ceramic and Metal Matrix Composites," Ed. K. Upadhy, TMS (Warrendale), p. 189, 1991.
57. W.A. Curtin, *Composites*, **24**, p. 98, 1993.
58. H. Hough, J. Demas, T.O. Williams, and H.N.G. Wadley, *Acta Metall. et Mater.*, In Press, 1994.
59. D.M. Elzey and H.N.G. Wadley, *Acta Metall. et Mater.*, In Press, 1994.
60. P.E. Cantonwine and H.N.G. Wadley, *Composites Eng.*, **4** (1), p. 67, 1994.
61. J.M. Duva, W.A. Curtin, H.N.G. Wadley, *Acta Metall. et Mater.*, In Press, 1994.
62. R. Vancheeswaran, D.M. Elzey, and H.N.G. Wadley, *Acta Metall. Mater.*, Vol. 44, No. 6, pp. 2175-2199, 1996.
63. R. Vancheeswaran, D.G. Meyer, and H.N.G. Wadley, *Acta Metall. Mater.*, Submitted.
64. H.N.G. Wadley et al, *Acta Metall. et Mater.*, **39** (5), p. 979, 1991.
65. C.V. Dodd and W.E. Deeds, "Analytical Solutions to Eddy Current Probe-Coil Problems," *J. Applied Physics*, **19** (6), pp. 2829-2838, 1968.
66. K.P. Dharmasena and H.N.G. Wadley, Review of Progress in Quantitative NDE, Vol. 10B, Eds. D.O. Thompson and D.E. Chimenti, Plenum Press, NY, p. 1111, 1991.
67. B. W. Choi, K. P. Dharmasena and H.N.G. Wadley, *Proc., Review of Quantitative Nondestructive Evaluation*, Vol. 12, Eds. D.O. Thompson and D.E. Chimenti, Plenum Press, NY, p. 1047, 1993.
68. J.M. Kunze, H.N.G. Wadley, *Acta Metall. Mater.*, **45**(5), pp.1851-1865, 1997.
69. Ed. B.E. MacNeal, MacNeal-Schwendler Corporation, *MSC/EMAS Modelling Guide*, 1991.
70. D.G. Meyer and H.N.G. Wadley, *Met Trans B*, **24**, p. 289, 1993.
71. P.E. Gill, W. Murray, and M.H. Wright, *Practical Optimization*, Academy Press, London, 1981.
72. Y. M. Liu, H. N. G. Wadley & J. M. Duva, "Densification of Porous Materials by Power Law Creep", *Acta. Metall. Met.*, **42**(7), pp. 2247-2260, 1994.
73. A. Zavaliangos, *Proc. Int. Workshop on Modelling of Metal Powder Forming Processes*, p. 287, Grenoble, France, July 21-23, 1997.
74. D. B. Gundel & F. E. Wawner, *Scripta Met D. V.25*, pp. 437-441, 1989.
75. G. Munger, D. J. Sypeck, H. Wadley, R. Rowland and P. Parrish, In Preparation, 1998.



## Process-Structure-Property Relationships Obtained with Natural Computation

Dr. Ton de Weijer  
Akzo Nobel Central Research  
Dept. Applied Fiber Physics  
Velperweg 76  
6800 SB Arnhem, The Netherlands

### Abstract

*The development of high performance yarns with properties that closely match the requirements of customers requires a detailed insight into the influences of process variations and structure arrangements on yarn properties. To obtain these relationships, use has been made of computation techniques whose basic principles are adopted from nature. These so-called natural computation methods have unique problem solving possibilities. The relationships between process settings, physical molecular structure and (thermo)mechanical properties of poly(ethylene terephthalate) yarns were determined by Artificial Neural Networks (ANNs). Although the internal structure of ANNs is incomprehensive with respect to the mechanisms of the modeled relations, it is a fast and accurate way to make data and relations between data-sets easily accessible.*

*From an effective process and product development point-of-view, it is interesting to be able to apply the relations that have been modeled with ANNs in a reverse way, i.e. to find possible structures or process settings resulting in a certain combination of desired properties. SYNGA was developed to realize this. It consists of a genetic algorithm in which an artificial neural network is embedded and serves as the 'knowledge-base' for the optimization procedure. The trained and validated ANNs, genetic algorithms and background knowledge in the form of texts and figures are implemented in a user-friendly software system called BESSY. In this way, knowledge concerning the relations between process conditions, physical structure and end-use properties of PET yarns are made accessible to other scientists.*

### Introduction

The core activity of industry is the manufacturing of products from raw materials with specific properties in efficient production processes. The added value of the product is predominantly determined by the technology. Therefore improvements in processability or product performance can be achieved if qualitative relations between the way the product is processed and its properties are available. An important drawback in the development of a fundamental understanding of industrial processes is that a technology can advance without accurate knowledge of the principles behind the advancement. Since it is important in many modern industries important to keep technologically ahead of competitors, research on fundamental aspects is often given minor importance.

## The use of experimental data

Recent developments in laboratory information systems and data storage capacities have resulted in the advent of models based on correlation between data-sets. As well as the many new developments in multivariate data analysis (in general), the concept of artificial neural networks has contributed significantly to this rising interest. Despite the large number of published papers on the *modeling* of experimental data, the *interpretation* of experimental data still forms a vital part of every scientific investigation. Large databases are nowadays often routinely generated with data on processes, physical and chemical structure, and properties of materials.

The problem of introducing the structure as an intermediate of process - property relationships is in the selection of structure variables. To make interpretation possible, the structure has to be characterized with a minimum number of quantities. One of the main problems is that the structure variables are often highly inter-correlated. Setting an experimental design on the process variables does not solve this problem since the structure is a *function* of the process conditions. A second problem is that the statistical data analysis is based on correlation, rather than causality. These correlation's do not imply causality although they are often interpreted as causalities in the literature. Some authors have addressed this problem in illustrative examples [1] [2]. These situations are in most cases evidently clear and are easily recognized by researchers. However, more subtle examples can be found in complex industrial and environmental data sets in which, in the first instance, the cause of the correlation's is unclear.

## Process - structure - property relationships

The close connection between process conditions, structure and properties can be clearly illustrated by the classical example of the different forms of carbon [3]. In Fig. 1 the phase diagram of carbon is shown. Pure graphite switches to diamond at 100 kbar and 3000° K at useful reaction rates. The application of these process conditions results in crystals with strong covalent bonds. Such carbon crystals are single molecules in which every carbon atom is linked through covalent bonds to four neighbors in a tetrahedral structure. Materials formed this way are often tough and unreactive and are not electrically conductive. Graphite, produced from pure carbon under milder conditions, is another form of solid carbon and is one of the softest materials known. It consists of layers of carbon bound together by covalent bonds into hexagons ( $\alpha$  form) or rhombohedral ( $\beta$  form). The hexagonal alpha type can be converted to the beta form by mechanical treatment, and the beta form reverts to the alpha form on heating above 1000°K. One valence electron on each carbon binds the sheets of covalent bonds together. These electrons have such limited mobility between the sheets that the conductivity perpendicular to the layers is about  $10^{-4}$  times that parallel to the layer. By sublimation of pyrolytic graphite at low pressures and temperatures above 2200°K so-called "white" carbon is formed which is a transparent birefringent material.

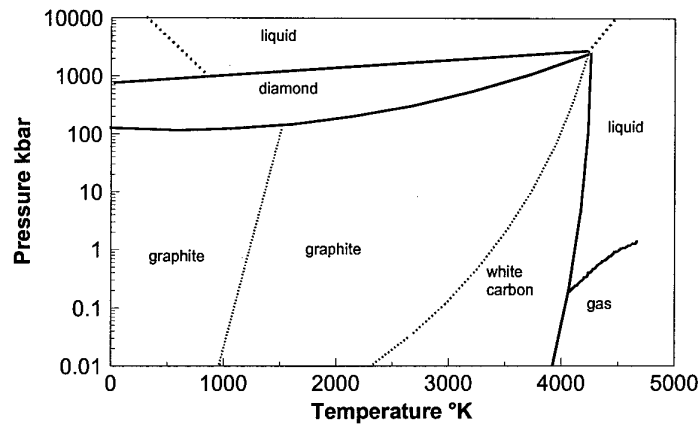


**Figure 1 The phase diagram of carbon. It shows that under different process conditions different forms of carbon are formed**

This classic example illustrates the close inter-relationship between the way a material is produced, its physical structure and the resulting properties. It shows that process, structure and properties are in causal connection to each other.

For efficient improvements in the performance and quality of a product, a profound understanding of these relationships is required. Structure and properties are both functions of process settings whereas the properties are functions of structure (see Fig.2).

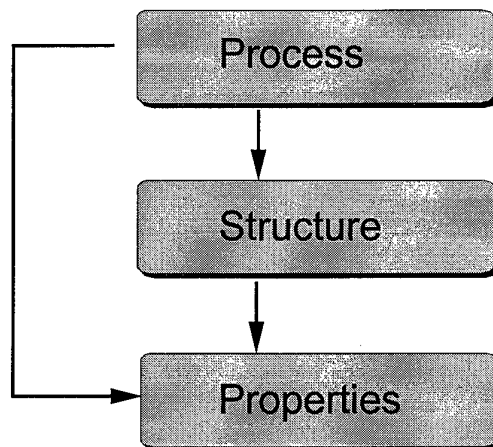


**Figure 2 The forward relations between process settings, structure and properties of materials**

**Statistical vs. physical models**

The structure - property relationship is often elaborated in physical models. In addition to such deterministic models, which have traditionally had strong roots in pure and applied research, statistical models play an important role in understanding these relationships. Both model types have their strengths and weaknesses. It is important to realize that these model types are complementary, not mutually exclusive.

The physical model and the statistical model may be regarded as the two extremes in the modeling of structure-property relationships. The term 'physical' implies the existence of proven basic laws from the natural sciences (physics, chemistry) applied to the material concerned. The aim of physical models is to provide a quantitative explanation for observed phenomena in terms of basic key parameters. Comparison of the predictions from the model with experimental data is often used to validate the model. In general, the development time of a physical model is long. A reason for this is that it is a continuous process of implementation and testing. Physical models often lack accuracy because of simplifications to the underlying equations (to make calculations easier) and because of inconsistency with the non-ideal behavior of the relation in practice. However once the model has been validated, it can be applied more generally than statistical models.

When it is not possible to describe the relation in well-defined physical quantities or when accurate predictions are required, a statistical model can be a useful tool for getting insight into the mechanisms that determine properties. The extrapolation capacities of statistical methods are poor since the model is confined to the experimental ranges on which the model is based. Experimentation in pilot plants and in laboratories results in general in a large amount of data production. If the experiments can be effectively and economically done, the use of statistical models instead of (or in addition to) physical models can be considered. A comparison between physical and statistical models is given in Table 1.

**Table 1 Some characteristics of various types of models**

	Physical model	Statistical model
Principle	physical theory causality	exper. data correlation
Development time	long	short
Experimental effort	low	high
Reasoning	in principle transparent	black box
Validation	exper. data	exper. data
Accuracy	low	high
Predictivity	high	limited

Once a statistical model has been developed it can help validate the physical model, since in this case pure relations (relations without variable contributions from other factors) can be derived. Experimentally, such pure relations can not be obtained since all structure parameters are functions of process settings. In a contrary way, validated physical models can help to find the essential factors, i.e. structure parameters, that influence the response that has to be modeled. In general, much experimental data is necessary to calibrate a statistical model and the pre-information obtained from physical models can reduce the number of experiments or measurements that have to be done.

## Artificial Neural Networks and Genetic Algorithms to obtain quantitative process - structure - property relationships

Artificial Neural Networks (ANNs) are gaining increasing popularity in different applications. Since the breakthrough in 1986, when a learning rule for complex ANNs was discovered [4], applications have frequently been published in the literature [5] [6]. Artificial Neural Network (ANN) was used to model the relation between the physical structure and mechanical properties of poly(ethylene terephthalate) (PET) yarns [7]. The relation was studied on a set of in total 554 drawn yarn samples that came from a variety of applied process conditions. The ANN, consisting of three layers of neurons, was trained using the physical structures and property measurements of these 554 yarns as input and output patterns respectively. All ten properties were fit to the physical structure within an acceptable variance for quantitative use.

### Calibration and validation results

A neural network for the relation between the structure and properties of PET yarns was trained as described above. After 600 iterations a minimum error in an independent testset was found. To illustrate the ability to estimate the measured yarn properties from the physical molecular structure of PET, a plot of the estimated breaking tenacity (BT) versus the measured breaking tenacity for the training-set and test-set is shown in Fig. 3. Comparable results with process parameters as input patterns could be established.

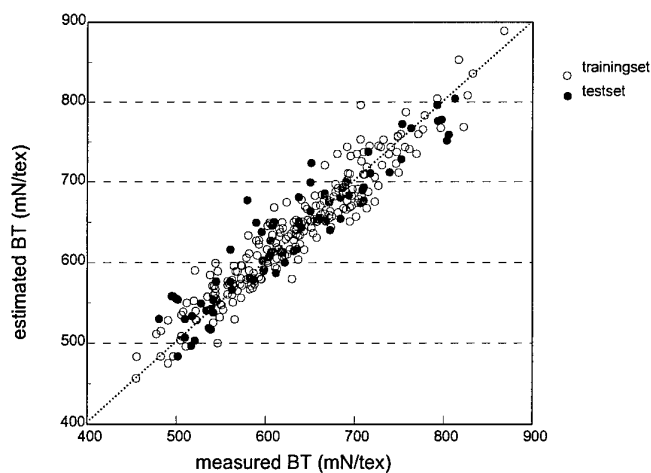


**Figure 3 Estimation of Breaking Tenacity by an Artificial Neural Network for the test-set and training-set**

### Modeling of stress-strain curves

The stress-strain curve obtained in uni-axial tensile tests is one of the most important mechanical properties of materials. In general, however, the response is complicated and models closely agreeing with the experimental data up to the point of rupture are not available. In the case

described above, some intermediate points and the end-point of the stress-strain curves are used. Since these points are the 'critical' stress-strain parameters, i.e. they determine the shape of the stress-strain curve to a large extent, no arguments can be given as to why it is not possible to predict the stress-strain curve as a whole. In order to test this, an artificial neural network with 5 input units, one hidden layer with 8 neurons and an output layer with 100 neurons was trained. The same test-set and training-set were used to calibrate and validate the model. The effect of each structure parameter, measured on the non-strained sample, on the form of the stress-strain curve can be considered independently. This is done by varying one signal of an input node while the other nodes are set at a constant value. By examination of the output nodes of the neural network, the influence of the pure effect on the stress strain behavior is examined. The valuable contributions of these exercises to the understanding of structure - property relationships is illustrated in the following example. As a measure of the level of the amorphous orientation, a factor based on sonic modulus measurements is chosen to be one of the structure parameters in the structure representation (Fas). It is generally acknowledged in polymer science and confirmed by the main effects calculated from the ANN that the average polymer chain orientation determines properties to a large extent. The value of Fas can theoretically vary from zero for fully disorientated, to one for perfectly orientated yarns. In practice the orientation parameter varied from 0.69 to 0.83 in this series of drawn yarns. The influence of chain orientation on stress - strain behavior has been widely discussed in the form of physical and empirical models [9] [10]. The statistical or empirical modeling of stress-strain curves based on a structure representation that is closely related to the well-known two-phase model of semi-crystalline polymers gives the pure contributions that can be used to test the physical models that have been proposed. An example of such a pure contribution, i.e. at the condition of all other structure parameters being constant, is shown in Fig. 4 in which the pure effect of the average polymer chain orientation via sonic modulus measurements (Fas) is depicted.

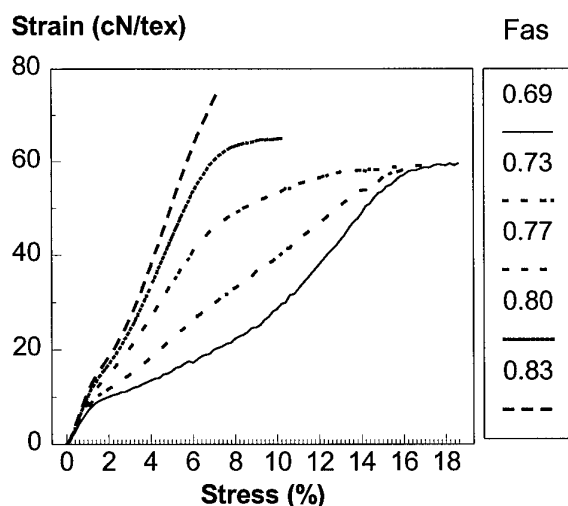


**Figure 4** Variation in stress-strain behavior as a function of the average polymer chain orientation (Fas) predicted by an artificial neural network. The other variables are set at constant values.

## Inversion of the forward relations

Another interesting relation for process and product development is the reverse relation to the one discussed, viz. the relation of mechanical properties to physical structure and process parameters. Development of yarns with optimum performance requires detailed insight into the influences of process variations and the structure arrangements of the chain elements on yarn properties. From an industrial point-of-view it is therefore interesting to know which physical structures give the combination of desired mechanical properties. Since this is an ambiguous and NP-complete relation it is not possible to use only a neural network. Hence an optimization technique (here, a genetic algorithm) is combined with an ANN trained for the forward-relation in order to search for optimal solutions for the reverse relation (Figure 5).

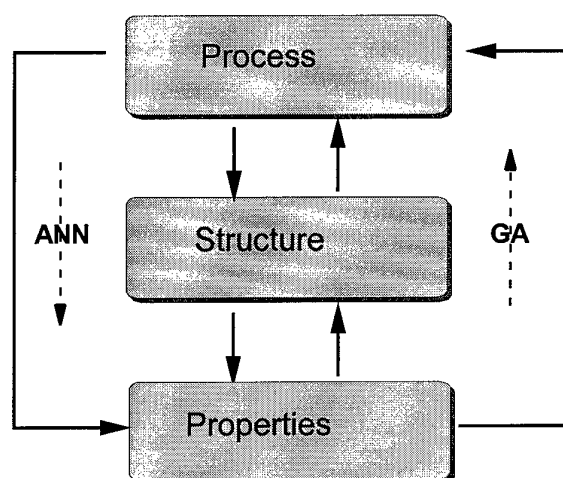


**Figure 5** The forward-relations have been modeled by ANNs. The ambiguous reverse relation is obtained with GAs using the trained and validated ANN for the forward relation

In this application each gene  $s$  is a set of five yarn structure characterization measurements and the evaluation function that partially consists of the trained ANN which predicts the mechanical and shrinkage properties  $\hat{Y}_n$  from  $s$ . In contrast to the basic execution cycle of genetic algorithms, our evaluation function is composed of two functions (Figure 6).

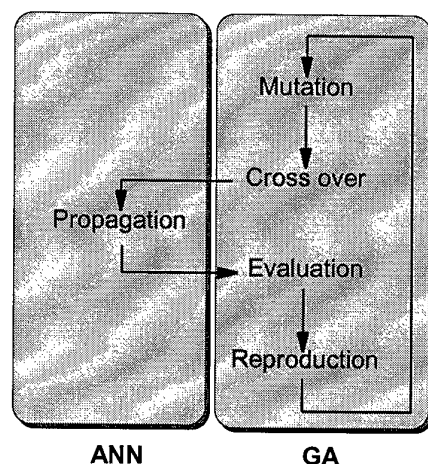


**Figure 6** Modification of the basic execution cycle of GAs. Genes are propagated through the ANN and evaluated

The first function propagates all state vectors through an ANN which has been trained for predicting PET yarn properties. The second function  $g$  transforms  $f(s)$  into a fitness value.

## Conclusions

The development of yarns with properties that closely match the requirements of customers requires a detailed insight into the influences of process variations and structure arrangements on yarn properties. In order to achieve this, use has been made of artificial neural networks and genetic algorithms. Although the internal structure of ANNs is incomprehensive with respect to the mechanisms of the modeled relations, it is a fast and accurate way to make data and relations between data-sets easily accessible. The trained and validated ANNs, genetic algorithms and background knowledge in the form of texts and figures are implemented in a user-friendly software system. In this way, knowledge concerning the relations between process conditions, physical structure and end-use properties of PET yarns are made accessible to other scientists. Although the discussed relations are mainly confined to synthetic yarns, the concepts are also applicable to other large scale production processes [10] [11].

## References

- [1] E.V. Thomas. A primer on multivariate calibration. *Anal. Chem.*, 66:795A--804A, 1994.
- [2] A.K. Dewdney. *200% of Nothing*. Wiley, New York, 1993.
- [3] P.W. Atkins. *Physical Chemistry*. Oxford University Press, London, 1984.
- [4] D. Rummelhart, G. Hinton, and R. Williams. Learning representations by back-propagating errors. *Nature*, 323:533--536, 1986.



- [5] J. Zupan and J. Gasteiger. Neural networks: a new method for solving chemical problems or just a passing phase. *Anal. Chim. Acta*, 248:1--30, 1991.
- [6] J.R.M. Smits. *Exploring the Possibilities of Applying Artificial Neural Networks on Problems in Analytical Chemistry*. PhD thesis, University of Nijmegen, Nijmegen 1993.
- [7] A.P. de Weijer, L. Buydens, G. Kateman, and H.M. Heuvel. Neural networks used as a soft-modeling technique for quantitative description of the relation between physical structure and mechanical properties of poly(ethylene terephthalate) yarns. *Chemom. Intell. Lab. Syst.*, 16:77--86, 1992.
- [8] M.G. Northolt, A. Roos, and J.H. Kampschreur. Birefringence, compliance, and viscoelasticity of poly(ethylene terephthalate) fibers. *J. Pol. Sci. Pol. Phys.*, 27:1107--1120, 1989.
- [9] D.W. van Krevelen. *Properties of polymers*. Elsevier, Amsterdam, 1990.
- [10] A.P. de Weijer, C. Lucasius, L. Buydens, G. Kateman, and H.M. Heuvel. Using genetic algorithms for an artificial neural network inversion *Chemom. Intell. Lab. Syst.*, 20:45--55, 1993.
- [11] A.P. de Weijer. *Process - Structure - Property Relationships Obtained with Natural Computation*. PhD thesis, University of Nijmegen, Nijmegen, 1995.

## Intelligent Process Control With Evolution Strategy

Dr. Heinz Offergeld, IBOS Qualitätssicherungssysteme GmbH  
Julicher Strasse 336, D-52070 Aachen, Germany

### Abstract:

The tasks of process systems are multi-faceted and all aimed at minimisation of expenditure and related costs. Irrespective of the level at which they are used, the aim of such systems should be the continuous improvement of production. A closed optimisation cycle is created whereby all information related to the production is analysed and feedback to the production process is given.

The basis of the introduced optimisation process is the evolutionary optimisation. Evolution is a very efficient optimisation process, which has produced astonishing results in nature. The evolution strategy uses the same basic principles as the biological evolution, such as mutation and selection.

The on-line optimisation is limited to the optimisation of the machine settings. This may only be a small area of the influencing factors, such as moulds, materials, human and environment, but it is the only area in which direct, on-line interventions can be made during a running production.

This paper describes the practical results which are achieved in using evolution strategy for the on-line optimisation of injection moulding processes. The results show that the productivity will be increased by up to 20 %.

### Introduction

The business infrastructure is subject to change, lean management and decentralised organisation structure, to name just two. It is therefore necessary to adapt the information systems of these businesses. Decisions are required. On the one hand, these have to be taken swiftly, but at the same time rely on well-founded information. It should be possible to change the sequence of events, without this causing a large administrative overhead. Again, centrally organised information systems have to make way for decentralised information structures. There is a need for networked, intelligent individual systems. As with the introduction of teamwork, there is a need for leaving purely centrally orientated management information systems (MIS), in favour of small autonomous units, which can be adjusted quickly to the changing needs and communicate with other systems via open interfaces. The administration of MIS should never claim to cover everything. It is only an aid, as the most important source of information is still man. A computer will never be able to reach decisions and can only ever provide the necessary information, or suggest solutions. There is a large range of MIS solutions in the areas of product planning, data administration and quality control.

As in mechanical engineering, certain standards are

gaining recognition within the MIS scene. These standards are strongly influenced by Microsoft. They include network solutions, Client-Server architectures, Windows NT, SQL databases, Ethernet, Token Ring and TCP/IP. It is not sensible and not at all possible to obtain all applications from one software-house, but it should be possible to integrate system components from several different sources. Complete stand-alone solutions often prove to be dead-ends and can only be changed with considerable financial expenditure. To fulfil the global claims of an information system, every system should possess these standards and not some 'reliable' proprietary interface. The same applies to the user terminal. It cannot be that for each and every piece of software, a separate terminal has to be installed at the machine. Through the use of standards, various systems can be used by one single monitor. This especially calls upon machine manufacturers to create standard interfaces for their terminals and controls.

With regard to the production, two differing information levels have to be distinguished: (Figure 1)

Higher level systems, which support in planning and execution of production processes and logistics as well as collect and condense information gathered during production. The condensed information is used for comparison of set and actual values and produces the necessary basis to adjust production, if required.

### Process Systems

Process systems are placed in the production and usually possess an interface to the production plant. These should support the employees at the machines with their work, but not remove any responsibility. (Figure 2)

The tasks of process systems are multi-faceted and all aimed at minimisation of expenditure and related costs. Irrespective of the level at which they are used, the aim of such systems should be the continuous improvement of production. A closed optimisation cycle is created whereby all information related to the production is analysed and feedback to the production process is given:

It may be that defect causes are able to be analysed and easily corrected, thereby leading to an increase in productivity, or product quality can be used to automate process intervention.

In the following, only process systems shall be looked at with the emphasis on on-line systems and their uses. Such systems are used in the following areas:

- Process Analysis
- Process Control
- Process Optimisation

- Process Regulation

The documentation and data analysis is placed in the higher systems, whereas the information is gathered in the process systems.

#### On-line optimisation

The on-line process optimisation and regulation is the end of a long chain of modifications to the moulded part and production process, all aiming at the facilitation of an effective and safe mass production.

Process optimisation already begins in the development phase and contains, beside rheological and thermic mould properties, the planning of quality assurance. In the examination phase, which partially overlaps with the creation of the mould, it has to be ascertained that the process is suitable for mass production. This, depending on the product, demands an intensive analysis of the process, to exclude weak points as early as possible by i.e. mould changes. The knowledge gained from the analysis has to be made available for the mass production process at a later stage. Mistakes in development cannot be rectified at a later stage and their effects can only be minimised. The processability demanded by SPC is a requirement for the mass production.

To aid the review phase, several software solutions are available to analyse the production process.

The basis of these solutions is always the classic methods of statistical testing. The main work here lies not in the test performance, but more so in the defining of the test plan and the critical evaluation of the results. This demands a great deal of process knowledge and statistical grounding.

The process monitoring can be achieved by machine parameters, process values and properties for each cycle. The tasks of process monitoring are:

- Documentation
- Sorting out of random, short term extremes via waste limits
- Creation of intervention events
- Reduction of measuring expenditure by quality prediction

The simple process monitoring is already integrated in modern machines and can be obtained as various options.

It has, for example, been realised by setting tolerance fields for specific machine parameters and process settings, such as the cavity pressure or the change-over pressure.

A further development of simple process settings monitoring would be the monitoring of properties.

To sum up, it can be said that at this point in time, it is possible to build up a usable quality prognosis for some quality values for specific moulded parts, for which reproducible measurements are available.

The on-line optimisation is limited to the optimisation

of the machine settings. This may only be a small area of the influencing factors, such as moulds, materials, human and environment, but it is the only area in which direct, on-line interventions can be made during a running production.

Optimisation is the systematic search for a compromise between the various maximal requirements. The compromise is defined via the weighting or priority of the separate requirements and qualities. The process optimum has been reached when production and quality assurance means have been fully exhausted. The working optimum is the set of significant parameters at which the relationship of overall quality to production cost is maximal.

The production at the running optimum means to control the process with regard to quality and economy. (Figure 3)

The production starts with the optimisation. Only afterwards can the intervention limits for the process be defined. These intervention limits can be determined from statistical calculations. Their determination by specification limits appears to be more useful. The change between optimisation and monitoring is made manually, if economical and technical quality is satisfactory. The optimisation has to be reactivated to further improve the overall quality, as in the phase of process monitoring, the only attempt made is to achieve the quality of the last setting.

As long as all qualities lie within the intervention limits during the monitored phase, no changes will take place during the process. If intervention limits are exceeded, the optimisation is automatically reactivated. The machine parameters are changed, until the quality lies within the intervention limits. In the process of monitoring, only documentation of quality and machine parameters takes place.

In contrast to the optimisation, regulation is aimed at maintaining the achieved level. This level, which need not be optimal, will be kept constant by changing of input settings. The continual optimisation equals a regulation. Both aim at keeping the quality of a product constant, but not the machine settings. The aim is the elimination of faults, which can be of many origins. It can be distinguished between time-related manifestations of faults and on the other hand, their causes.

#### *accidental, short-term faults*

These faults can only be eliminated with better machine settings, i.e. by achieving a more robust production point. Example: every 50 or 100 cycles, a waste unit is produced.

#### *systematic faults*

These are recognisable in the statistical graphs as a trend and can, for example, be caused by temperature drift. By resetting machine parameters, these can be partially eliminated.

#### *erratic faults*

These can, for example, be caused by changes of material, machine down-time, unsystematic manual

intervention. The machine settings have to be changed immediately.

The results for the CD injection moulding are a good example for the usage of integrated process optimisation and regulation. Through the use of the optimisation system, to be described later, it was possible to lower cycle times by an average of over 10 % and at the same time, reduce the waste by 1/3. The quality control was maintained by visual examination and liner-integrated scanners. (Figure 4)

Pure process regulations, which are not based on continuous optimisation, are only starting to be made available. These are either based on purely mathematical (regression analysis, neural networks), or physical methods.

Even if a complete quality control cycle, which includes all quality characteristics from measurable values to attributive characteristics and economic values such as cycle time, does not appear to be feasible in the short term, the aimed intervention as in for instance colour or part change, which would not anticipate interactions is sensible, compared to regulation via a continual optimisation, as it has a faster reaction time.

Up to now, the usual order of events in optimisation and regulation of machine settings, is that the employee at the machine judges the quality of the product and economic indicators e.g. cycle time. He decides which settings are to be changed at the machine and which operating level should be tested for improvement. The result of the optimisation is hereby very much dependent on the experience and motivation of the personnel and the time available.

### Evolution Strategy

The basis of the now introduced optimisation process is the evolutionary optimisation. Evolution is a very efficient optimisation process, which has produced astonishing results in nature. The evolution strategy uses the same basic principles as the biological evolution, such as mutation and selection. (Figure 5)

In biology, mutation is the spontaneous change of the genotype, selection the survival of those individuals best adapted to the environment. Via the selection, this strategy is capable of 'learning'. The evolution strategy for the optimisation of technical systems tries to use these advantageous mechanisms.

In the following figure, the approach of the strategy is demonstrated using a simple example. (Figure 6)

The main advantages of this procedure are:

largely fault independent and efficient.  
no need for the existence of model concepts  
good relationship between convergence speed and safety.

The strategy can work without knowledge of the process. The advantage of the procedure lies in the fact that existing knowledge of the process can be incorporated, even if it is only partial. Even if a complete model description of injection moulding is not possible, a lot of the partial dependencies are known.

This partial knowledge can be used in the evolution strategy to speed up the process convergence.

The approach of the optimisation system is very similar to the approach of the personnel.

The personnel adjust the machine using their experience and knowledge of injection moulding. This experience and knowledge may be universally valid, or valid for a specific machine-mould-material combination. In areas where no experience is available, he would vary some machine parameters slightly, to be able to judge the effect on the product and thereby gain new experience. Better operating levels are used as starting points for further variations. (Figure 7)

The system is connected to the injection moulding machine via the host machine interface and can therefore change and read parameters like a user. The evaluation of quality is facilitated by a valuation station, where the manual evaluation takes place. The data from automated measuring systems are read in via interfaces. When all quality evaluations and process values have been read in, the machine setting will be altered slightly, starting with the previously best machine setting. Only when the next evaluation is available, can machine parameters be optimised. Integrated into a network, the process and quality documentation is stored in a database, so that amongst other things, SPC documentation can be created. The evaluation station terminal can also be used as a PDC (process data collection) station.

Not only technical aspects, such as quality requirements, are taken into account in the optimisation, but also economical aspects.

The aims of optimisation are:

- fulfilment of technical requirements
- minimal cycle time
- high degree of robustness

The following figure illustrates exemplary the changes in quality during optimisation, for a two component part of a toy. The visual characteristics are valued using the school grading system in comparison to a reference part. 'One' means very good and 'five' means waste. The torque was obtained from a measuring instrument. On one hand, contrasting quality changes can be seen and on the other hand, it can be seen that the optimal production point is a compromise of several requirements. (Figure 8)

The robustness of the injection moulding process, or the safer process is continually gaining more importance. The stability concept in production was included in the discussion by the introduction of SPC. Taguschi and his methods. Taguschi distinguished, like the classic statistics, with the quality characteristics between the mean value of quality and the deviation of the quality values. Both quality characteristics are independent of each other, according to Taguschi. A quality value may lie with its mean value precisely on the required value, the deviation may, at the same time, be considerable. This gives the impression of a high standard of quality, but at the same time a high level of wastage is seen.

Compared to this, an operating level should be preferred that does not lie precisely on the required value, but gives a smaller deviation.

For the optimal operation of the machine, all characteristics that are important for the quality must be considered and taken into account. These are:

Deviation of quality characteristics

and Distance of quality characteristic from the intervention limits.

From these criteria, the best possible compromise must be found.

The optimisation has to consider all quality characteristics (inclusive of economical). These have to be freely defined, depending on requirements.

An important point is the setting of priorities for the separate quality characteristics. The importance of each quality characteristic decides the direction of optimisation or the achievable aim of the optimisation.

In figure 9, the results of an optimisation for a turbine wheel are shown. It can be seen that it is possible to optimise the quality characteristics on one hand and the deviation of the characteristic on the other. Robustness and quality requirements do not necessarily exclude one another. (Figure 9)

Deviation of specific quality characteristics should only be considered if the quality of the process will be altered considerably. The measuring expenditure is increased quite considerably by this.

Computer solutions are more and more in use by companies and are a very capable means to cut costs and increase transparency within the company. The production and business orientated solutions have to be viewed in connection with each other. There is a great risk with software solutions, to get into dependencies and dead-ends. To avoid this, care should be taken on choice of up-and-coming standards and open interfaces. On-line optimisation increases productivity. In connection with on-line quality estimates, the measuring expenditure can be reduced. Integrated regulations can be useful in isolated cases. The introduction of on-line systems demands on one hand, some organisational work, which also increases the transparency within the company, and on the other hand, mould-specific expenditure. This mould-specific expenditure has a very good correlation with attainable benefit for items with larger production runs. For small runs, the organisational stability gains importance. This organisational stability includes on-line systems as an integral part of the information system. Depending on the job start, the machine settings and evaluation plan are sent to the work place. The procedure is clearly defined and, so to speak, as a by-product, quality, production and process data is accumulated. The job data is prepared by the PPS system as target data and the actual production data is sent back to the PPS system.

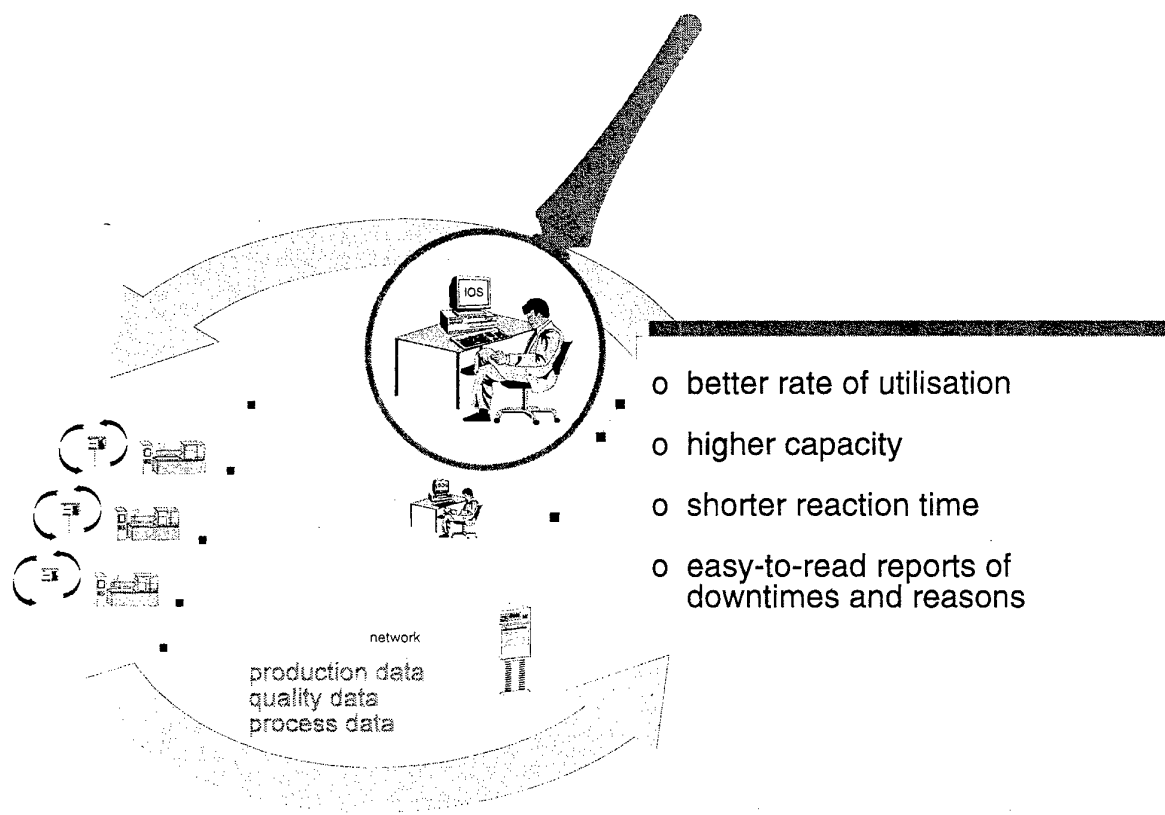


figure 1: Information Levels

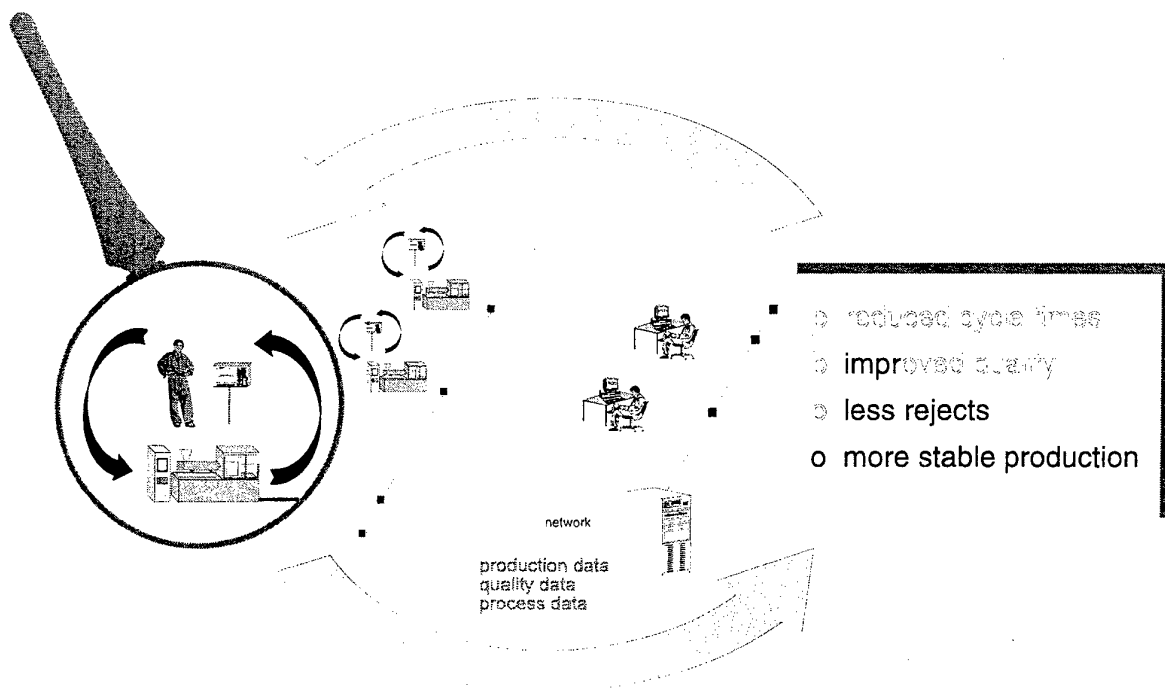


figure 2: Information System in Production

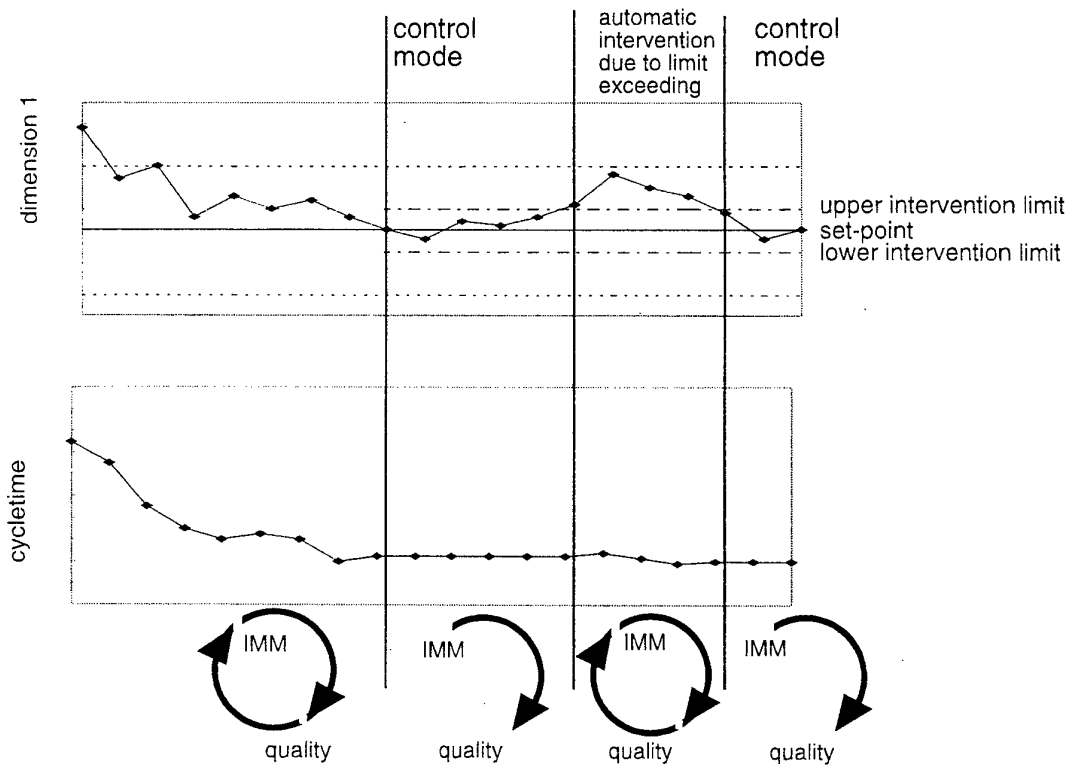


figure3: inter-relationship of process optimisation and process regulation

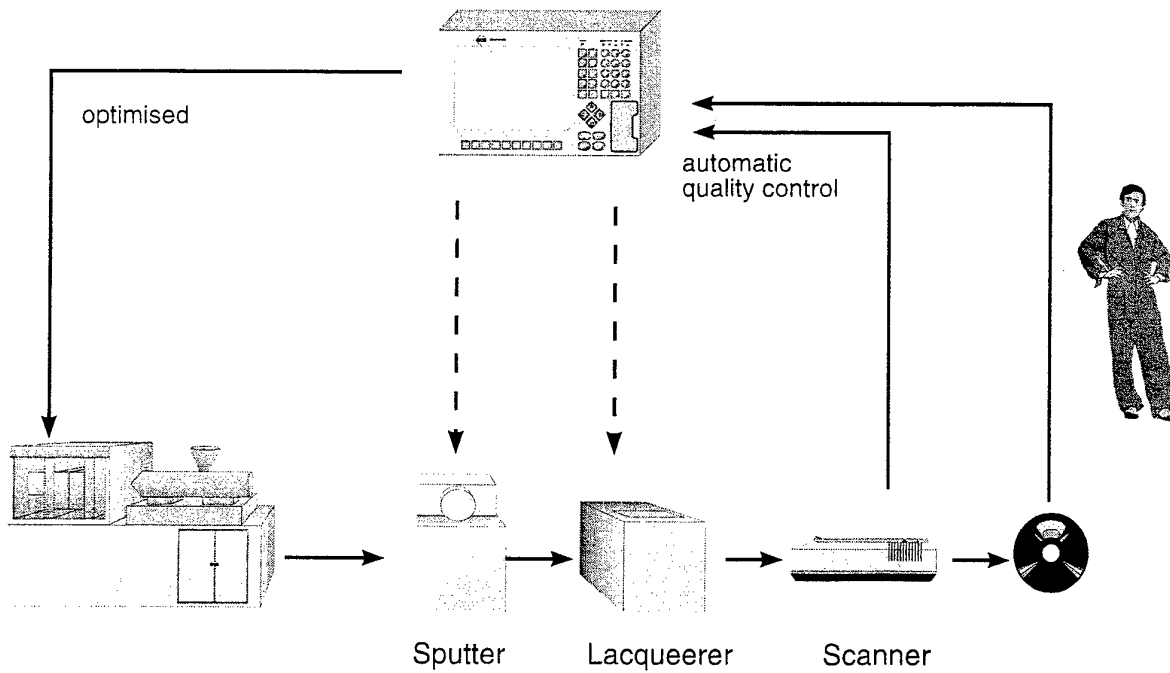


figure 4: Quality control in CD-production

	<b>mutation</b>	<b>selection</b>
biology	random change of genetic material	selection of lifeform which is the best adapted to enviroment
engineering	random change of free system parameters	validation and selection of best fitted system

figure 5: Basic principles of the evolution theory

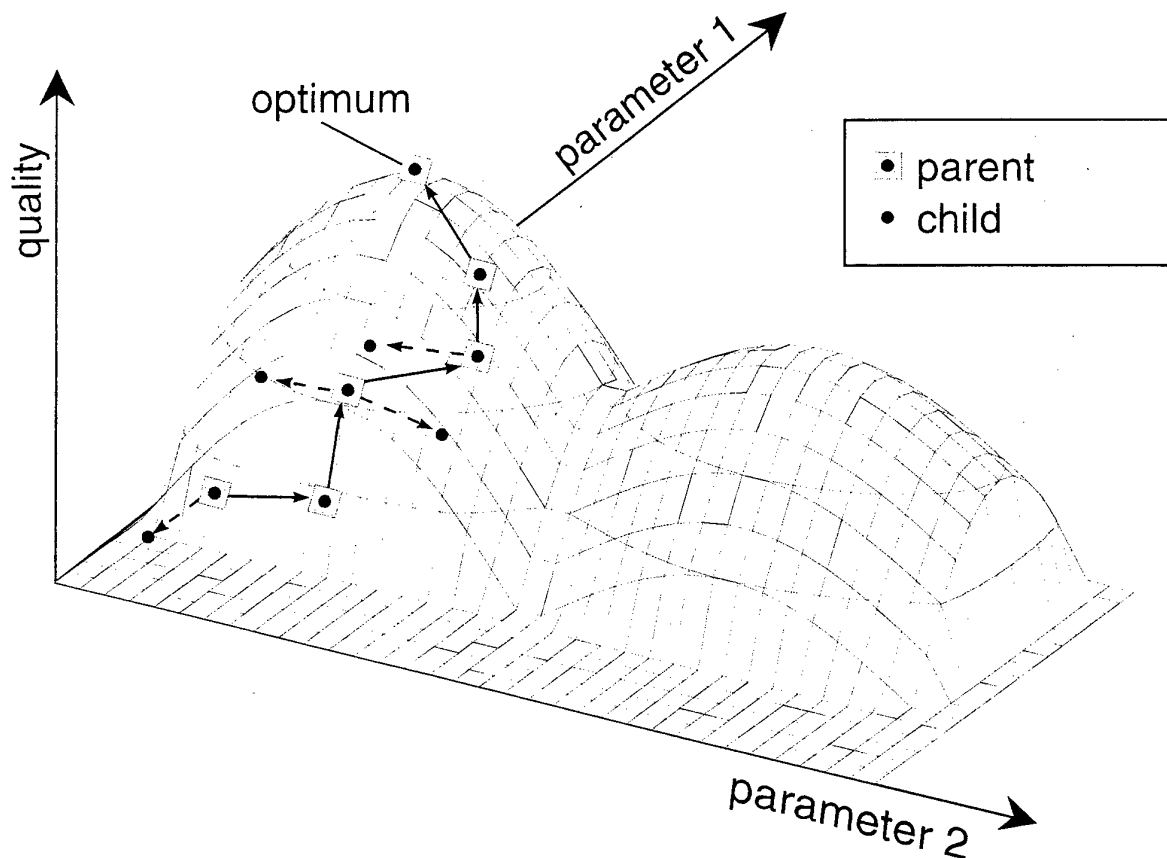


figure 6: Strategy to find the optimum





figure 7: Manual valuation of quality characteristics

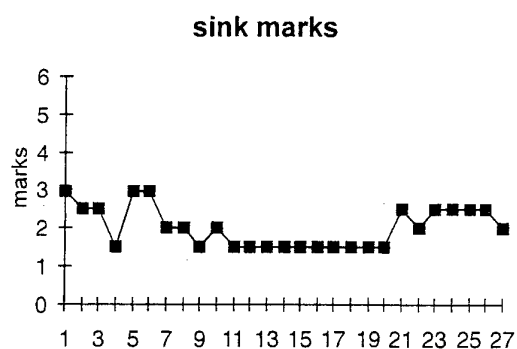
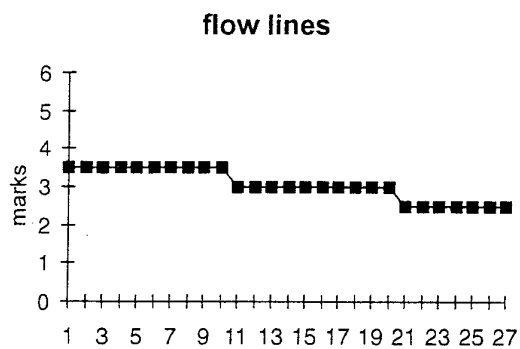
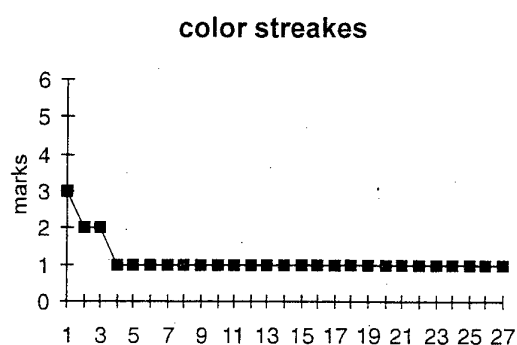
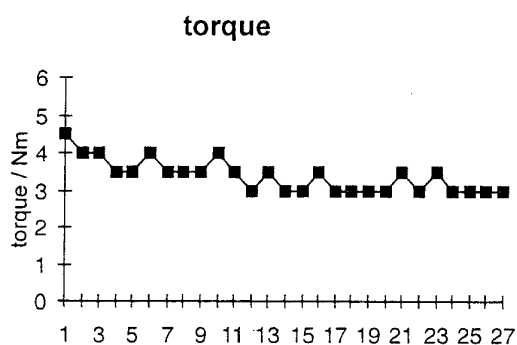
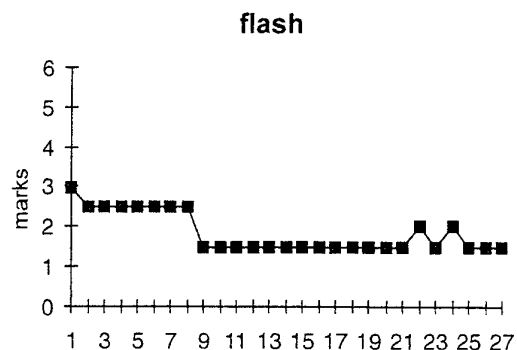
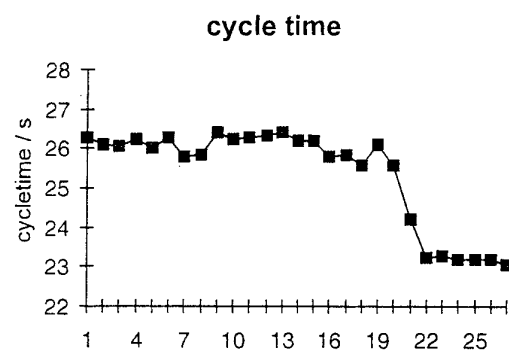


figure 8: Step-wise improvement of quality

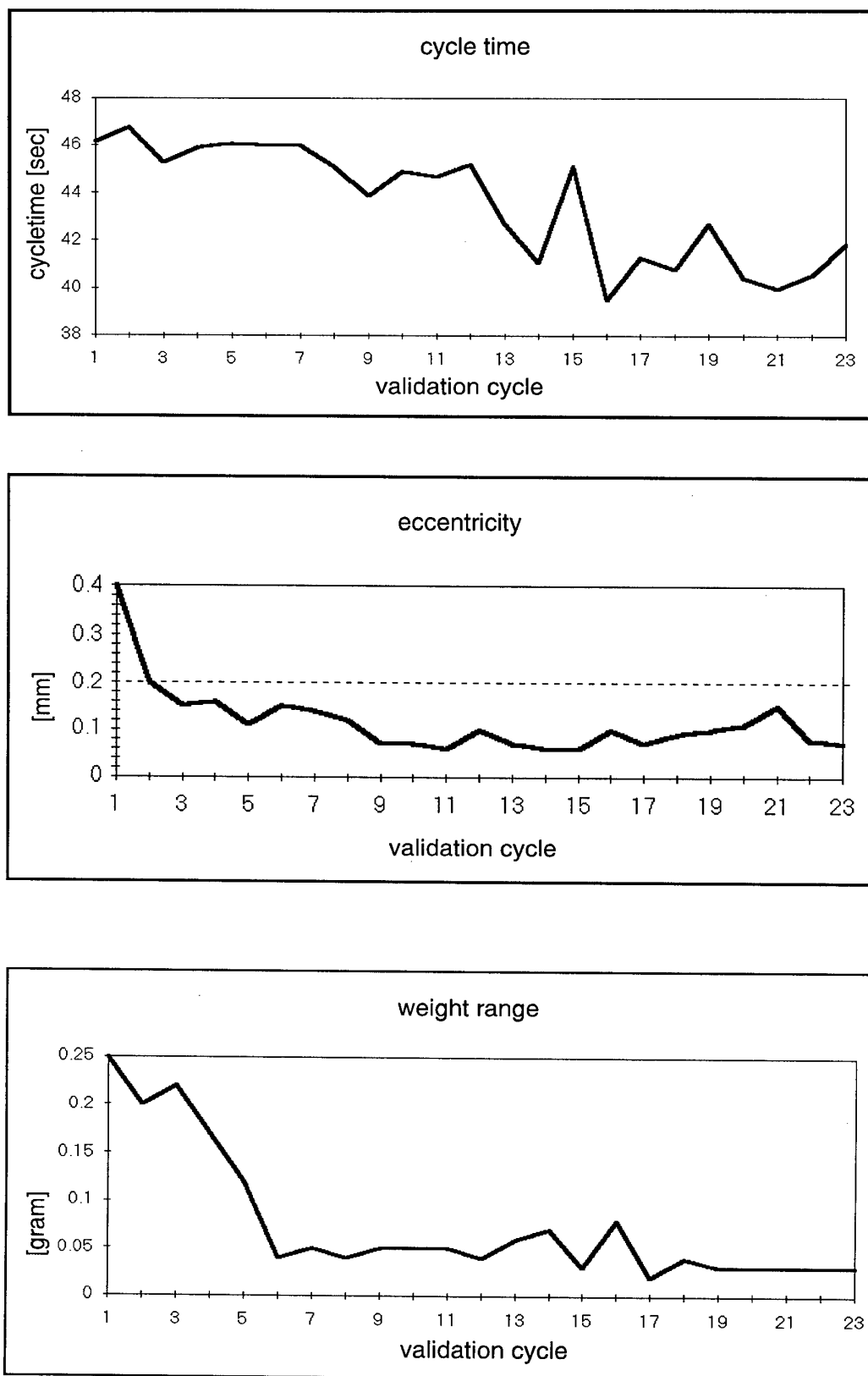


figure 9: Quality characteristics and deviation

## Establishing Best Practice in the Design and Manufacture of Hollow Titanium Fan Blades

Dr G A Fitzpatrick  
ROLLS-ROYCE plc, Fan Systems  
P.O. Box 3, Barnoldswick, BB 18 5RU  
UK

and

A D Lloyd  
ROLLS-ROYCE plc, Fan Systems  
P.O. Box 31, Derby, DE24 8BJ  
UK

### SUMMARY

Rolls-Royce has designed and developed highly efficient lightweight titanium fans for civil engine applications in the thrust range 22000 lbs to over 100000 lbs. These wide chord fan designs are hollow and snubberless, and their fabrication has required the development of joining and forming technologies as well as a thorough understanding of material behaviour.

The first generation wide chord fan design is a honeycomb-cored fabrication. It entered service via the RB211-535E4 aeroengine in 1984. This technology has subsequently been applied to the IAE V2500 engine and the RB211-524G/H powerplants.

Technological research continued into the 1990's to develop an alternative lighter fan concept for larger thrust engines. This resulted in the second generation wide chord fan design which exploits solid-state diffusion bonding for joining the fabrication and superplastic forming for the development of the internal core. As well as reducing component weight, there was also a need to economise product cost and to shorten the design-make process. Rolls-Royce, therefore, launched its Fan Key System to electronically integrate engineering and manufacturing activities whilst, at the same time, incorporating process modelling for the optimisation of the key manufacturing technologies.

These latest advances have been applied to the Trent 700 engine which entered service in 1995 and, subsequently, to the Trent 800 powerplant. Their flexibility is now allowing the development of the swept fan concept for higher thrust versions of the Trent 800 engine, and the application of these technologies to appropriate military projects.

### 1. INTRODUCTION

On modern large jet engines, the fan makes a major contribution to powerplant thrust and efficiency. In fact, at take-off, it generates about 75% of the total engine thrust. Under these circumstances, the fan must be capable of developing sufficient power for aircraft safety after impacts by birds and other debris. It must also resist fatigue stresses during every flight. These requirements have driven the design fundamentals and manufacturing technology developments. Aerodynamic and mechanical integrity considerations and other issues

such as weight, noise and cost, therefore, comprise the essential design criteria.

Conventional fan blades are manufactured from solid titanium alloy forgings and have been traditionally designed with mid-span snubbers to counteract vibrational instability. However, they cause a loss in aerodynamic performance with corresponding penalties in fuel consumption. Rolls-Royce, therefore, removed the snubbers from the fan for aerodynamic efficiency, increased its chord for natural stability, and proportionately reduced the number of blades per assembly. The resultant hollow fan design satisfies severe service operational conditions. The construction of Rolls-Royce hollow fan designs is shown schematically in Figure 1. In both cases, external titanium alloy skins

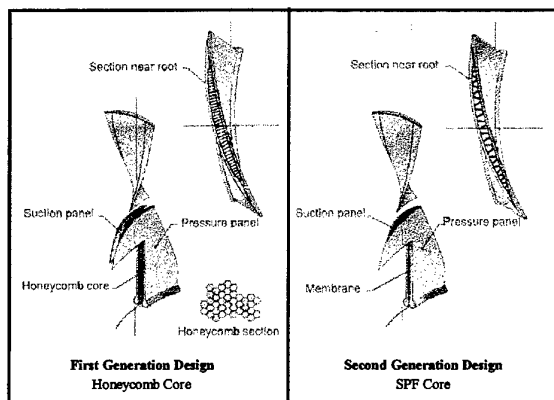


Figure 1: Wide Chord Fan Constructions

are separated and supported by an internal titanium alloy core. High integrity diffusion bonding and hot-forming are the key manufacturing technologies.

### 2. TECHNOLOGIES FOR HOLLOW TITANIUM FAN BLADES

First generation hollow fan designs are manufactured as a fabrication of external titanium alloy panels and a parasitic internal titanium alloy honeycomb core joined by a low pressure liquid-phase diffusion bonding process. Such a fan set is some 20% lighter than its solid equivalent.

Demonstrator programmes for the later generation of fan design were accelerated during the mid-1980's and early 1990's to acquire fundamental engineering data, develop

High pressure solid-state diffusion bonding is used to join these second generation designs. They also incorporate a superplastically formed corrugated core which largely supports its own centrifugal load. This results in a fan blade which is some 15% lighter than its first generation equivalent. Further significant engine weight reductions accrue from a correspondingly lighter fan disc, containment casing and front support structure.

The optimisation of hot-die forming and superplastic forming has been crucial for the accurate dimensional control of external and internal component features. Process modelling has also been used for the development of the important manufacturing parameters. In addition, as the design/make process is complex and lengthy and involves many disciplines, Rolls-Royce has linked all the activities in the conception, design, manufacture and evaluation of a hollow fan via a totally integrated computer-based operation, the Fan Key System.

Second generation fan designs are manufactured as an assembly of external titanium alloy panels and a central titanium alloy membrane sheet (reference 1). The cleaned external panels have their mating faces coated with a barrier layer in a developed pattern. The three-piece flat pack is then assembled for the subsequent diffusion bonding heat-treatment process. All these operations take place in a clean-room complex which provides the necessary environmental controls to prevent particulate contamination within the joints of the component. The assembly is then heat-treated in a high temperature pressure vessel under computer control. Diffusion bonding occurs at all the uncoated surfaces.

The manufacturing sequence then exploits the natural superplasticity of duplex fine-grained titanium alloys. The diffusion bonded pack is inflated with an inert gas at elevated temperature between precision machined metal dies to develop the internal corrugated core by superplastic forming whilst simultaneously forming the component's external aerodynamic shape. Computer control of this operation as well as die-set shape maintenance guarantees the dimensional tolerances, temperature distribution and strain-rate necessary for the production of a conforming component. Assurance of the product is provided by a comprehensive verification procedure supplemented by extensive process monitoring. The manufacturing cycle is completed via selective NC machining and surface processing operations.

For the production of all its hollow titanium fan blades, Rolls-Royce has made significant investment over recent years in facilities, special-to-purpose plant and equipment and in processing technologies. In addition, a local area network captures all the data from the key digitally controlled processes for their verification, SPC monitoring and traceability.

Recent innovations have included a dedicated and isolated diffusion bonding facility for the fabrication of second generation components. It accommodates only those processes which are essential for the production of diffusion bonded parts and excludes all other manufacturing processes which may produce malign particulate contaminants. At the heart of this facility is a clean-room complex which provides the required environment for the assembly of the parts. It is operated to strict working procedures, and its environment and manufacturing processes are subjected to continuous automated monitoring and surveillance.

The Fan Key System (Figure 2) is a totally integrated,

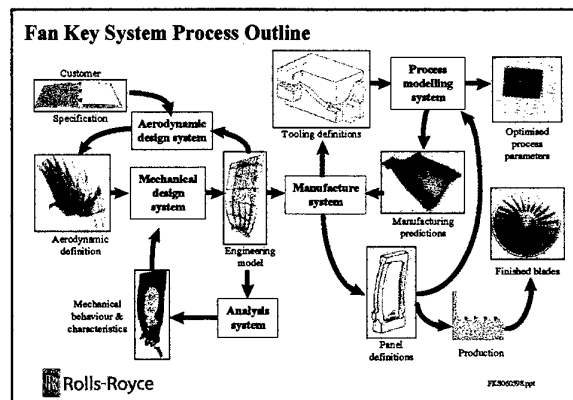


### Figure 2: Fan Key System Process Outline

computer-based design-to-manufacture system which straddles both the Engineering and Manufacturing functions. It comprises a number of linked systems: the aerodynamic system, the design geometry system, the mechanical analysis system, the manufacturing system and the process modelling system.

The aerodynamic system uses computational fluid dynamics tools to generate the component's external shapes. Additional features which satisfy mechanical design and manufacturing requirements are then incorporated via the design geometry system to produce the definitive engineering model. This is then manipulated by the manufacturing system to "reverse engineer" the data in order to produce component details, tool tapes, component machining and inspection data, and the material condition-of-supply. Process modelling

contributes to the accurate interpretation of the design intent.

## 2.4 Process Modelling

A process model is an advanced computer simulation of a manufacturing process. State-of-the-art finite element analysis - similar to that used during the engineering design process - has been used to make the process modelling of fan technologies a reality.

The process modelling system for the DB/SPF fan blade is illustrated in Figure 3.

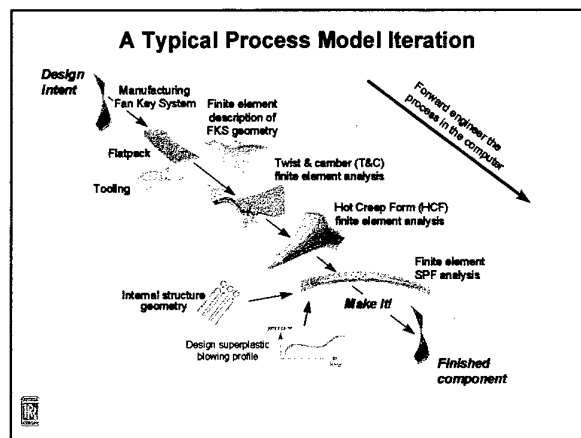


Figure 3: Process Model Iteration

The process model is supplied with Fan Key System CADDs definitions of the material condition-of-supply and the tooling for each manufacturing operation. In order to accurately predict the final product, each of the key manufacturing processes has been modelled.

A typical process/product development cycle can contain many iterations. The benefit of process modelling is that the key processes can be observed and optimised virtually in the computer in advance of the production of expensive tooling. It also avoids the need for trial-and-error component manufacture.

## 3. THE FUTURE

The Trent engines now in service on large twin aircraft form a significant part of Rolls-Royce's future strategy for civil engines. Wide chord fan technology is a key contributor by providing a greater thrust for a given fan diameter, better fuel efficiency and better resistance to foreign object damage. Derivatives of these engines will power new aircraft projects such as the Airbus Industries A340-500/600 and the long range Boeing 777 (reference 2). They will utilise modules from both the Trent 700 and Trent 800 engines with a minimum of re-design. Rolls-Royce is also developing an even more advanced fan concept, the swept fan, which benefits from the proven flexibility of the diffusion bonding and superplastic forming technologies and the Fan Key

System. This design increases flow capacity and efficiency over current wide chord fans and it reduces sensitivity to bird strikes due to a higher tip stagger (reference 3).

The next major military aircraft development is the Joint Strike Fighter (JSF). Rolls-Royce is participating with Lockheed Martin in its shaft driven lift fan engine and with General Electric for the development of an alternative propulsion engine. Both these applications will incorporate wide chord fan technologies (reference 3).

## 4. SUMMARY

First generation wide chord fan designs on medium thrust-rated engines have demonstrated reduced fuel consumption and enhanced resistance to component and engine damage during extensive operational experience. Second generation wide chord fans are in service on the higher thrust-rated Trent aeroengines and have delivered the predicted weight and cost advantages. The development of hollow titanium fan blades for Rolls-Royce's portfolio of civil engines has contributed to commercial and technological competitiveness, and the concept is being extended to all relevant future engine applications. The Fan Key System and process modelling will be further enhanced to optimise the fan design-make process.

## Acknowledgments

The authors wish to thank ROLLS-ROYCE plc for permission to publish this paper. They would also like to recognise the contributions made by many colleagues to the developments reported.

## References

1. G A Fitzpatrick, J M Cundy. "Rolls-Royce's Wide Chord Fan Blade - The Next Generation", Seventh World Conference on Titanium, San Diego, USA June 1992.
2. P Ruffles. "Trent in World Markets". I.Mech.E.150th Anniversary Symposium, London, UK July 1997.
3. P Ruffles. "Beyond Whittle - Innovation in Gas Turbines". 4th International Charles Parsons Turbine Conference, Newcastle, UK November 1997.

# Guaranteeing 100 % Quality Through Closed Loop Process Control

O. Schnerr, W. Michaeli  
 Institut für Kunststoffverarbeitung an der RWTH Aachen (IKV)  
 Pontstraße 49  
 52062 Aachen  
 Germany

## SUMMARY

A special method of guaranteeing quality has been developed at IKV which is titled "Closed-loop Quality Control". This firstly permits the prediction of Quality of injection moulded parts out of process variables and secondly uses the correlation between process conditions and the quality of the moulded part to control the process.

With this systems for online quality control there is a possibility to reduce the scrap production without employees to a minimum. Environmental influences and charge deviations can be compensated. An on-line documentation of the quality of every moulding is a by-product of the controller.

## LIST OF SYMBOLS

$A$	feedback matrix
$B$	input matrix
$D$	feedback matrix
$C$	output matrix
$k$	time factor
$\vec{u}(k)$	input vector
$\vec{x}(k)$	state space vector
$\vec{y}(k)$	output vector
$T_{\text{Mould}}$	mould temperature
$T_{\text{Melt}}$	melt temperature
$P_{\text{Cav}}$	cavity pressure
$S_{\text{Screw}}$	screw position
$v_{\text{Inj}}$	injection velocity
$P_{\text{Hold}}$	holding pressure

## 1 INTRODUCTION

The most important production process of plastic parts is injection moulding. The essential characteristics of this process are

- The direct transformation from the raw material to the finished product,
- No or only little necessity of refinishing of the product,
- Possibility of fully automatic processing and
- High reproducibility of the production.

The injection moulding generates parts which reach from microstructure parts with dimensions of a few micrometers to large containers with a weight of 100 kg. An injection moulding machine consist of the following assembly groups

- Plasticizing unit,
- Clamping unit,
- Mould,

- Temperature Unit,
- Control Devices and
- Machine bed.

In the plasticizing unit the thermoplastic material, delivered by the raw material producer as granulate or powder, is melted and homogenised by rotation of a screw within a cylinder, supported by external heating. The melted material is injected into the mould by the axial thrust of the screw. The task is to form and cool the flowing melt. Each mould is composed at least of two halves so that it is possible to open it along the parting line in order to automatically eject the mouldings. The clamping unit transports the movable mould half and applies the required clamping force during the injection phase. With help of a temperature unit the mould is kept at a temperature adjusted to the moulding process. The production process is divided into three phases. During the metering phase the raw material is melted and homogenised. In the injection phase the melt is injected into the mould by the axial thrust of the screw. Here, pressures from 300 to 3000 bar occur. The injection phase ends with the volumetric filling of the mould. Subsequent to this is the holding phase during which the volume contraction of the cooling plastic is compensated. Melt is injected into the mould until the viscosity within the moulding is increased to such an extend, that no more material movements are possible. During this phase moulding characteristics such as dimensions and inner characteristics are influenced decisively. Following up the holding phase the moulding is cooled down to release temperature during the residual cooling time and subsequently ejected.

## 2 MOTIVATION

In the injection moulding process the important quality characteristics strongly depend on the produced moulding. For technical applications such as faction pipe systems for petrol engines high dimensional accuracy and strength are required. For mouldings with high optical demands such as compact discs or in general mouldings for optical use, characteristics such as the surface quality or orientation of the molecules are of importance. There are different quality characteristics which exist for products produced in injection moulding depending on the range of application. No universally valid moulding characteristics can be defined.

All quality characteristics strongly depend on influences to the production process. The complex structure of the production system injection moulding machine admits no direct control of the steps determining the moulding quality, the filling and cooling in the mould. Rather process values which are only indirectly associated with proceedings in the mould are controlled by the control devices. During the injection phase the axial velocity of the screw is regulated by the position of a hydraulic valve. The relevant process value for the mould quality in this phase is the velocity of the melt front in the

cavity. In the holding pressure phase the control value is the hydraulic pressure at the same valve. But the most important process condition is the cavity pressure caused by the melt.

A physical model building associating the set values screw velocity, hydraulic pressure and the resulting mould pressure, which characterises the moulding process also during the injection phase, a constant velocity of the melt front leads to a constant moulding pressure gradient, is not possible due to several reasons. The compressibility of the hydraulic oil and the melt, the leakage of the melt in the cylinder and the closing behaviour of the check valve, which prevents the melt from flowing back along the screw during the injection phase, are examples for constantly varying influences on the process. A far bigger problem represents the used raw material itself. Besides the huge amount (>5000) of different plastics used in injection moulding, characterised among others by different melt viscosity and compressibility, there are deviations within charges of raw materials caused by the chemical production process. Additional deviations of volumes of reinforcing materials, such as glass fibres and other additives occur.

During the development of a strategy to increase the quality of injection moulded products by directly controlling the moulding quality the above described problems have to be considered.

### 3 STATE OF ENGINEERING FOR THE CONTROL OF INJECTION MOULDING MACHINES

For some years the control of machine values has been state of the art. The controlled values are measured by sensors and corrections are initiated if necessary. These controls, distinguished by the phases of the moulding process, are the velocity control of the movement of the screw and the control of the hydraulic pressure during the holding pressure phase. Independent of these phases controllers are used to regulate the melt and moulding temperatures.

These systems are normally insufficient to guarantee constant moulding quality. Effects of material deviations and many other additive influences on the process cannot be compensated with their help. All these interference factors influence the quality of the produced mouldings. But the quality is decisive for the value of a moulded part, so it is obvious to use the quality directly as a control value. Pressure, velocity and temperature regulations are still important because they guarantee the exact compliance with the set machine parameters. The quality control is superimposed on these controllers and calculates new machine set values during each cycle with the aim to produce optimal quality. In the past controllers which supervise one quality characteristic have been developed (Ref. 1). Different methods have been realised. These are classic concepts such as PID-Control and more modern ones such as modern Fuzzy-Control. The control with PID-Control shows, that a fixed control structure can not be given and the practical use is linked to a high development effort for the control of different mouldings. Likewise tested Fuzzy-Systems are based on a description of problems. Typical are rules of the following kind "If the moulding temperature is too low, then increase the set value of the temperature unit". A further characteristic of the Fuzzy-Systems are poorly defined classifying functions to groups. An element can belong to a group as a part. According to the grade of this relation the following condition is fulfilled. "If the moulding temperature is little too low, then increase the set value of the temperature unit only a little bit". The controllers with Fuzzy-Logic showed better results than the ones with PID-behaviour. But both present a high complexity in

the dimensioning phase. In practice not only the compliance with one quality characteristic is required, but there are a number of given quality characteristics to follow. Both strategies require a complicated implementation of multiple value controllers. Independent controllers for each quality characteristic often generate competing machine set values and so the use of such systems is very restricted.

The aim of the investigations and developments at the IKV is the synthesis of controllers to supervise several quality characteristics simultaneously. In particular the special characteristics of the injection moulding process, a cyclic process with non-linear dependencies, have to be considered.

### 4 STRUCTURE OF A QUALITY CONTROL SYSTEM

Figure 1 shows the structure of a quality control system developed for the injection moulding process (Ref. 1). Basis is the quality prediction with empirical process models developed at the IKV. From measured process values (e.g. moulding pressure and cavity wall temperature) characteristic values (average values or integrals) are calculated, which serve as input values for a quality model. This model calculates the quality of the actual produced moulding online from the characteristic values. The differences between the calculated quality characteristics and the belonging set of quality values serves as input values for the controller. Each cycle new, optimal machine set values are sent to the machine control via the machine interface. Time dependent and time independent effects of the change of the machine set values to the process and the moulding quality are considered.

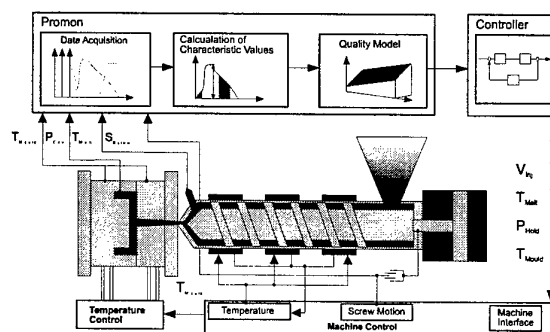


Figure 1: Structure of Quality Control System

### 5 MODELLING OF THE INJECTION MOULDING PROCESS

A system to control quality characteristics consists of different mathematical models, depending on routine performance and certain constellations of the control section. To be able to characterise the injection moulding process two models have to be supplied. The first one registers the statistical, consequently time-independent correlation between the process values and the quality characteristics (quality model). These dependencies can be modelled by statistical process models. They are increasingly substituted by algorithms developed by the research field of artificial intelligence, for example Neural Networks (Ref. 2, Ref. 3). The aim here can be defined as the application of "self-learning" characteristics and capabilities,



which make it possible to realise even non-linear dependencies between process values and quality marks.

The second model registers the correlation between machine set values and process values. The time-independent correlation between the machine set value injection velocity and the measured process value screw movement is registered by this model. Additionally the time-dependent correlation between machine set values and process values is also represented by this model. The dependency of the measured process value melt temperature belongs to the set values of the cylinder temperatures. The model is build by so called parametric estimation. Typical for this procedure is a model, the parameters of which are approximated by mathematical processing. During the control synthesis conducted it appeared, such as the parametric estimation the Least-Square-Algorithm which works similar to the algorithm used by regression analysis, is specially useful. Advantages are the robust behaviour, the good convergence with noisy signals and the universal usability and an easy handling of the algorithm.

For both models experiments have to be conducted to achieve the necessary information of the production process. The time-independent model is developed with data from experiments based on the design of experiments. The information to calculate the time-dependent models have to be determined neutralised by jump experiments. Figure 2 shows a jump experiment in which the set value melt temperature has been increased. Also shown is the measured melt temperature.

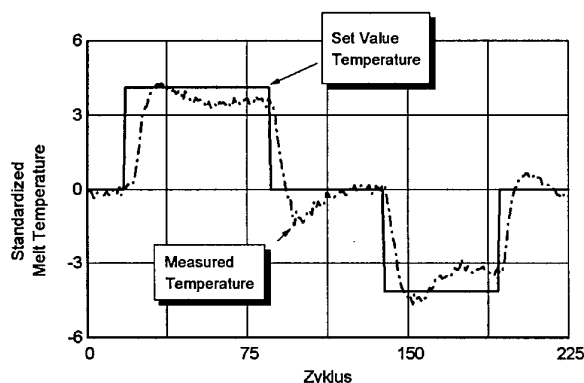


Figure 2: Jump response melt temperature

In the past few years a subsection of control engineering going back to Rudolf Kalman obtains a growing importance due to rapidly increasing computer power. It is the synthesis of control systems in the state space. This theory defines variables between the input and output of a system that characterise the inner state of this system. Due to this non-linear and time-variant problems can be solved. But this theory is also suitable for non-linear and time-invariant systems. It allows examinations of the system behaviour which could not be investigated with the classic control theory. The development of multiple value control systems is possible without conducting a disconnection in one value systems.

During the transition to the state space the differential equitation of order  $n$ , stemming of the parameter estimation of the time-dependent process model, are transformed into difference equitations of the first order. Figure 3 is shows the structure of the process model. Where the input vector is the vector of machine set values and the output vector the process values:

$$\bar{x}(k+1) = A\bar{x}(k) + B\bar{u}(k)$$

$$\bar{y}(k) = C\bar{x}(k) + D\bar{u}(k)$$

using

$\bar{x}(k)$	state space vector
$\bar{y}(k)$	output vector
$\bar{u}(k)$	input vector
$A, D$	feedback matrix
$B$	input matrix
$C$	output matrix
$k$	time factor

With the help of the quality model and these output values the calculation of the reaction of the quality characteristics on a changing of the machines set values is possible.

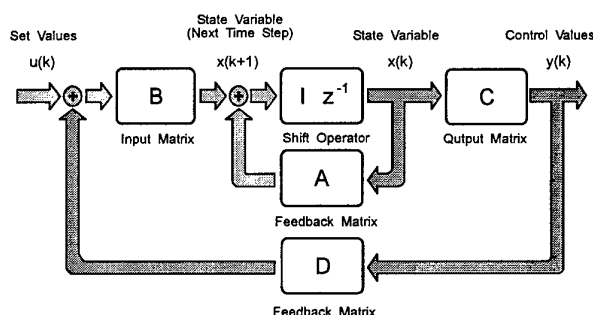


Figure 3: Flow chart of state space description

If the behaviour of the injection moulding machine is known in the state space then two requirements, controllability and observation of the system have to be investigated. The controllability of the process is a criteria for the transferability of a process state into another one in a limited time. The observation requires that enough process values are available to declare the state of the process. If both requirements are met a suitable controller can be developed for the system.,

## 6 CONTROL STRATEGIES

In the following three strategies realised for quality control are presented: The control concept steady state, the Lueneberger-Observer and the control with Kalman-Filter and drift compensation (Ref. 4).

The steady state control concept is characterised by neglecting the time influence and leans mainly upon the time independent part of the machine model. The machine set values are not corrected at the end of each cycle. New set values are calculated only when all transient state of the last change are decayed. The dynamic behaviour of the system is only necessary to calculate the length of the sample and control intervals.

The disadvantage of this concept is the delayed reaction to disturbances due to sub sampling. A solution for this problem can be found through a return of the state variables which describe the inner behaviour of the system. However they are not available in injection moulding process which means that they have to be estimated with the help of the time dependent machine model. New control adjustments are calculated with

the estimated inner behaviour. Reliable machine set values are only produced if the actual state is corresponding with the estimated state. For test a theoretical quality is calculated with the help of the model. If this is consistent with the quality calculated from process values the reality is reflected very well by the model. Otherwise the model is corrected with the Lueneberger-Observer so such a way that the difference between calculated and actual quality becomes minimal. The developed control system with observer is able to convey the process out of any start state to a set state. However external disturbances are not considered.

The third implemented control system is the control by Kalman-Filter. Permanently appearing disturbances as system or measurement noise which also characterise the injection moulding process are corrected with this concept. Kalman-Filter and Lueneberger-Observer have a similar kind of effect. The Lueneberger-Observer is used for occasional initial disturbances at the beginning, but the Kalman-Filter is used when stochastic disturbances appear. To control permanent disturbance such as material deviations and changing environmental influences a drift compensation is used additionally. The structure of the controller used is shown in Figure 4. In the upper part the real process is shown. The values A, B, C and D are unknown and are calculated with the help of jump tests and following system identification. The controller R is determined by minimising an accuracy function. It calculates from the current estimated state the new machine set values which are given to the real process via the machine interface. Simultaneously these parameters are applied to the inputs of the model and so the next state of the system is estimated. The outputs  $y$  of the model of the system represent the quality calculated by the state space model. This calculated quality can be compared with the quality  $y'$  which is calculated out of the process values of the real process. The mistake appearing there is applied back to the state space model and minimised via the Kalman-Filter and the drift compensation. So the model is adapted to the real process.

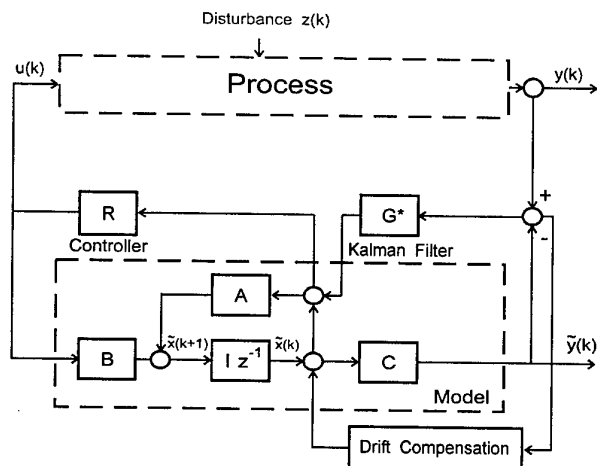


Figure 4: Quality Control System with Kalman Filter and Drift Compensation

## 7 APPLICATION OF CONTROL STRATEGIES

The three control concepts have been realised for a box shaped test component. A length and width, the shrinkage at a defined point and the part weight have been chosen as quality characteristics to be controlled. The double cavity mould used here was equipped with a pressure sensor in each cavity and a

temperature sensor per part of the mould. Additionally the melt temperature is measured by an infrared sensor in the screw antechamber. Included in the control are the values hydraulic pressure and screw position out of the machine control. A fully controlled hydraulic injection moulding machine was used. The data transfer from the controller, realised in MATLAB (Ref. 5) on a standard PC to the injection moulding machine is applied via machine interface. The data acquisition and calculation of characteristic values is done with the Software PROMON (Ref. 6).

The identification of the quality model is carried out with the help of test data, which have been gained with a design of experiments. Varied machine set values have been holding pressure, injection velocity, melt and mould temperature. For the model used the following accuracies resulted for the characteristics length, width, shrinkage and weight: 97,3%, 92,4%, 82,4% and 99,2%. After the jump experiments and identification of the differential equations have been transformed into the state space. The requirements observation and controllability were fulfilled so that the controller could be developed for this system.

During the following simulation phase, the control strategy of steady state, in which time behaviour is used only for the determination of sampling intervals, showed a promising behaviour. The controller reacts to disturbances already after only a few cycles, however, not later than after one sampling interval. A single controller intervention was enough to return the controlled quality characteristic close to nominal values. The control strategy using the Lueneberger-observer reacts very quickly to disturbances. Strong oscillations due to disturbances in the system make a stable simulation difficult. During the simulation, the control with Kalman-filter showed a similarly positive behaviour like the control steady state. After 30 cycles, the controller has compensated the occurring disturbance without showing any sign of over oscillation. Courses of the integral of mould cavity pressure and injection energy could be returned to nominal values within approximately five cycles.

The developed controllers, being optimised during the simulation, were field-proven in the process. The controller's behaviour regarding disturbances and guide was examined by increasing one machine adjusting parameter to a set value and evaluating the course of the quality quantities. During field application, the above mentioned machine settings were disturbed. In the following, only the disturbance of the after-pressure is to be examined, since the other machine adjusting parameters exhibited a similar behaviour. As could be expected, disturbing the packing pressure with a value of -50 bar had its main effects on the integral of mould cavity pressure.

For the steady space control concept a sample rate of 10 cycles, showed the best results in the simulation, was used for the test. After the run of one sample interval after a disturbance a correcting variable intervention of the controller followed. At the end of the second sample interval (10 cycles) the controller interfered again and corrected the quality to the value desired. The disturbance has been compensated fast and without over oscillations (Figure 5). This behaviour characterises the behaviour of the disturbance variable of the controller. If the disturbance ceases, the answer of the controller describes the leading behaviour, the reaction of the controller to a new set value. 10 cycles after cessation of the disturbance the controller intervenes into the process, further 10 cycles later a second intervention follows. About 20 cycles after cessation of the disturbance the quality reaches the new set value.

Already during the phase of the controller synthesis and simulation a non stable behaviour appeared for the controller with Lueneberger-Observer. Without disturbance the controller conducted stable during the practical use, but with a disturbance a huge oscillation of the values between the tolerance appeared. There is no sensible control with the controller with Lueneberger-Observer possible. This can be explained by the accidental disturbances during the injection moulding process.

Therefore, the use of the control concept applying the Kalman-Filter should exhibit better results. Figure 6 demonstrates the behaviour of the controller during a disturbance of the holding pressure. After the 69<sup>th</sup> cycle a disturbance of the holding pressure was applied, which was corrected effectively. After about 8 cycles and repeated intervention the set value is reached. Cessation of the disturbance leads to a reflected course of the leading behaviour. A partly bigger deviation in some quality characteristics can be explained by the integer parameters of the set values moulding and melt temperature.

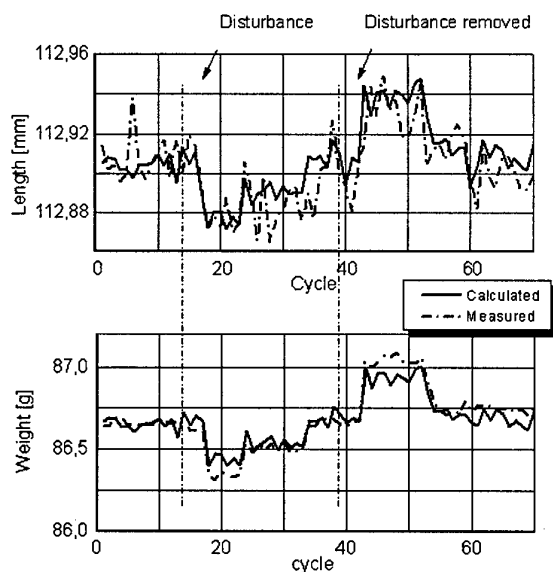


Figure 5: Practical Test of Steady State Control Concept for a Disturbance

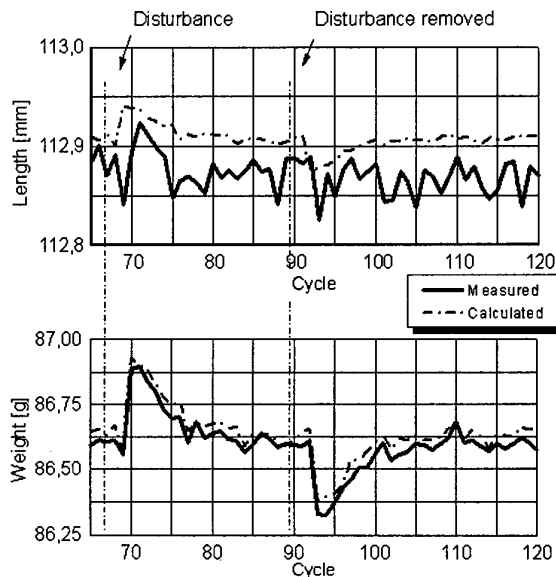


Figure 6: Practical Test of Kalman Filter Control Concept for a Disturbance

## 8 QUALITY CONTROL THROUGH THE STRATEGY OF EVOLUTION

Another strategy for quality control of moulded parts is the strategy of evolution, well known from biology. Here, the controller is substituted by an optimiser. Basic principles of this method are mutation, i.e. a random change in the process, and selection, i.e. choosing an advantageous change. The new point in the quality mountain (Figure 7), arising from a change in the setting of machine parameters, is called "descendant". A favourable change is called "parent". A simple selection scheme is the survival of the best out of three descendants. Through mutation, three descendants are produced from one parent; normally in this process all parameters are changed at the same time. Selection now decides which of the three descendants is the most valuable and will thus be chosen to serve as a parent for the next mutation. The other two mutations are turned down. After this step mutation of the new parent is continued. The process thus reaches optimum quality. Figure 7 demonstrates a course for an optimisation using the evolutionary method. In case more than one parent is used when working with this method, it can be called a population. Through recombination two parents produce one common descendant by a random process. Recombination is an important method for overcoming secondary maximum. Through a limited lifetime of the parents, determined e.g. by a maximum number of optimising steps, a certain robustness of the process against disturbances can be obtained. Similarly, the number of parents' descendants can be changed. Parents being especially successful are rewarded with more frequent mutations. In the field of biology this method is called vitality. In the practical application of this strategy a disturbance of the holding pressure could be compensated within 15 steps. Generally, thus, also this method of evolutionary optimisation can be used to control the quality moulded parts.

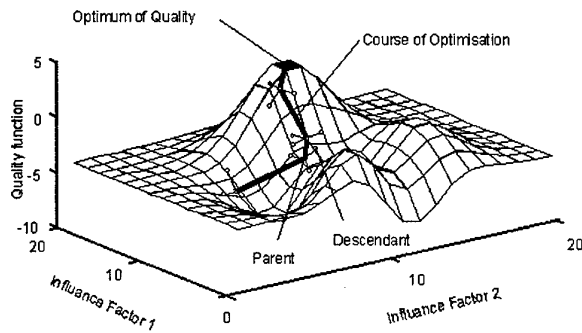


Figure 7: Quality Function and Course of Optimisation

## 9 NEW CONTROL CONCEPTS

With the application of artificial neural networks an improvement of the prediction quality could be reached in the quality control (Ref. 2, Ref. 3). This is based on the one hand on a simplified model building and on the other hand on the possibility to model even non-linear correlation between the process characterising values and the quality. Also attributive moulding characteristics can be predicted more effective than else with the necessary method of logistical regression (Ref. 2). In order to use neural networks for quality control some changes in the structure of the networks have to be done, which enable the reproduction of also time-dependent correlation as they are considered in the state space controller. The neural networks used for quality prediction consist of several neurones where the information processing takes place, leaning upon the image of the human brain. These neurones are linked together with weights and arranged in layers. At the input layer of a neural network the process values are applied and at the neurones of the output layer the calculated quality characteristics can be read. During a training phase learning data are presented to the neural network, so that the network learns the dependencies between process values and quality marks. In the following practical phase of the neural network only the on-line calculated values are given to the network and the quality characteristics are calculated. Previous production cycles are not taken into consideration. But this is absolutely necessary for the quality control, so that additional elements as

external shift operators or internal delay elements are necessary for the system identification, to consider previous process cycles (Ref. 3). During the dimensioning of neural controllers two problems have to be considered: Generating useful set values and inversion of the system models. To dimension the controller different methods can be used. There are direct and indirect procedures to distinguish. The first generates new set values directly from the quality deviations. Indirect methods use a model with which the state of the system is estimated and on this basis new machine values are calculated (Ref. 7). Because of the non-linear, time variant behaviour of the injection moulding process these procedures promise the best success.

## 9 CONCLUSIONS

It appeared that both the steady space as also the control concept with Kalman-Filter are suitable to control the quality of injection moulded parts. The last procedure shows a more reproducible behaviour than the time-independent concept, because it reacts immediately after the occurring of a disturbance with a compensation reaction.

With the presented systems for quality control there is a possibility to reduce the scrap production without employees to a minimum. Environmental influences and charge deviations can be compensated. An on-line documentation of the quality of every moulding is a by-product of the controller.

## 10 REFERENCES

1. Vaculik, R., "Regelung der Formteilqualität beim Spritzgießen auf der Basis statistischer Prozeßmodelle", Dissertation at the Technical University of Aachen, 1996
2. Michaeli, W., Schnerr O., "Attributive Merkmale überwachen", *Plastverarbeiter*, January 1998, pp 30-32
3. Schnerr, O. "Neural Networks for Quality Prediction and Closed Loop Quality Control in Automotive Industry", Society of Plastic Engineers Antec'98, Atlanta 1998
4. Föllinger, O., *Regelungstechnik*, Hüthig Buch Verlag GmbH, Heidelberg, 1990
5. N.N. MATLAB Reference Guide, The Math Works Inc, Natick, Mass., 1992
6. N.N., *Handbuch zur Meßdatenerfassungs- und verarbeitungssoftware PROMON*, Gierth & Wybitul Ing. GmbH, Baesweiler, 1995
7. Peinemann, F.W., *Neuronale Regelungskonzepte zur sensomotorischen Koordination von Industrierobotern*, VDI-Verlag, Düsseldorf, 1996

# INTELLIGENT PROCESSING IN A HOT ROLLING MILL FOR STRUCTURAL STEELS

P.J. van der Wolk, C. Dorrepaal, J. Sietsma, S. van der Zwaag

Delft University of Technology  
Laboratory for Materials Science  
Rotterdamseweg 137  
2628 AL Delft  
The Netherlands

## 1. SUMMARY

To control the properties of a steel, both its composition and the applied heat treatment are of paramount importance. During the hot rolling process the cooling process is of main importance to control the properties of a steel. The effect of the cooling applied after hot rolling is usually described with CCT diagrams, as these describe a steel's transformation behaviour under continuous cooling conditions. The determination of a single CCT diagram is very time consuming; nevertheless it is necessary for each new steel composition, as the transformational behaviour is very sensitive to the chemical composition of a steel. Therefore in the present paper the CCT diagram has been modelled as a function of chemical composition using neural networks. To do so, a large number of CCT diagrams have been converted from a graphical format into a numerical format; these data have been used to fit a neural network model. This model reproduces the original CCT diagrams quite accurately, and is able to predict CCT diagrams for new steel compositions. Besides, in this way the effect of a single alloying element can be isolated; the effects of alloying elements on the CCT diagram as calculated with the model are in line with metallurgical knowledge. The number and accuracy of the CCT diagrams currently available is limited, which limits the validity of the model. The validity of the model can in principle be extended by using more and more accurate CCT diagrams.

## 2. INTRODUCTION

Hot rolling mills (Figure 1) take up a major part in the bulk production of structural steels. These mills reduce an up to 10 m wide steel slab from a original thickness of 225 mm to a thickness as low as 1 mm, where both shape and properties of the end product—a steel sheet—need to meet very narrow specifications. Therefore, the hot rolling process requires a very tight process control.

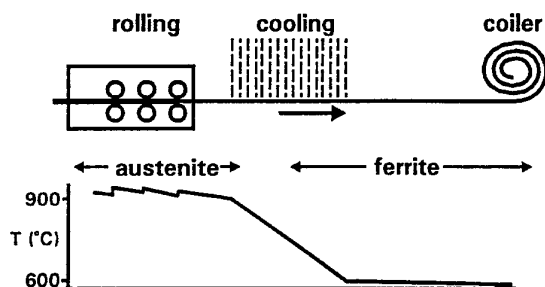


Figure 1: Schematic representation of the hot-rolling process of steel sheet, and the temperature development during the rolling process.

The properties of a rolled steel sheet are mainly determined by two factors: its composition and the applied heat treatment. The composition has already been set during casting prior to the rolling process, setting limits to the steel's final properties. Its final properties are fine tuned by the heat treatment during hot rolling, in particular the cooling process after rolling.

To allow the large deformation needed for rolling, the steel is kept in the austenitic state, at temperatures well above 700 °C throughout the rolling process. However, before coiling the steel needs to be fully transformed into its ferritic state to avoid the occurrence of phase transformations in the coil, which would result in inhomogeneous properties of the steel sheet.

Stahl 41 Cr 4  
(Schmelze 3)

II-105 (

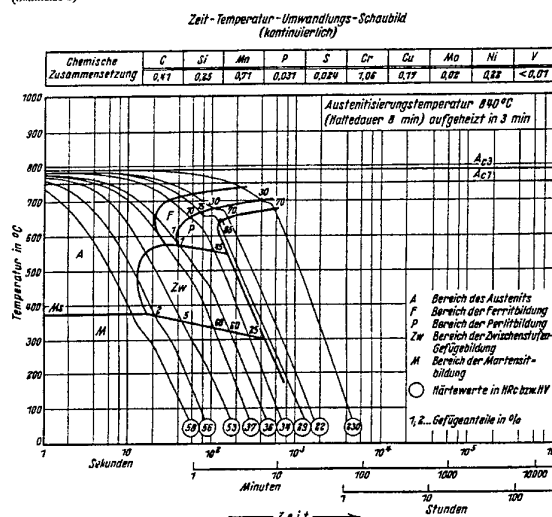


Figure 2: Example of a CCT diagram. Note that the time along the horizontal axis is on a logarithmic scale resulting in a curved line for a constant cooling rate. In this diagram the austenite phase fields is indicated with 'A', ferrite with 'F', pearlite with 'P', bainite with 'Zw', and martensite with 'M'. Volume fractions of each phase are given as percentages along the cooling curve, and hardness values are given in the circles at the bottom of the cooling curves.

In between rolling and coiling the steel is cooled by water jets, where the cooling rate is the main factor determining the effect of the heat treatment on the properties of the steel sheet. Limitations of current hot rolling installations only allow cooling at a fairly constant cooling rate. So the heat treatment during rolling is mainly controlled by two temperatures: the temperature after the last rolling stand, and the temperature after cooling. The temperature after the last stand results from the rolling process, and is sensitive to fluctuations in the rolling process, such as throughput speed, reduction of each stand, temperature of stands, etc. To minimise fluctuations in this temperature, the rolling process needs to be feedforward controlled, requiring an accurate quantitative model of the rolling process. For this purpose a neural network [1] can be used. This final rolling temperature in combination with the cooling condition controls the coiling temperature. Besides from the temperature after the

last stand, the temperature after cooling results from the cooling process, for which models on a physical basis [2] are available.

To control the properties of the final product, the dependency of the properties on the cooling rate needs to be known. For the continuous cooling case this information is commonly given in a Continuous Cooling Transformation (CCT) diagram; an example is given in Figure 2. In a CCT diagram a number of cooling curves, each with a different cooling rate, is drawn, on which the start and end temperatures of each occurring phase transformation have been measured. These temperatures are then used to draw the boundaries of a phase field for each phase, a temperature-time field marking the formation of a single phase. Additionally, the microstructure and the hardness of the final product for a single steel composition are also given in the CCT diagram. The austenitising temperature, the starting temperature of each measurement, corresponds with the temperature after the last stand in the hot rolling mill. Measuring such a CCT diagram for a single steel composition is a very time consuming task. Therefore, to gain information about transformations in new steel grades more easily, it is highly desirable that CCT diagrams can be predicted. The models that have been constructed for this purpose up to now can be divided into physical and statistical models. Physical models [3] [4] try to explain the relation between the parameters of the heat treatment process using the physical principles of phase transformations. In theory, such models are able to predict the CCT diagram of an arbitrary steel grade. However, a CCT diagram is very sensitive to the composition, and the influence of the alloying elements on steel transformation kinetics is not yet sufficiently understood for the accurate prediction of a CCT diagram. Hence, a comprehensive physical model for CCT diagrams is beyond current reach. In contrast to physical models, statistical models attempt to describe a process without considering its physical background explicitly. In general, these models link the independent (input) process parameters to the dependent (output) process parameters by fitting functions to a large number of measured data. For modelling the CCT diagram, the input parameters are the austenitising temperature and the chemical composition, and the output parameters are a representation of the phase fields in the CCT diagram.

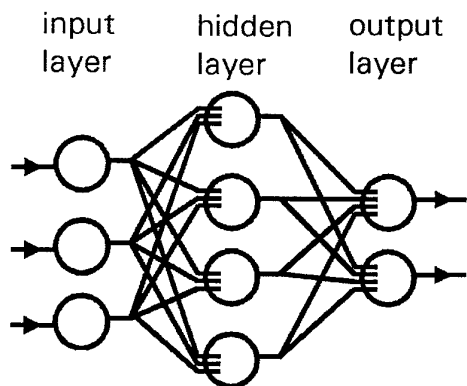


Figure 3: Representation of a hierarchical feedforward neural network. Information is transferred from left to right; the circles represent the nodes.

Vermeulen [5] [6] has shown for vanadium containing steels that neural networks (ANNs) are a type of statistical models that are very suitable for predicting transformation start and end lines in CCT diagrams. However, his model is based on only a small amount of data, limiting its application range. This limitation has been alleviated in the present neural network model. The new model covers a wider range of steel grades and diagrams with varying characteristics. CCT diagrams with separated and

adjacent phase fields are incorporated in the model. The model combines CCT diagrams from various sources. The ANN model and the basic data processing is comparable to that described in [5] [6], hence only the essentials and the improvements in the model are described here. Although the present model incorporates both phase fields, microstructure and hardness values, the current paper only deals with the modelling of the phase fields, which is the most difficult aspect of modelling CCT diagrams.

In Section 3 neural network modelling is described briefly. In Section 4-6 the modelling process of CCT diagrams is described in detail. The resulting model is discussed in Section 7.

### 3. NEURAL NETWORKS

A wide variety of neural networks exist [7] for a wide variety of applications; this section only discusses the basic features of the type used for this research, the hierarchical feedforward neural network [8] which is widely used for modelling. A diagram of this type of neural network is shown in Figure 3. The basic unit in a neural network is its processing element, called a node or a neuron. In a hierarchical neural network these nodes are ordered in layers. The network is called feed-forward, because the nodes process the information in one direction only, from input to output. Each node in a layer is connected to each node in the preceding layer; the network is called to be fully connected. To each connection a weight factor is attributed. The number of nodes in the input layer equals the number of input parameters. The number of nodes in the output layer equals the number of output parameters. The optimum number of intermediate – hidden – layers and the number of nodes in each hidden layer depends on the complexity of the problem, and it is up to the researcher to determine this.

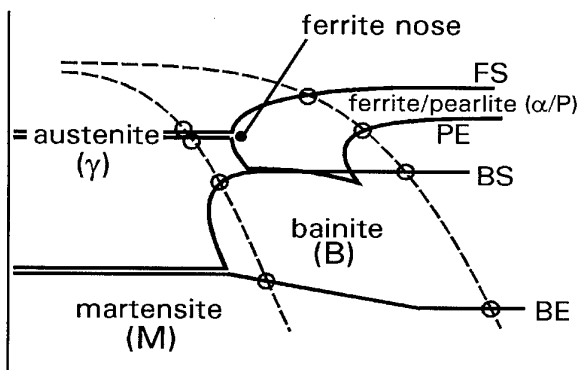


Figure 4: The conversion of a CCT diagram into numerical data. The intercepts (circles) between a cooling curve (dotted line) and the transformation start (FS, BS) and end lines (PE, BE) are determined for a large number of cooling curves. The transformation lines have been extended artificially to have a fixed number of 4 intercepts with each cooling curve.

Each node computes the scalar product of its input values and the weight factors involved and passes this value to a sigmoid transfer function, which produces the output signal of the node. To determine the weight factors –the actual modelling– the neural network has to be trained. For this training algorithm various algorithms have been developed in the literature; for this research the momentum version of the backpropagation of error training rule [9] is used. The procedure is started by presenting input and output data of one sample to the network, which, with its randomly initialised weight factors, calculates the output, the predicted value. This predicted value is compared with the actual or target value of the sample. The difference between target and predicted value –the error in the prediction– is a measure for the

weight factor correction. This correction takes place in the reverse direction—back propagation of error—; first the weight factors of the output layer are corrected, and then the weight factors of the nodes in the hidden layer. Next, this procedure is repeated for the next sample. Once the weight factors have been adapted for all samples (i.e. the first training cycle), this training cycle is repeated until the differences between calculated and target output values are minimised sufficiently. At a certain point in the training procedure the network starts to model not only the functional dependencies between input and output parameters but also the noise in the data set. This is called overtraining. To prevent the network from overtraining, the dataset is split into a relatively large training set and a smaller test or validation set. The weight factors in the network are adjusted using the data in the training set only. In the case of overtraining, the error for the training set decreases while that for the test set increases with further iterations. The weights determined after the iteration for which the error in the test set is at its minimum are used for the neural network model.

#### 4. DATA PROCESSING

Figure 2 shows that the information on start and end temperatures of phase transformations is in a graphical format, whereas the neural network is only able to process numerical information. Therefore CCT diagrams need to be converted into a numerical format. A large number of conversion schemes can be conceived; the one used for this model is an intercept method. In the intercept method, a number of fixed test lines is drawn over the diagram, where the intercepts of these lines with the phase boundaries in the CCT diagrams determine coordinates describing the diagram. An advantage of intercept methods above grid methods is that the diagram can be represented by a relatively small number of data, as all data point at the relevant phase boundaries instead of describing large phase fields. The isochro-

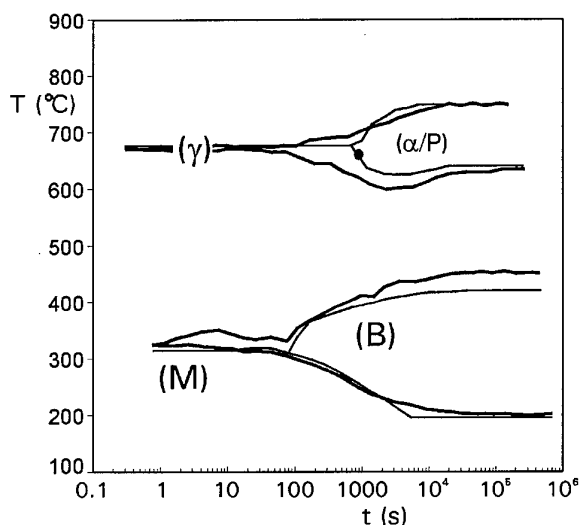


Figure 5: CCT diagram repredicted for the steel with composition A in Table 2, where the thick lines are the predicted lines. Here the original output of the neural network is shown, so without connecting the FS and PE line to the ferrite nose.

nal cooling curves are especially interesting as test lines, as they approach the real cooling curves, thereby making the model easily extendible with information such as the hardness reached on cooling, and the fractions transformed material. On each cooling curve four intercepts are defined, characterised by their temperature values as indicated in Figure 4. The first two intercepts match the ferrite-start temperature (FS) and the pearlite-end tem-

perature (PE), defining the joint ferrite and pearlite phase field, and the last two intercepts match the bainite-start temperature (BS) and the bainite-end temperature (BE) defining the bainite phase field. For the conversion of each CCT diagram 32 cooling curves with cooling rates ranging from 750 °C/s to 0.001 °C/s have been used. Artificial intercepts are defined for cooling rates at which not all phases form. At high cooling rates the ferrite start temperature and the pearlite-end temperature are extended to smaller times through the austenite phase field, and the bainite-start and end lines are extended along the martensite-start line, implicitly defining the martensite phase field. At low cooling rates, the bainite-start and end temperatures are extended horizontally to longer times. Figure 4 illustrates this conversion process. To reconstruct the diagram, the reverse procedure is applied to the data calculated by the network.

The reconstruction gives rise to some practical problems, in particular the accurate prediction of the ferrite nose position. The time and temperature of the ferrite nose (Figure 4) are modelled separately, to improve the prediction of this industrially very relevant feature, and to facilitate the removal of the predicted ferrite-start and pearlite-end temperatures between the location of the ferrite nose and the temperature axis. Another practical problem concerns the bainite phase field. In many CCT diagrams the bainite phase field ends abruptly along a cooling curve (Figure 2), and if the BE line (Figure 4) had been chosen to follow this end line of the bainite phase field, two intercepts at adjacent cooling curves for the bainite end temperature may have shown values as much as 300 °C apart. Although such discon-

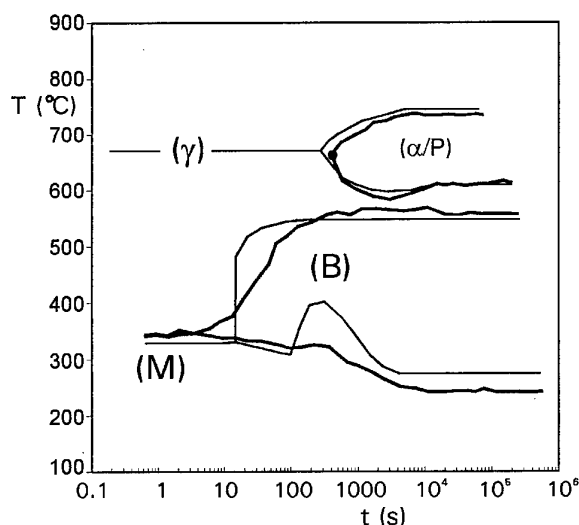


Figure 6: CCT diagram repredicted for the steel with composition B in Table 2. In this figure (and all following figures) the FS line and the PE-line have been connected to ferrite nose to construct the joint ferrite and pearlite area.

tinuities pose no problem to the conversion procedure, they do have a detrimental effect on the modelling process, which is suppressed by artificially extending the bainite area to infinitely low cooling rates. To reconstruct the diagram, the end of the bainite area can be determined with the model for the microstructure: the highest cooling rate for which the fraction of bainite is negligible determines the end of the bainite area. This aspect is not considered in the present paper.

#### 5. DATA SELECTION

The CCT diagrams used for the model have been selected from atlases available in the literature. Two atlases have been used: a collection from the molybdenum steel company [11] [12] and a collection from the VDEh [13]. The steel ranges covered are

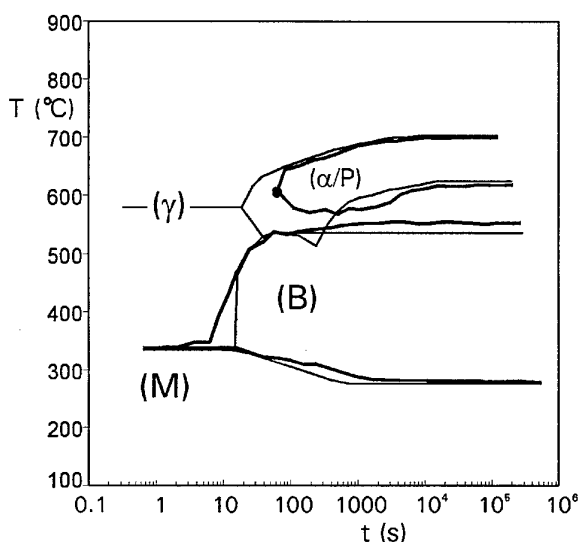


Figure 7: CCT diagram repredicted for the steel with composition C in Table 2.

listed in Table 1.

The CCT diagrams available for this model are by no means evenly spread over the compositional domain, so the range of each alloying element merely gives an indication of the validity of a model based on these data.

## 6. NEURAL NETWORK MODELS

The neural network model described here has been trained using the data processed as described. For practical reasons, the model is split up into two separate networks: one predicting the phase fields of the CCT diagram and one predicting the position of the ferrite nose. The phase field model has one hidden layer with 12 hidden nodes, and gives the relation between 12 input parameters (austenitising temperature, %C, %Si, %Mn, %Cr, %Cu, %P, %S, %Mo, %V, %B, and %Ni) and 128 output parameters (FS, PE, BS, and BE for 32 cooling curves). All models have been trained using the Kennard and Stone algorithm [14] to select a training and validation set. This algorithm sorts the available data by maximising variation in input parameters for the first 75% of the data, which are then chosen for the training set, leaving the remaining 25% for the validation set.

## 7. RESULTS AND DISCUSSION

The neural network model can be evaluated in at least two ways. The most common way of evaluating a statistical model is to look at the residual standard deviation of the model. However, as the original data contains a large number of artificial intercepts which are modelled relatively easily, the value is calculated for the standard deviation of *all* output parameters of the neural network model is lower than the standard deviation of the *relevant* output parameters, i.e. the temperature values describing phase fields of each CCT diagram, discarding the artificial intercepts for each diagram. Therefore the standard deviation of the model is not discussed here.

Also, the model can be evaluated by comparing CCT diagrams from the database to the CCT diagrams as predicted by the neural network for the same composition, which will be discussed in Section 7.1.

The effect of a single alloying element can be calculated by choosing a base steel composition and calculating CCT diagrams for varying amounts of one alloying element. Section 7.2 shows the effect of the carbon, manganese and chromium content on the transformation behaviour of steels with a base composition

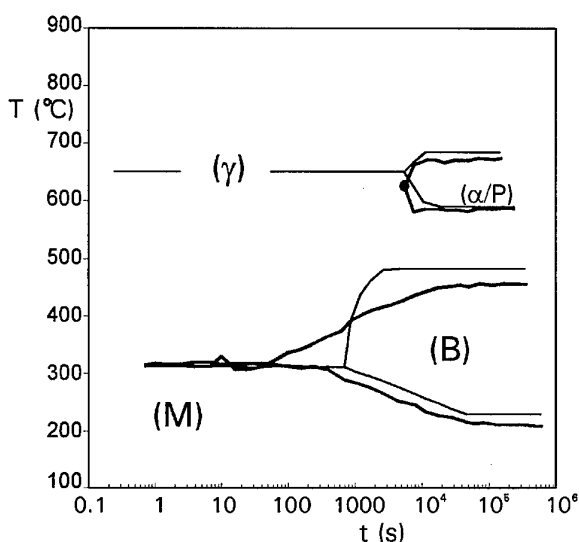


Figure 8: CCT diagram repredicted for the steel with composition D in Table 2.

as given in Table 2.

### 7.1 Reprediction of CCT-diagrams

Figures 5-8 show four examples of reconstructed diagrams using the model for four steel compositions given in Table 2.

The Figures 5 and 6 show two diagrams that are accurately predicted. Figures 7 and 8 show two diagrams that are less well predicted, and show the errors that are most commonly encountered in this model: Figure 7 shows that a joint ferrite/pearlite phase field for which the pearlite-end line shows a pronounced minimum, are sometimes poorly predicted. In such cases the model tends to show a wider gap between the phase fields than in reality. Figure 5 shows that the noses of ferrite and pearlite are sometimes difficult to estimate. The separate prediction of the noses of the diagram overcomes this problem. A similar effect to a lesser extent is observed for the bainite nose. Adding a separate prediction of the bainite nose would improve the prediction of the bainite phase field.

The dots in Figures 5-8 indicate the predicted ferrite-noses. As shown, they determine the position of the nose rather well, which is especially useful when this nose is difficult to distinguish from the predicted intercepts, as in Figure 5.

### 7.2 Influences of alloying elements

Using this model, the effect of alloying elements on CCT diagrams has been studied in more detail. The effects of carbon, manganese and chromium are given here for a steel with base composition as listed in Table 2. Figure 9 shows the effect of carbon by varying the carbon content from 0.17 to 0.53 percent. Carbon is known to depress all transformations, shifting them to lower cooling rates. Here, the joint ferrite and pearlite phase field and the bainite phase field move to longer times with increasing carbon content, indicating that these phases form at lower cooling rates at higher carbon levels. Besides, adding carbon shifts all phase fields to lower temperatures. So for a fixed cooling rate, these transformations start at lower temperatures with increasing carbon level. At the low carbon level the joint ferrite/pearlite phase field and the bainite phase field clearly overlap, which is erroneous from a physical point of view. Close to this particular composition the original data set did not contain any measured CCT diagrams, and as the two phase areas are predicted independently from each other, such overlap is not



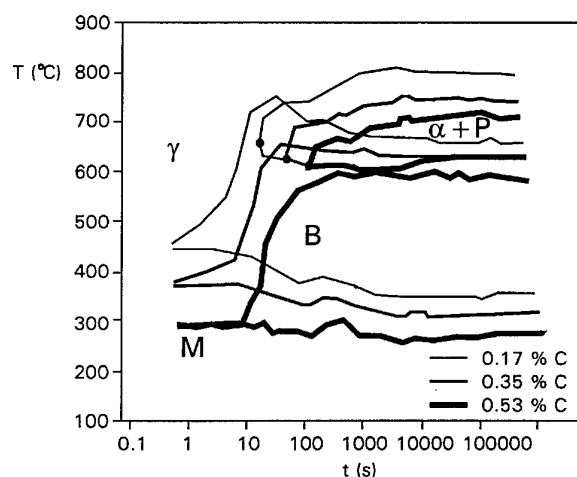


Figure 9: The effect of the carbon content on the CCT diagram on a steel with Base composition as given in Table 2.

excluded in the current modelling approach. To suppress this effect additional restrictions need to be imposed to the model.

For all plots the diagrams with a high alloy content have a slightly jagged appearance, which is known to indicate that the model is affected by the low number of diagrams present in the specific part of the compositional range.

The effect of the manganese content is shown in Figure 10. From the literature it is known that manganese retards most transformation reactions. With increasing manganese content the ferrite, pearlite, bainite, and martensite phase fields are indeed moved to lower temperatures. Furthermore the ferrite and bainite nose are moved to lower cooling rates and a slight gap is created between the joint ferrite/pearlite phase field and the bainite phase field at higher contents of manganese. So effectively, the phase fields encompass a smaller temperature range. The effect of manganese is clearly non-linear: increasing the manganese content from 0.29 to 1.14 mass % only shifts the bainite phase field to slightly lower temperatures, whereas a further increase of equal size results in a further yet much larger shift of the bainite phase field.

The effect of the chromium content is shown in Figure 11. Adding chromium to this steel again moves most transformations to lower temperatures; however in contrast to the effect of carbon and manganese, adding chromium does not affect the pearlite-end temperature at all, and only slightly depresses the ferrite-start temperature. In contrast, the bainite phase field shows a large shift to lower temperatures with increasing chromium content. Due to this difference in effect on the joint ferrite/pearlite phase field on the one hand and the bainite phase field on the other hand, chromium causes a large temperature gap to appear between the two phase fields.

## 8. CONCLUSIONS

A statistical model has been developed that describes and predicts CCT diagrams well over a wide range of steel compositions. Both the position and the size of the phase fields in which the phase transformations take place are well predicted. With some minor adjustments the model is applicable for the prediction of CCT diagrams for common use. This model can easily be extended to predict the entire CCT diagram, including hardness values and microstructural information. The definition of the ferrite nose facilitates the prediction of a correct CCT diagram; adding other points, such as a bainite nose, may further facilitate the representation of predicted CCT diagrams. The current approach results in a model in which the influence of alloying

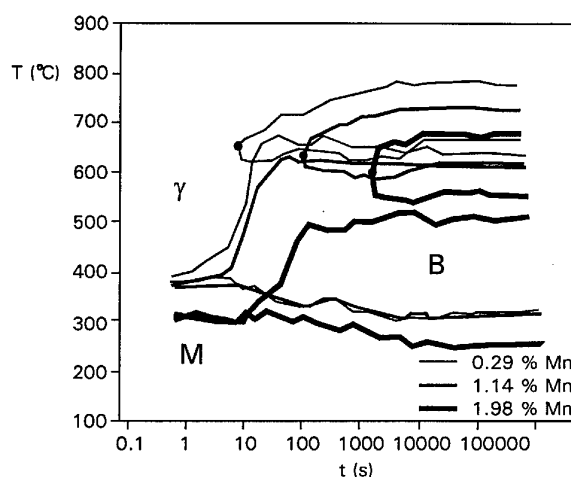


Figure 10: The effect of the manganese content on the CCT diagram of the Base steel as given in Table 2.

elements can easily be shown.

In general, the trends in the effects of the alloying elements on the steel transformation behaviour is predicted correctly. Both decreasing temperatures and shifts in phase fields show up in the predicted diagrams. Also, the ferrite nose position shifts under influence of alloying elements in the direction as expected from metallurgical knowledge. The same applies for the hardness values and fractions of transformation product.

## 9. Acknowledgements

Financial support through the ECSC D3 research program is gratefully acknowledged.

- [1] W.G. Vermeulen, A. Bodin, S. van der Zwaag, Prediction of the strip temperature of steel in a hot strip steel mill using Artificial Neural Networks, *Steel Research* 68 (1997), 1, 20–26.
- [2] F. Hollander, Mathematical models in metallurgical process development, The Iron and Steel institute, 123, London (1969).
- [3] Umemoto, *ISIJ Int.* 32(1992), 306–315.
- [4] G. Krielaart, submitted to *Steel Research* 1997.
- [5] W.G. Vermeulen, P. van der Wolk, P.F. Morris, S. van der Zwaag, *Steel Research*, 68 (1997), 72–79.
- [6] P. van der Wolk, W. G. Vermeulen, S. Van der Zwaag: 2nd International Conference on Modelling of metal rolling processes, Eds. Beynon J.H. et alii, The Institute of Materials, London, 1996, p. 378.
- [7] D.T. Pham, An introduction to artificial neural networks, in *Neural networks for Chemical Engineers*, A.B. Bulsari, editor, Elsevier science publishers, Amsterdam (1995), pp. 1–32.
- [8] P.J. van der Wolk, Modelling material production processes using hierarchical artificial neural networks, TU Delft (1994).
- [9] R. Hecht-Nielsen, *Neurocomputing*, Addison-Wesley Publishing Company, Reading, Massachusetts (1990).
- [10] J. Zupan, J. Gasteiger, *Neural Networks for Chemists*, An Introduction, VCH Verlagsgesellschaft, Weinheim (1993).
- [11] G.F. Van der Voort (Ed.): *Atlas of time-temperature diagrams for irons and steels*, ASM International, Reading PA, 1991.
- [12] W.W. Cias, *Phase transformation kinetics and hardenability of medium-carbon alloy steels*, Climax Molybdenum Company, Greenwich, 1973.

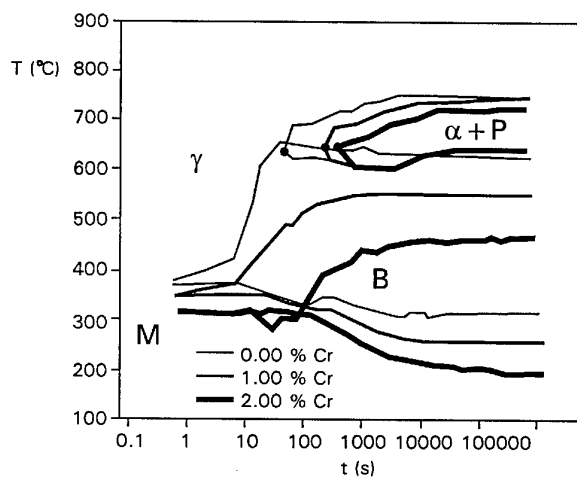


Figure 11: The effect of the chromium content on the CCT diagram of the Base steel as given in Table 2.

[13] Atlas zur Wärmebehandlung der Stähle, Verlag Stahleisen mbH., Düsseldorf, Germany, 1954.

[14] R.W Kennard, L.A. Stone, Technometrics, 11 (1969) 137-149

Table 1: Minimum and maximum values (in mass %) for each alloying element present in the model.

	min	max
C	0.09	1.42
Si	0.08	1.62
Mn	0.29	1.98
P	0.00	0.044
S	0.00	0.054
Cr	0	2.29
Mo	0	1.02
Ni	0	4.56
V	0	0.31
B	0	0.0040

Table 2: Composition (mass %) and austenising temperatures (°C) of the four steels shown in Figures 5-8.

Steel	T <sub>aust</sub>	C	Si	Mn	Cr	Mo	Ni
A	900	0.35	1.55	0.86	1.21	0.58	2.10
B	810	0.40	0.33	0.80	0	0.79	0
C	822	0.38	0.33	0.85	0.74	0.01	1.46
D	830	0.38	0.34	0.82	0.75	0.74	1.46
Base	900	0.35	0.49	0.86	0	0.27	0

# Intelligent Control Strategies for Metal Forging Processes

J. C. Malas

W. G. Frazier

Materials & Manufacturing Directorate

Air Force Research Laboratory

Wright-Patterson Air Force Base, Ohio 45433, U.S.A.

## 1 SUMMARY

Advanced process design and intelligent control methods are needed for significant improvements in metalworking processes such as forging. Some of the distinguishing aspects of forging processes which present formidable challenges to employing intelligent control strategies are the lack of sensors for real-time measurement of the variables to be controlled; limited dynamic actuation for sufficient control authority; and development of efficient models for control system design. Also, in press forging there is basically only one dynamic control parameter which is ram velocity; but there are multiple static control parameters such as initial workpiece temperature, die temperature, preform shape, and die geometry. The existing models for high fidelity analysis of gross plastic deformation processes are too computationally intensive for practical design and real-time control. A suitable architecture of a intelligent material processing system for multi-step thermomechanical processes is proposed. The components of the IPM framework include: open-loop process design, feedback compensation, feedforward compensation, and learning and adaptation systems. Some recent progress in dynamic modeling and optimal design techniques for workpiece material behavior, material flow in dies, and equipment responses are discussed. Illustrative simulation examples showing feedback compensation in disk forging process and feedforward compensation for microstructure control demonstrate potential benefits of intelligent control strategies.

## 2 INTRODUCTION

An effective way for metalworking industries to realize significant cost savings and quality improvements is through new strategies for process design and control. The application of optimization principles and intelligent control approaches to dynamic processes, such as forging, will save money due to reductions in the total number of process operations, wear and tear on equipment systems, scrap material, and the overall energy requirement. In addition, advanced process design and control methods will enable achievement of superior dimensional tolerances, near-net shapes, more precise control of microstructures and mechanical properties in metal forged components. However, the nature of forging and other metalworking operations does not permit the straightforward application of methods used for Intelligent Processing of Materials (IPM), since difficulties arise from scarce dynamic actuation and sensing capabilities. An extended IPM strategy for overcoming restrictions of controllability and observability in a single metalworking process is to design the forming and heating operations for optimized sequential actuation, and then

employ process models and existent measurements for feedforward and feedback control.

For intelligent control techniques to be most efficient, they should be preceded by well-designed processes. A generally accepted definition of a well-designed process is one that is pareto optimal, i.e., no design objective can be improved without degrading at least one other design objective. Indeed, optimal design enables effective tradeoff of competing design objectives, including controllability and robustness goals which have a significant impact on the complexity of the control system design.

Optimal process design requires that the entire processing system be viewed as a whole. This can be achieved through systematic application of modeling, optimization, and control theory principles. In its most basic form, optimal process design involves: 1) developing models of material behavior, thermomechanical processes, and equipment responses, 2) using these models along with appropriate optimization techniques to determine the best sequence of processing operations, 3) using available measurements to insure that the optimized material and process conditions are realized, and 4) using artificial intelligence techniques to improve performance through automated learning. Difficulties arise from the fact that modeling always involves some form of error, whether it is in the mathematical structure (linear or nonlinear, lumped or distributed, etc.) or in the values of the parameters of the mathematical model. Beyond obtaining suitable models, the task of finding the optimal process conditions requires the formulation of a mathematical statement which completely matches the design intent including control issues such as process actuation and sensing considerations.

Implementation of intelligent control strategies requires judicious selection and placement of sensors and actuators if adequate observability and controllability are to be realized. This is especially difficult in materials processes, such as forging where the control inputs and sensors are usually located on the boundary of the process while the quantity to be controlled is internal to the process. For example, in press forging some basic control parameters are ram velocity, die temperature, preform shape, and die geometry. These are essentially boundary quantities that have to be used for controlling internal process quantities such as metal flow, microstructures and residual stresses. Since *in-situ* sensor technologies are nonexistent for key internal variables, the key role of models relating them to measurable parameters and the corresponding optimal design philosophy become critically important for intelligent control. Although the challenges in

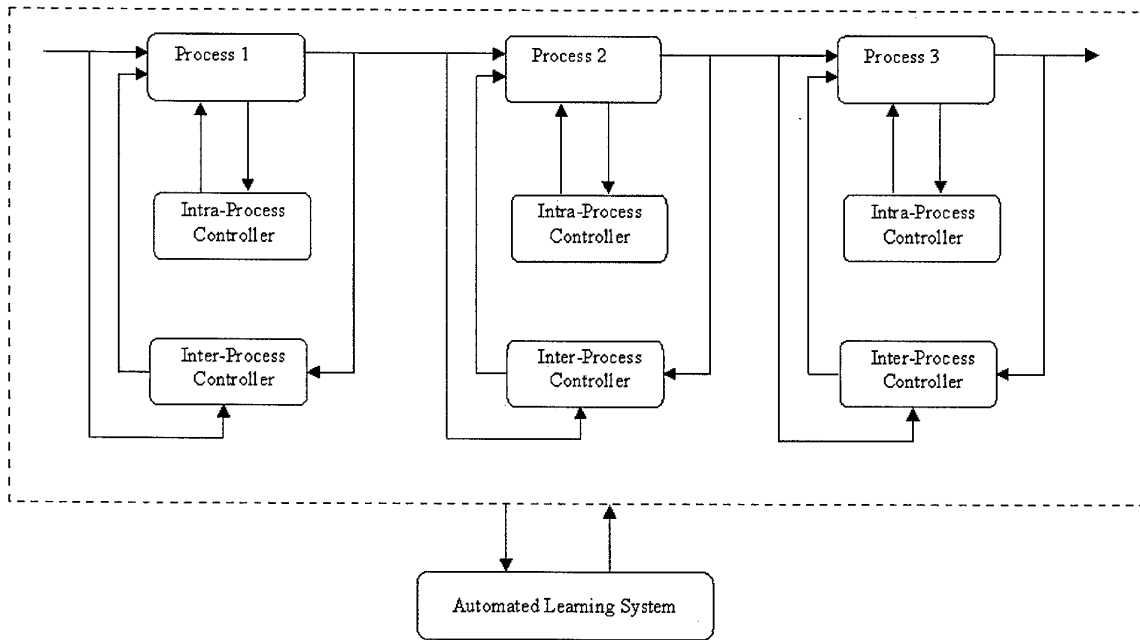


Figure 1. Illustration of a multiple-step intelligent processing framework.

forging processes are formidable, many difficulties can be mitigated through the integration of dynamic system engineering principles, optimization techniques, and intelligent control methods.

### 3 ARCHITECTURE OF AN INTELLIGENT MATERIAL PROCESSING SYSTEM

To achieve desired physical properties and geometrical shape, material processing systems typically consist of a sequence of unit processes, each designed to bring the starting workpiece closer to the desired final condition. The need for multiple steps is driven by the fact that only in a few circumstances, can the actuation capabilities of a single process provide sufficient controllability to transform the initial workpiece state (microstructure and shape) to the desired product state. Even in cases where the necessary controllability exists in a single step process, the performance of the process may be highly sensitive to variations in process parameters, thereby making robust control in a single step impossible. In a well-designed material processing system, each unit process provides at least one actuating capability that cannot be *robustly* or economically provided by one of the other unit processes.

Figure 1 illustrates a multiple-step, intelligent processing framework that utilizes intra-process feedback control and inter-process feedback and feedforward control. The intra-process feedback compensation is used for the traditional purpose of continuous process variable regulation or tracking. The inter-process feedforward compensation is used to send corrective information to subsequent unit processes that are to act on the product in order to bring the process back to the optimal trajectory. Inter-process feedback is employed to provide information to prior unit processes so that they can take the

necessary corrective action to ensure that the next unit workpiece will more closely follow the optimal trajectory. Inter-process sensing is shown as being distinct from intra-process information because often measurements that can be made between processes cannot be made during the process. Finally, an intelligent learning algorithm collects information from all the sensors in order to develop improved process models, modify the definition of optimal trajectories, and improve the feedback and feedforward control laws. Although not shown, the initial design of the sequence and control parameters of the particular unit processes using model-based optimization principles is an essential component in achieving an optimal design with robust performance. In order that the intelligent control system works effectively in improving the process, it is not sufficient to simply have sensors, feedback and artificial intelligence functions in place and well implemented. The initial design must not only be stable, but also reasonably close to the optimum. Table 1 summarizes the function of the four components of this IPM architecture.

### 4 OPEN-LOOP PROCESS DESIGN

This component of IPM does not usually receive as much attention as the control aspects, although it should play a critical role in all IPM efforts. Open-loop process design determines the unit processes consisting of the overall manufacturing enterprise, the processing conditions for each of the unit processes, and the sensors and actuators. Only after these issues have been determined is it possible to intelligently configure the control systems and the learning system. Design is especially important in processes such as forging where the capability of reliable mathematical models and analysis tools for the various systems far exceeds that of available sensor technologies for feedback and feedforward control.

TABLE 1. Components of IPM Architecture

Component	Sub-component	Function	Focus
Open-Loop Process Design	Dynamical Math Modeling	Describes transient and steady-state process behavior	Individual part & Part-to-part
	Optimal Design	Selects processes & process trajectories to achieve economical performance and robustness	Individual part & Part-to-part
Feedback Compensation	Intra-process	Maintains optimal process trajectories during individual unit processes in the face of Uncertainty	Individual part
	Inter-process	Maintains optimal process trajectories across multiple processes	Part-to-part
Feedforward Compensation	Brings process back to the optimal trajectory using subsequent processes		Individual part
Learning and Automatic Redesign	Remodeling	Uses sensed data to improve accuracy of process models	Individual & Part-to-part
	Redesign	Improves designs of optimal trajectories, feedback and feedforward compensators	Individual & Part-to-part

#### 4.1 Modeling

Manufacturing processes can be described as stochastic nonlinear dynamical systems. The manufacturing enterprise (i.e., global system) consists of the entire sequence of unit processing steps to produce a component. The unit processes such as forging or heat treatment can be decomposed into sub-systems (i.e., workpiece material, tooling, equipment, control system, etc) which can be decomposed further. A typical systems representation for metal forging system is illustrated in Figure 2. Mathematical models and analysis tools for forging processes consist primarily of dynamical models of thermo-mechanical material behavior, interactions between the tooling and the workpiece, and response of the forming equipment.

Dynamic models of material behavior are especially important, since the real-time measurement of material microstructure is a virtual impossibility. Models and design techniques for controlling microstructure during deformation have been developed to address critical issues such as stability, transient and steady-state response, and robustness of processing trajectories. Lumped-parameter modeling tools such as the Dynamic Material Map [Ref. 1,2] are used to efficiently identify stable processing regimes in temperature and strain-rate space for deformed material. Recently, a comprehensive hot working guide [Ref. 2] based on dynamic material modeling approach was published covering over 170 different metallic systems. A typical material processing map is shown

in Fig. 3. Process design windows are identified using stability analyses, power dissipation analyses, apparent activation analyses, and other empirical metallurgical information. As shown in Fig. 3 for 316L Stainless Steel, material process maps help find process design windows for precise microstructure control and reduced sensitivity to process variations. Within these desirable regimes, dynamical state-variable models of microstructure evolution can be developed and used to identify precise processing trajectories for achieving desired microstructures.

Combining the state-variable models of microstructure evolution with models of process mechanics, such as FEA, UBET, upper-bound analysis, slab analysis, and their extensions, the distributed parameter nature of deformation processes can be handled. In order to design for control of dimensional tolerances and microstructural gradients more effectively, a new kind of process model is emerging that is based predominately on geometrical mapping relationships between starting and finishing shapes [Ref. 3]. A notional example of process modeling via shape-change mapping of preform geometry and blocker die shape is illustrated in Fig. 4 for an axisymmetric rotor forging sequence. A strong emphasis is placed on geometry because many die design issues are driven by the shape of the part and much less by the particulars of the workpiece properties and material flow. This is not to say that material and mechanics issues are not important, but just that many design questions can be answered without

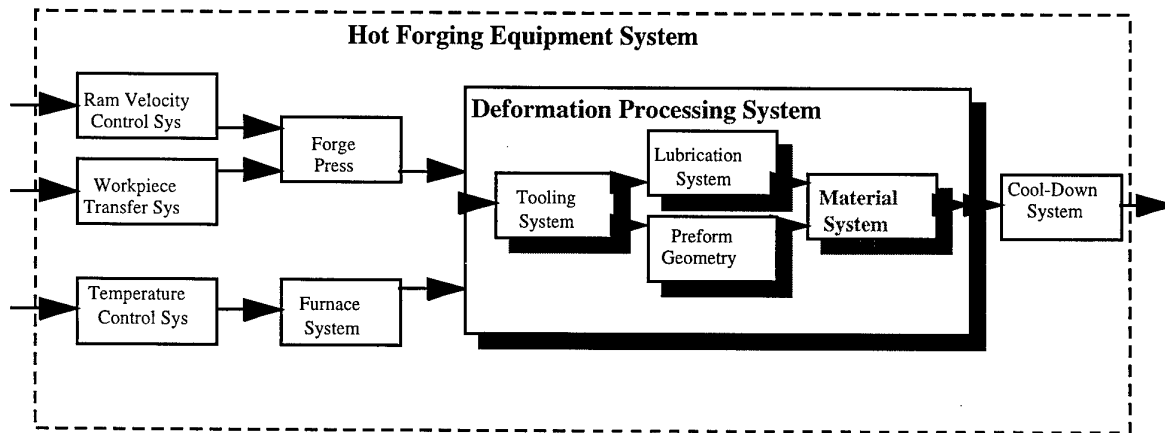


Figure 2. Typical systems representation for metal forging processes

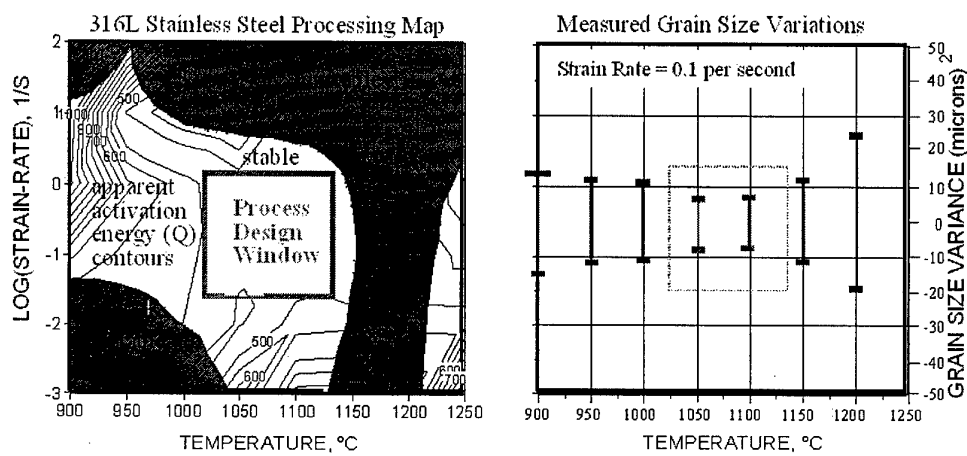


Figure 3. Example of Material Processing Map with design window and unstable regions identified.

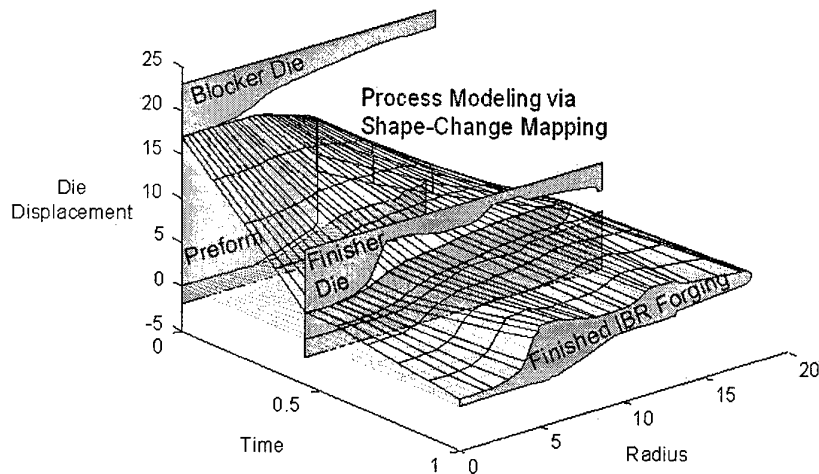


Figure 4. Illustration of shape-change trajectory with respect to die profile and displacement.

resorting to detailed simulation of physical phenomena. With optimization techniques, the new process modeling approach is well suited for microstructure control, minimizing residual stresses, and maximizing tool life.

Dynamic models of equipment systems are useful, if not essential, for determining the desired adjustable parameter settings for coincident tracking of the equipment response with optimized commands. In general, furnaces and forming machinery possess a range of time-varying performance capabilities that can be tuned with certain off-line software and hardware adjustments. Recently, a high fidelity dynamic model of a 1000 ton Erie forge press was developed [Ref. 4] using a commercial software package called Simulink (The MathWorks, Inc., Natick, MA). The state-of-the-art in simulation of dynamic systems includes software packages that not only aid the engineer in building simulation models, but also facilitate the interpretation of results by means of sophisticated graphical user interfaces. Figure 5 shows a block diagram constructed using Simulink to model the 1000 ton forge press including the accumulator, pump, servo-manifold, fluid dynamic effects, and the ram. Using the Simulink model for dynamic system analyses has resulted in significant improvements in the precision of ram speed control and in the smoothness of servo-valve responses, as shown in Fig. 6. Indeed, dynamic modeling of equipment systems is an important part of open-loop process design since it is central to realizing optimized, time-varying material processing conditions.

An important aspect of this component of IPM for forging is the use of the appropriate models for the design stage. For instance, the individual models for the various aspects of forging processes can be used in a coupled way or independently with the assumption of minimal coupling. The use of coupled, highly complex models at the processing system design stage is often impractical because of the number of individual processes that must be considered. Fortunately, simpler models (analytical, empirical, or a combination) with little or no coupling can be used effectively at this design stage as long as

they are used within their domain of validity. Note that while simpler forging models usually require the deformation path to be somewhat idealized, experience has shown that simpler deformation paths are more robust, even if ideal performance is not as high as with an alternative process.

#### 4.2 Optimal Design

The use of optimization principles in the system design is an essential component of application of IPM to forging processes. Processes that are designed without utilizing optimization techniques are highly sensitive to designer bias. By correctly specifying design criteria such as objectives (wants) and constraints (needs), mathematical optimization techniques can be used in conjunction with models to find processing system design solutions that are optimal in some user-defined sense. The choice of what constitutes a constraint or objective is usually clear, but there are situations in which the distinction is not so obvious. For example, it may be desired that cost be minimized (objective) subject to certain specifications (constraint), or on the other hand, it may be desired that quality be maximized (objective) subject to cost limits (constraints).

In multiple-step processes, such as forging, design of the process usually involves selecting the sequence of unit processes as well as the possibly time-varying parameters for each of these processes. By using models of the available unit processes, the optimization algorithm can determine the best sequence of processes and their parameters--in other words, an optimal processing "trajectory" can be found that will meet all the design criteria. Recently, trajectory optimization techniques have been successfully applied to the design of extrusion processes [Ref. 5,6]. As illustrated in Fig. 7, optimized material trajectories in strain, strain-rate, and temperature space were determined for extruding plain C steel to a specific shape and grain size. Subsequently, the optimized material trajectories were used to directly calculate the corresponding open-loop process control parameters, namely, extrusion die throat geometry, ram velocity profile, and billet temperature

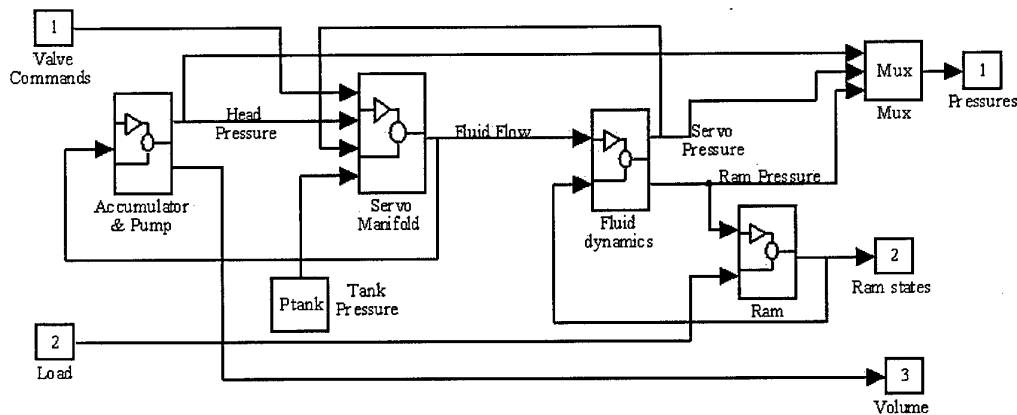


Figure 5. Simulink block diagram model of 1000-ton forging press.

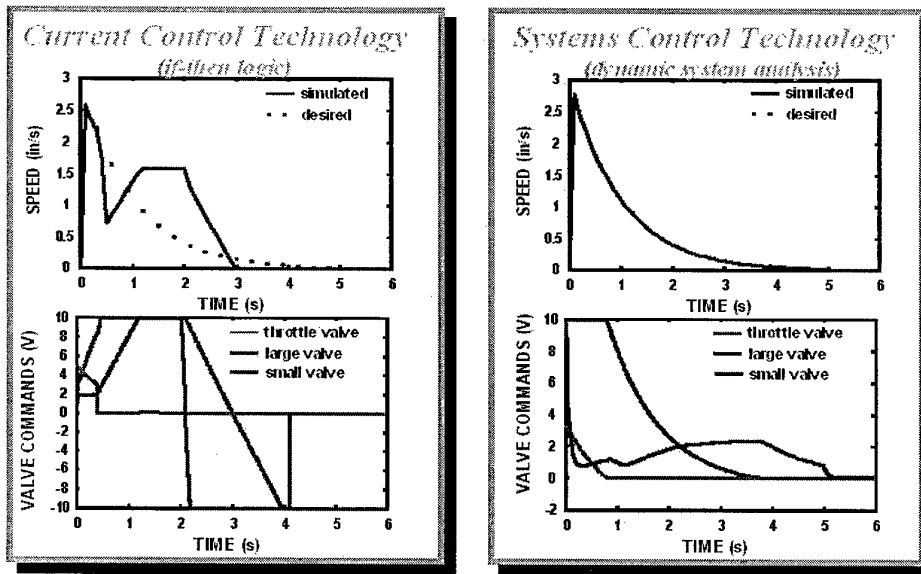


Figure 6. An illustrative comparison of state-of-the-art forge press control capability and improved dynamic systems analyses approach.

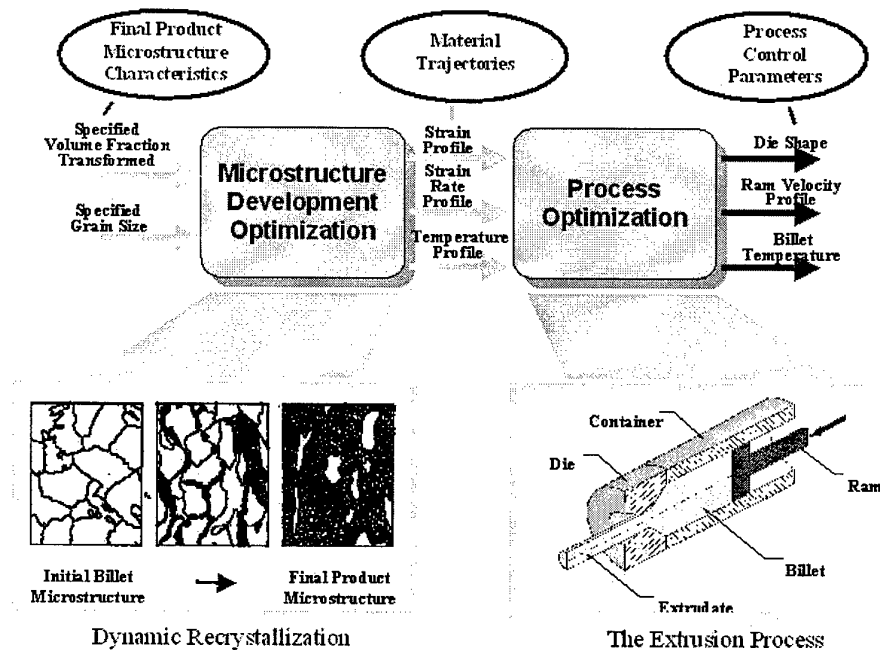


Figure 7. A schematic of a two-stage approach for open-loop process design of a metal extrusion process. Also shown are typical microstructural changes and a extrusion process diagram.



which are needed for realizing the optimized conditions.

If configured to do so, the trajectory optimization algorithm can design the process to be robust with respect to model error and unexpected process variations, thereby reducing the burden on the feedback systems. It is also possible for the optimization algorithm to determine optimal placement of actuators and sensors for good controllability and observability (the ability to estimate unmeasured process states using models and measured data) properties. This leads to the well-known control systems design principle that optimal open-loop process design is a *prerequisite* to the effective use of feedback control, feedforward control, and sensor-driven learning systems.

Forging process optimization requires the design of several parameters, including initial workpiece temperature and dimensions, number of dies, die temperatures, and deformation rate (ram speed) profile. Other design parameters include the initial billet's heat-up profile, possible thermomechanical billet conditioning steps and subsequent heat treatment profiles quenching steps, and machining steps. Utilizing appropriate models together with optimization algorithms, an optimal forging process can be designed to meet cost and quality specifications while also ensuring that the design is robust. Progress in this area is described elsewhere. [Ref. 7, 8]

### 4.3 Emerging Tools for Forging Process Design

The status of some emerging design tools and their interrelationships for the open-loop process optimization of the workpiece material system, the deformation processing system, and the hot forging equipment system are summarized as follows:

*Material Processing Maps:* for selecting metal forming temperatures and ram speeds. (Status: need some further theoretical and experimental validation studies)

*Microstructural Trajectory Optimization:* for obtaining temperature, strain and cooling rate profiles for microstructure control. (Status: need some experimental validation studies)

*Shape-Change Optimization:* for obtaining billet geometry and forming die(s) for optimize material flow. (Status: need extensive theoretical and experimental validation studies)

*Equipment Modeling:* for setting parameters for optimum equipment response. (Status: commercially available simulation software)

*Discrete Event Optimization:* for minimizing cost of a sequence of manufacturing operations. (Status: need extensive theoretical and experimental validation studies)

All of these new process design tools are based on principles and methods from *dynamic systems engineering* approaches. They can be used separately or together as described idealistically below.

- (i) Use material process maps to determine practical range for feasible hot deformation conditions.
- (ii) For conceptual design of manufacturing approach, use discrete event optimization to determine (a) the number and

sequence of thermomechanical processes, (b) the nominal processing conditions for each operation, and (c) the initial billet size and metallurgical condition.

(iii) Use microstructural trajectory optimization to determine idealized hot deformation & heat treatment parameters for precise microstructure control. (If possible, use optimized shape solutions from (iv) in optimization criteria.)

(iv) For intermediate level of design, use shape-change optimization to determine preform geometry and blocker die designs. (If possible, use optimized microstructural control parameters from (iii) in optimization criteria.)

(v) Use equipment modeling and feedback control to assure the dynamic equipment response determined from microstructural trajectory optimization, shape-change optimization, and/or other consideration is truly realized.

(vi) For detailed validation of design solution, use existing finite element analysis programs and/or subscale material processing experiments.

## 5 FEEDBACK CONTROL SYSTEM DESIGN

Feedback compensation has traditionally played an important role in most IPM structures and implementations. In IPM, feedback can be used in two very different ways, each having the same fundamental objective: improve the overall performance of the system by increasing its robustness to unanticipated process variations, unknown disturbances, and model error. These are 1) Intra-process feedback and 2) Inter-process feedback. It is a widely accepted and well documented fact that while feedback can be used to achieve many process performance goals, its unique contribution is its ability to provide robustness with respect to the unknown. However, it is *not* effective in the face of inadequate models because of the danger of introducing instabilities that were not previously present in the process. i.e., feedback control can introduce instabilities where none existed prior to its use in the process. This illustrates the irony that feedback control when used correctly, can reduce the effect of model uncertainty, but can worsen the effect of model uncertainty, when used incorrectly (without an *adequate* model).

### 5.1 Intra-process feedback

One of the primary uses of feedback control in the context of IPM is termed *intra-process feedback*. This is the traditional role of feedback, i.e., regulate some set of variables to ensure that they follow a specified trajectory as a function of time (in this case an optimal trajectory). It is important to realize that the feedback control does not have to be designed to regulate the sensed variables only, but may be designed to regulate *estimates* of non-sensed variables. Techniques for designing feedback compensators and estimators (observers) are well covered in the control engineering literature [Ref. 9]. It is important to note that in this framework, the intra-process feedback compensators are used in real-time to affect the outcome of the process with respect to a single workpiece only, and not subsequent workpieces. They are used to make sure that an individual process does what it is told. Because of the lack of sensors for measuring and actuators for affecting quantities of interest in real-time such as workpiece dimensions and microstructure,

intra-process feedback has been primarily applied to the control of positions and velocities of equipment, temperatures, and average pressures. For instance, controllers have been designed that provide high performance and robustness for controlling ram velocity of modern hydraulic forge presses [Ref. 4]. As the model fidelity and computational capabilities increase allowing the use of observers, it will be possible to apply intra-process feedback control to variables that are not directly measurable, such as microstructure.

## 5.2 Inter-process feedback

Feedback can be used to affect subsequent workpieces via *inter-process feedback*. In this application, information from the output of a process is used to make corrections to the desired trajectory that the process variables should follow for the next workpiece. This use of feedback tends to be outside the realm of traditional feedback control theory and is unique to manufacturing processes. However, the practice is widely employed in industry through everyday trial-and-error adjustments to process parameters. The design of automatic controllers for this function is supported by application of sampled-data control techniques [Ref. 10]. In this case, the data from the output of a process is modeled as a sample from a continuous process that is only available on a periodic basis. Inter-process feedback is particularly applicable to forging because several variables of interest that cannot be measured or actuated in real-time for intra-process feedback control can be measured after the completion of the process.

## 5.3 Feedforward Control

Feedforward compensation finds its primary application in making adjustments for *measurable* disturbances between processing steps. For example, if the output of one forging deformation operation does not achieve the desired microstructure, the error can be fed to a subsequent heat treating step to adjust the desired temperature versus time profile so as to bring the microstructure back to the designed optimal trajectory in an *optimal manner*. Techniques for calculating the new optimal inputs based upon the amount of measured disturbance are described in the literature [Ref. 11]. In general, feedforward compensation applies only to correcting the trajectory of an individual workpiece, not to the trajectory of subsequent workpieces.

## 6 LEARNING AND ADAPTATION SYSTEM

The use of automatic learning and adaptation systems was the original reason for the coining of the term "intelligent" in IPM. This springs from the human-like learning capabilities of artificial neural networks and the qualitative, human-like reasoning associated with fuzzy logic. These systems or techniques are excellent at making effective use of sensor data to automatically improve process models, redesign optimal trajectories, and tune feedback and feedforward control laws [Ref. 12, 13]. In the presented hierarchical structure, the learning system is responsible for ensuring that over the time, the manufacturing sequence remains optimal even as long-term process variations and biases develop.

## 7 SIMULATION EXAMPLES OF CONTROL APPLIED TO METAL FORMING

### 7.1 Feedback Control: Disk Forging Example

In this example forging ram pressure feedback is used to directly control ram velocity in order to indirectly control deformation rates and final die closure. Precise control of deformation rates is important to avoid defect formation, enhance metal flow characteristics, and achieve desired microstructure states. Additionally, precise control of die closure is an obvious requirement for achieving specified dimensional tolerances. This feedback control example involves a simulation of a well-studied isothermal titanium disk forging problem [Refs. 14]. As shown in Fig. 8, three different metal flow patterns develop during the die filling process: (a) upsetting, (b) backfill of die cavity, and (c) flash formation. The changes in the metal flow pattern are "actuated" by distinct changes in boundary conditions associated with the die geometry that can be observed using ram pressure measurements.

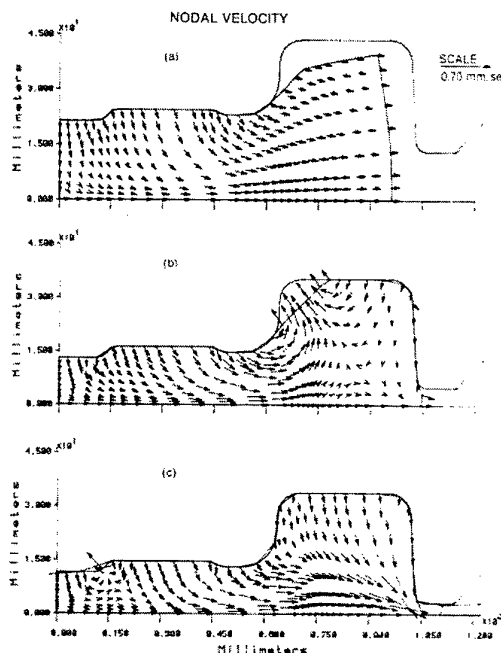


Figure 8 Nodal-point velocity plots of disk-forging simulation at 48% (a), 68% (b), and 72% (c) reductions in workpiece height.

The strategy in this example problem was to control the ram velocity according to the following schedule: maintain a constant velocity of 50 mm/s until the workpiece contacts the outer die wall; change the velocity to 25 mm/s until the die position reaches 55 mm; and then stop the ram. Figure 9 shows the forging load versus time. At approximately 48 s the load increases rapidly, corresponding to the workpiece contacting the

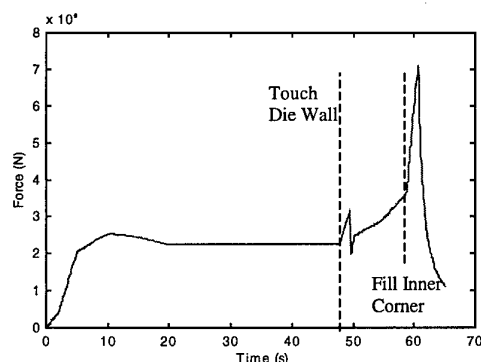


Figure 9 Plot of forging load versus time for disk-forging simulation.

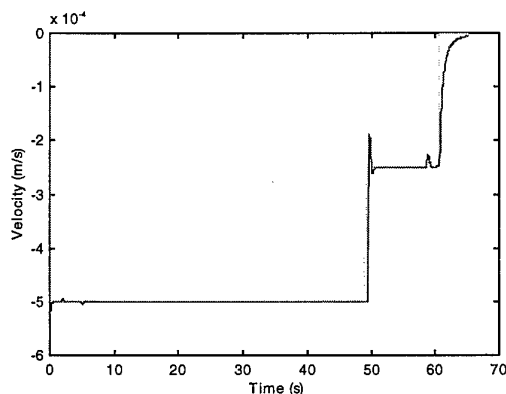


Figure 10 Plot of velocity versus time for disk-forging simulation.

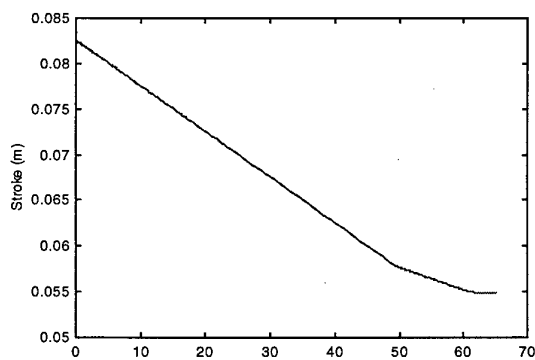


Figure 11 Plot of stroke versus time for disk-forging simulation.

outer die wall. In response to the rapid increase in load, the press control computer decreases the desired velocity to 25 mm/s as shown in Fig. 10. As expected the load profile shifts downward because of the decrease in velocity. From 50 s to 58 s the load increases again as the die cavity is filled.

Upon filling, the load increases very rapidly, and excess material exits the die cavity through a small gap known as the flash area. Subsequently, the ram position reaches 55 mm and the ram stops as shown in Fig. 11. In the context of the intelligent processing framework described earlier, this example demonstrates that pressure measurements can be used to detect important forming events for intra-process feedback control. This strategy leads to indirect feedback control of process quantities such as metal flow, microstructure, and dimensional tolerances.

## 7.2 Feedforward Control: Microstructure Development

Because deviations from the optimal open-loop process design commonly occur in early processing operations, it is desirable to be able to change subsequent processing operations to optimally correct for the deviations and achieve the required design goal. In this example, a workpiece temperature measurement is used to recalculate the optimal processing trajectory for producing desired final microstructure characteristics. Under normal processing conditions, the workpiece is preheated, hot worked, and cooled. This particular processing sequence for plain carbon steel was optimized to achieve a specified final grain size and final strain, while minimizing temperature rise during hot working.

The conditions for the nominal case are assumed to be: a starting temperature of 1273 K, a final grain size between 33 and 35 microns, and a final strain of 2.0. The corresponding optimal strain-rate trajectory for the hot working operation is described by the solid line in Fig. 12. Details of the optimization procedure are discussed elsewhere [Refs. 5,6]. To illustrate how feedforward control can be used to compensate for deviations in the preheat temperature, assume that the workpiece is overheated by 22 K. If the nominal optimal strain-rate trajectory is used the grain size specification will not be achieved. Therefore, it is necessary to calculate a modified optimal trajectory corresponding to the new preheat temperature of 1295 K. The modified trajectory is described by the dashed line in Fig. 12. The relative change between the two curves is consistent with known metallurgical relationships among strain-rate, temperature, and grain size. Figure 13 shows the grain size changes with time during hot working and air cooling operations. In the nominal case, the final grain size at the end of air cool is 33 microns, and in the modified case it is 35 microns. The corresponding temperature responses are shown in Fig. 14. In the context of the intelligent processing framework described earlier, this example demonstrates that temperature measurements can be used to correct process deviations via inter-process feedforward control.

## 8 CURRENT IMPLEMENTATION CHALLENGES

Further work is needed in the development of *in-situ* sensors and dynamic material behavior models in order to successfully achieve quality and cost benefits of IPM. Sensors are needed for measuring the state of the workpiece such as grain flow pattern, residual stresses, and microstructural characteristics. While highly desirable to directly sense material states, it appears to be more feasible to observe them indirectly through die closure, material velocity, temperature and pressure measurements. Sensors are also needed for monitoring process parameters such as friction, that directly affect tool life and material flow. In addition, the vast majority of existing material

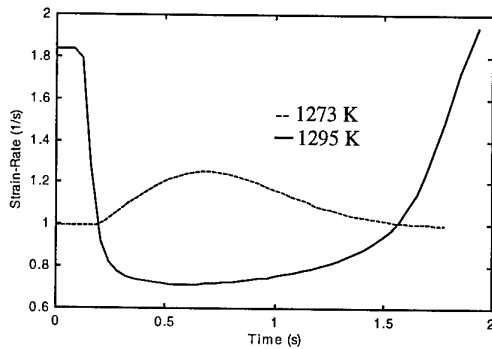


Figure 12 Optimal strain-rate trajectories for nominal and modified cases.

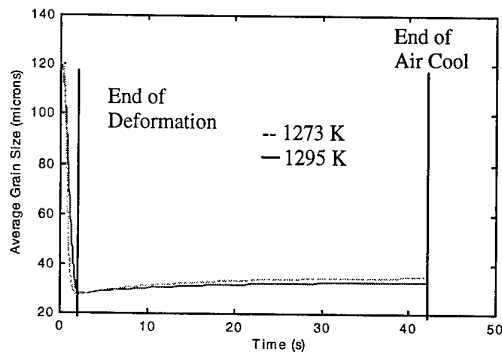


Figure 13 Average grain-size evolution for nominal and modified cases.

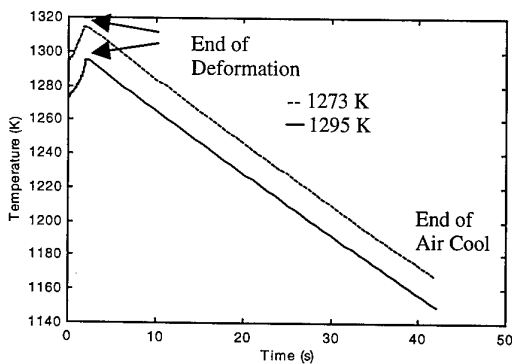


Figure 14 Workpiece temperature response for nominal and modified cases.

behavior models represent only responses to specific input conditions and are not general enough for representing actual conditions. For example, even the so-called "dynamic" microstructural models for thermomechanical processing are

based on constant testing conditions of temperature and strain-rate. The emerging IPM framework will be useful in focusing model and sensor development as well as help forging industries to achieve superior quality and cost benefits.

## 9 REFERENCES

1. Malas, J.C. and Seetharaman, V. "Use of Material Behavior Models in the Development of Process Control Strategies," *JOM*, Vol. 44, No.6, pp. 8-13, 1992.
2. Prasad, Y.V. R. K. and Sasidhara, S., "Hot Working Guide - A Compendium of Processing Maps," ASM International, Materials Park, Ohio, 1997.
3. Frazier, W. G. and Malas, J.C., "Forming Superalloy Disk & Flat Shaped Products," Unpublished AFRL Technical Report, WPAFB, OH, 1998.
4. Frazier, W. G., et. al., "Model and Simulation of Metal Forming Equipment," *Journal of Materials Engineering and Performance*, Vol. 6, No. 2, pp. 153-160, ASM International, 1997.
5. Malas, J.C., et. al. "Optimization of Microstructure Development During Hot Working Using Control Theory," *Metallurgical Transactions*, Vol 28A, No.9, pp. 1921-1930, 1997.
6. Frazier, W.G., et. al., "Application of Control Theory Principles to the Optimization of Grain Size During Hot Extrusion," *Journal of Materials Science and Technology*, Vol. 14, No.1, pp. 25-31, 1998.
7. Gunasekera, J., et. al., "The Development of Process Models for Use with Global Optimization of a Manufacturing System," *Proceedings of ASME International Mechanical Engineering Congress*, Atlanta, GA, 17-22 Nov. 1996.
8. Malas, J.C., et. al., "Interactive Simulation System for Design of Multi-Stage Material Processes," *Processings of International CIRP Design Seminar*, Los Angeles, CA, Oct. 8-10, 1997.
9. Skelton, R.E., *Dynamic Systems Control*, John Wiley & Sons Inc., New York, 1988.
10. Phillips, C. H. and Nagel, H. T., *Digital Control System Analysis and Design*, Addison-Wesley, 1996.
11. Stengel, R.E., *Optimal Control and Estimation*, Dover, New York, 1994.
12. Hagen, M.T., Demuth, H., and Beale, M., *Neural Network Design*, PWS, New York, 1994.
13. Beale, M. and Demuth, H.B., *Fuzzy Systems Toolbox*, PWS, New York, 1994.
14. Gegel, H.L., et. al., "Modeling Techniques Used in Forging Process Design," *Metals Handbook*, ASM, Metals Park, OH, Vol. 14, 9<sup>th</sup> ed., pp. 417-438, 1988.

## INTELLIGENT PROCESSING OF P/M MATERIALS

William E. Frazier<sup>1</sup>, Jeffrey Waldman<sup>2</sup>, and Phillip A. Parrish<sup>3</sup>

1. Naval Air Systems Command  
Aerospace Materials Division  
Patuxent River, MD 20670

2. Drexel University  
Department of Materials Engineering  
Philadelphia, PA 19104

3. MATSYS, Inc.  
Springfield, VA 22151

### **SUMMARY**

Emphasis is being placed on the acquisition of affordable, reliable, and sustainable advanced airframes and propulsion systems. Net-shape processing of high performance structural materials is of significant technological interest because of its potential for decreasing the cost and enhancing the performance of these aircraft components. Component cost is reduced because of the intrinsic high material utilization and a reduction in machining and finishing operations. The net-shape, hot isostatic press (HIP) consolidation of particulate materials (P/M) is considered one of the enabling technologies for the consolidation of costly and difficult to melt-process materials. This paper explores the benefits of P/M processing and focuses on the development of an intelligent hot isostatic press (IHIP) [1].

### **INTRODUCTION**

Hot isostatic pressing (HIP) is a well established commercial process [2-4]. HIP processing is performed in a pressure vessel and involves the simultaneous application of hydrostatic pressure (usually through Argon gas) and heat (typical temperatures range between 400 & 2000 °C).

HIP is used to process metals, ceramics, composites, and coatings for a diverse variety of applications [2]. It is used in order to improve the properties of high performance castings, e.g., joint replacements in the medical community and structural titanium and aluminum aerospace castings. HIP is employed to close casting porosity and break up harmful inclusions that can reduce the material's fatigue and fracture properties. HIP technology is also utilized to join metal-ceramic, ceramic-ceramic and metal matrix composites components. HIP can be used to pressure infiltrate graphite and porous ceramic components. The machine tool industry makes extensive use of HIP technology in the manufacture of ceramic carbide and cemented carbide cutting tools.

HIP technology is also used in order to consolidate powder metals and ceramics (e.g., superalloys, titanium and alumina). HIP processing of net-shape components from powder materials offers the advantages of lower cost. Cost reductions are achieved through enhanced material utilization and reduced machining costs.

#### **HIP Models for Powder Materials**

The HIP consolidation of powder materials has been investigated by a number of researchers [5-10]. Analytic equations describing the densification of P/M have

been developed and used to generate HIP maps. These maps for the densification of a powder material indicate the dominant consolidation mechanism operating under specified temperature, pressure and density [11, 12]. Figure 1 is an example of a HIP map generated for  $Al_3Ti$  [13].

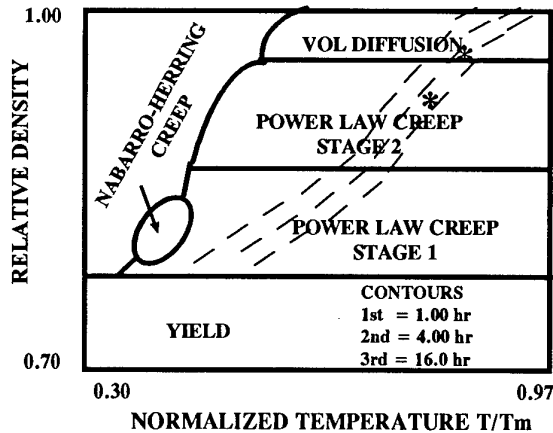


**Figure 1 - A HIP Processing Map for  $Al_3Ti$  Consolidated at 173 MPa.**

The constitutive equations used to generate these HIP maps assume an isostatic stress state. However, HIPed components do experience shape distortion as a result of deviatoric stresses developed within the component. Powder packing, can material, can configuration, temperature gradients, shell formation, and powder bridging are some of the possible causes of shape distortion.

### Intelligent Processing of Materials

Intelligent processing of materials is emerging as an effective way of producing high quality products. Intelligent processing permits the material's own response to real-time processing conditions (e.g., temperature, pressure) to control its processing schedule.

## INTELLIGENT HIP DEVELOPMENT

### Program Structure

Defense Advanced Research Project Agency (DARPA) and Naval Air System's Command

(NAVAIR) jointly sponsored the development of an intelligent hot isostatic press (IHIP). Under contract N62269-91-C-0247, the prime contractor, BDM, structured a program consisting of University of Pennsylvania, University of California, Santa Barbara, Massachusetts Institute of Technology, and Cambridge University [1]. Industrial experts from IMT and Crucible Steel were also part of the development team.

### Model Development

Constitutive models for the consolidation of powder materials were developed based upon micromechanics principles. The models developed built upon the Ashby's methodology of dividing HIP consolidation into two stages.

However, the presence of non-hydrostatic stresses necessitated the inclusion of deviatoric stresses in the constitutive laws governing consolidation. Three dimensional constitutive models describing the stress state of a component being HIPed were developed, implemented and validated.

Stage one models apply when the component density is below 0.9 of theoretical; stage two models are used at component densities between 0.9 and 1.0 of theoretical. Models for plastic yield, power law creep, and lattice and grain/particulate boundary diffusion were developed for both stage one and two consolidation. In addition, a model was developed to transition between the two stages.

### Model Verification

In order to validate these models steel canisters filled with tool steel powder were HIPed under different temperature and pressure schedules as shown in Figures 2 & 3. The deformed shapes that were obtained through numerical simulation agreed with the results obtained experimentally.

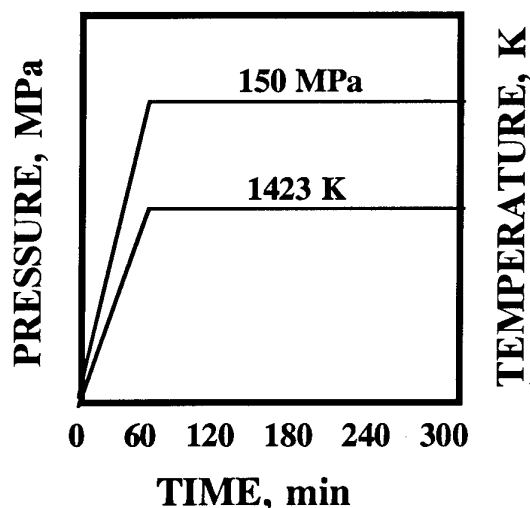


Figure 2 - Typical HIP Processing Schedule

The HIP profile presented in Figure 2 is representative of a typical commercially used process schedule. The HIP vessel is heated and pressurized concomitantly in order to take advantage of the pressure achieved through the thermal expansion of the argon gas. The application of this process schedule resulted in significant shape distortion. The simulation indicated that the shape change occurred when plastic yielding mechanism was active during the initial stages of HIP.

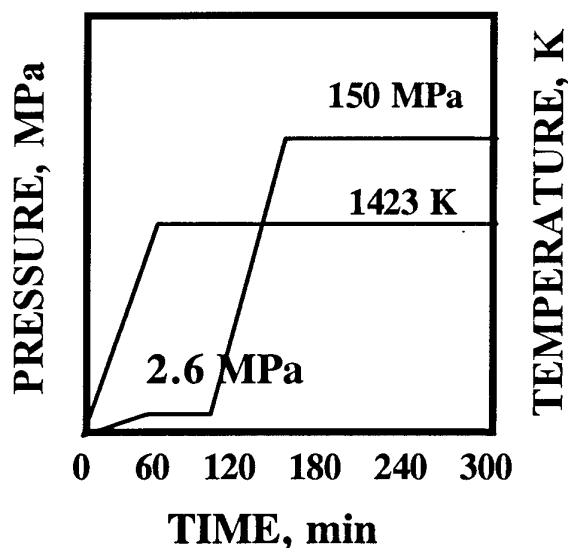


Figure 3 - Power Law Creep Dominant HIP Process Schedule

The HIP process schedule illustrated in Figure 3 resulted in significantly less shape distortion than the previous process schedule. The temperature of the HIP vessel and the work piece is raised prior to the application of significant pressure. In this manner, consolidation due to plastic yield was minimized and that due to power-law creep was maximized.

The commercial HIP industry does not favor this process schedule since it places a great deal of strain on the mechanical pumps. Indeed, some pumps are not able to achieve these high pressures. It also lengthens the time required to HIP a component since commercial process specifications typically require a fixed hold time at a specified temperature and pressure.

#### Control System

The Intelligent Control System (ICS) integrates process modeling and prediction, intelligent control algorithms, and *in situ* sensors. The ICS utilizes a Process Design Tool (PDT) to assist in the design of HIP process schedules and to predict the density of the material following processing.

The functional requirements of the ICS were defined as follows:

1. Alter the process schedule based upon the current state of the system and *a priori* knowledge of the system.
2. Operates in real-time.
3. Asynchronously communicates with the system's other control hardware components.
4. Concisely represent process states in a coherent manner.
5. Is user friendly.
6. Generates and manages process cycles.

The physical configuration of the ICS is illustrated in Figure 4. The main components of the system consists of a SPARC Work Station, a HP 4194 analyzer, a HP 4x1 Relay, and an eddy current sensor.

The ICS is based on a feedforward/lag control algorithm. The feedforward/lag provides process control based upon the apparent density tracking error and its integral with respect to time. When the actual density leads the planned density, the corrective action is to slow the process by lowering the temperature. Conversely, when the actual density lags the planned density, the corrective action is to increase the temperature. Pressure control throughout this portion of the HIP cycle is in a tracking (free floating) mode. The pressure change is a function of temperature according to the gas law relationship.

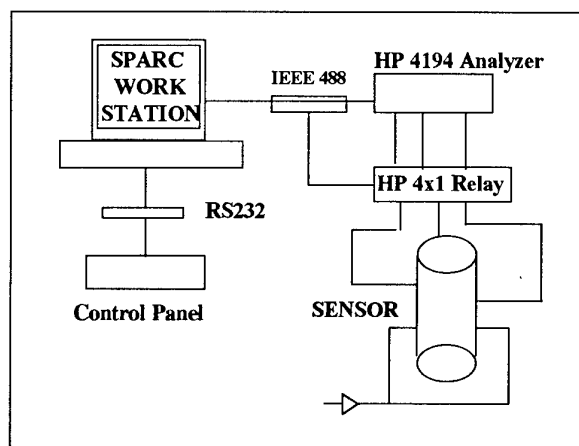


**Figure 4 - Intelligent Control System Configuration**

The ICS utilizes a graphical user interface (GUI) for all major HIP functions. It also provides graphical representation of the process profiles with continuously updated status and trend information. The PDT provides for advanced recipe generation with density prediction. The system includes a high temperature *in situ* sensors for measuring dimensional changes and uses algorithms for estimating component density.

### Sensors

Conventional HIP processing utilizes temperature and pressure sensors. Unfortunately these sensors do not tell you about how the component being HIPed is responding. The functional requirements for

IHIP sensors are to monitor component density, shape changes, and grain size during HIP processing in order to determine how metal is reacting to the HIP process parameters.

**Eddy Current Sensors:** Two types of eddy current sensors were developed: (1) A global eddy current sensor that enabled the measurement of can diameter, and (2) A proximity eddy current sensor that measured the gap between the component and the sensor. Used together, these sensors permit the measurement of dimensional changes and thereby facilitated the calculation of component density.

The eddy current sensors were constructed from machinable boron nitride ceramic hollow cylinder and platinum thermocouple wire coils. The configuration of the global eddy current sensor is shown in Figure 5. The primary coils are used to apply a high frequency electromagnetic field; the secondary coils sense the field induced in the component.

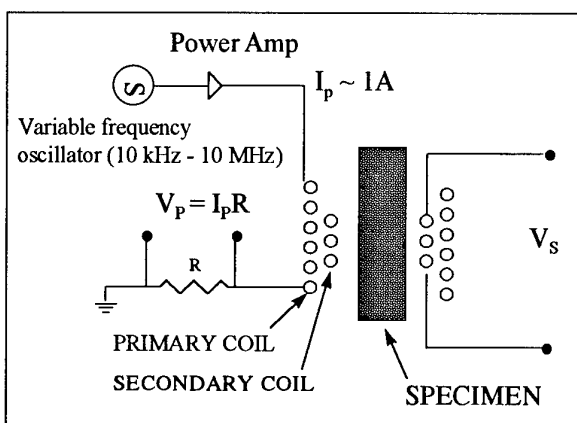


**Figure 5 - Global Eddy Current Sensor**

The imaginary and real components of impedance are measured at frequencies ranging between 10Hz and 1MHz. A plot of the imaginary and real components of impedance is shown in Figure 6. As the density of the material being HIPed increases, its diameter decreases. As the distance between the sensor and the work-



piece increases, the curves shift. The extent of the shift can be calibrated to allow a precise calculation of the components diameter, and thus, its density.

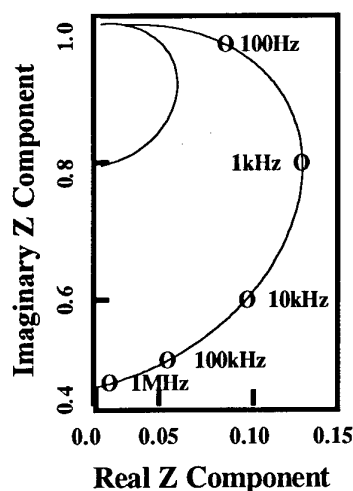


Figure 6 - Global Eddy Current Sensor Data: Left: following HIP, Right: before HIP

Thermal expansion of the Pt wire coils during HIP processing resulted in unpredictable anomalous readings. Both the primary and secondary coils expand axially and radially. Figure 7 - illustrates the evolution of sensor design. In the initial configuration, the coil wires were unconstrained. An intermediate configuration,  $ZrO_2$  was used to affix the coils. The final design confined the coil wire to grooves in the BN substrate having the same dimensions as the wire. This proved to be the most reliable and predictable design.

**Acoustic Sensor:** A prototype acoustic sensor was developed in order to measure grain size. The velocity of the ultrasonic wave depends upon effective moduli, relative density, and pore shape & size. Figure 8 illustrates the relationship between density, grain size, and density. Attenuation of the ultrasonic wave depends upon grain size, relative density, pore shape & size.

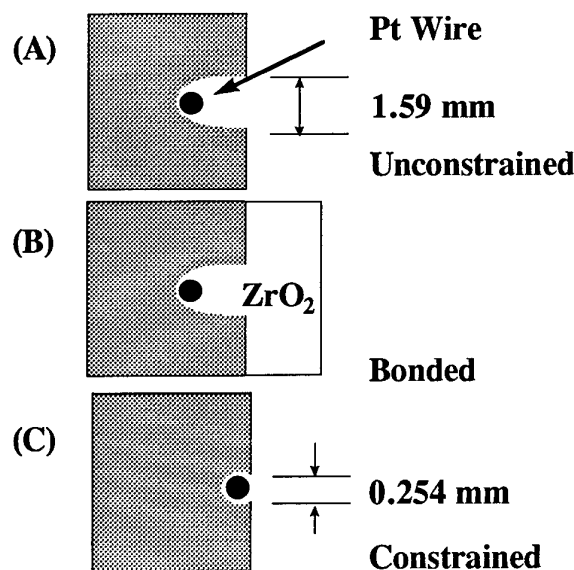


Figure 7 - Design Evolution of the Global Eddy Current Sensor: (A) Unconstrained, (B) Bonded, and (C) Constrained.

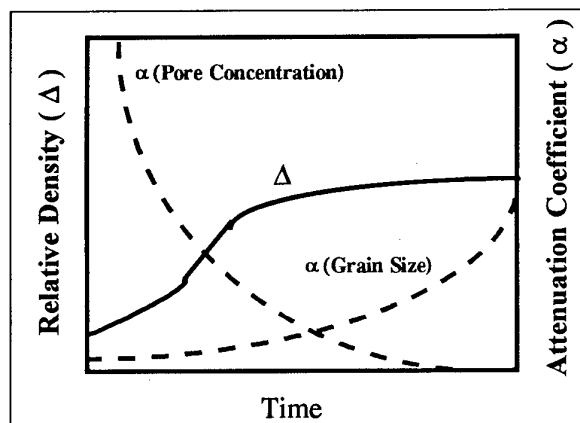
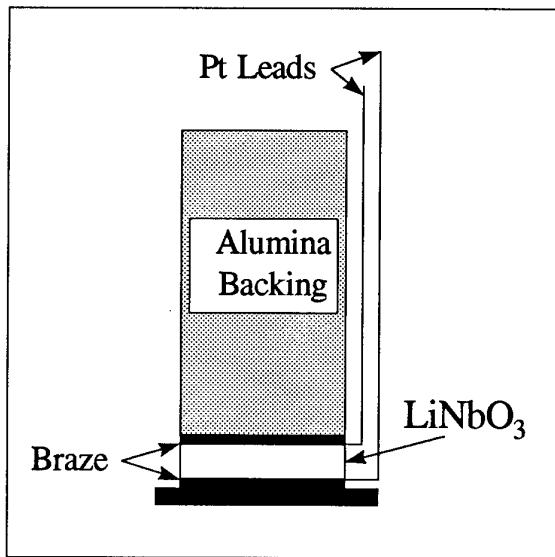


Figure 8 - The Effect of Porosity and Grain Size on Acoustic Attenuation.

A schematic of the prototype acoustic sensor is shown in Figure 9. The sensor uses a high temperature piezoelectric material  $LiNbO_3$ , Pt wire leads, and alumina for the body and wear plate.



**Figure 9 - Acoustic Grain Size Sensor**

A major concern in the design of the sensor was the mitigation of thermally induced stresses. The coefficients of thermal expansion for the materials used in the sensor are provided in Table I. The design resulted in a 0.1% CTE mismatch between 25-950 °C and an 89% acoustic transmission efficiency.

**Table I - Thermal and Acoustic Properties of the Grain Size Sensor.**

Material	CTE	Acoustic Impedance
Al <sub>2</sub> O <sub>3</sub>	8.8 x 10 <sup>-6</sup>	39.0 x 10 <sup>6</sup>
LiNbO <sub>3</sub>	10.6 x 10 <sup>-6</sup>	31.9 x 10 <sup>6</sup>
AgCu10Ti	9.24 x 10 <sup>-6</sup>	

The use of this acoustic sensor was demonstrated at temperatures up to 600 °C. At higher temperatures, stresses due to CTE mismatch caused premature failures. In addition, the sensor experience diminished high temperature sensitivity due to oxygen loss from the piezoelectric ceramic, viz., LiNbO<sub>3</sub>. The feasibility of measuring grain size during HIP processing was validated in bench top investigations. Pore and grain boundaries both contribute to ultrasonic attenuation; however, when the density of the component exceeds 0.95 of its theoretical,

grain boundary scattering becomes the dominant source of ultrasonic attenuation. Furthermore, ultrasonic attenuation increases with increasing grain size.

## **CONCLUSIONS**

1. Intelligent HIP processing of materials offers the potential to enhanced both the affordability and the mechanical & physical properties of advanced aircraft components.
2. An intelligent HIP consisting of *in situ* sensors, constitutive models, and an intelligent control system was developed and implemented on a NAVAIR HIP.
3. Developmental testing demonstrated the ability of *in situ* eddy current sensors to accurately measure dimensional changes on cylindrical components in the harsh HIP environment.
4. The feasibility of measuring grain size using acoustic sensors was demonstrated. The grain size sensor performed satisfactorily up to 600 °C.

## **REFERENCES**

1. Phillip A. Parrish, Tony Zahrah, and David P. Voss, Intelligent HIP Processing of Intermetallic Alloys. Final Contract Report N62269-91-C-0247, (BDM Int. Arlington, VA, February 1995)
2. R. Widmer, "The Role of Hot Isostatic Pressing-Now and in the Future," Advanced High-Temperature Alloys: Processing and Properties, (ASM, Materials Park, OH, June 1985), 105-116.
3. R.M. Conaway, "Cost-Effective Isostatic Forging," Advanced Materials & Processes, 6(1989), 35-39.
4. R. Widmer, "The Current Status of HIP Technology and Its Prospects for the 1990's," (Fourth Annual Conference on Isostatic Pressing, Stratford-Upon-Avon, U.K., 5 Nov 1990).

5. A.S. Helle, K.E. Easterling, and M.F. Ashby, "Hot-Isostatic Pressing Diagrams: New Developments," Acta Metallurgica, 33(12)(1985), 2163-2174.
6. W.-B. Li, K.E. Easterling, and M.F. Ashby, "Instantaneous and Residual Stresses Developed in Hot Isostatic Pressing of Metals and Ceramics," Metallurgical Transactions A, 22A(May 1991), 1091-1071.
7. J.J. Wlassich, M.F. Ashby, D.R. Blanchard, B.L. Henniges, D.W. O'Brien, "Modeling of Densification and Coarsening During Hot Isostatic Pressing," Intelligent Processing of Materials, ed. H.N.G. Wadley and W.E. Eckhart, Jr. (Warrendale, PA: The Metallurgical Society, 1989), 207-224.
8. M.M. Carroll, "An Empirical Model for Hot Isostatic Pressing of Metal Powders," Metallurgical Transactions A, 17A(1986), 1977-1984.
9. S.V. Nair and J.K. Tien, "Densification Mechanism Maps for Hot Isostatic Pressing (HIP) of Unequal Sized Particles," Metallurgical Transactions A, 18A(1987), 97-107.
10. A.S. Helle, K.E. Easterling, and M.F. Ashby, "Hot-Isostatic Pressing Diagrams: New Developments," Acta Met. (33)(12)(1985), 2163-2174.
11. M.F. Ashby, HIP 6.0 - Sintering and Isostatic Pressing Diagrams, (Cambridge University Engineering Department, Trumpington St., Cambridge UK, Jan. 1990).
12. M.F. Ashby, HIP 6.0 - Software for Constructing Maps for Sintering and Hot Isostatic Pressing, (Cambridge University Engineering Department, Trumpington St., Cambridge UK, Feb. 1990).
13. Mary E. Donnellan and William E. Frazier, "Interfacial Reactions in Al<sub>3</sub>Ti Composites," SAMPE - The 8th International Conference on Composite Materials, Honolulu, July 1991.

## PROCESS MODELLING AND CONTROL FOR COLD HEARTH REFINING OF INTERMETALLIC ALLOYS

R M Ward, T P Johnson and J M Young  
 IRC in Materials for High Performance Applications  
 University of Birmingham, Edgbaston  
 Birmingham, B15 2TT, UK

**SUMMARY**

Manufacturing processes can be tailored to a specific product using empirical knowledge. Such knowledge is not necessarily generic, which means that it may be difficult to respond to changes in market requirements. Empirical knowledge, while extremely valuable, may also not be enough to suggest changes to the processing route which could increase quality. Process modelling can provide a deeper level of understanding of the influence of process parameters on product quality, in a form which can be more easily transferred to new manufacturing situations. In particular, process modelling can highlight strategies for process control and identify necessary sensors.

These ideas can be applied to the cold hearth melting process. Relationships between the goals of the process, process modelling, sensing and control will be discussed in the light of the challenges which the cold hearth melting of titanium alloys presents.

**BENEFITS OF PROCESS MODELLING**

There is more than one way to work towards the goal of manufacturing a good quality product as economically as possible. One approach is to make use of empirical information, gathered during production, to slowly adapt the process recipe until satisfactory products are achieved with a sufficiently low reject rate. Providing that the required quality can be reached, and the working environment and product requirements do not change, this is quite adequate. Clearly though, if the desired product quality can not be achieved by this strategy then an alternative is needed. Furthermore, if some factor in the working environment changes (such as a change in one of the feed materials, or ageing of the equipment etc.), then it may take considerable time to adapt the recipe to accommodate this. Finally, to make a different product (e.g. of 50% bigger diameter), the existing recipe might not be much use. Faced with any of these situations an alternative is needed, because there is insufficient knowledge of the effects of processing conditions on the final product.

A second approach, which can work alongside the first and benefits from the information and insight gained from the empirical approach, is to develop a process model. This model need only be as complex as is required to differentiate the sub-processes occurring within the overall process. (If resources allow and the possible gains justify it, the sub-processes can be modelled as full fluid-dynamic / chemical / mechanical systems. One author (Ref. 1) writes that [fluid dynamic and solidification modelling] '...is bringing significant benefits to the casting industry', and that 'current modelling techniques are capable of confining mistakes in process design to the computer').

In other situations, simple qualitative / phenomenological models may be enough. Once the individual sub-models have been identified, it can be beneficial to determine which are significant (in terms of impacting final quality, use of expensive resources etc.). Knowledge of the important sub-

processes also helps determine which aspects of the process are important to be able to sense and control. This is useful because the ability to sense and control process variables is becoming increasingly important in metallurgical applications. Examples range from those already at the stage of widespread industrial use, such as the sensing and control of the head of steel in continuous casting tundishes, and automated welding, through to more recent developments, such as sensing and control of electron beam vapour deposition processes (Ref. 2), measurement of coating thickness in vacuum strip steel metallizing process (Ref. 3), and other applications detailed in this conference.

Again, given that appropriate sub-processes have been identified, it may also be possible to identify which are limiting in terms of time or power usage, and which will be affected by scale. This kind of information will be useful to address any of the following areas: The need to improve quality; Coping with environmental change; Changing the product (in response to changing market need).

**APPLICATION TO COLD HEARTH REFINING**

The IRC has a plasma melting facility which is capable of producing ingots of 100mm, 125mm and 150mm diameter and of up to 1.4m in length in a range of alloys, in an inert atmosphere.

**Details of the process**

The IRC furnace (shown diagrammatically in figure 1) incorporates two 150 kW plasma torches. Their motions are servo-hydraulically controlled in repeating patterns by a Macintosh-based system, with manual override to either adjust or suspend the pre-programmed patterns if necessary. The first torch is known as the 'hearth torch': When at 'A' it melts the feedstock 'B' into a water cooled copper hearth; at 'C' it maintains a liquid pool on top of the solidified 'skull'; and at 'D' it pushes liquid into the water cooled copper crucible over a notch at 'E'. As in the hearth, the first material poured into the crucible solidifies due to the high rate of heat extraction, and as more material is poured into the crucible, a liquid pool forms on top of this solid, kept hot by the second plasma torch. As heat is continually withdrawn through the crucible walls, this liquid pool does not grow indefinitely. Instead, as the crucible base is withdrawn and liquid material is continually added from the hearth, the crucible melt pool reaches a steady-state size, and an ingot is gradually produced.

The feed and withdrawal rates are automatically matched to a desired casting rate with the option of a small additional oscillation, i.e. dither, being imposed on the withdrawal to control surface finish. Before melting, the furnace is evacuated to a predetermined pressure, typically of <4 Pa. Provided the leak up rate is considered acceptable, the furnace is then backfilled with argon to a pressure of approximately 110 kPa, which is maintained throughout the melting process. Helium is used as the torch plasma gas. Further details can be found elsewhere (Ref. 4,5).

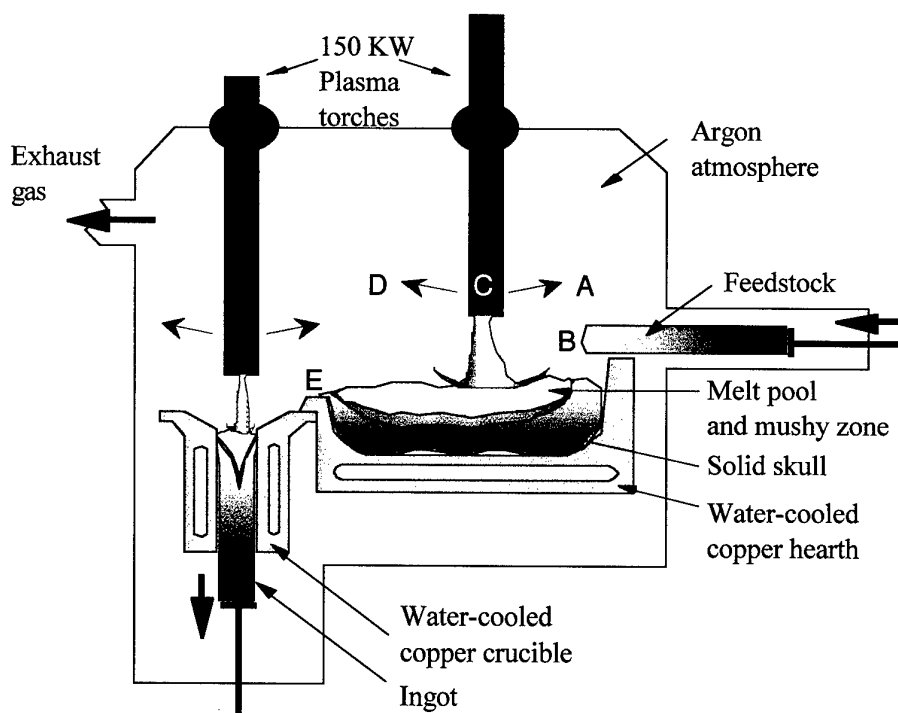


Figure 1: Schematic diagram of the IRC plasma furnace.

A number of different feed materials have been used, but the commonest have been 'compacts' (blocks made from pressing a mixture of granulated or powdered elements and master alloys - figure 2), and solid billets.

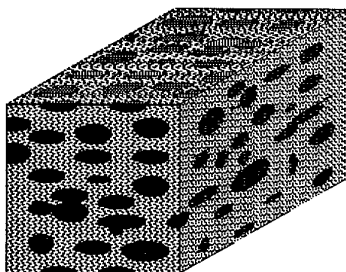


Figure 2: 'Compact' feedstock

#### Determination of ingot quality

One focus of the work at the IRC in Materials has been the development, production and characterisation of advanced titanium-based alloys. A large number of gamma-titanium aluminide ingots have been produced, both single melted (i.e. straight from compacts) and double melted (i.e. by remelting a bar previously made from compacts). A particular observation on first melt bars of this alloy was that, although commercial analysis by X-ray fluorescence (XRF) indicated good chemical homogeneity, use of a smaller analysis area (4mm diameter spot as opposed to 30mm) by Glow Discharge Optical Emission Spectroscopy (Ref. 6) revealed the presence of periodic variations in aluminium concentration. (In double melted bars however the heterogeneity was greatly reduced, and any pattern less regular if observable at all). It was decided that, as these variations in single-melted bars could affect further processing of the material, a means of production which would eliminate them would have to be adopted.

#### Methods for improving quality

Following the approach of slow adaptation, the initial course of action was to double melt all ingots which required compact feedstock, as this had been observed to produce homogeneous material. This had the downside of increasing the time, energy and staff needed per ingot.

To help find an alternative solution, a simple qualitative process model was proposed, based on the empirical experience which had been accumulated (figure 3). This was by no means a complete list or accurate description of the processes occurring during cold hearth melting, but it helped to indicate areas for further investigation.

Initially, referencing literature on solidification processes in (mostly larger scale) ingot production (Refs. 7-10) it was thought that processes occurring during solidification (labelled as '1' in figure 3) might be responsible for the patterns of aluminium variation observed. This was investigated, and it was found that the variations in aluminium concentration in an ingot had the same period as variations in the casting rate, (and that this period corresponded to the time taken to melt each successive group of feedstock compacts). However, trials indicated that although deliberately imposed changes of casting rate were found to affect the pattern of aluminium variation, the extent of that variation did not appear to be controlled by them (Ref. 11). This indicated that the melting and subsequent mixing of compacts (labelled '2') might be the most important factor.

To investigate this, production of a test ingot of the alloy Ti-48Al-2Mn-2Nb (At%) was halted when final set of compacts were all half-melted. The remaining compact material was separately melted, homogenised, and chemically analysed. It was found to be depleted in aluminium, indicating that aluminium was probably melting before the titanium, although the two were finely divided and interspersed with each other in the compacts.

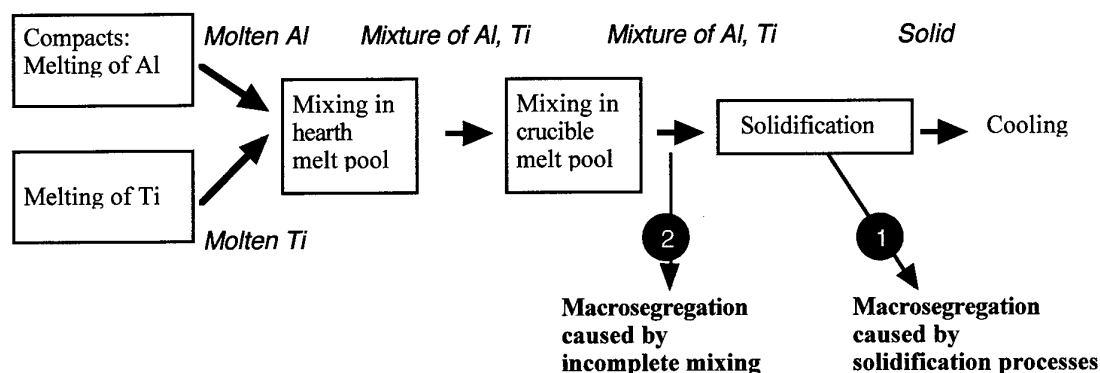


Figure 3: Initial model of some processes occurring during cold-hearth refining

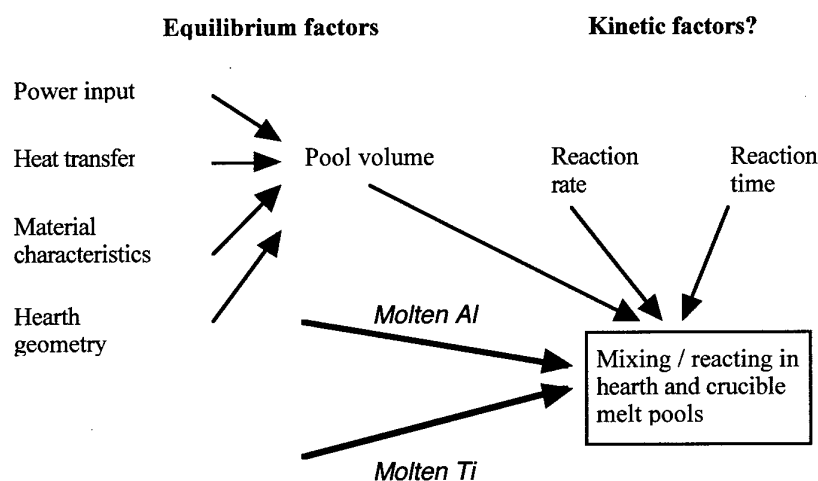


Figure 4: Detailed model of the mixing sub-process

The preferential melting of aluminium was further verified by melting only the first half of a compact into the hearth, and chemically analysing the small deposit which it produced. As expected, the deposit (consisting of the first liquid to be produced) was found to be enriched in aluminium, leaving the remainder of the compact depleted.

Given that the compacts were not producing a homogeneous composition of liquid over time, one solution to improving the final ingot quality was to attempt to improve the mixing (or reacting) of the different elements in the hearth and crucible. The following modification to the 'mixing' sub-process model was proposed (figure 4):

To assess the importance of the various factors which might control the effectiveness of mixing, an ingot was produced with different casting rates for successive regions, and was then sectioned and chemically analysed. The overall range of variation of aluminium concentration was not found to be dependent on the local casting rate, except possibly at the highest rate used (which was faster than would normally be used). This supported the view that the efficiency of mixing was not limited by kinetic factors, but by the equilibrium position. Based on this evidence it was decided to attempt to increase the mixing volume available.

The simplest possibility was to alter the geometry or heat transfer in the hearth. (This was because the material characteristics were fixed, it was not possible to increase

the applied power significantly, and the crucible geometry was fixed by the product dimensions).

Increasing the surface area of the molten pool through using a wider or longer hearth would have required more input power to combat the increased losses from radiation, convection and conduction. An attempt was therefore made to increase the pool depth. Anecdotal evidence had suggested that making the hearth deeper did not increase the pool depth much; this was somewhat surprising, so it was decided to develop a simple 1-dimensional analytical model of the hearth to help understand the situation.

#### Process modelling

A simple, analytical model of a 1-dimensional vertical cut through a hearth was created (figure 5).

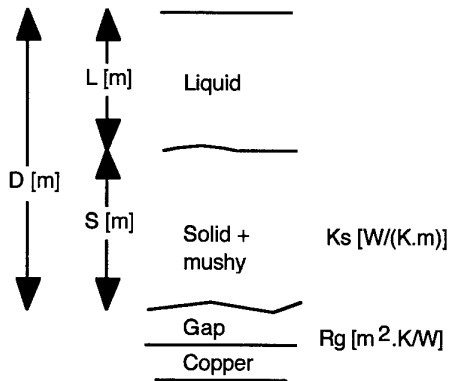


Figure 5: 1-dimensional representation of the plasma melting hearth

The details of this model are given elsewhere (Ref. 12), but one initially surprising aspect of the analytical solution obtained was that the depth of the hearth (assumed to be equal to the total depth of material),  $D$ , did not appear as a term on its own in the expression for liquid depth ( $L$ ). Instead, it appeared in conjunction with the thermal conductivity of the solid ( $K_s$ ) and the thermal resistance between the solid skull and the hearth ( $R_g$ ) in the following form (with  $\psi$  representing a non-dimensional expression for efficiency):

$$L = (K_s \cdot R_g + D) \cdot \frac{1}{1 + \frac{1}{\psi}}$$

The expression  $K_s \cdot R_g$  represents a distance, numerically equal to the thickness of skull material which would present the same thermal resistance as the gap between the hearth and the solid skull. Thus the gap represents a layer of 'virtual solid'. A sensitivity analysis of the effect upon the liquid pool depth of varying the gap resistance (and hence the thickness of this layer of 'virtual solid'), the top surface superheat, and the hearth depth from their default values is shown below (figure 6):

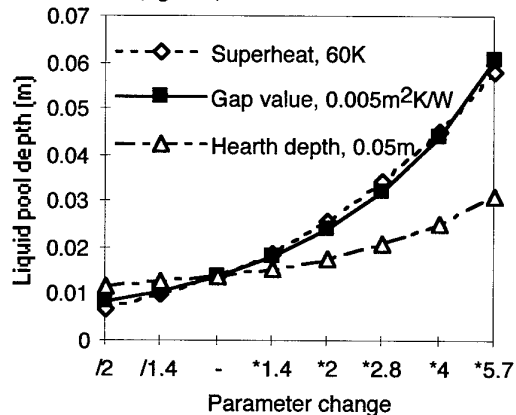


Figure 6: Sensitivity analysis of the effects of different process variables on liquid pool depth in the IRC plasma furnace hearth

Representative values for the IRC plasma melting facility were used. Although the results were clearly not always valid (many effects such as change of skull shape with temperature etc. were not taken into account) an interesting trend was predicted - that insulating the bottom of the hearth could be more effective than making it deeper in terms of increasing the liquid pool depth.

### Experimental procedure

To test this, two Ti-48Al-2Mn-2Nb (At%) ingots of 100mm diameter were produced under otherwise similar conditions - one with an insulated hearth, and one (as normal) without. For insulation, layers of ceramic matting were placed between the base of an existing Ti-48-2-2 skull and the copper hearth in order to increase the thermal resistance of the gap, although it is recognised that this is not compatible with clean melting. (Alternative means of increasing the thermal resistance for this purpose have been proposed and are being studied).

### Experimental results

During production it was observed that the melt pool in the hearth had a larger surface area when the insulating layer was used than without it. Longitudinal macro slices were cut from the ingots and maps of chemical composition were produced using an Oxford Instruments XGT 2000 Energy Dispersive X-Ray Fluorescence scanning analyser, which generated spatial maps of the concentration of different elements. The instrument was more sensitive to titanium than aluminium, so the maps of titanium concentration are shown below (figures 7,8):

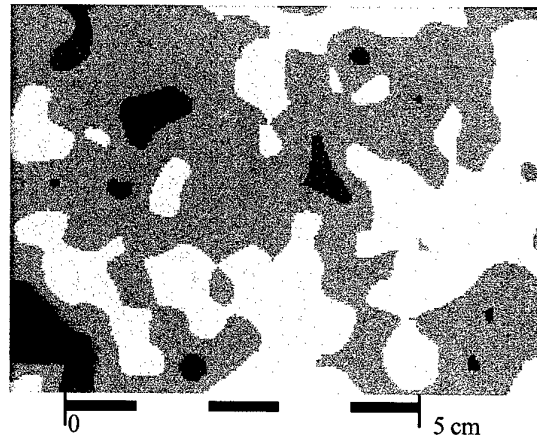


Figure 7: Map of concentration of titanium in a longitudinal macro-slice from a single-melted gamma-titanium aluminide ingot, using an insulated hearth

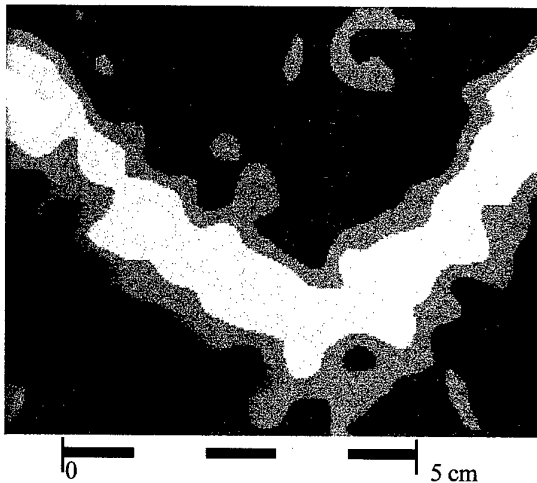


Figure 8: Map of concentration of titanium in a longitudinal macro-slice from a single-melted gamma-titanium aluminide ingot, produced conventionally

The measurements were obtained without standards, giving non-dimensional intensity scales measured in counts per second (cps). However, the same relationship between greyscale value and titanium concentration was used for both images. The section from the single-melted bar produced with the insulated hearth (figure 7) displayed a smaller range of variation in its titanium content (standard deviation,  $s=2.8$  cps) than that produced conventionally (figure 8,  $s=4.0$  cps). It is believed that the increased mixing volume available was responsible for this, as other process conditions were kept as similar as possible. That being the case, process control for this situation is quite simple: the most important goal is to keep the mixing volume as big as possible, rather than to necessarily be able to prevent disturbance of a particular pool size.

There are other benefits from maximising the pool volume during cold hearth processing, specifically for removing inclusions from the material being processed. (Inclusion removal is extremely important for aerospace material destined for compressor and turbine disc applications, as it improves low-cycle fatigue life - Ref. 13). There are two main mechanisms for inclusion removal during cold hearth processing - buoyancy driven separation, and dissolution (Refs. 14,15). Both of these removal mechanisms occur whilst inclusions are in the melt pool - thus, the longer the residence time, the more likely it is that complete inclusion removal will be achieved. Therefore since residence time depends on pool volume, pool volume is directly implicated in inclusion removal capability (Ref. 16).

## CONCLUSIONS

Modelling helps the improvement of a process and its adaptation to changing circumstances, as well as helping to define the goals for sensing and control.

Applying a simple thermal model to maximising the mixing volume in the hearth of the IRC plasma melter suggested the use of an insulating layer, beneath the solid skull, and that this would be more beneficial than making the hearth itself deeper.

Sections from a (single-melted) ingot of gamma-titanium aluminide produced with an insulated hearth displayed less variation in concentration of titanium (and hence aluminium) than those from an ingot produced conventionally.

Increasing the molten pool volume in the hearth also aids inclusion removal.

## REFERENCES

- Hogg, J.C. "Application of process models in the Casting Industry", in *Solidification processing 1997: Proceedings of the 4th Decennial International Conference on Solidification Processing*, J.Beech and H.Jones (eds.), 7-10 July 1997, Univ. of Sheffield UK, Dept. Of Engineering Materials, University of Sheffield, pp. 116-120.
- Anklam, T.M., Berzins, L.V., Braun, D. G., Haynam, C., McClelland, M.A., Meier, T. "Evaporation monitoring and composition control of alloy systems with widely differing vapor pressures", in *Proc. Electron Beam Melting and Refining State of the Art 1994*, Ed. R bakish, Bakish Materials Corp., po box 148, Englewood NJ 07631 USA, pp.94-104.
- Wenzel, D., Esche, H.J. and Pilz, J., "Coating thickness measurement by XRF in vacuum strip metallizing plants", in *Proc. Electron Beam Melting and Refining State of the Art 1994*, Ed. R bakish, Bakish Materials Corp., po box 148, Englewood NJ 07631 USA, pp. 78-85.
- Ward, R.M. "Temperature sensing for cold-hearth melting processes", in *Ti '95 Science and Technology* ed. P.A. Blenkinsop, W.J Evans, H.M. Flower (London: Inst. of Materials, 1996), pp. 1478-1485.
- Young, J.M. and Patel, S.J. "Cold hearth plasma melting of nickel base superalloy APK 12", in *Proc. 1994 Int. Symp. on Liquid Metal Processing and Casting*, ed. A. Mitchell, J. Fernihough, American Vacuum Soc., 1994, pp. 65-77.
- Johnson, T.P., Dowson, A.L. and Ward, R.M. "The determination of macrosegregation patterns in Fe, Ni and Ti-base alloys by glow discharge optical emission spectroscopy", accepted for publication in *Scripta Mat*, 1998
- Flemings, M.C., *Solidification Processing*, New York:McGraw Hill, 1974
- Bertram, L.A. and Zanner, F.J., "Plasma and magnetohydrodynamic problems in vacuum consumable arc remelting", in *Metallurgical applications of magnetohydrodynamics*, London : Metals Society, 1984, pp. 283-300
- Blackburn, M.J. and Malley, D.R., "Plasma Arc Melting of Titanium Alloys", in *IRC'92 - Processing, Properties and Applications of Metallic and Ceramic Materials*, M H Loretto and C J Beevers (eds.), MCE Publications Ltd., 1992, pp. 99-118
- Tripp, D.W. and Mitchell, A., "Segregation and Hot-Topping of titanium alloy ingots", in *Proceedings of the 1989 Vacuum Metallurgy Conference*, Ed. L.Herbier and J.Cordy, American Vacuum Society, 1989
- Godfrey-Macha, B, PhD: *Segregation Mechanisms in PACH Melted Ingots of Gamma-TiAl*, Engineering Faculty, University of Birmingham, 1997
- Ward, R.M., PhD: *Sensing and Controlling the Plasma Arc Cold Hearth Refining Process*, Engineering Faculty, University of Birmingham, 1998, in preparation
- Shamblen, C.E. and Chang, D.R., "Effect of inclusions on LCF life of HIP plus heat treated powder metal Ren  95", *Metallurgical Transactions B*, vol. 16B, 1985, pp. 775-784
- Shamblen, C.E. and Hunter, G.B., "Titanium base alloys clean melt process development", in *Electron Beam melting and refining: State of the art 1989*, Bakish Materials Corporation, 1989
- Jarrett, R.N., "Removal of defects from titanium alloys with electron beam cold hearth melting", in *Electron Beam melting and refining: State of the art 1986*, Bakish Materials Corporation, 1986
- Menzies, R.G., Shamblen, C.E., Backman, D.G. and Hunter, G.B., "Process design and control for aircraft engine materials", in *Electron Beam melting and refining: State of the art 1992*, Bakish Materials Corporation, 1992,

## ACKNOWLEDGEMENTS

This work was financed by the EPSRC as part of the IRC's foundation research programme. Thanks to the IRC's Director, Mike Loretto and to the Plasma Melting Team for their support and efforts, and thanks to our colleagues Barbara Macha-Godfrey, Tony Dowson and Yuyuan Zhao for their helpful comments.



# LASER ULTRASONIC MEASUREMENT OF MICROSTRUCTURE EVOLUTION DURING METALS PROCESSING

Marc Dubois, André Moreau, Andrew Dawson, Matthias Militzer<sup>†</sup>, and Jean F. Bussière

Industrial Materials Institute, National Research Council Canada  
75 Mortagne, Boucherville, Québec, Canada, J4B 6Y4

<sup>†</sup>The Centre for Metallurgical Process Engineering, The University of British Columbia,  
Vancouver, British Columbia Canada, V6T 1Z4

## ABSTRACT

Laser-ultrasonics, a technique based on the generation of ultrasonic waves by a pulsed laser and on their detection by a laser interferometer, was used to monitor microstructure evolution during austenitization and phase transformations of A36 and IF steels, and during the sintering of a green powder metal iron compact. Ultrasonic attenuation measurements allowed the observation of grain growth during austenitization and of nucleation and growth during phase transformations. A calibration based on the metallographic evaluation of austenite grain sizes on quenched steel samples was obtained to quantitatively relate ultrasonic attenuation to austenite grain sizes. Ultrasonic velocity measurements also allowed the monitoring of the first two stages of the sintering process in a green powder metal iron compact. The laser-ultrasonic technique provided, in real-time, microstructural information that could only have been obtained laboriously using traditional metallographic techniques. The results presented in this paper establish laser-ultrasonics as a powerful laboratory tool to study microstructural evolution at high temperatures.

## 1. INTRODUCTION

During metal processing at high temperatures, the microstructure must be controlled to optimize operation costs and to confer the required properties to finished products. This control is achieved by a judicious combination of mechanical deformations, thermal treatments, and alloying elements. Generally, process control could be improved if the values of these control parameters were adjusted based on high temperature measurements of the microstructure during processing. In some cases, an adjustment could even be done in real-time, leading to increased yield and enhanced product quality. Consequently, a high temperature technique for microstructure evaluation would be extremely useful. Laser-ultrasonics provides microstructure measurements in real-time and offers the potential to be usable on-line.

Ultrasonics has provided for many years excellent methods to characterize steel microstructure [1]. The information may be provided in real-time but ultrasonic measurements at high temperatures are not easily obtained using conventional ultrasonic transducers. Laser-ultrasonics, a technique based on the generation of ultrasonic waves by a pulsed laser and on their detection by a laser interferometer, is a truly remote technique [2] (standoff distances of order 1 m) and works well at high temperatures [3-6].

Ultrasonic attenuation has already been measured during phase transformations and during austenite grain growth

using laser-ultrasonics [4], conventional piezoelectric transducers [7], and electromagnetic transducers [8,9]. Unfortunately, the accuracy of the data obtained did not allow a reliable evaluation of microstructure at high temperatures. The development of laser-ultrasonics in recent years has allowed more accurate ultrasonic measurements at high temperatures, making possible even quantitative evaluation of microstructural features such as grain size.

Ultrasonic measurements have also been used to monitor the sintering of ceramic compacts. One group ingeniously coupled ultrasonic transducers at room temperature to the hot ceramic compact through acoustic wave guides [10,11]. A few authors [12,13] have already used laser-ultrasonics to monitor the sintering of ceramics, but no similar work was found on powder metal (PM) compacts.

In this article, the capabilities of laser-ultrasonics to characterize the microstructure during high temperature processing are demonstrated. The ultrasonic attenuation or velocity was monitored in steel and iron samples during three different high temperature processes: austenite grain growth, phase transformations and sintering. The results obtained using laser-ultrasonics data are compared to conventional techniques to characterize microstructure such as metallographic observations and dilatometry measurements.

## 2. ULTRASONIC SCATTERING THEORY

Ultrasonic attenuation is caused by various microstructural parameters but is, for most metals, primarily due to grain scattering. The relationship between attenuation and grain size depends on the ratio of the acoustic wavelength,  $\lambda$ , to the average of some measure of grain size,  $D$ . Generally, three regimes are considered [1]:

$$\text{Rayleigh regime } (\lambda \gg D) \quad \alpha = K_r D^3 f^4$$

$$\text{Stochastic regime } (\lambda \approx D) \quad \alpha = K_s D f^2$$

$$\text{Diffusion regime } (\lambda \ll D) \quad \alpha = K_d / D$$

where  $\alpha$  is the attenuation coefficient,  $K_r$ ,  $K_s$ , and  $K_d$  are constants of the material and  $f$  is the ultrasonic frequency ( $f = V/\lambda$ , where  $V$  is the ultrasonic velocity). For the specimens studied here, the ratio of the ultrasonic wavelength to the average grain size is such that the scattering lies between the Rayleigh and the stochastic regimes. Therefore, the ultrasonic attenuation is expected to increase with grain size. From here, it will be assumed that the three scattering regimes are covered by the following single equation [14]:

$$\alpha = K(T) D^{-\gamma} f^{\gamma} \quad (1),$$

where  $K(T)$  is a variable that depends on the material and on temperature, and  $\gamma$  is an exponent that varies continuously between 0 and 4, depending on whether the ultrasonic wavelength is small or long as compared to  $D$ .

At the temperatures considered in this paper, two phases can be present in steel and iron: ferrite, stable at room temperature and austenite, stable above 910°C in pure iron. Other phases present in steels, such as cementite, will be neglected because of the relatively low content of alloying elements in the samples. The crystallographic structure of ferrite is body-centered-cubic and that of austenite is face-centered-cubic. From an ultrasonic point of view, both structures are considered as cubic and are characterized by only three elastic constants:  $C_{11}$ ,  $C_{12}$ , and  $C_{44}$  [15]. The elastic constants of pure ferritic iron are known at all temperatures below the equilibrium transformation temperature [16] but the elastic constants of austenite are only available at one temperature, 1150°C [17]. In the Rayleigh regime, ultrasonic attenuation in cubic crystals is proportional to the square of the factor  $(C_{11} - C_{12} - 2C_{44})$  [18], also known as anisotropy factor. The values of this factor are -171.4 GPa in ferrite at 900°C [16] and -122 GPa in austenite at 1150°C [17]. The difference between the two values is roughly 30%, which is small when compared to the variations in ultrasonic attenuation that will be presented. Therefore, the effect of the elastic constant differences between austenite and ferrite will be neglected in a first approximation, as well as any absorption effect that may be caused by the phase transformation [19]. Consequently, ultrasonic attenuation variations during phase transformations will be interpreted hereafter as originating only from grain size variations.

### 3. EXPERIMENTAL SETUP

For all laser-ultrasonic experiments presented in this paper, samples were placed in a radiant furnace equipped with windows transparent to the laser radiation wavelengths. The sample temperature was measured with a thermocouple spot-welded approximately 5 mm from the edge of the laser detection spot.

Ultrasonic waves were generated using an excimer laser at an optical wavelength of 248 nm (ultraviolet). Pulse duration was 6 ns, pulse energy was 250 mJ, and the laser-beam was focused on the sample into a nearly uniform rectangular spot of approximately 4x6 mm<sup>2</sup>. The optical power density was high enough to vaporize some material from the sample surface. However, no measurable change of sample thickness was observed after experiments involving thousands of light pulses.

Ultrasonic displacements were detected on the opposite surface of the sample with a laser interferometer based on a 3 kW long-pulse Nd:YAG laser running at 20 Hz and a confocal Fabry-Perot interferometer operating in the reflection mode [20]. The repetition rate of the Nd:YAG laser limits the time resolution of the measurements to 50 ms. For surface displacements much smaller than the 1.064- $\mu$ m wavelength of the detection laser and for ultrasonic frequencies higher than 5 MHz, the electronic output of the interferometer is approximately proportional to the surface displacement. The detection laser beam was focused on the sample into a uniform disk approximately 5 mm in diameter.

Figure 1 shows a typical single-shot signal obtained from an ASTM-A36 steel sample at 1200°C. Fourier transforms on the first and second echoes were made, and the ratio of these power spectra divided by twice the thickness provided the ultrasonic attenuation as a function of frequency. When measured, the time delay between two ultrasonic echoes,  $\Delta t$ , was determined by numerical cross-correlation [21]. When only one pulse was observed, as it occurred during the sintering measurements,  $\Delta t$  was deduced from its arrival time.

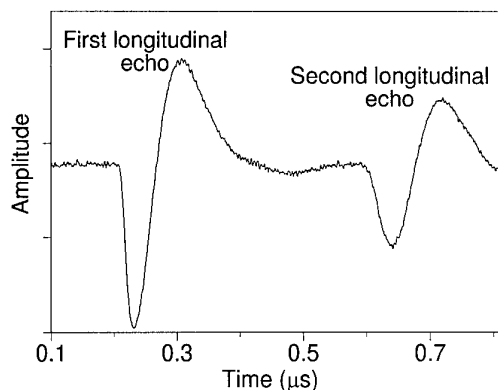


Figure 1 Ultrasonic signal obtained from an A36 steel sample at 1200°C

The three following sub-sections give the specific experimental details related to each particular experiment set.

#### 3.1. Phase Transformations

Laser-ultrasonic measurements were made during heating and cooling A36 and IF steel samples through phase transformations. The samples were machined into 25x25 mm<sup>2</sup> x 1 mm specimens from as-received hot-rolled material (transfer bars) provided by the Gary Works of US Steel. The two faces of each sample were parallel within 25  $\mu$ m over the 25x25 mm<sup>2</sup> area, and the average deviation of the surface profile about its mean line ( $R_a$ ) was smaller than 1  $\mu$ m. For such small values, the lack of parallelism and the surface roughness were assumed to have no effect on the attenuation at the ultrasonic frequencies considered in this article [22]. Ultrasonic measurements were performed near the center of the 25x25 mm<sup>2</sup> area. Table I gives the chemical composition of the steel samples.

Table I Chemical composition (wt%) of the A36 and IF steel samples.

Steel	C	Mn	P	S
A36	0.17	0.74	0.009	0.008
IF	0.0028	0.17	0.011	0.006
Steel	Si	Cu	Ni	Cr
A36	0.012	0.016	0.010	0.019
IF	0.009	0.020	0.014	0.029
Steel	Al	N	Ti	Nb
A36	0.040	0.0047	--	--
IF	0.027	0.0029	0.035	0.035

In addition to laser-ultrasonic measurements, dilatometry measurements were made on tubular A36 and IF specimens (50 mm long with an inner diameter of 8 mm and a wall thickness of 1 mm) to quantify, for comparison, the austenite-to-ferrite transformation kinetics. These measurements were made on a Gleeble 3500 TS thermal simulator which reproduced the heating and cooling conditions of the radiant furnace during the laser-ultrasonic measurements on the IF and A36 steel samples.

### 3.2. Austenite Grain Growth

The samples used for the laser-ultrasonic measurements during austenite grain growth were the same as those described previously in section 3.1.

For the quantitative evaluation of austenite grain size from ultrasonic attenuation, diffraction effects should be considered. These effects depend on the acoustic Fresnel parameter  $S$  which is defined by  $S = \lambda z / a^2$ , where  $\lambda$  is the acoustic wavelength,  $z$  is the distance traveled by the ultrasonic wave, and  $a$  is the generation laser spot radius. At a frequency of 15 MHz,  $S$  was smaller than 0.15 for the first two longitudinal echoes. For such small values of  $S$ , the ultrasonic waves are essentially plane waves so that no diffraction correction is required [23].

### 3.3. Sintering of a green PM iron compact

The iron PM compact sample tested was disk-shaped, formed by uniaxial compaction of high purity water atomized iron powder [24] in a 38.1 mm diameter cylindrical die under a load applied by a hydraulic press. While no lubricant was admixed with the powder, the die walls were lubricated by applying a spray coating of zinc stearate to reduce friction and tool wear. 48.5 grams of iron powder were pressed under a maximum pressure of ~650 MPa to produce an iron disk compact with a thickness of 5.93 mm and a density of 7.13 g/cm<sup>3</sup> (~9% porosity).

Thermal expansion was measured in the direction of compression on a small corner cut from the green compact. This experiment was conducted in a commercial dilatometer that reproduced the thermal conditions of the radiant furnace during the laser-ultrasonic monitoring of the sintering process.

## 4. RESULTS AND DISCUSSION

### 4.1. Phase transformations

Laser-ultrasonic attenuation at 15 MHz was monitored while A36 and IF steel samples were heated from room temperature to 1000 or 1100°C at a rate of 5°C/s, during 10 and 15-minute holding periods, and during cooling back to room temperature. The cooling was obtained by simply turning off the furnace elements. The cooling rate was approximately 1°C/s at 700°C. The attenuation at 15 MHz is presented as a function of temperature in figures 2a, 2b and 4 where the austenite fractions during cooling and heating are also indicated.

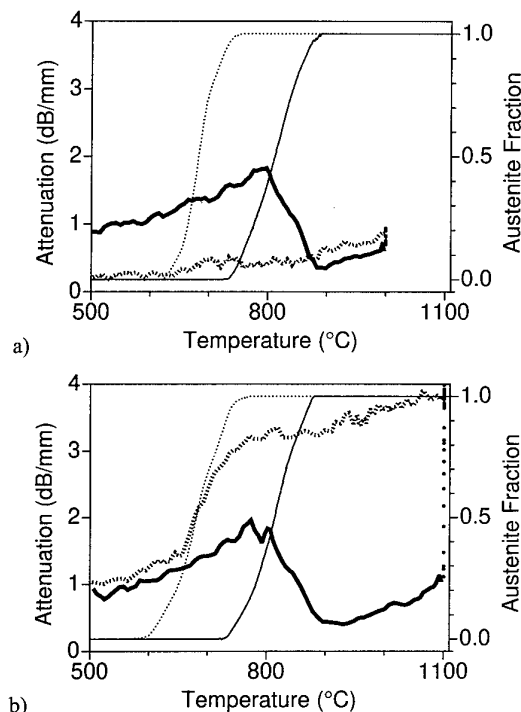


Figure 2 Attenuation measurements at 15 MHz in A36 steel samples during heating (thick solid line), cooling (thick dotted line) and isothermal treatment at a) 1000°C b) 1100°C (bold dots). A moving average of 3 was used to smooth the attenuation data. The austenite fractions during cooling (thin dotted lines) and heating (thin solid lines), as measured by dilatometry, are also indicated.

During heating an A36 sample to 1000°C (figure 2a), the ultrasonic attenuation increased slowly from ~0.9 dB/mm at 500°C to almost 2 dB/mm at 800°C, dropped to ~0.3 dB/mm between 800°C and 900°C, which corresponds to the transformation temperature range, and increased again with temperature above 900°C to reach ~0.7 dB/mm at 1000°C. While temperature was maintained constant at 1000°C for 15 min., the ultrasonic attenuation increased slightly to 0.9 dB/mm. During furnace cooling (at approximately 1°C/s), the attenuation decreased monotonically from 0.9 to 0.2 dB/mm at 500°C, showing no special feature during the transformation. The attenuation measured during cooling at 500°C is considerably lower than the attenuation measured at the same temperature during heating.

During heating an A36 sample to 1100°C (figure 2b), the ultrasonic attenuation behaved similarly to what was observed during the heating to 1000°C. Above 1000°C, the ultrasonic attenuation increased slowly with temperature to reach ~1 dB/mm at 1100°C. While the temperature was maintained at 1100°C for 10 min., the attenuation increased further to ~3.8 dB/mm. During cooling, the attenuation decreased slowly to ~3 dB/mm between 1100°C and 700°C. During the phase transformation, the ultrasonic attenuation decreased more rapidly to a value of ~1.2 dB/mm. When the phase transformation was completed, the attenuation decreased approximately at the same rate as before the transformation to reach ~1 dB/mm at 500°C, an attenuation slightly higher than the value measured at the same temperature during heating.

These results are interpreted as follows. During heating, the elastic constants of ferrite vary with temperature [16] and cause a monotonic increase in ultrasonic attenuation between 500°C and 800°C. In the phase transformation range, austenite nucleates and forms a finer microstructure than the prior ferritic structure. The smaller austenite grains cause a decrease in ultrasonic attenuation. When a sample was heated to 1000°C for 15 min. (figure 2a), the austenite grain size did not increase significantly because AlN precipitates pinned the austenite grain boundaries [25,26]. During cooling back through the phase transformation region, ferrite nucleated and formed grains having approximately the same size as the prior austenite grains. Consequently, no sudden change in attenuation is associated with this phase transformation. The resulting ferrite microstructure is finer than it was before thermal processing, as confirmed by comparing the microstructures shown in figures 3a and 3b. However, when a sample is heated to 1100°C for 10 min., significant austenite grain growth occurs, which results in a marked increase in attenuation (figure 2b). The transformation during cooling then produces a ferrite microstructure which is finer than the prior austenite grains but comparable to the as-received microstructure, as confirmed by the micrographs of figure 3. Consequently, the attenuation dropped back to levels similar to those observed initially during heating.

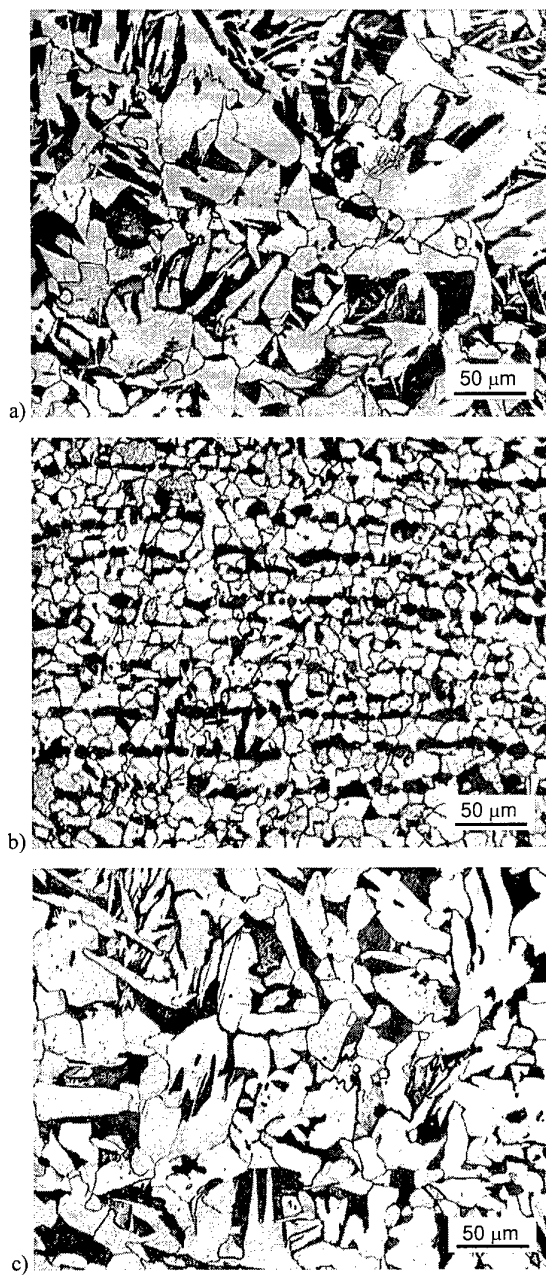


Figure 3 Optical micrographs of A36 steel samples: a) as-received and austenitized at b) 1000°C, and c) 1100°C. (Nital 4%).

Figure 4 shows the ultrasonic attenuation measured during the thermal cycle of the IF steel sample. The fraction of austenite, measured by dilatometry during an identical thermal treatment, is also shown in Figure 4. Micrographs of the IF sample after this experiment and of the as-received IF material are presented in Figure 5.

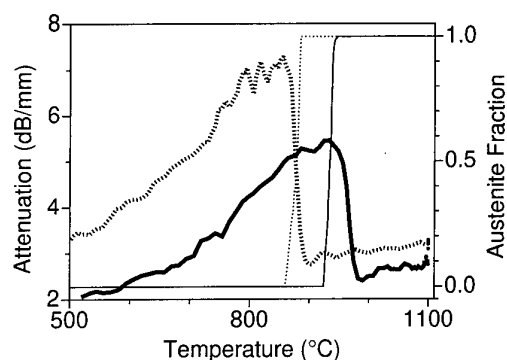


Figure 4 Attenuation measurements at 15 MHz in an IF steel sample during heating (thick solid line), cooling (thick dotted line) and isothermal treatment at 1100°C (bold dots). A moving average of 3 was used to smooth the attenuation data. The austenite fractions during cooling (thin dotted lines) and heating (thin solid lines), as measured by dilatometry, are also indicated.

During heating the IF steel sample, the ultrasonic attenuation increased slowly from ~2 dB/mm at 500°C to ~5 dB/mm at 900°C. Above 900°C, the attenuation dropped sharply to ~2.3 dB/mm during the phase transformation, and increased again slowly with temperature above 1000°C to reach ~2.7 dB/mm at 1100°C. While temperature was maintained constant at 1100°C for 10 min., the attenuation increased to ~3 dB/mm. During cooling back through the phase transformation, the ultrasonic attenuation in the IF sample sharply increased from ~2.5 dB/mm to ~7 dB/mm.

During heating and before cooling through the transformation temperature range, the attenuation behaved similarly to what was observed previously for the A36 steel. The elastic constant variations with temperature caused a monotonic increase in ultrasonic attenuation as temperature increased from 500°C to ~850°C. During heating through the phase transformation range, austenite nucleates and forms a finer microstructure than the prior ferritic structure. This finer microstructure caused a decrease in the ultrasonic attenuation. While holding at 1100°C, the austenite grains grow, causing a slight increase of attenuation.

During cooling, however, the attenuation behavior in the IF steel was significantly different from that observed in the A36 steel. The sharp increase of attenuation while cooling back through the phase transformation is attributed to the formation of ferrite grains larger than the prior austenite grains. Micrographs show that the IF steel sample isothermally treated at 1100°C has very large ferrite grains, some of them having linear intercepts in the order of 500  $\mu\text{m}$  (Figure 5), whereas the as-received material is characterized by a grain size of only ~40  $\mu\text{m}$ .

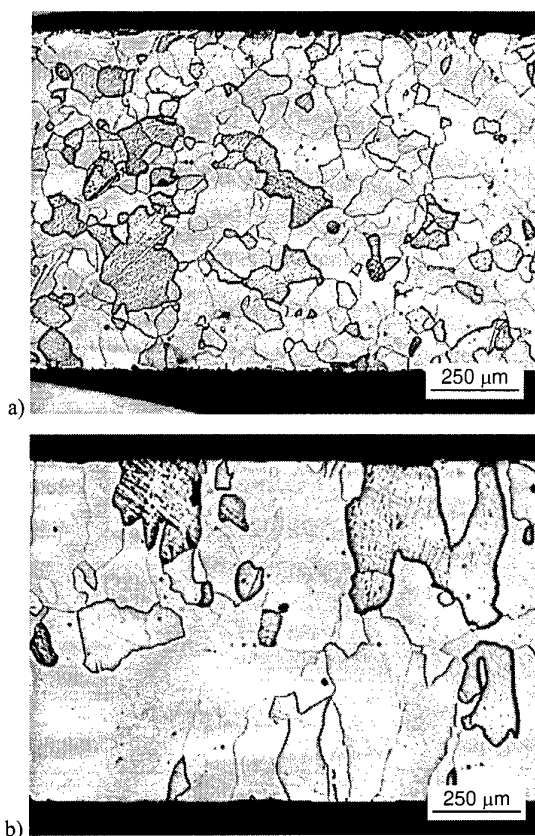


Figure 5 Optical micrographs of IF steel samples: a) as-received and b) after heat treatment at 1100°C and cooling at 1°C/s. (Nital 2%)

In low carbon steels, such as A36, the growth rate of the new ferrite phase in austenite is limited by diffusion of carbon in austenite. In IF steels and other ultra-low carbon steels, the diffusion of carbon is no longer a limiting factor. The austenite-to-ferrite transformation is then interface-controlled with comparatively high transformation rates [27,28]. As a result, the ferrite microstructure can be very coarse. In a previous study of air-cooled IF steels [29], ferrite grains were observed, in some cases, to be larger than the prior austenite grains. In the present study, the formation of even larger ferrite grains was favored because the cooling rate of 1°C/s is slower than the 5°C/s cooling rate [30] of the IF samples studied in [29].

#### 4.2. Austenite grain growth

To obtain quantitative measurements of austenite grain sizes, a calibration was developed using the results of a previous study on austenite grain growth [31]. In this set of experiments, austenite grain growth was studied as a function of time and temperature using quenching and standard metallographic practices on A36 steel samples. The specimens, machined from an as-received transfer bar, were heated at a rate of 5°C/s to different maximum temperatures above 950°C and held at these temperatures for up to 15 min.

The equivalent area diameter, EQAD, i.e. the diameter of a circle having an area equal to the mean area of the measured grains, was chosen to quantify grain size. For most

measurements, the observed grain size distribution was approximately log-normal, with a standard deviation of 0.3.

Abnormal grain growth was observed at 1000°C and in the first minute at 1050°C. Abnormal grain growth is a deviation from normal grain growth such that the growth is restricted to a relatively small number of grains whilst the remainder are virtually unaltered until they are consumed [32]. When abnormal growth occurs, grain size distribution differs from log-normality and is usually bimodal. Furthermore, the evaluation of EQADs using metallography is more complex because at least two different magnifications are needed to characterize grains of very different sizes.

In the new set of experiments described in this article, the heating schedules of the previous study [31] were reproduced for maximum temperatures of 1050, 1100, 1150, and 1200°C for A36 steel samples machined from the same transfer bar. Experiments at 1050 and 1100°C were repeated to assess the reproducibility of the measurements.

Grain growth appeared to be mostly completed within a few minutes from the moment the maximum temperature was reached. Therefore, it was assumed that no further grain growth occurred during cooling after the samples were held at their austenitizing temperatures for 10 or 15 min. It was also assumed that the change in ultrasonic attenuation during cooling is only caused by  $K(T)$  of equation (1). Our measurements have shown that ultrasonic attenuation decreases linearly with decreasing temperature from austenitizing temperatures to 800°C with an average slope of  $2.26 \times 10^{-3}$  dB/(mm °C). Therefore,  $K(T)$  may be expressed as:

$$K(T) = K(1100^\circ\text{C}) + K_c \cdot \Delta T, \quad (2)$$

where  $K_c = 2.26 \times 10^{-3}$  dB/(mm °C) and  $\Delta T = T - 1100^\circ\text{C}$ .

Equation (1) indicates that the exponent  $\gamma$  can be extracted either from the relationship of frequency with attenuation or from the relationship of grain size with attenuation. Experimentally,  $\gamma$  was obtained from the slope of a log-log plot of attenuation vs. frequency. For austenite grain sizes larger than 100  $\mu\text{m}$  in A36 steel,  $\gamma$  was equal to  $1.5 \pm 0.2$  at 15 MHz. Therefore, according to equation (1), the ultrasonic attenuation at 15 MHz should be proportional to the square root of grain size, or equivalently, grain size should be proportional to the square of the ultrasonic attenuation at 15 MHz.

Using equation (2), the 15 MHz ultrasonic attenuation measured at temperatures between 1050 and 1200°C was converted to an ultrasonic attenuation at 1100°C and compared to the EQADs measured by metallography. Figure 6 presents this comparison where EQADs corresponding to abnormal grain growth were excluded. The solid line is a parabolic fit of the EQADs larger than 100  $\mu\text{m}$  to the ultrasonic attenuation. Clearly, the prediction obtained from equation (1) is verified. The rms. residual to the least squares fit is 14  $\mu\text{m}$ , that is approximately 10% of the average EQAD. This fit can be used to calibrate the ultrasonic attenuation in terms of EQAD for austenite grains, when the austenite grain size exceeds 100  $\mu\text{m}$ . For EQADs smaller than 100  $\mu\text{m}$ , the calibration is not expected to be valid because the slope of the log-log plot of attenuation vs. frequency differs from 1.5. A calibration for EQADs smaller than 100  $\mu\text{m}$  cannot

be obtained using the metallographic EQADs coming from [31] because this range of EQADs corresponds to abnormal grain growth conditions, and consequently very few points are available.

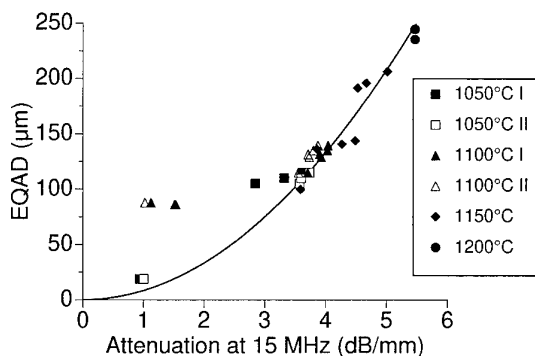


Figure 6 Austenite EQADs in A36 steel measured by metallography vs. attenuation at 15 MHz converted to a temperature of 1100°C. Experiments at 1050°C and 1100°C were repeated. The solid line is a parabolic least square fit.

Using the above calibration, laser-ultrasonic attenuation values were converted to grain sizes and plotted as a function of time for austenitizing temperatures of 1100°C and 1150°C. These curves are shown in figure 7 where metallographic measurements are also included. The agreement between both techniques is generally excellent. The rapid increase in grain size in the first minutes and the slow changes at longer times indicated by the metallographic measurements are correctly reproduced by the laser-ultrasonic measurements but with a much improved time resolution.

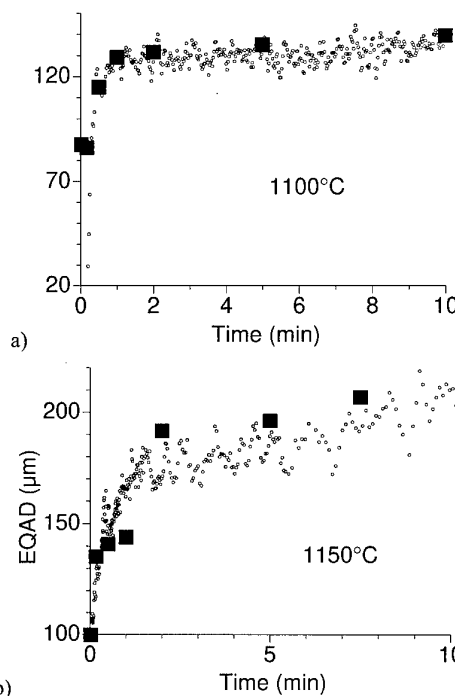


Figure 7 Comparison of austenite EQADs estimated from ultrasonic attenuation measurements (O) with those measured by metallography (■) for austenitization at a) 1100°C and b) 1150°C in A36 steel samples. A moving

average of 3 was used to smooth attenuation data. Time  $t = 0$  corresponds to the time at which the temperature measured by the thermocouple spot-welded on the sample reached the austenitizing temperature.

The calibration obtained with the A36 steel samples was used to estimate the austenite EQADs during the austenitization of an IF steel sample. The EQADs measured by ultrasonic attenuation at 1100°C and 1150°C are plotted in Figure 8. At austenitizing temperatures, carbon steels are single-phased. For single phase metals, ultrasonic attenuation is attributed mainly to grain scattering which is sensitive to grain size. Therefore, the obtained calibration is expected to be valid for all fully austenitized carbon steels, including IF steels. However, further experimental verifications would be desirable to confirm this assertion.

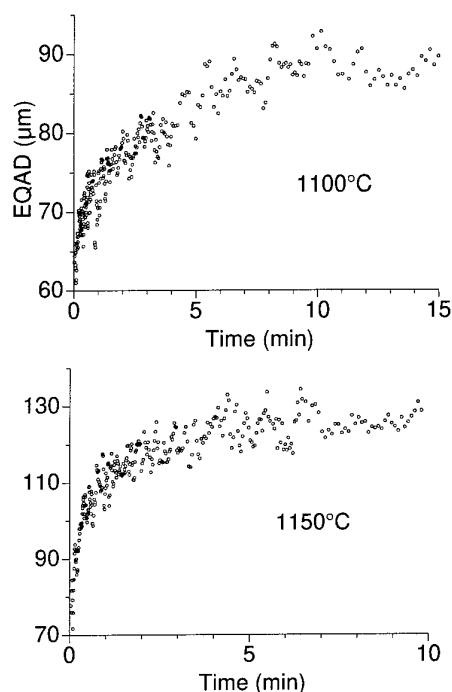


Figure 8 Austenite EQADs estimated from ultrasonic attenuation at 15 MHz during austenitization at a) 1100°C and at b) 1150°C in IF steel samples. A moving average of 3 was used to smooth data. Time  $t = 0$  corresponds to the time at which the temperature measured by the thermocouple spot-welded on the sample reached the austenitizing temperature.

#### 4.3. Sintering of a green powder metal (PM) iron compact

In several PM texts [33,34], three stages of sintering are defined. In as-pressed green compacts, the powder particles are weakly held together by a mechanical inter-locking mechanism. The powder particles are separated by small air-gaps and the weak inter-particle bonding is exemplified by the high attenuation of ultrasonic vibrations transmitted through it [35-37]. At comparatively low temperatures, stage I sintering occurs, during which these small inter-particle gaps are bridged. Stage I sintering, which is alternately referred to as the necking and bonding of particles, occurs at comparatively low temperatures because of the relatively large resulting reduction of surface area and its associated free energy. At higher temperatures,

stage II sintering begins wherein inter-particle necks grow, pores shrink and the compact densifies. Stage II sintering requires significant diffusion of material within the compact and occurs at higher temperatures because the associated surface area reduction is much less than for stage I sintering. Stage III, the final stage of sintering, which will not be discussed here, refers to such processes as grain coarsening and pore closure that result in negligible densification. In reality, all three stages of sintering occur simultaneously and prescribed temperature ranges are merely those where one stage dominates [33].

Ultrasonic velocity was monitored during the sintering of a green PM iron compact. The compact was heated at 10°C/min., maintained at 1200°C for 30 min., and cooled at 10°C/min. The observed variation in the propagation delay was much larger than the total variation of the thickness due to thermal expansion ( $<1.5\%$ ) as measured by dilatometry. Consequently, a constant compact thickness of 5.93 mm was assumed and the longitudinal ultrasonic velocity was simply calculated by the ratio of twice the constant thickness over the measured ultrasonic delay.

In figure 9, the longitudinal velocity is displayed as measured during the sintering of the green iron compact. Initially and below 500°C, the ultrasonic velocity is low because the ultrasound is retarded in traversing weak inter-particle links. Between 500°C and 700°C, stage I sintering probably occurs, improving inter-particle bonding and causing the ultrasonic velocity to rise by more than about 50%. Between 600°C and 900°C, the ultrasonic velocity decreases slightly due to a softening of the elastic constants of iron [16]. During the 0.5 hour holding time at 1200°C, the increase with time in ultrasonic velocity is consistent with the compact densification associated to stage II sintering.

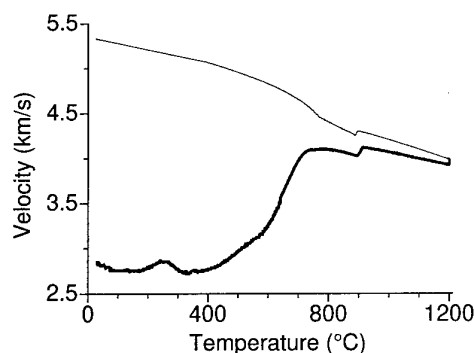


Figure 9 Ultrasonic velocity measured in a green iron compact during a thermal cycle in an argon atmosphere. The compact was heated at 10°C/min. (thick line), maintained at 1200 °C for 0.5 hours (dots), and then cooled at 10°C/min. (thin line).

The  $\alpha \rightarrow \gamma$  transition is clearly evident as a discontinuity in velocity which occurs at  $910 \pm 5^\circ\text{C}$ , in good agreement with  $T(\alpha \rightarrow \gamma) = 912^\circ\text{C}$  [38]. The observed discontinuity must result from a real change in the ultrasonic velocity at the transition temperature, since it cannot be accounted for by the negligible ( $\sim 0.15\%$ ) associated shrinkage, as measured by dilatometry. Another feature that occurs during cooling is the abrupt change of slope that occurs at  $770 \pm 5^\circ\text{C}$ , in good agreement with the Curie temperature of  $770^\circ\text{C}$  [16], where the ferromagnetic to paramagnetic transition occurs in ferritic iron. Inverted cusp-like

discontinuities were reported [16,39] in the temperature dependence of the ultrasonic velocity during the slow heating of iron, as it passes through the Curie temperature.

Figure 10 shows the time evolution of the ultrasonic velocity during the 0.5 hour holding time at 1200°C. A simple exponential was fitted to the data and yield time constants of approximately 20 min. This plot is interesting because it might directly be used to determine necessary holding times at the maximum temperature during sintering.

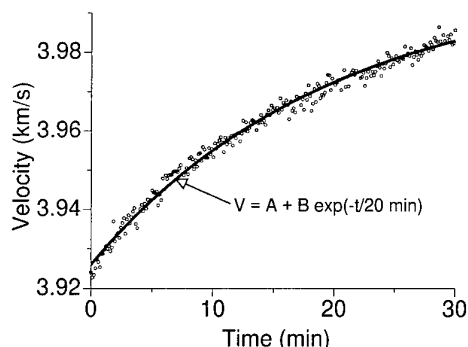


Figure 10 Ultrasonic velocity as a function of time measured in a green iron compact while the temperature was maintained at 1200 °C for 0.5 hours. The solid line is an exponential fitted to the data.

## 5. CONCLUSION

A new technique to monitor microstructure in real-time during high temperature processing of iron and steel was presented. This technique, based on the generation and detection of ultrasound using lasers and called laser-ultrasonics, was used to monitor three different processes: austenite grain growth and phase transformations in steels, and sintering of a green PM iron compact.

The measurements presented showed that this new technique provided the austenite grain growth kinetics at a given austenitization temperature in a single experiment with a time resolution far superior to the resolution obtained using lengthy conventional metallographic techniques. During phase transformations, ultrasonic attenuation allows real-time evaluation of microstructure that otherwise would have required laborious manipulations. Finally, ultrasonic velocity was shown to provide information about inter-particle bonding and densification during the sintering of a green PM iron compact.

In the near future, laser-ultrasonics will greatly facilitate laboratory studies on high temperature microstructure. In a more distant future, laser-ultrasonics may also be used in industrial processes for real-time feedback control.

## 6. ACKNOWLEDGMENTS

The financial support received from the American Iron and Steel Institute (AISI) and from the United States Department of Energy (DOE) for part of this work is gratefully acknowledged.

## 7. REFERENCES

- [1] K. Goebbels, *Materials Characterization for Process Control and Product Conformity*, CRC Press, Boca Raton (1994).
- [2] C. B. Scruby and L. E. Drain, *Laser-Ultrasonics: Techniques and Applications*, Adam Hilger, Bristol, (1990).
- [3] J.-P. Monchalain, C. Néron, J.F. Bussière, P. Bouchard, C. Padioleau, M. Choquet, J.D. Aussel, C. Carnois, P. Roy, and G. Durou, "Laser-Ultrasonic: from the Laboratory to the Shop Floor", *Physics in Canada*, vol. 51, pp. 122-130 (1995).
- [4] C.B. Scruby and B.C. Moss, "Non-Contact Ultrasonic Measurements on Steel at Elevated Temperatures", *NDT & E International*, vol. 26, no. 4, pp. 177-189 (1993).
- [5] M. Dubois, A. Moreau, M. Militzer, and J.F. Bussière, "Laser-Ultrasonic Monitoring of Phase Transformations in Steels", submitted to *Scripta Mater.* (1998).
- [6] O.N. Senkov, M. Dubois, and J.J. Jonas, "Elastic Modulus of Titanium-Hydrogen Alloys in the Temperature Range 20°C to 1100°C", *Metall. Mater. Trans. A*, 27A, pp. 3963-3970 (1996).
- [7] E. P. Papadakis, L. C. Lynnworth, K. A. Fowler, and E. H. Carnevale, "Ultrasonic Attenuation and Velocity in Hot Specimens by the Momentary Contact Method with Pressure Coupling, and some Result on Steel to 1200°C", *J. Acoust. Soc. Am.*, vol. 52, no. 3, pp. 850-857 (1972).
- [8] D. M. Boyd and P.D. Sperline, "Noncontact Temperature Measurements of Hot Steel Bodies using an Electromagnetic Acoustic Transducer [EMAT]", in *Review of Progress in Q.N.D.E* vol. 7, pp.1669-1676, Plenum Press, D.O. Thompson and D.E. Chimenti, ed., New-York (1988).
- [9] S.S. Lee and B.Y. Ahn, "EMAT Application at High Temperature", *Nondestr. Test. Eval.*, vol. 7, pp. 253-261 (1992).
- [10] P. Komarenko, R.W. Messler, Jr., H. A. Scarton, "Ultrasonic in situ monitoring of sintering in alumina", *International Journal of Powder Metallurgy*, Vol. 30, 1994, pp. 67-76.
- [11] R.W. Messler, Jr. and P. Komarenko, "In situ monitoring of ceramic structures", *Advances in Powder Metallurgy*, Vol. 2, 1994, pp. 127-139.
- [12] A. Moreau and J. T. Jones, "Laser-ultrasonics Assess High-Temperature Elastic Properties", *Ceramic Industry*, vol. 144, no. 3, pp.45-46 (1995).
- [13] K.L. Telschow, J.B. Walter and G.V. Garcia, "Laser ultrasonic monitoring of ceramic sintering", *Journal of Applied Physics*, Vol. 68, 1990, pp. 6077-6082.
- [14] S. Serabian and R. S. Williams, "Experimental Determination of Ultrasonic Attenuation Characteristics Using the Roney Generalized Theory", *Mater. Eval.*, vol. 36, no. 8, pp. 55-62 (1978).
- [15] B.A. Auld, *Acoustic Fields and Waves in Solids, Volume I, 2nd edition*, R.E. Krieger Publishing Company, Malabar, Florida, (1990).
- [16] D.J. Dever, "Temperature Dependence of the Elastic Constants in alpha-Iron Single Crystals: Relationship to Spin Order and Diffusion Anomalies", *J. Appl. Phys.*, vol. 43, no. 8 pp. 3293-3301 (1972).
- [17] J. Zarestky and C. Stassis, "Lattice Dynamics of gamma-Fe", *Phys. Rev. B*, vol. 35, no. 9, pp. 4500-4502 (1987).



- [18] E. P. Papadakis, "Revised Grain-Scattering Formulas and Tables", *J. Acoust. Soc. Am.*, vol. 37, no. 4 pp. 703-710 (1965).
- [19] M. Fukuhara and A. Sampei, "Elastic Moduli and Internal Friction of Low Carbon and Stainless Steels as a Function of Temperature", *ISIJ Int.*, vol. 33, no. 4, pp. 508-512 (1993).
- [20] J.-P. Monchalán, R. Héon, P. Bouchard, and C. Padioleau, "Broadband Optical Detection of Ultrasound by Optical Sideband Stripping with a Confocal Fabry-Perot", *Appl. Phys. Lett.*, vol. 55, no. 16, pp. 1612-1614 (1989).
- [21] J.-D. Aussel and J.-P. Monchalán, "Precision Laser-Ultrasonic Velocity Measurement and Elastic Constant Evaluation", *Ultrasonics*, Vol. 27, 1989, pp. 165-177.
- [22] R. Truell, C. Elbaum, and B.B. Chick, *Ultrasonic Methods in Solid State Physics*, Academic Press, New-York (1967).
- [23] G.S. Kino, *Acoustic Waves: Devices, Imaging, and Analog Signal Processing*, Prentice-Hall, Englewood Cliffs (1987).
- [24] Atomet 1001HP high purity, water-atomized iron powder, granulometric distribution inferior to 250  $\mu\text{m}$ , Available from Québec Metal Powders Limited.
- [25] T. Gladman and F.B. Pickering, "Grain-Coarsening of Austenite", *J. Iron Steel Inst.*, vol. 205, pp. 653-664 (1967).
- [26] F. G. Wilson and T. Gladman, "Aluminium Nitride in Steel", *Int. Mat. Rev.*, vol. 33, no. 5, pp. 221-286 (1988).
- [27] R.W.K. Honeycombe, *Steels, Microstructure and Properties*, Edward Arnold, London, (1981).
- [28] R.H. Goodenow, and R.F. Hehemann, "Transformations in Iron and Fe-9 Pct Ni Alloys", *Trans. AIME*, vol. 233, pp. 1777-1786 (1965).
- [29] G.H. Akbari, C.M. Sellars, and J.A. Whiteman, "Austenite and Ferrite Grain Sizes in Interstitial Free Steel", *J. Mater. Sci. Technol.*, vol. 11, pp. 1261-1265 (1995).
- [30] Private communication between Marc Dubois and J.A. Whiteman from the department of Engineering Materials, University of Sheffield.
- [31] M. Militzer, A. Giumelli, E.B. Hawbolt, and T.R. Meadowcroft, Austenite Grain Growth Kinetics in Al-Killed Plain Carbon Steels, *Metall. Mater. Trans.*, vol. 27A, pp. 3399-3409 (1996).
- [32] P. Cotterill and P.R. Mould, *Recrystallization and Grain Growth in Metals*, p. 300, John Wiley and Sons, New-York, (1976).
- [33] A. Salak., *Ferrous Powder Metallurgy*, Cambridge International Science Publishing, Cambridge, UK, 1995, pp. 105-146.
- [34] R. M German, *Powder Metallurgy Science* (second edition), Metal Powder Industries Federation, Princeton, NJ, 1994.
- [35] A. LeR. Dawson, S. Pelletier and J. Bussière, "Ultrasonic Evaluation of Iron Powder during Compaction", *Advances in Powder Metallurgy*, Vol. 2, 1996, pp. 7-303 - 7-313.
- [36] A.L. Dawson and J. Bussière, "Ultrasonic Characterization of Iron Powder Metallurgy Compacts during and after Compaction", *Advanced Performance Materials*, vol. 5, 1997, pp. 97-115.
- [37] A.L. Dawson, L. Piché and A. Hamel, "On-line Ultrasonic Monitoring of Iron Powder during Compaction", *Powder Metallurgy*, Vol. 39, 1996, pp. 275-280.
- [38] TAPP 2.0 - *A database of Thermochemical And Physical Properties*. available from E. S. Microware: Hamilton, OH; 1993.
- [39] C.W. Garland, "Ultrasonic Investigation of Phase Transition and Critical Points", *Physical Acoustics*, Vol. 7, edited by W. P. Mason and R. N. Thurston, Academic Press, New York, 1970, pp. 51-148.

# Modelling of Ti alloy Melting by EBCHM: Impact of Process Parameters for Hard-alpha Dissolution

J.P. Bellot\*, A. Jardy\*, S. Bourguignon\*\*, D. Ablitzer\*

\* Laboratoire de Science et Génie des Matériaux Métalliques (UMR CNRS 7584)  
INPL, Ecole des Mines de Nancy, 54042 Nancy Cedex France

\*\* SNECMA, Département Matériaux et Procédés  
77550 Moissy-Cramayel France

## SUMMARY

The random occurrence of the hard-alpha defect in rotating part used for aero-engines has been one of the main materials problems in the manufacture of quality titanium alloys for some time. The Electron Beam Cold Hearth Melting (EBCHM) process has shown a great promise in being able to refine Ti alloys and to eliminate hard-alpha inclusions by dissolution or settling. A research programme has been launched, with the aim of specifying the remelting process parameters required for the elimination of the defect.

Hence the mathematical model of the refining step of the EBCHR process has been developed at the Nancy School of Mines. The model allows calculation of the maps of the velocity, turbulence intensity, temperature and chemical composition in the cold hearth.

An experimental and theoretical studies of the hard-alpha defect behaviour in liquid titanium have been carried out. The experimental part of the work consists in immersing of synthetic defect into a titanium liquid bath for a known length of time and analysing it by microprobe after the experiment. In parallel, a kinetic model of dissolution, which computes the transient diffusion of the interstitial solute with alpha and beta intermediate phases, has been developed.

In order to predict the potential removal of this kind of defect during the remelting operation, the calculation of the particle trajectory and the kinetic model of dissolution have been coupled. It allows the simulation of the history of the defect in terms of positions and shrinkage or growth of the particle in the metal liquid bath. Results for different process parameters are presented and discussed.

## INTRODUCTION

The low density inclusions known as hard-alpha particles remain major potential defects for the use of titanium alloys. These exogenous inclusions can have a wide variety of origins [1]. They contain high concentrations of interstitial elements (principally N, but also O and C), locally stabilizing the alpha phase and markedly increasing the melting point, so that the particle remains solid during the melting process, while the associated increase in hardness can promote fracture initiation in the metal. Moreover, the coherency between the enriched region and the surrounding matrix makes the defect difficult to detect by non-destructive inspection techniques, even after deformation. Indeed, a number of failures of rotating turbine components have been attributed to hard alpha defects. The density of these interstitial-rich inclusions varies with composition, but remains close to that of the alloy matrix. Thus, based on its theoretical density, a TiN particle should sink in a bath of liquid titanium, whereas an inclusion of stabilized alpha phase should float. However, the density may differ from the theoretical value due to microporosity, which is observed in certain types of hard alpha particles.

In recent years, the Electron Beam Cold Hearth Refining (EBCHR) process has emerged as either an alternative or a complement to vacuum arc remelting, since it is capable of enhancing the elimination of hard alpha inclusions by dissolution or sedimentation. In this technique, the purification and solidification stages are clearly separated, as shown schematically in figure 1. A first electron gun melts the charge, which can have a variety of forms (ingot, sponge or recycled scrap), and the molten metal flows into a shallow water-cooled crucible, where one or more further electron guns maintain the temperature of the liquid metal. At the other end of the hearth, the metal flows over the outlet lip into a water-cooled copper mold to form the secondary ingot. One of the major functions of the cold hearth furnace is to separate inclusions heavier than the liquid by sedimentation, while at the same time increasing the high temperature residence time of lower density particles in order to ensure their complete dissolution.

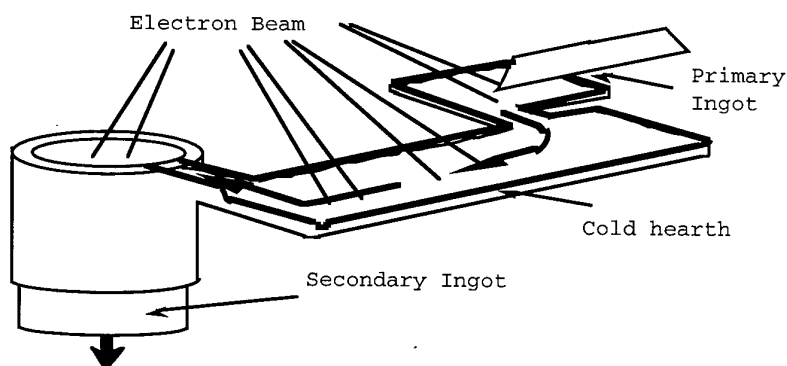


Figure 1 - Schematic representation of the E.B.C.H.R. process

The growing industrial interest in the electron beam melting and refining processes is illustrated by an abundant literature and by the annual "State of the Art" conference devoted to this technique [2], now entering its second decade. However, in spite of its importance, mathematical modeling is a means of investigation which has so far been little employed in this field of application. Tripp and Mitchell [3] evaluated the depth of liquid metal in the hearth using a 3-dimensional thermal model, while in the United States, Shyy and Pang [4] developed a numerical simulation of the thermohydrodynamic behavior of a secondary ingot produced by EB remelting. A finite element model describing the curved interfaces between the solid, liquid and vapor phases has been employed to study the volatilization of aluminium during the melting of a titanium alloy in an axisymmetrical crucible [5].

Several experimental studies [6-8] have been devoted to the mechanisms of the dissolution of hard-alpha particles in liquid titanium. They have all emphasized the complexity of the dissolution process, which is controlled by the diffusion of nitrogen into the liquid, and in certain cases, by the diffusion of alloying elements from the melt to the particle. Dissolution rates have been proposed, based on experimental results obtained by dissolving nitrided particles of either dense titanium [6] or titanium sponge [7]. Unfortunately, these kinetics consider neither the size, the geometry, nor the initial concentration of interstitial elements, and are thus difficult to apply. Jarret [8] appears to be the only author to have published a theoretical analysis in which the rate of dissolution of a hard-alpha particle is associated with its trajectory in a cold hearth furnace. Although the representation of the metal flow in the crucible and the dissolution law employed were considerably simplified compared to the complexity of the real situation, this work clearly reveals the interest of this type of approach for determining the furnace dimensions necessary to ensure the complete elimination of defects.

The aim of the present study was to combine models developed by the authors for both the EBCHR process and hard-alpha particle dissolution [9,10] in order to predict the history of a defect in the cold hearth furnace, in terms of its position, size and composition.

#### NUMERICAL SIMULATION OF THE EBCHR PROCESS

##### Descriptive model

In order to represent the thermophysical mechanisms as precisely as possible, a complete descriptive model was established, taking into account all the different phenomena involving momentum, heat and solute transport, together with their interactions. The model respects the geometry of the corresponding process step, with a three-dimensional representation. The model assumes that the scanning frequency of the electron beam(s) is sufficiently high to maintain a steady state regime [11,12].

Particular attention has been paid to the representation of the complex mechanisms that occur at the surface of the liquid metal, and which are specific to the electron beam process. The model thus describes the distribution of heat energy at the beam impingement point, together with the scanning pattern of the beam or beams over the liquid surface. Evaporation fluxes are calculated for the base metal atoms and particularly for those of volatile solute elements, using Langmuir's law, whose validity under typical process conditions was verified both experimentally [13] and theoretically [14]. The model takes into account thermocapillary (Marangoni) convection induced by the steep temperature gradients at the beam impact point, together with the resulting turbulent flow and its effects on the different transport phenomena.

The cold hearth model calculates the thickness of the solidified skull, in which only diffusional transport phenomena are considered.

## Transport equations

In order to take into account the effect of turbulence on the overall transport processes, Boussinesq's turbulent diffusivity concept was applied to the three transport equations (Eqs. 1 to 3). These equations assume the thermophysical properties ( $\rho$ ,  $\lambda$ ,  $\mu$  and  $C_p$ ) to be independent of temperature, except for the gravitational source term in the Navier-Stokes equation, which describes the effects of thermal and solute-induced convection forces.

$$\rho (\mathbf{v} \cdot \nabla) \mathbf{v} = \nabla((\mu + \mu_t) \nabla \cdot \mathbf{v}) - \nabla P + \rho \mathbf{g} - \frac{\mu}{K} \mathbf{v} \quad (1)$$

$$\rho C_p \mathbf{v} \cdot \nabla T = \nabla((\lambda + \lambda_t) \nabla T) \quad (2)$$

$$\mathbf{v} \cdot \nabla \omega_i = \nabla((D + D_t) \nabla \omega_i) \quad (3)$$

The zero velocity value in the solid and the specific flow conditions in the interdendritic regions are modeled by adding a source term in equation (1). The permeability  $K$  is calculated using the Kozeny-Carman law:

$$K = K_0 \frac{g_1^3}{(1 - g_1)^2} \quad (4)$$

In equation (4),  $g_1$  represents the fraction of liquid

$$g_1 = \frac{T - T_{sol}}{T_{liq} - T_{sol}} \quad (5)$$

so that  $0 < g_1 < 1$  if  $T_{sol} < T < T_{liq}$

The variation of density with temperature and chemical composition are taken into account only in the gravitational force term in equation (1), by introducing thermal expansion coefficients  $\beta_T$  and  $\beta_C$ :

$$\beta_T = - \frac{1}{\rho} \left( \frac{\partial \rho}{\partial T} \right)_{P, \omega_i} \quad (6)$$

$$\beta_C = - \frac{1}{\rho} \left( \frac{\partial \rho}{\partial \omega_i} \right)_{P, T} \quad (7)$$

In order to reduce the computing time for the 3D simulation, an algebraic model for the mixing length was preferred to the  $k$ - $\epsilon$  model. Indeed, the turbulent viscosity depends directly on the local mean velocity gradients in the liquid metal and on a mixing length  $l_m$ :

$$\mu_t = \rho l_m^2 \sqrt{\frac{\partial v_i}{\partial x_i} \left( \frac{\partial v_i}{\partial x_j} + \frac{\partial v_j}{\partial x_i} \right)} \quad (8)$$

where  $i$  and  $j$  are the indices of the spatial coordinates. In practice, the mixing length was taken to be equal to 10% of the depth of molten metal. The turbulent conductivity  $\lambda_t$  and turbulent solute diffusivity  $D_t$  which appear in Equations 2 and 3 are determined from  $\mu_t$  as follows:

$$\frac{C_p \mu_t}{\lambda_t} = 1 \quad \text{and} \quad \frac{\mu_t}{\rho D_t} = 1 \quad (9)$$

## Conditions at the walls

The heat flux density corresponding to contact and radiation losses at the crucible walls is expressed as a heat transfer coefficient,  $h$  (losses by radiation occur across the gap caused by solidification shrinkage).

## Conditions at the bath surface

A precise description of the power distribution beneath the beam and its movement over the bath surface is incorporated in the model. At its point of impact with the bath, the beam energy is assumed to have a Gaussian distribution [15,16], while the beam can describe a circular or linear scanning pattern, repeated at different points on the bath surface. The metal surface radiates heat to the furnace walls, at a flux density given by:

$$\Phi_r = \sigma' \epsilon_r (T_{metal}^4 - T_{wall}^4) \quad (10)$$

The volatilization flux density for species  $i$  is given by Langmuir's law:

$$\Phi_{v,i} = \frac{a_i P_i^0(T)}{\sqrt{2\pi M_i R T}} \quad (11)$$

while the saturating vapor pressure  $P_i^0$  for each metal species is given as a function of temperature by Dupré's law.

Local surface tension gradients in the bath give rise to shear stresses (Marangoni effect):

$$\tau = \mu \frac{\partial v_i}{\partial x_j} = \frac{\partial \sigma_s}{\partial x_i} \quad (12)$$

The derivative of  $\sigma_s$  with respect to  $x_i$  is separated into  $(\partial \sigma_s / \partial T)$ , which is a thermodynamic parameter, and  $(\partial T / \partial x_i)$ , which can be calculated:

$$\tau = \left( \frac{\partial \sigma_s}{\partial T} \right) \left( \frac{\partial T}{\partial x_i} \right) \quad (13)$$

### Numerical solution and results

The Phoenix commercial finite volume calculation code was used to solve the transport equations (Eqs. 1, 2 and 3) in the steady state regime, based on a three-dimensional cartesian geometry. The Navier-Stokes equations were solved using the SIMPLEST algorithm. Numerous modules were added to the code in order to adapt it to the case considered (boundary conditions, solidification, etc.). For the example treated below (80 000 cells), the computing time required was about two days on 100 Mflop HP K260 computer.

The model calculates the distributions of velocity, temperature and solute content in the hearth furnace.

### NUMERICAL SIMULATION OF THE DISSOLUTION OF A HARD-ALPHA TYPE INCLUSION

#### Dissolution mechanism

Consider a nitrogen-enriched titanium particle immersed in a bath of liquid titanium. It is subjected to the transfer of both heat and matter. Comparison of the Fourier numbers for heat and matter indicates that heat transfer is much more rapid than the transport of nitrogen inside the particle:

$$\frac{Fo_T}{Fo_M} = \frac{\alpha}{D_N} > 10^3 \quad (\text{at the liquidus temperature})$$

where  $\alpha$  is the thermal diffusion coefficient and  $D_N$  is the coefficient of diffusion of nitrogen in titanium.

Dissolution of the hard-alpha defect is thus controlled by nitrogen diffusion. Dissolution experiments on nitrided titanium particles in a bath of liquid titanium [10] have shown that the nitrogen diffusion process, which is of the interstitial type, is governed by the Ti-N phase diagram [17]. The transfer of nitrogen from the solid to the liquid causes the formation of a peripheral solid layer of beta phase, whose thickness varies, depending on the intensity of the liquid metal flow around the particle. For low liquid flowrates, where the convective transport of matter is limited, initial growth of the particle can thus be observed.

#### The principal assumptions

Both the particle considered and the surrounding liquid are assumed to have compositions in the binary Ti-N system. The hard-alpha defect is assumed to be 100% dense, with spherical symmetry, and enriched solely in nitrogen. The temperature is considered to be uniform throughout the particle and thermodynamic equilibrium is

assumed to be maintained at all times at the phase interfaces.

#### Equations solved - initial and boundary conditions

The equation given below for the diffusive transport of nitrogen is solved in each of the phases which compose the hard-alpha defect (figure 2) :

$$\frac{\partial \rho_N}{\partial t} = \frac{1}{r^2} \frac{\partial}{\partial r} \left( r^2 F D_{N,i} \frac{\partial \rho_N}{\partial r} \right) \quad (14)$$

where  $i$  is the phase concerned ( $\alpha$ ,  $\beta$  or liquid) and  $\rho_N$  is the weight concentration of nitrogen.

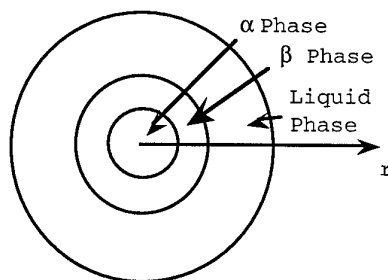


Figure 2 - Schematic representation of a hard-alpha defect in the model

The contribution of convective transport in the liquid phase is accounted for via a multiplying factor  $F$  associated with the diffusion coefficient.  $F$  is equal to 1 in the solid. The positions of the solid/solid and solid/liquid interfaces are calculated from the requirement of conservation of matter at the interfaces :

$$(\phi_1 - \phi_2).dt.S = \Delta V(\rho_{N,1} - \rho_{N,2}) \quad (15)$$

Where  $\phi_1$  and  $\phi_2$  are the flux densities at the interface between phases 1 and 2 (e.g.  $\alpha$  and  $\beta$  phases),  $dt$  is the time during which the interface exchanges take place,  $\Delta V$  is the difference in volume between phases 1 and 2, and  $\rho_{N,1}$  and  $\rho_{N,2}$  are the nitrogen concentrations on either side of the interface.

Since the system is closed, the boundary conditions at the extremity of the liquid phase surrounding the particle and at the center of the particle correspond to zero matter flux. At the solid/solid and solid/liquid interfaces, the coexistence of two phases imposes zero variance (i.e. a binary system at fixed temperature and pressure). Consequently, the compositions at these points are imposed and are determined by the Ti-N equilibrium diagram.

The initial composition profiles within the particle and the liquid are defined in an input data file.

### Numerical solution

The calculation is broken down into two stages. In the first step, the matter transport equation is solved for each region of the system (solid and liquid phases) by the finite volume method. The concentration values are obtained at all points in each phase, in a manner which is completely independent of the neighboring phases. In the second step, the interaction between the different phases is taken into account via the conservation of matter at the interfaces. For each instant in time, the nitrogen content at any point of the system and the respective proportions of the different constitutive phases are thus determined. The specific mass of the particle, which is assumed to be fully dense, can be obtained from those of the separate phases together with their corresponding volumes.

### CALCULATION OF THE PARTICLE TRAJECTORY

A spherical particle in a moving fluid is subjected to 3 forces (figure 3) :

- the weight of the particle :  
 $P = \rho_p V_p g$
- the buoyancy force :  
 $A = -\rho_f V_p g$
- the resultant  $F$  of the actions of the fluid on the sphere, which can be broken down into:
  - the drag force :  
 $T = -\frac{\pi}{2} R_p \rho_f u C_x u$
  - the inertial force :  
 $I = -\frac{1}{2} V_p \rho_f \frac{du}{dt}$

Where  $V_p$  is the particle volume,  $\rho_f$  and  $\rho_p$  are the fluid and particle densities,  $C_x$  is the drag coefficient,  $u$  is the relative velocity of the particle ( $V$  is the fluid velocity) and  $R_p$  is the particle radius.

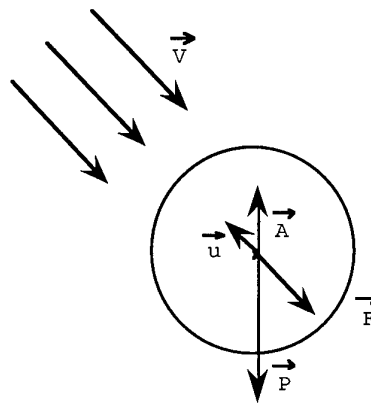


Figure 3 - Forces exerted on a particle placed in a flowing liquid.

The fundamental dynamics equation is solved with the aid of an explicit temporal representation :

$$m\dot{V} = P + A + T + I \quad (16)$$

Knowing the velocity at all points, by successively integrating the acceleration, it is possible to obtain the relative and absolute velocities, together with the position of the particle as a function of time.

### COMBINATION OF THE PARTICLE TRAJECTORY CALCULATION WITH THE DISSOLUTION MODEL

The hard-alpha particle dissolution model and the trajectory calculation have been coupled in order to predict the history of a defect in the cold hearth furnace. To do this, it is also necessary to use the results of the simulation of the temperature and fluid velocity distributions in the EBCHR furnace.

At a given instant, and for a given position of the defect in the furnace, knowledge of the local temperature and liquid metal velocity enables the nitrogen diffusion coefficients to be determined in the solid and liquid phases. In a first step, the dissolution model provides the composition profile, together with the size and the density of the defect. This data is used in a second step to calculate the particle trajectory, giving its new position. The two steps are then repeated for each time increment. The calculation stops when the particle comes in contact with the solid skull at the bottom or sides of the crucible, when it leaves the furnace over the exit lip, or when it disappears due to total dissolution.

When the particle reaches the surface of the liquid bath, its vertical coordinate is held constant, while the calculation of its position in the two other directions continues.

### IMPACT OF PROCESS PARAMETERS

In order to show the interest of the numerical tool developed, a theoretical melting run has been simulated using the operating conditions given in table 1.

Metal remelted	Ti CP
Melt rate (kg/hr)	310
Superheat at the cold hearth inlet (°C)	150
Length and width of the cold hearth (m)	1.0 0.4
Height of the skull (m)	0.08
Heat input at the surface of the cold hearth (kW)	225
Type of pattern of the beam scanning	line

Table 1 : Operating conditions

The model calculates the distribution of velocity and temperature in the hearth furnace. The shape of the skull, obtained by plotting the liquidus isotherm, is illustrated in figure 4. The metal flow is reduced to a thin film of liquid, representing on average only 20% (1.5 cm) of the total depth of metal in the crucible (8 cm). In these conditions, where the heat flux is uniformly distributed over the surface, the thickness of the liquid film is relatively homogeneous. The surface flowrates are of the order of 2-3 cm/s at the outlet, whereas over the majority of the crucible they are on average from 1 to 2 cm/s. Due to natural convection and the Marangoni effect, the temperature gradients at the walls lead to multiple recirculation currents, which are superimposed on the overall metal flow between the inlet and outlet channels. These recirculation currents ensure good temperature uniformity at the bath surface. The maximum temperature attained is 1855°C.

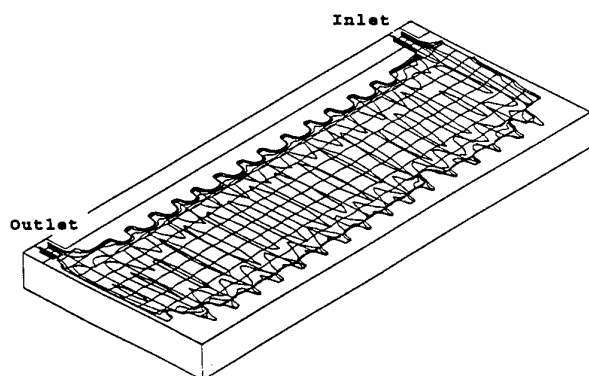


Figure 4: shape of the skull (liquidus isotherms)

The trajectory of a hard-alpha type defect has been simulated for a particle introduced

near the inlet of a cold hearth furnace. The influence of its size and density on its trajectory have been studied.

Initial particle sizes of 1000, 500 and 200  $\mu\text{m}$  have been treated. Their densities were fixed at a constant initial value. Their initial velocities and accelerations were assumed to be zero. The initial composition of the alpha-phase defect was taken to be uniform and equal to 7.5 weight % nitrogen.

Whatever the particle radius, when the imposed density is greater than that of the liquid, it sinks almost instantaneously and joins the metal solidified at the bottom of the crucible. When the imposed particle density is lower than that of the liquid, the defect rises to the surface and is entrained by the surface flow towards the crucible wall, where it is trapped by the solid metal. The initial radius has little effect in these cases.

The behavior of a defect with a density close to that of the liquid has also been examined. In these conditions, the defect trajectory follows a stream line of the fluid flow. Defects with radii of 1000 and 500  $\mu\text{m}$  cross the furnace and flow out over the exit lip without being fully dissolved. Only the 200  $\mu\text{m}$  radius defect is completely eliminated by dissolution (figure 5). Because of the marked fluid flow around the particle throughout its trajectory, the surface layer of beta phase is little developed.

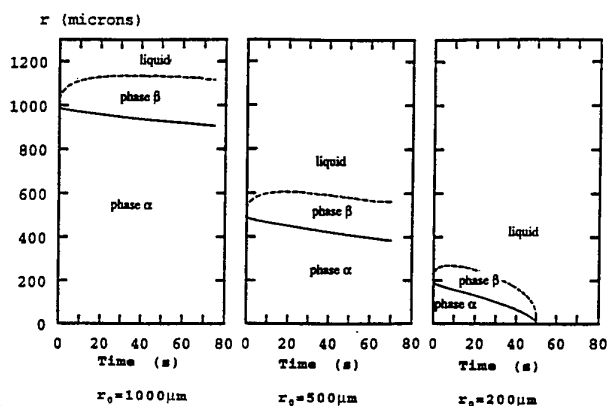


Figure 5 - Evolution of the size of the three defects during the dissolution process

We have simulated the trajectories of these defects for a casting rate of 500 kg/h. The figure 6 reports the trajectories of particles (with a neutral density of 4065  $\text{kg/m}^3$ ) for three initial sizes and for the two different casting rates. The increase of the casting rate reduces the residence time of the particle within the hearth furnace and allows the survival of a 200  $\mu\text{m}$  radius particle.

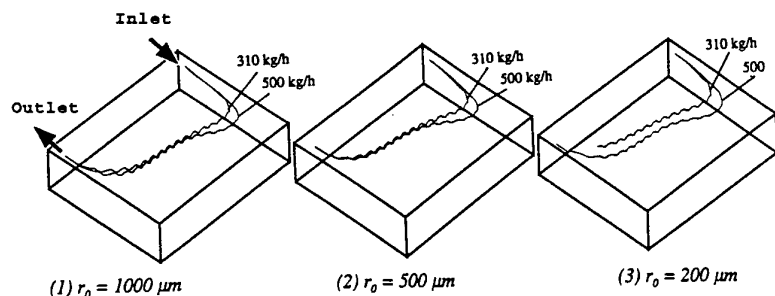


Figure 6: Trajectories of particles with a neutral density of  $4065 \text{ kg/m}^3$

As a result of this analysis, a survival/removal map has been plotted (figure 7) which provides the basic framework for understanding defect removal in the cold hearth.

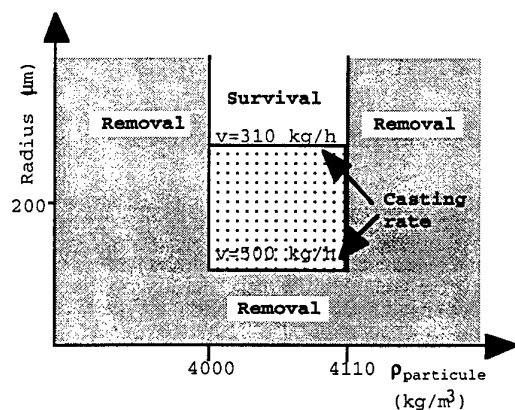


Figure 7: A survival/removal map of the hard-alpha defects

Combining the different mechanisms we have plotted the boundaries predicted for dissolution, sedimentation or flotation as a function of particle size and relative density.

#### ACKNOWLEDGMENTS

The authors are grateful to Prof. Alec Mitchell for the dissolution experiments carried out at the University of British Columbia (Canada).

#### References

1. C.E. Shamblen, Technical Information Series Report R89AERB141, General Electric Aircraft Engines, Cincinnati, Ohio, Jan 31 1989.
2. R. Bakish, "The state of the art in electron beam melting and refining", Journal of Metals, (1991), vol. 43, pp. 42-44.
3. D.W. Tripp, A. Mitchell, M. Hayden, "The effect of power on the thermal regime in an EB hearth". Proc. Conf. on Electron Beam Melting and Refining - State of the art 1986, RENO (USA), edited by R. Bakish, pp. 30-44.

The variation of the melting rate is also taken into account, and hence larger particles require a longer residence time in the bath.

#### CONCLUSION

A dissolution model has been developed based on solution of the matter transport equations in the transient regime, for particles with binary compositions.

The proportion of the different phases composing the particle have been calculated, together with the solute distribution both within them and in the surrounding liquid. Results have been presented for the dissolution of nitrogen-enriched 100% dense titanium particles immersed in liquid titanium.

The trajectory of a spherical particle in a moving fluid has been calculated by solving the fundamental dynamics equation.

The combination of these two models provides all the information necessary to determine the trajectory of a dense hard-alpha type particle dissolving in a bath of liquid metal.

This technique has been applied to the refining crucible of the EBCHR furnace, for which a numerical model was already available. The principal results indicate that particles whose density is very different from that of the liquid either settle rapidly to the bottom of the furnace or rise to the surface where they are transported to the solidified skull on the crucible walls. Particles of which the relative density in relation to the liquid is less than 3 % follow a stream line of the fluid flow. The study of the impact of process parameters (such as the casting rate) provides a survival/removal map which gives the basic framework for understanding defect removal in the cold hearth.



4. W. Shyy, Y. Pang "Modeling of turbulent transport and solidification during continuous ingot casting", Int. J. Heat Mass transfer, Pergamon Press, (1992), vol. 35, pp. 1229-1245. 11
5. K.W. Westerberg, M.A. McClelland, B. Finlayson, "Numerical simulation of material and energy flow in an E-Beam Melt Furnace", Proc. Conf. on Electron Beam Melting and Refining - State of the art 1993, RENO (USA), edited by R. Bakish, pp. 153-166. 12
6. A. Guillou, J.P. Bars, E. Etchessahar, J. Debuigue, D. Charquet, "Dissolution du nitrure de titane dans le titane liquide et dans le TA6V", The Sixth Conf. on Titanium, Cannes (France) 1988, pp.697-699 13
7. J.L. Henry, S.D. Hill, J.L. Schaller, T.T. Campbell, "Nitride Inclusions in Titanium Ingots", Met. Trans., 4 (1973), pp.1859-1864 14
8. R.N. Jarret, "Removal of Defects from Titanium Alloys with E.B.C.H.R. " Proc. Conf. on Electron Beam Melting and Refining - State of the art 1986, RENO (USA), edited by R. Bakish, pp. 332-346. 15
9. J.P. Bellot, E. Floris, A. Jardy, D. Ablitzer, "Numerical Simulation of the E.B.C.H.R. Process", Proc. Conf. on Electron Beam Melting and Refining - State of the art 1993, RENO (USA), edited by R. Bakish, pp. 139-152. 16
10. J.P. Bellot, A. Mitchell, "Hard-alpha particle behaviour in a titanium alloy liquid pool", Proc. Conf TMS, San Francisco (USA) 1994, pp. 1187-1193 17
- H. Nakamura, A. Mitchell, "The effect of beam oscillation rate on Al evaporation from a Ti-6Al-4V alloy in the E.B. melting process", ISIJ Int., Vol. 32, 1992, pp. 583-592.
- D. Tripp, A. Mitchell, M. Hayden, "The effect of power on the thermal regime in an EB hearth", Proc. Conf. on Electron Beam Melting and Refining - State of the art 1993, RENO (USA), (1993), edited by R. Bakish, pp.30-44.
- M. Ritchie, A. Mitchell, "The effect of pressure on evaporation during EB melting", Proc. Conf. on Electron Beam Melting and Refining - State of the art 1996, RENO (USA), (1996), edited by R. Bakish, 110-125.
- J.P. Bellot, H. Duval, D. Ablitzer, "Validity of the Kinetic Langmuir's law for the volatilization of metallic elements in vacuum metallurgy", Proc. Symp. of gas interactions in nonferrous metals processing, TMS Annual Meeting, Anaheim (USA), (1996), edited by D.Saha, pp. 109-124.
- J. Goldak, A. Chakravarti, M. Bibby, "A new finite element model for welding heat sources", Met Trans B, Vol 15, (1984), pp. 299-305
- P.S. Wei, Y.T. Chow, "Beam focussing characteristics and alloying element effects on high-intensity electron beam welding", Met. Trans B, Vol 23, (1992), pp.81-90
- T.B. Massalski, J.L. Muray, L.H. Bennet, H. Baker, " Binary Alloy Phase Diagrams", American Society for Metals, Metals Park, Ohio 44073.

## AUTOMATED FABRICATION TECHNOLOGIES FOR HIGH PERFORMANCE POLYMER COMPOSITES

M. J. Stuart, N. J. Johnston, and H. B. Dexter,  
NASA Langley Research Center, Hampton, VA 23681 USA  
and

J. M. Marchello and R. W. Grenoble  
Old Dominion University, Norfolk, VA 23529 USA

**SUMMARY:** New fabrication technologies are being exploited for building high performance graphite-fiber-reinforced composite structure. Stitched fiber preforms and resin film infusion have been successfully demonstrated for large, composite wing structures. Other automate processes being developed include automated placement of tacky, drapable epoxy towpreg, automated heated head placement of consolidated ribbon/tape, and vacuum-assisted resin transfer molding. These methods have the potential to yield low cost, high performance structures by fabricating composite structures to net shape out-of-autoclave.

**KEYWORDS:** automation, powders, ribbon, tape, robot, tow placement, resin transfer molding, resin film infusion

### 1.0 INTRODUCTION

To be economically viable for high performance applications, fiber reinforced polymer composite fabrication must utilize high quality material forms and fully exploit automated processing technology. Selected automated processes employed in the composites industry include the textile processes of weaving and braiding in combination with vacuum assisted resin transfer molding (VARTM) and resin film infusion (RFI) and automated tow/tape placement (ATP).

Stitched preforms combined with VARTM have significant potential for enabling cost effective composite structures. A popular VARTM method is a technique called SCRIMP™ that has gained widespread use for cost-effective fabrication of large thick glass structures such as one-piece boat hulls. In a VARTM method (Ref 1), resin is injected under vacuum directly into a textile preform laid in a mold, namely, a one-sided tool used in conjunction with a flexible bag. The use of preimpregnated fabric or unitape is eliminated thereby eliminating freezer storage of prepreg materials and subsequent shelf life problems. Resin and fiber are used in the lowest cost forms. RFI technology reached its zenith with the development of stitched preforms impregnated with high performance aerospace epoxies such as 3501-6 to make thick wing cover panels which were used to fabricate wing boxes under a contract to The Boeing Company in Huntington Beach, CA (Ref 2). The major elements of this technology will be discussed. Automated cost-effective fabrication of dry stitched preforms will be described in connection with both VARTM and RFI.

The automated placement of composite tow/tape is one of the more promising fabrication methods for rapid, cost effective, net shape composite part manufacture (Ref 3). To apply this technique in various aerospace research programs, NASA Langley Research Center is emphasizing an approach where preconsolidated high temperature, thermoplastic, graphite fiber reinforced ribbon or tape is thermally welded on-the-fly (Ref 4). This approach provides for in-situ consolidation of the part and eliminates the need for laborious debulking and autoclave post-placement processing. Results will be presented for fabrication of preconsolidated composite ribbon and tape and automated fiber placement.

### 2.0 STITCHED PREFORMS AND RESIN TRANSFER MOLDING

#### 2.1 Fabrication of Textile Preforms

High quality fiber preforms are required to produce high quality composite parts using resin transfer molding (RTM) processes. Various types of textile material forms have been used to fabricate near net shape preforms for resin transfer molding of composite aircraft structures (Fig 1). Multiaxial warp knitting is a highly tailorable automated process that produces multidirectional broadgoods for large area coverage. Two-

dimensional and three-dimensional braids are used to create stiffeners, frames and beams with complex cross-sections. Through-the-thickness stitching is an effective way to debulk preforms and to achieve improved out-of-plane strength and damage tolerance of composite structures.

Major advancements have been made in through-the-thickness stitching technology during the past 25 years (Fig 2). Early stitching studies by NASA and McDonnell Douglas (now Boeing) used a limited capacity, extended arm, single needle machine to produce preforms for damage tolerance testing. The next generation stitching machine was computer controlled and utilized quilting technology. This machine was limited in size and stitching speed so NASA and McDonnell Douglas entered into a contractual agreement with Ingersoll Milling Machine Company and Pathe Technologies, Inc., to develop a high speed, multiple head stitching machine capable of stitching large wing skins for commercial aircraft. This second generation machine is shown in Figure 3 and has four stitching heads that can stitch a preform 3.0m by 15.2m by 38.1mm at 800 stitches per minute. The stringer stiffened preform shown on the advanced stitching machine was used to produce a wing cover panel for the NASA Advanced Subsonic Technology Composite Wing Program.

#### 2.2 Vacuum Assisted Resin Transfer Molding (VARTM)

VARTM processes have been used for many years to fabricate fiberglass reinforced composite structures. The U.S. Naval Surface Warfare Center in Bethesda, MD has been the major promoter of this technology for composite marine applications (Ref 5). The major advantages of VARTM processes compared to conventional autoclave processes are the lower cost of tooling, reduced cost of energy to cure composite parts, and almost unlimited part size (i.e., no size constraints based on the size of the autoclave). Until recently, VARTM was primarily used to fabricate glass reinforced polyester and vinyl ester composites. However, due to recent developments in resin and preform technologies, aircraft manufacturers are beginning to show significant interest in VARTM processes for graphite-epoxy and graphite-bismaleimide composite systems. One drawback to VARTM processes has been its low fiber volume fraction compared to the higher fiber volume fractions achievable with autoclave processes. However, stitching and debulking methods have been developed to achieve preforms that are near net shape with little or no further compaction required during processing.

NASA has conducted contractual research with Seemann Composites, Inc. to establish the feasibility of another VARTM process to produce aircraft quality composite structures. A proprietary process, called SCRIMP™ (Seemann Composites Resin Injection Molding Process) utilizes a resin distribution media to achieve full wet-out of the preform (Fig 4). In addition, Seemann has developed a reusable bagging concept that eliminates most of the costs associated with conventional bagging procedures. Seemann Composites has also demonstrated SCRIMP™ for lightly-loaded general aviation aircraft structures. A concept using one-sided tooling and a graphite preform for a small aircraft fuselage section has been demonstrated (Fig 5a, 5b). Current and future tooling developments for integral heating will eliminate the need for oven cure and postcure of composite parts fabricated with VARTM processes.

NASA is also investigating the feasibility of SCRIMP™ to produce aircraft quality heavily-loaded primary structures. Additional technology development is required to achieve dimensional control and acceptable fiber volume fractions for thick structural elements. Innovative tooling concepts will be

required to meet typical assembly tolerances for aircraft structures. Stitching will be required to achieve near net shape for the preform prior to resin injection. The reusable bagging concept for a three stringer panel representative of wing structure is shown in Fig 6. The ease of removing this bag from the stiffened panel is illustrated in Fig 7, and the finished panel (after resin injection and cure) is shown in Fig 8.

### 2.3 Resin Film Infusion (RFI)

RFI is another process being pursued by NASA and The Boeing Company to develop cost-effective wing structures for commercial transport aircraft. The RFI process developed by Boeing (formerly McDonnell Douglas) consists of an outer mold line tool, an epoxy resin film, a near net shape textile preform, an inner mold line tool, and a reusable vacuum bag. Thick film plates of resin (called "resin slabs") are placed on the outer mold line tool, and the preform and inner mold line tools are placed on top of the resin. The entire assembly is covered with a reusable vacuum bag, and the part is placed inside an autoclave. After the resin is melted, vacuum pressure is used to infuse resin into the preform. Once infiltrated, the part is cured under pressure and temperature in the autoclave. The keys to producing aircraft quality parts with the RFI process are understanding the compaction and permeability characteristics of the preform and understanding kinetics and viscosity profiles for the resin as a function of temperature.

The stiffening elements and tooling blocks must be precisely located to achieve the required dimensional tolerances. The advanced stitching machine discussed previously (Fig 3) was used to locate structural details such as ply drops, stiffeners, interleaved spar caps, and rib clips. Fig 9 shows a vacuum bagged wing panel prior to infusion and cure. Fig 10 shows the completed composite panel after cure. It should be noted that the cured composite wing panel has no mechanical fasteners since all the stiffening elements are stitched to the skin.

To eliminate trial and error process development, analytical models are required to predict resin flow into textile preforms. The models must be verified through precise experiments to demonstrate the modeling accuracy. Three-dimensional models are required to capture response adequately for complex preforms such as wing cover panels that contain stitched/knitted fabric skins and stitched/braided stiffeners. The objectives of the analytical model are to predict the resin flow front position, resin viscosity, and degree of resin cure as a function of temperature and time. A 3-D RFI process simulation model is under development by Virginia Polytechnic Institute and State University (Ref 5). The RFI simulation includes resin flow, heat transfer, and thermochemical elements. A schematic of the 3-D finite element model for infusion of a stitched blade stiffener is shown in Fig 11. Experiments are currently being conducted to verify accuracy of the 3-D finite element model. For a two-stringer stitched panel, the predicted temperature distribution was within 6 percent of measured temperature and the predicted resin wet-out times were within 4 to 12 percent of measured times.

### 3.0 AUTOMATED TOW/TAPE PLACEMENT

Materials and processing evaluation activities carried out with a prototype machine at Langley were an integral part of several NASA aerospace research programs involving even larger and more sophisticated proprietary machines being developed at several corporate research laboratories. These NASA/industry research programs are addressing ATP material form development as well as ATP requirements such as precise control of robot head positioning, material placement rates, heat delivery to the lay-down zone and cut/add, start/stop capability.

#### 3.1 Preconsolidated Composite Ribbon and Tape

Automated tow/tape placement (ATP) requires high quality, fully consolidated, thermoplastic ribbon and tape with precise dimensional tolerances. NASA has developed ways to fabricate the required product forms subject to the following restrictions: (a) utilize no solvents that would have to be removed in subsequent fabrication steps; and (b) avoid melt impregnation since high performance, high molecular weight thermoplastics such as polyimides and polyarylene ethers have high melt

viscosities. Melt viscosities for candidate resins were lowered by judicious alteration of the molecular weight and main chain manipulation, even to the point where RTM and RFI processes were enabled with some of the resins. The scheme finally developed at Langley utilized impregnation of finely ground polymer powder particles onto a spread, unsized carbon fiber tow bundle followed by thermoplastic forming of the powder-coated tow (called a towpreg) into consolidated ribbon and tape.

Processes for making towpreg have been developed from both slurry and dry powder techniques (Ref 6). An optimized process, called the "powder curtain" was found to be the most efficient way of distributing the polymer particles throughout continuous filament tows (Fig 12). The resulting towpreg yarn was flexible, bulky, and abrasive. Composite laminates were made with this material by frame-winding followed by press molding. These laminates had mechanical properties (Table 1) that compared quite favorably to properties from laminates made from solution prepregging followed by devolatilization and press molding (Ref 7).

Heated, robotic placement heads are generally designed to utilize stiff, preconsolidated ribbons or tapes having consistent cross-section, properties very different from the towpreg described above. A number of debulking techniques were studied to convert powder-coated towpreg yarns into stiff, fully preconsolidated ribbon and tape (Ref 8). Issues included towpreg material quality, transverse squeeze-flow, appropriate timing for heating and pressure application, and tool contact/release. Several processing methods were designed, built and experimentally evaluated. Four powder-coated towpreg yarns, Aurum™-500/IM-8, PIXA-M™/IM-7, LARC™-IA/IM-7 and APC-2™ (PEEK/AS-4) were used in this evaluation. Reactive plasticizers and solvents were excluded. The work concentrated on the fabrication of 0.63 cm wide ribbon from two 12K IM-7 powder coated tows and 7.6 cm wide tape from 25 powder-coated tows (Ref 8, 9).

A novel processing technique was developed for fabricating the consolidated ribbon/tape. The processing equipment was comprised of two primary components (Fig 13). The ceramic hot bar fixture facilitated transverse melt squeeze flow while the cool nip-roller assembly solidified the ribbon/tape into preconsolidated ribbon/tape with consistent cross-section. The heat transfer and pulling force were modeled from fundamental principles to develop a basic understanding of the process for application to a variety of polymer materials.

#### 3.2 Automated Fiber Placement

Fiber placement differs from filament winding in that it requires the tow placement tool tip to contact the surface of the part rather than floating off the part. This allows for placement in non-geodesic paths which may be required for complex parts (Ref 3). Contrasted to filament winding, which is limited to continuous placement on closed part geometry, ATP with its cut/add capability can place on open as well as closed parts.

Specific work cell configurations for fiber placement depend upon the geometry of the parts to be fabricated. However, the following elements are common to all fiber placement machines:

- Placement Head
- Automated Machine Platform
- Electronic Controls and Software
- Placement Tool

During automated placement, preconsolidated composite ribbon or tape is fed from spools through a delivery system located on the placement head. A band of collimated ribbons or a tape is placed with heat and pressure to laminate it onto the work surface.

The placement head is a stand-alone end effector that feeds, cuts, places, and laminates the ribbons or tape (Ref 10). The placement head is supported by an automated machine platform. This platform is usually a commercially available gantry or an articulated arm unit to which additional degrees of freedom may be added (Ref 3).

A prototype automated thermoplastic fiber placement machine for materials and processing evaluation has been developed by NASA (Ref 11). The machine, shown in Fig 14, was manufactured by Automated Dynamics Corporation (ADC) and is comprised of an Asea Brown Boveri robotic arm with an ADC thermoplastic fiber delivery head (Fig 15) and placement tools. The latter are comprised of both flat and cylindrical steel tooling. The computer control system and software for the work cell were jointly developed by ADC and Composite Machine Company (CMC). ADC performed the total system integration.

Machine development for thermoplastics has dealt with the use of hot gases, lasers, focused infrared radiation (IR) and combinations of these heat sources. The most effective heat source was a hybrid focused infrared-hot gas tandem. A reflector and compact IR lamp was placed as close to the nip point as possible to deliver, concomitantly with the heated nitrogen gas torch, the highest heat flux to the nip region (Ref 12). This arrangement allowed the compaction roller to operate at much lower temperatures than normally used which, in turn, reduced sticking of resin and fiber onto the roller. Unidirectional panels placed under conditions of optimum strength had an average crack initiation toughness comparable to those of autoclave processed panels; without the additional heat source, unacceptable interfacial strengths would have resulted at lower roller temperatures. Current work also is directed toward start-on-the part, turning radius limitations, autoadhesion requirements, and development of sensors that give on-line part quality information. The latter would yield a remarkable cost-savings for fabrication of commercial aerospace composite structure when used to repair defects during on-line placement.

Analytical consolidation models have been developed to relate ATP machine design, operating parameters, and sensor readings to the processing conditions necessary for making quality composite parts. In-situ bonding models have served to establish a processing window bounded by the upper and lower limiting values of the processing conditions within which acceptable parts can be made. The models attempt to describe the mechanisms involved in the ATP process. These include heat transfer, tow thermal deformation and degradation, intimate contact, bonding and void consolidation (Ref 13). Finite element analysis, neural networks and fuzzy logic techniques have been used in these computer-based models (Ref 14). Most recently, a new start-on-the-part transient model for in-situ ATP of thermoplastics has been developed (Ref 15).

One of the primary purposes for developing models has been to aid on-line control. The computer execution time is therefore critical. Currently, even in their most simplified form, most models take too long for predictive use on-line. As a result, the models are run off-line for various parameters in the processing window and a computer look-up table is constructed that can be used as a guide to on-line control (Ref 14).

During the past year, in-situ consolidated laminates have been prepared from high temperature polyimides such as AURUM™ PIXA/IM7, AURUM™ PIXA-M/IM7 and LARC™ PETI-5/IM7 and polyarylene ethers and sulfides such as APC-2™ (PEEK)/AS4, APC-2™ (PEEK)/IM6, PEKK/AS4 and PPS/AS4. The thermosetting materials such as the LARC™ PETI-5/IM7 require a high temperature postcure to optimize their performance. Some properties of PEEK and PIXA panels made by ATP on large industrial equipment are given in Table 2 and compared with properties obtained from panels made by hand lay-up/autoclave procedures. The ATP panels exhibited from 85 to 93 percent of the properties of composites made by hand lay-up/autoclave. These results indicate that heated head ATP technology can be used to effectively fabricate quality, high performance composite laminates. The goal for ATP structures is to achieve parity with the mechanical properties from structures processed using hand lay-up/autoclave techniques.

#### 4.0 CONCLUDING REMARKS

Major advancements have occurred in the automated fabrication of composites containing textile preforms. Automated processes that produce multidirectional broadgoods for multiaxial knitting coupled with a second generation stitching machine with 4 heads have pushed the resin infusion and resin transfer molding technologies to a high level of accomplishment. Wing cover panels have been successfully fabricated from integrally woven preforms utilizing an outer mold line tool, epoxy resin film, near net shape textile preforms, an inner mold line tool and a reusable vacuum bag via resin film infusion. Low cost vacuum assisted resin transfer molding (VARTM) processes are now being applied to the fabrication of aircraft quality, heavily-loaded primary structure.

Significant progress has been made in developing automated heated head tow/tape placement technology for the fabrication of high performance composite structures. The key activities included development of methods for making quality thermoplastic ribbons and tape, determination of machine design and operating requirements for in-situ placement, and establishment of a base knowledge of the fundamental mechanisms involved in both ribbon/tape preparation and in-situ consolidation.

ATP studies during the period ahead will include the validation of focused infrared/hot gas heating and development of on-line sensors and start-on-the part methods. Particularly important will be material qualification studies at NASA and the fabrication of large test specimens and component structures at several industrial laboratories. VARTM processes need further development to show that aerospace quality parts can be fabricated that have the desired hot/wet mechanical performance. Resin transfer molding modeling studies will focus on the prediction of resin flow into complex textile preforms to insure high quality, high speed fabrication at lower costs.

#### 5.0 REFERENCES

1. Critchfield, M. O., et al, "Low-Cost Fabrication Of Composite Ship Structures Using Vacuum-Assisted Resin Transfer Molding", Proceedings of the Composites in Marine Applications Symposium, November, 1992, Seattle, WA.
2. Hawley, A. V., "Detail Design Development Of A Transport Aircraft Composite Wing", Sixth NASA/DoD Advanced Composites Technology Conference, NASA CP 3326, June 1996, pp 131-154.
3. Smith, A. and Anthony, D., "Robotic Placement of Complex Thermoplastic Structures", Internatl. SAMPE Tech. Conf. Series, 24, 1992, pp 101-115.
4. Johnston, N. J.; Towell, T. W.; Marchello, J. M. and Grenoble, R. W., "Automated Fabrication of High Performance Composites: An Overview of Research at the Langley Research Center", Eleventh International Conference On Composite Materials, Gold Coast, Australia, July 14-18, 1997. Proceedings, 4, 1997, pp 85-91.
5. Loos, A. C., et al. "Resin Film Infusion (RFI) Process Simulation Of Complex Wing Structures", Proceedings of the Fifth NASA/DoD Advanced Composites Technology Conference, NASA CP 3294, Volume 1, Part 2, pp 811-833.
6. Baucom, R. M. and Marchello, J. M., "Powder Curtain Prepreg Process", J. Adv. Materials, 25, 1994, pp 31-35.
7. Hou, T. H., Johnston, N. J., Weiser, E. S and Marchello, J. M., "Processing and Properties of IM7 Composites Made From LARC™-IAX Polyimide Powders", J. Adv. Mtls., 27 (4), 1996, pp 37-46.
8. Sandusky, D. A., Marchello, J. M. and Johnston, N. J., "Ribbonizing Powder Impregnated Towpreg", Sci. Adv. Matl. Process Eng. Series, 39, 1994, pp 2612-2625.
9. Belvin, H. L., Cano, R. J., Grenoble, R. W. and Marchello, J. M., "Fabrication of Composite Tape from Thermoplastic Powder-Impregnated Tows", Internatl. SAMPE Tech. Conf. Series, 28, 1996, pp 1309-1316.

10. Steiner, K. V., Faude, E., Don, R. C. and Gillespie, J. W., "Cut and Refeed Mechanics for Thermoplastic Tape Placement", Sci. Adv. Matl. Process Eng. Series, 39, 1994, pp 116-125.
11. Towell, T. W., Johnston, N. J., Grenoble, R. W., Marchello, J. M. and Cox, W. R., "Thermoplastic Fiber Placement Machine for Materials and Processing Evaluations", Sci. Adv. Matl. Process Eng. Series, 41, 1996, pp 1701-1711.
12. Grenoble, R. W., Tiwari, S. N., Marchello, J. M., and Johnston, N. J., "Hybrid IR-Gas Heater For Automated Tow Placement", International SAMPE Symposium and Exhibition, Science of Advanced Materials and Process Engineering Series, 43, 1998.
13. Hinkley, J. A. and Marchello, J. M., "Thermoplastic Ribbon-Ply Bonding Model", NASA Tech. Mem. 110203, September 1995; Hinkley, J. A., Working, D. C. and Marchello, J. M., "Graphite/Thermoplastic Consolidation Kinetics", Sci. Adv. Mtls. Process Eng. Series, 39, 1994, pp 2604-2611; Hinkley, J. A., Marchello, J. M. and Messier, B. C., "Characterization of Polyimide Composite Ribbon Weld Bonding", Sci. Adv. Mtls. Process Eng. Series, 41, 1996, pp 1335-1345.
14. Ranganathan, S., Advani, S. G. and Lamontia, M. A., "A Model for Consolidation and Void Reduction during Thermoplastic Tow Placement", Internatl. SAMPE Tech. Conf. Series, 25, 1993, pp 620-631.
15. Costen, R. C. and Marchello, J. M., "Start-On-The-Part Transient Model For In-Situ Automated Tape Placement Of Thermoplastic Composites", International SAMPE Symposium and Exhibition, Science of Advanced Materials and Process Engineering Series, 43, 1998.

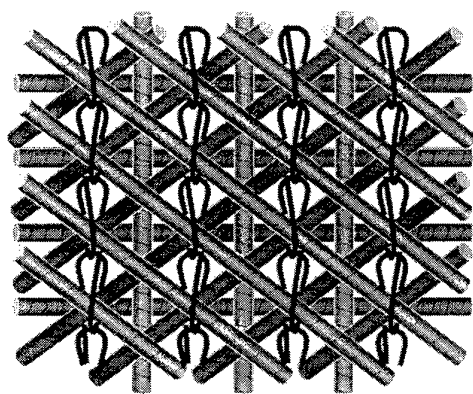
Table 1. Mechanical properties of LARC™ IAX/IM7 polyimide composites made by solution and powder-coated prepreg\*

Property	Test Temp., °C	Solution Coated	Powder Coated
SBS Str., ksi	RT	15.8	22.1
	177	7.9	8.9
0°Flex. Str., ksi	RT	213	314
	177	105	213
0°Flex Mod., msi	RT	18.6	19.8
	177	15.1	19.8
0°Compress. Str., ksi	RT	167	202
0°Compress. Mod., msi	RT	23.4	23.7

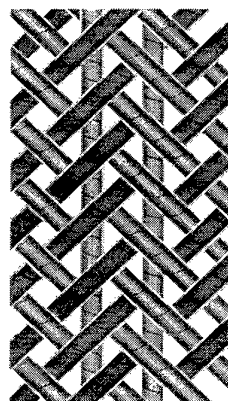
\*Data normalized to 60/40 fiber/resin vol. %; Polyimides were formulated to 4% offset in favor of the diamine and endcapped with phthalic anhydride.

Table 2. Open Hole Compression Strengths of Quasi-isotropic Thermoplastic Composites

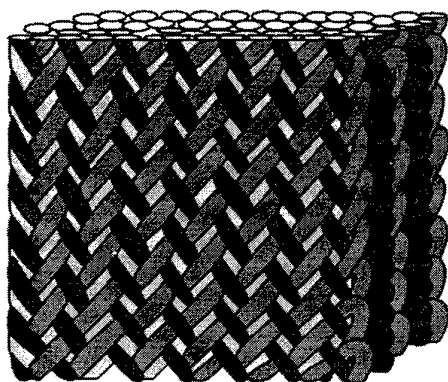
Process	APC-2™ (PEEK)/AS4	APC-2™ (PEEK)/IM6	AURUM™ PIXA/IM7
Hand Lay-up/Autoclave	47 ksi	46 ksi	46 ksi
Adv. Tow Placement	40 ksi	43 ksi	39 ksi
% Retention	85	93	85



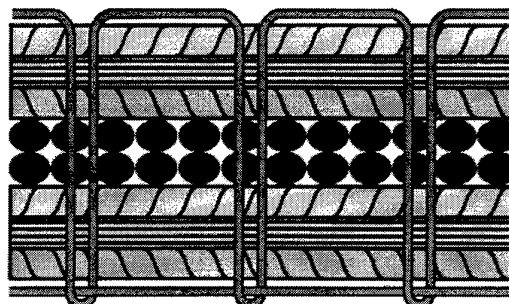
**Multiaxial warp knit**  
(stitched & unstitched)



**2-D triaxial braid**  
(stitched & unstitched)



**3-D braid**



**Knitted/stitched**

Figure 1. Textile material forms.

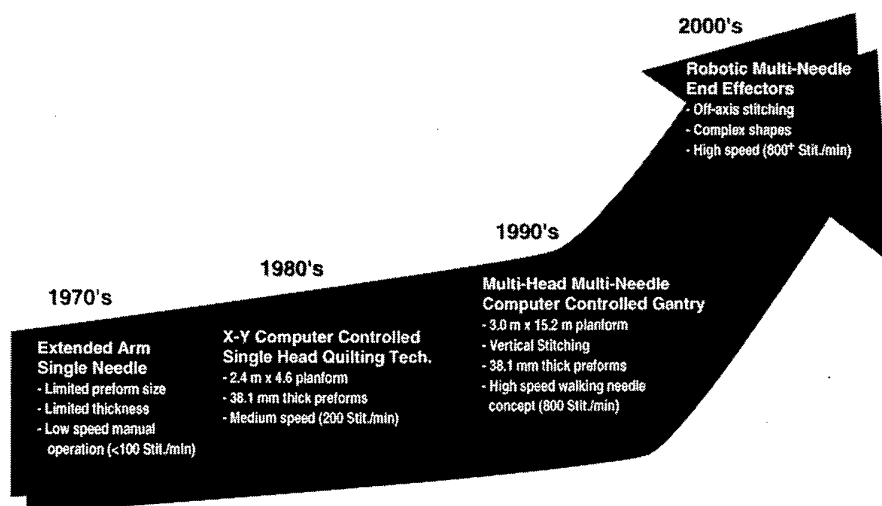
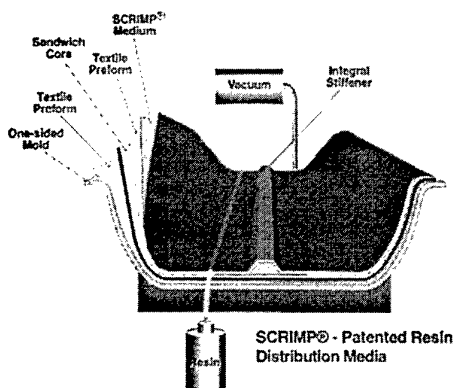


Figure 2. Evolution of stitching technology.



Figure 3. Stitched semi-span wing lower cover preform.

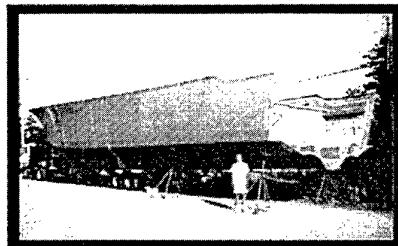


**Advantages of low-cost RTM process:**

- Resin and fiber used in lowest cost form
- Prepreg process eliminated
- Freezer storage & shelf life problems eliminated
- Low-cost, one-sided tooling
- Low energy, low pressure out-of-autoclave processing
- Utilizes net-shape, damage tolerant textile preforms
- Large integral structure minimizes secondary bonding and fastening

**Challenges for aircraft applications:**

- Out-of-autoclave cure resins with adequate properties
- Dimensional tolerances with low-cost tooling



90 ft, one-piece boat hull fabricated with SCRIMP® process

Figure 4. Low-cost vacuum assisted resin transfer molding process.

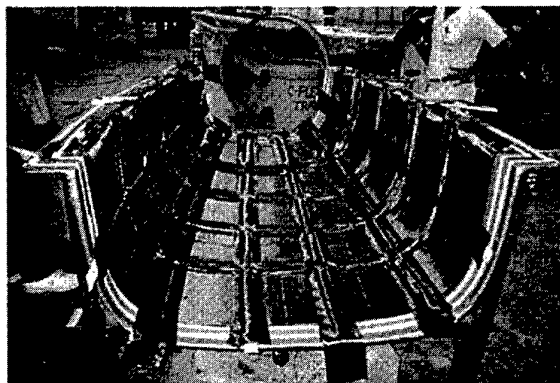


Figure 5a. Vacuum assisted resin transfer molding tooling for fuselage section.

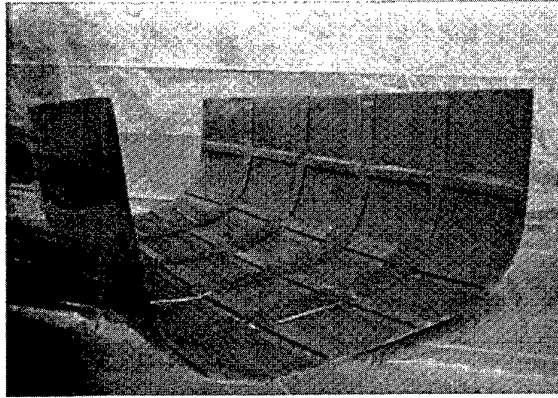


Figure 5b. Completed fuselage section.

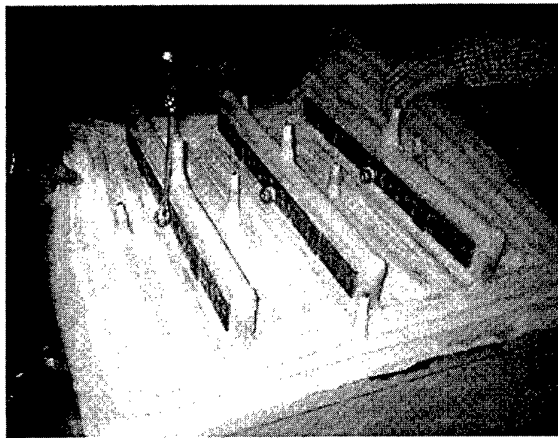


Figure 6. Reusable vacuum bag for VARTM of stiffened panel.

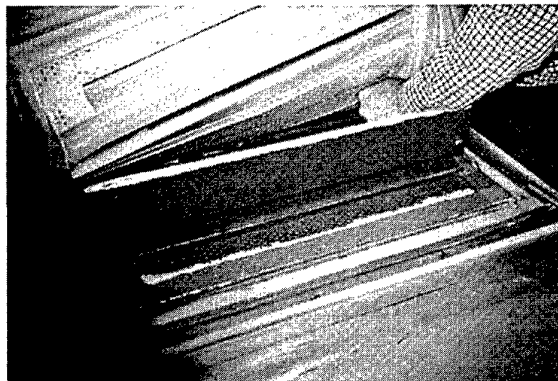


Figure 7. Removal of reusable vacuum bag from VARTM stiffened panel.



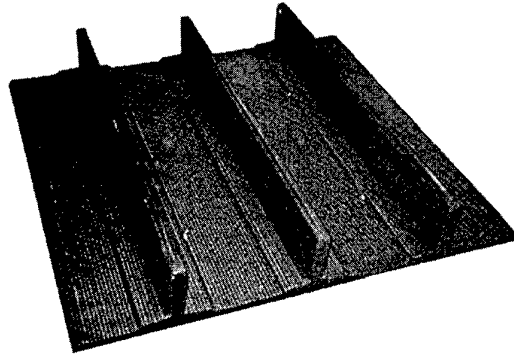


Figure 8. Stiffened panel fabricated by VARTM.

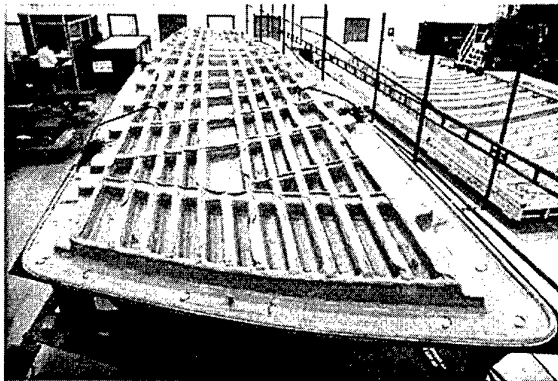


Figure 9. Vacuum bagged semi-span wing tool proof article prior to cure.

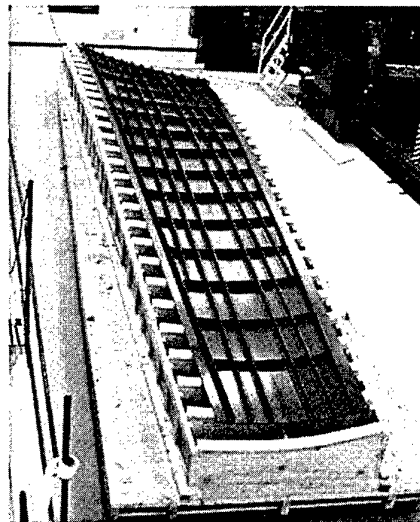
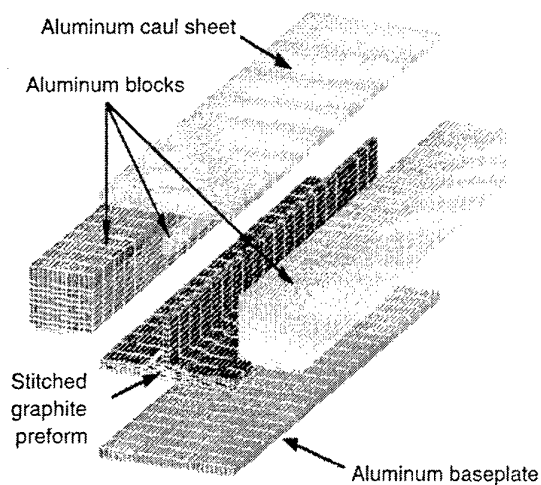


Figure 10. Semi-span wing tool proof article after cure.

### Ply Drop Off Single Blade Stiffener Preform/Tooling Assembly



### Program Structure

- Flow
- Heat Transfer
- Resin Kinetics
- Resin Viscosity
- Preform Compaction
- Residual Stress and Warpage

Figure 11. Three-dimensional resin film infusion model.

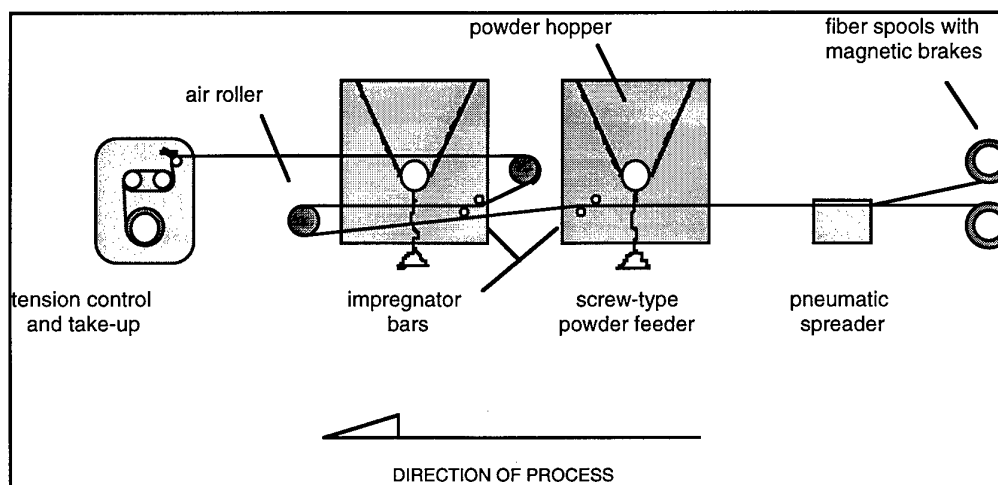


Figure 12. Schematic of the NASA Powder-Coating Line.

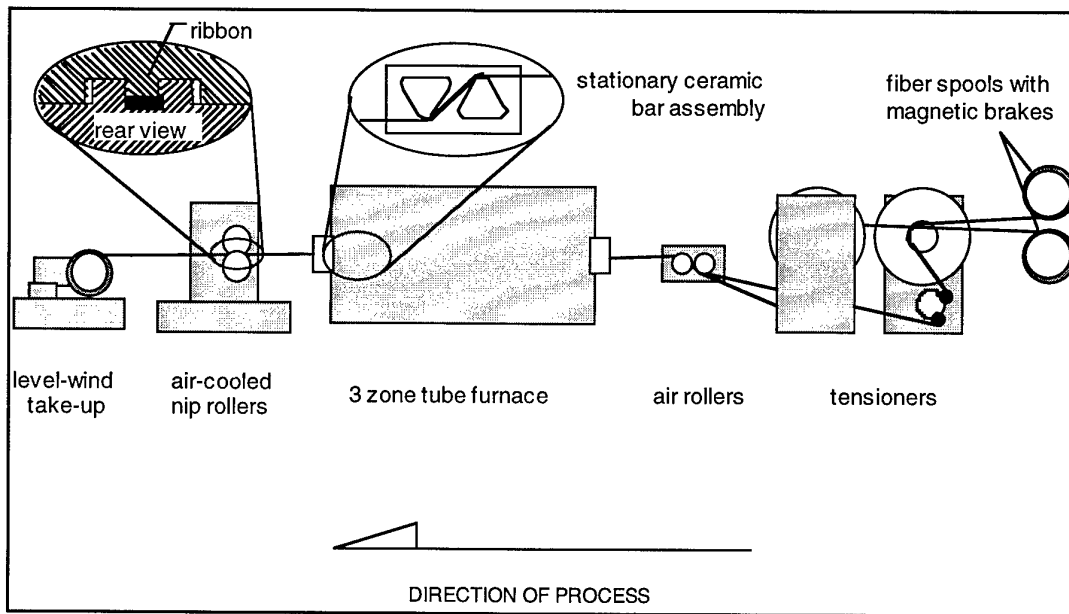


Figure 13: Schematic of NASA Ribbon/Tape Line.

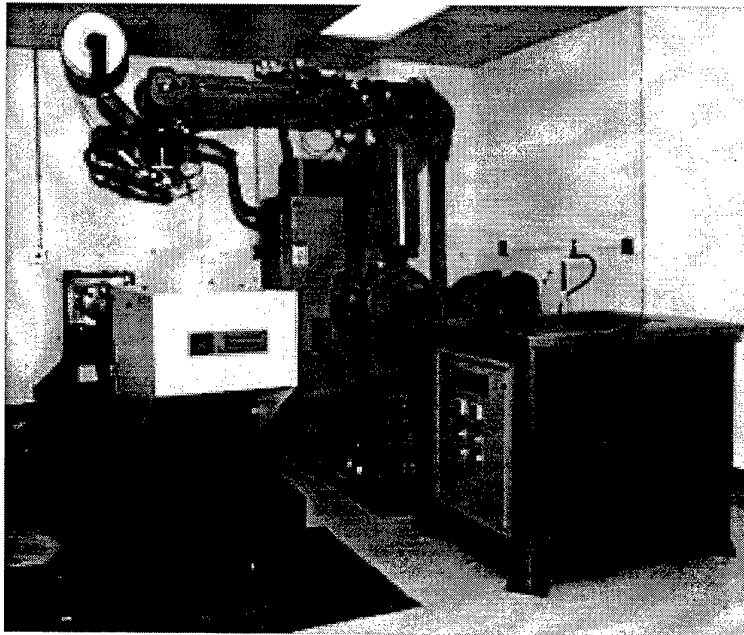


Figure 14. Photograph of NASA Robot, Heated Head and Heated Flat Tool.

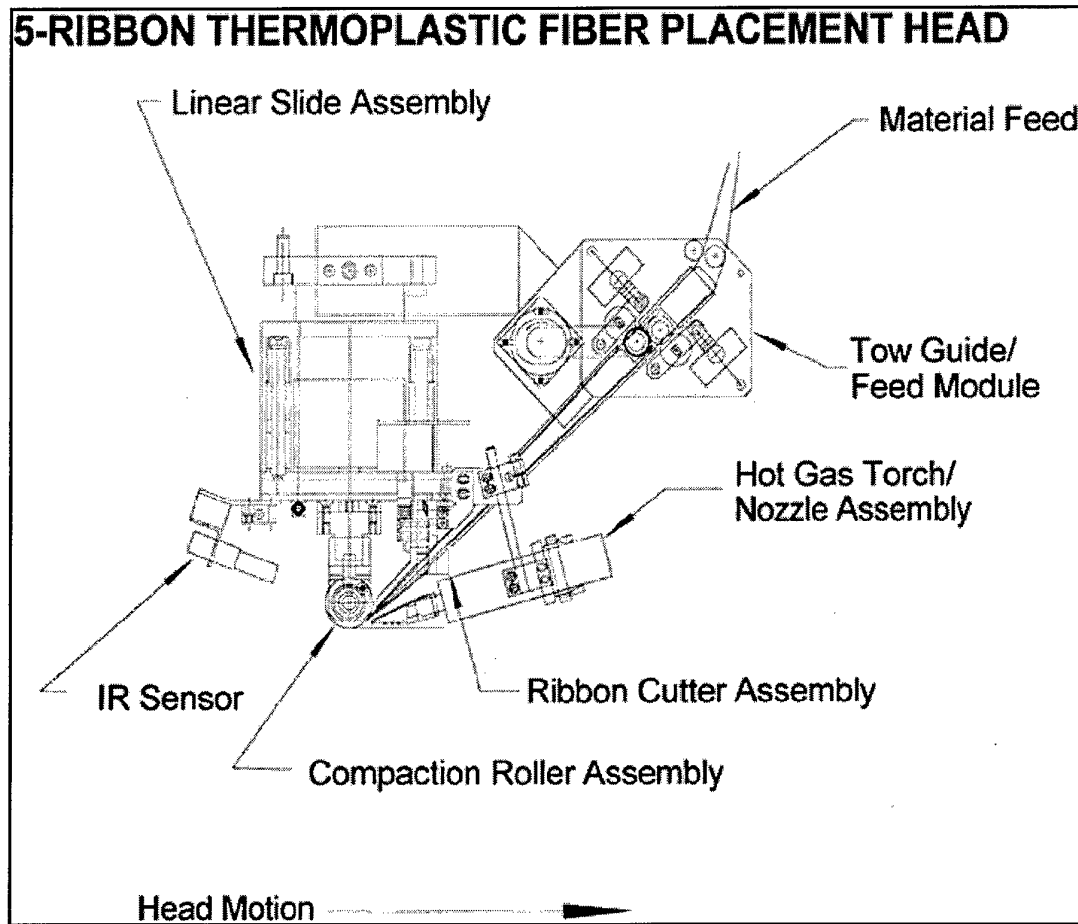


Figure 15. Schematic of the NASA Heated Head.

## Remote Cure Sensing of Polymer Composites

\*Dr D A Pullen, DERA, 2008 Bldg A7  
Farnborough, Hampshire GU14 0LX, UK

Dr D Attwood, BAe, Bristol, UK

Dr I Partridge, Cranfield University, Cranfield, UK

Mr M Batchelor, BAe, Bristol, UK

Dr G Cracknell, Shorts Brothers, Belfast, UK

\* lead author

### Abstract

Cure monitoring of polymer composites has been investigated for many years, but there is still not a fully interactive system control available in the marketplace which can provide, in real-time, a direct measure of the chemical and physical state of the matrix resin throughout the whole cure. The potential of such a system to aid improved cost effective manufacturing is still a strong driving force for its development to be justified. This paper describes work which endeavoured to critically review and further develop aspects of such a system and provide a realistic assessment of future efforts required for its realisation.

### Introduction

Polymer composite components, principally as a result of the high costs associated with the purchase and processing of the raw materials, have for many years been the preserve of the advanced technology driven aerospace and defence industries. In recent years there has been increasing demand for reductions in processing costs, and with market diversification the drive has been towards lower cost routes. This is now reflected in the aerospace industry by the development of techniques previously used for non-aerospace structures such as resin transfer moulding for increased volume of complex components and vacuum-only curing for increased versatility in the manufacture of large structures with smaller investment in specialist equipment. However, despite these lower cost alternatives the autoclave will still maintain a vital role as one of the principal production routes of aerospace components.

Composite components, regardless of the processing route tend to be processed using inflexible cure cycles which take no account of the state of the polymer matrix prior to, during or after the cure. The temperature regime of the processing cycles tend to be verified by thermocouple data which in itself provides no

direct measure of the processing events occurring within the composite component. The effect of the processing schedule on the mechanical performance of the cured composite has often not been fully evaluated or understood so that deviations from the planned cycle often lead to part rejection because the structural integrity cannot be validated without its destruction.

Cure of thick composite sections of low thermal conductivity and large heat transfer resistance results in gradients of temperatures and, hence, resultant degree of cure within the part. This can lead to non-uniform curing, resulting in large residual stresses and possible exotherm. The industry responds to this by slow heat up rates and conservative cure cycles to minimise these effects. An approach where cure cycles could be developed and controlled from real-time measurements related to physical and chemical changes in the curing system would offer the most efficient processing routine where the degree of confidence in the structural integrity of the component would be raised considerably.

The optimisation of the processing cycles may only be realised through a thorough understanding of the composite matrix system and its relationship to the physical and mechanical properties of the cured component. In new manufacturing techniques such as RTM and vacuum-only cure there is an even greater need for full appreciation of resin systems and how they behave during processing and, ultimately, to establish the relationship of this behaviour to end-use mechanical performance.

The industry is awaiting an Intelligent Knowledge Based System which can relate detected response in real time with actual events taking place during cure and, hence, adjust the process control system. DERA has been involved in cure monitoring of polymer composites for some time, collaborating with other industrial partners to

critically assess various aspects of such an IKBS, where appropriate developing further technology and improve understanding and confidence in real-time process monitoring. The ultimate aim has been to gain a better appreciation of the likelihood of realising such an interactive process, with recommendations for further development work.

One of the fundamental challenges of process control is to initially identify those features of the resin matrix that relate most closely to the processing events taking place during cure and their association with the mechanical performance of the cured component. At present, an expensive quality control process involving thermal and mechanical performance determination is the only method for evaluating the degree of cure of the specimen. The sensitivity of typical mechanical performance screening tests used were investigated to identify the key features of composite performance which are affected by changes in processing conditions.

Effective control of processing cycles requires the development of a simple sensing technique by which to monitor and control the changes deemed fundamentally important to the evolution of mechanical properties during cure. This programme focused on dielectric sensing since considerable experience of this technique has been gained through various DERA-funded research projects at Cranfield University. Of the sensing techniques available, dielectric cure sensing of epoxy composites is the most mature with several comprehensive published reviews highlighting the scope of its effectiveness and limitations prior to this programme<sup>2,3</sup>.

Sensor use within composite parts is generally considered to be limited because of their intrusive nature and the high costs of a "disposable" sensor system to the manufacturer. Work in this programme has investigated the suitability of a number of commercial sensors presently available and identified the need for further developments in sensor design to overcome the practical issues associated with the limited number of commercial sensors available in the marketplace.

To be able to correlate raw detection data to the behaviour of a specific material or processing environment, materials and processing models are required. These are mathematical equations

which represent a particular property of the material as a function usually of time or temperature, or the temperature/pressure environment that a particular component geometry will see in the specific processing technique. Many studies have published models for simple epoxy systems which can be used as the basis for developing more specific models for more complex commercial systems. At present, however, each model to be developed requires considerable experimental validation and hence, this approach is very time consuming and resin specific.

Various aspects of a comprehensive model to describe the cure process of one RTM resin was developed by Cranfield University based on the application and integration of a number of theoretical concepts including chemical kinetics of cure, diffusion and chemo-viscosity all linked to sensor generated data. The suitability of the model for use with other resins was then investigated. Sowerby Research Centre were involved in supporting the experimental validation of the modelling work.

Considerable efforts were also placed in the development of software capable of controlling the data logging, analysing it and representing it graphically with addition of the models to allow extraction of information of events such as vitrification and gel point for specific resins. It was noted that for an interactive system to control processing the software was required to be user-friendly and visual during cure. A basic software package was brought to the programme by Cranfield and further developed using EPSRC funding to support the work of this programme.

### **Experimental Programme**

The experimental programme aimed to investigate 3 main aspects of effective real-time cure sensing:-

1. understand more clearly the relationship between mechanical properties and processing conditions for polymer composites
- 2 further develop methods for in-situ cure monitoring of the matrix resin in polymer composites
- 3 develop models for predicting and optimising the cure cycle of the polymer composite component

In all aspects the practical issues of applying and using the technique were considered, prompting future work.

### **1. Composite Performance Evaluation**

Fibredux 924 and Fiberite 934 were selected for investigation since they are both typical 2nd Generation epoxy resin systems widely used in the aircraft industry. In addition, Hexcel RTM6 was considered for manufacture of laminates using resin transfer moulding.

In each case a range of cure cycles was chosen to investigate the performance sensitivity of the system to changes in cure, ranging from no hold to 2 hours hold at a cure temperature of 180°C.

#### **Physicochemical Performance Evaluation**

Thermal analysis was used to determine degree of cure and Tg in support of the mechanical test programme. For each composite laminate manufactured these features were measured. In general, there was a trend of increasing Tg with increasing cure time, as shown in Figure 1 for Fiberite 934 as an example.

It was also apparent that especially for F934 the attainment of a consistent limiting Tg was achieved early on in the isothermal hold region. It could be inferred that the recommended cure cycle is very conservative, with a significant safety margin built in.

#### **Mechanical Performance Evaluation**

To determine the mechanical performance of composite specimens several tests were identified as being sensitive to matrix performance. These included in-plane shear performance evaluation, being representative of quality control screening tests typically used to validate performance. In addition, open-hole compression, was determined, considered to be a more complex test, generating data typically used for design. For each system performance was determined at ambient and 120°C, and the performance retention calculated. The aim was to investigate which test, if any, proved more sensitive to highlighting performance changes as a consequence of processing changes.

Table 1 shows a summary of results for F934, indicating both mechanical performance and Tg. It was found that significant extents of cure were achieved for most laminates, even if the hold time at the cure time was very short. This resulted in a

performance retention in excess of 75% in most cases. In general, for all systems considered, the mechanical performance evaluation showed that even in tests which are deemed more sensitive to matrix performance there was little variation in percentage retention of performance as a consequence of cure parameters for either of the two tests.

Although it has been recognised that perhaps hot wet conditioned or fatigued specimens may have shown a greater variation in performance with respect to differences in extent of cure it was still surprising that dry 120°C testing did not show a greater drop in performance, especially for some of the apparently undercured laminates.

However, it does question the effectiveness of expensive quality control mechanical testing to validate adequate performance when it has been shown in this programme that simple Tg determination by thermal analysis is the most sensitive measure of extent of cure.

### **2 Dielectric Cure Monitoring**

The experimental work in this area was divided into the laboratory scale neat resin evaluation to further validate the sensing technique and the large scale monitoring of curing laminates in an aggressive manufacturing environment. Many practical aspects of cure monitoring were not fully appreciated until the technique was used in both an autoclave and RTM tool.

#### **2.1 Dielectric Sensing of Neat Resin Cure**

In recent years, considerable efforts have been made in monitoring real-time the curing process of thermoset matrix composites. As part of these efforts, various cure monitoring methods have been proposed, of which the dielectric technique appeared to be the most promising. This technique consists of three major steps. 1. Measurement of a signal relative to some dielectric property of the material. 2. Conversion of the measured signal to the actual value of the dielectric property. 3. Conversion of the experimentally determined dielectric property to the viscosity and degree of cure of the materials. Of these three steps the first two are well in hand with technology and models existing to convert signals to dielectric properties.

When the programme started the existing dielectric techniques and supporting software could only determine the time of minimum

viscosity and the time to reach full cure. No system could also provide direct information about either the viscosity profile or degree of cure as a function of dielectric response during the whole cure cycle.

Investigation of the relationship between thermal and dielectric analysis of epoxy resins demanded considerable effort to validate the real-time response of the dielectric cure monitoring technique with actual physical changes in the resin structure. This work was critical to identify and understand this relationship, and built upon considerable expertise in the interpretation of dielectric response during epoxy cure previously gained through DERA funded research programmes with Cranfield.

In addition, a suitable model was required for the particular resin to enable actual viscosity and extent of cure values to be calculated. This is discussed further in section 3.

#### Thermal Analysis

Analysis of polymers during cure using conventional differential scanning calorimetry (DSC) produces details of heat capacity change as a function of temperature and time. By using a temperature profile representative of an epoxy cure cycle the total heat flow during cure can be calculated by the area under the curve. Modulated DSC is a technique which has been shown to identify changes in heat capacity of curing resins which would be masked by enthalpic changes when measured using conventional DSC.

Experiments performed in this programme showed that in the isothermal section of a typical cure profile there was a distinctive reduction in heat capacity identified by MDSC which was found to correspond to the point at which the rate of increase in  $T_g$  as a function of time at the isothermal cure temperature began to reduce and the  $T_g$  of the resin had reached the cure temperature of the system, as determined by DMTA, shown in Figure 2. The time and extent of cure at which this feature occurred was found to be reproducible and full analysis of this work is detailed in Refs 1 and 6. Work by Richardson and Savill<sup>7</sup> is also consistent with the suggestion that the change in specific heat capacity is directly associated with the vitrification of the resin.

#### Dielectric Sensing Equipment

The arrangement of dielectric sensing equipment used to monitor cure is shown schematically in Figure 3, indicating the internal and external connection of leads from the sensor; the multiplexer, which collects the electrical signals emerging from the sensor or sensors and a frequency response analyser, which converts these signals to the real and imaginary parts of the complex impedance of the system under test. Finally the control PC, which controls the sensing process and integrates all the data to represent it graphically.

#### Dielectric Analysis

Dielectric analysis of the curing resin followed the same temperature profile used for MDSC, with impedance measurements made throughout this profile in the frequency range 100Hz to 1MHz. This data was analysed to obtain the frequency dependence of the dielectric loss  $\epsilon''$  and three dimensional plot of  $\log \epsilon''$  against cure time and logarithmic frequency for the isothermal part of the cure is shown in Figure 4. A previous publication<sup>5</sup> by workers at Cranfield describes the detailed analysis of features of these plots and their relevance to chemical and physical changes affecting the development of crosslink structure, defined by the  $T_g$ , during the resin cure. In the plot there are characteristic changes in  $\log \epsilon''$  along the time axis with increasing time.

For a given temperature these characteristic features are frequency dependent, appearing at increasing time with decreasing frequency and are known to be related to gel and to the  $T_g$  or vitrification point<sup>5</sup>. These features are reproducible for this resin, with similar features at different times seen for other resins. These have been identified previously as the point of maximum flow and end of cure respectively.

The time at which vitrification occurs has been found<sup>5</sup> to correspond with the peak in  $\epsilon''$  when determined at 1 Hz. By extrapolation of the plot of  $\log \epsilon''$  against isothermal hold time, shown in Figure 5, the time is found to be approximately 53 minutes. This corresponds with the time at which  $T_g$  levels out, also taken to indicate vitrification, previously determined by DMTA studies, establishing an important correlation.

This correlation of the measurements made using dielectric analysis and proven chemical and



physical changes identified by DMTA and MDSC has been vital to the acceptance that confidence can be placed in dielectric response measurements as an interpretative tool during the curing of resin systems. Work is now underway to improve direct measurements made at 1Hz, eliminating the need for the extrapolation.

## 2.2 Dielectric Sensing of Composite Cure

The lessons learnt in dielectric sensing of neat resin cure were applied to composite cure in both an autoclave, carried out at Shorts, and in an RTM mould, carried out by Airbus. In both cases laminates which were produced for the performance test programme were monitored while they cured to allow direct comparison between dielectric response and ultimate performance as a consequence of variable processing conditions.

### Autoclave Cure Monitoring

The data generated by the dielectric sensing of composite laminates during autoclave cure proved more difficult to interpret than that generated in a laboratory environment. The sensor and connector wires were sensitive to background electrical interference from the oven and pressure equipment. This created a high noise level on the traces produced in initial measurements. Better earthing and isolation was required and modifications to the path of the wires out of the press-clave improved the noise level further. In the analysis of dielectric data it is the relative change in response which is considered rather than absolute values. It has been found from experience that baseline values vary considerably due to the environment in which measurements are made.

All laminates cured in the autoclave had one dielectric sensor on top of the laminate, placed in one corner between the top porous PTFE layer and the bagging material. Extra layers of porous PTFE were placed above and below the sensor to shield it from the carbon fibres, but still allowing impregnation of the resin. Leads from the sensors ran out from the laminate through the edge of the vacuum bag seal to a multipoint connector.

In general, the 3D plots from the composite laminates were similar to those from the neat resin plaques, although the baseline noise level was even greater. Similar features identified as being associated with real events in the cure

mechanism of the resin were also evident in the dielectric response determined during an autoclave cure. It was, however, identified that representing these changes as a 2D plot of dielectric loss against time for a chosen single frequency produced a clearer image of changing response and features associated with gel and vitrification. For clarity, a frequency was chosen at which there was a relatively large observed change in response with time. An example of a typical trace can be seen in Figure 6, with the significant increase in dielectric conductance and capacitance as the resin melts and flow, the characteristic peak at maximum flow, the point of inflexion corresponding to gel point and the plateau at vitrification.

Knowing the point of maximum flow is important since it is believed that application of pressure at this point will be more effective in producing high fibre volume fractions by inducing closer fibre packing, and reducing springback in components caused by induced stresses. Knowing that gel point has been reached if a vacuum bag bursts is important in deciding whether to abort a run or not. Knowing when vitrification has been achieved and that the corresponding  $T_g$  is adequate is the overriding feature of deciding whether a component is adequately cured or not.

Laminates were also cured where sensors were placed in the centre of the plies as well as on the top and bottom of the laminate to assess the difference between signals through the thickness. In addition, thermocouples were also inserted in the same positions in the laminate. A thick 104 ply laminate was investigated and Figure 7 shows the trace produced for this cure. The lag observed in both the thermocouple and dielectric sensor readings from the centre of the laminate to the top and bottom are representative of the thermal lag across the laminate. In addition, once the laminate begins to cure there is evidence of a slight exotherm in the centre, shown by a temperature increase, and a resultant dielectric response increase. This indicates that the exotherm has actually advanced the cure of the resin in this part of the laminate. Detection of the exotherm by thermocouples only could not have shown whether additional cure was initiated as a consequence.

### 2.3 RTM Cure Monitoring

Dielectric monitoring inside the RTM tool highlighted further problems with the set-up. Again, a sensor was initially placed on top of the laminate in one corner, shielded on both sides by porous PTFE. Extra problems with earthing from fibres and tooling were found, and safe exit of the sensor wires from the tool was a problem since they tended to break due to a lip between the top and bottom of the tool. Sensors with longer lead out strips were required and the tool itself was redesigned to eliminate the lip, shown in Figure 8. The temperature control of the RTM mould created large electrical interference as the oil heaters switched on and off to maintain a constant ramp-up rate. This all added to the baseline noise level of the signal.

An example of a trace from the RTM cure is shown in Figure 9, indicating that despite all these engineering problems adequate signals were produced. As in the autoclave cure of a thick laminate, features such as overshoot of temperature resulting in slight exotherms were detected by the sensors. In addition, uneven filling and resin pressure changes due to leaks and resin movement were also easily detected, even if they weren't quantified in this instance.

One of the most important conclusions from the RTM work was the ability to easily detect events occurring as a consequence of variations in processing of the resin. This highlights the opportunities for dielectric measurement as a means for monitoring not only cure but also the variation in response as a consequence of changes in other processing parameters such as pressure. In processing techniques such as RTM the responsibility to effectively combine resin and fibres has been placed with the end-user rather than the materials manufacturer. No amount of care with cure of the resin will produce quality panels if the component formation is inadequate.

### 3 Modelling

Although the correlation between chemical and physical events and dielectric response has been identified experimentally, actual viscosity and degree of cure values at any time can only be calculated using an appropriate kinetic or chemorheological model. Once a model has been identified or verified for a material the control software can use this to identify features of the resin for comparison with real-time monitoring.

This was developed for RTM6, enabling these values to be known in real time throughout the cure. The development of these models requires considerable experimental validation, and has proven to be resin or system specific.

This is adequate to illustrate the fundamental correlation but not practical for a process control system. It would not be economically viable if every new system had to be analysed in detail in every cure regime possible to allow adequate control by cure monitoring.

For full process monitoring other aspects of the processing environment need to be represented by a suitable model. Figure 10 shows the whole process model schematically, indicating how it links with aspects of the sensing technique. It shows how sensing can be used to determine both Tg and viscosity if the correct model for the material is used to analyse the data.

One aspect of the model that was not investigated in this programme was a heat transfer model to represent the 3D properties of the resin by the action of temperature. If multi-array sensing was developed, for instance, in an RTM mould with an appropriate model it would then be possible to predict the state of cure through the component if thermal conductivity and diffusion properties of the material and the surrounding tooling were known. This requires considerable further effort.

### 4.Intelligent Knowledge Based System

The essence of the IKBS is a database of information on materials, tooling, processing considerations, materials performance and dielectric response. This would be stored or entered from previous runs and would be linked to the main process control software to, initially allow specific information on the process and material to be entered and, then to suggest the most appropriate tooling materials to use. Once the cure cycle is running the control software can then access the IKBS at any stage to consider at that moment in time whether the cure had progressed sufficiently to produce adequate performance. This will then feed back a signal to either stop or continue the cure. This is represented schematically in Figure 11.

Within the timescale of this programme it was never anticipated that the IKBS would be fully interactive. It was expected that a system would

be produced which would demonstrate the data that had been developed during the project.

The Intelligent Knowledge-based System that could be developed would encompass experimental dielectric runs, relevant mechanical and physicochemical data, specific materials models, the data analysis package and the process controls. This would enable past experiences to be drawn upon in future on-line processing runs when a decision has to be made whether the component in its present state of cure is structurally sound or requires further curing. This would then be translated back to the process controls in a feed-back loop.

### Conclusions and Recommendations

1. It has been shown that significant changes in the extent of cure of a number of resin systems manifests itself in a proportional change in  $T_g$  but typical matrix-dominant mechanical tests showed little difference in % performance retention after testing at 120°C dry. Further investigations of performance retention after exposure to a hot/wet environment or fatigue may have shown more significance differences between various cure profiles.

2. Increased confidence in the validity of dielectric sensing for use in process monitoring has been gained during the programme, with the correlation between characteristics of sensed response and previously identified physical features such as maximum flow, gel point and vitrification being demonstrated. This would lead to more controlled curing of components and realisation of property potential with a resultant efficient use of material.

3 The ability to also detect features of the manufacturing route and, hence, aid optimisation of the materials processing is a valuable asset to the technique, reducing materials waste and, hence, cost. The benefits to the manufacturing industry of a technique that could monitor the complete processing route are far greater than for cure monitoring alone.

4. The development of in-situ multi-sensing is an additional extension to this technology, with combinations of the most appropriate and efficient sensing techniques monitoring co-incidentally to maximise process control. This could encompass continuous health monitoring

once in service, offering potential in marine and bridge structures in particular.

5. It has been apparent throughout the programme that adequate software support is vital to effective process control and data analysis. At the beginning of the programme a suitable commercial package was not available and as a consequence progress of the sensing work suffered throughout the programme. Significant advances in commercial software packages have been made in recent years, with the release of LABVIEW, which could be used to form the basis of a system-specific package for use in future work.

6. Materials modelling is a requirement for system-specific process control. The existing methodology for development and validation of models for each material is time consuming and this will detract from the perceived benefits of process monitoring. Application of more powerful modelling tools and generic methodologies is required to combine the large amount of effort already placed in this area and to provide a solution which would require minimal experimental data input which, in future, materials suppliers could supply with the release of new materials.

### Acknowledgment

DERA wishes to acknowledge the financial support for this work from The Department of Trade and Industry and from The Ministry of Defence.

### References

1. Maistros G M et al, Polymer, 33, No. 21, (1992), PP4470-78
2. Ciriscioli P, SAMPE Journal, Vol.25, No.3, May/June 1989, pp35-43
3. Kranbuehl D et al, 36th Intl SAMPE Sym, Apr 15-18, 1991
4. Reading M, TRIP, 1(8), 1993,248
5. Karkanis P et al, ICAC'97, Glasgow Sept 1997.
6. Maistros G et al, Compos.Sci.& Tech. 53(1995)355
7. Richardson et al, Polymer, 16(1975) 153

Table 1 Summary of In-Plane Shear Results For F934

Specimen ID	Cure Cycle	Strength 120 C % Retn	Modulus 120 C % Retn	Tg, dry
comp 8	18 mins 17° C	78.6	79.4	215.1
comp 9	27 mins 180°C	75.9	79.8	204.7
comp 10	83 mins 177°C	83.2	85.2	207.5
comp 11	120 mins 177°C ramp up rates = 3°C/min	79.4	79.9	208.3
comp 2	60 mins 160°C	63	74.8	165
comp 3	1 min 177°C	70.1	82.3	208.7
comp 5	50 mins 177°C	78.2	82	209.6
comp 1	120 mins 177°C	78.7	85.2	211.1
comp 7	148 mins 177°C ramp up rates = 1°C/min	75.3	90	190.5

Figure 1 Glass Transition vs Degree of Cure For RTM6

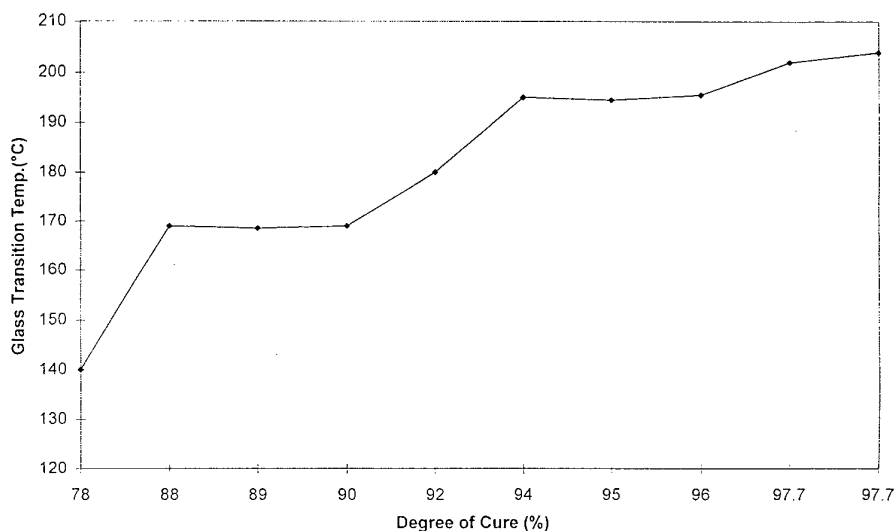


Figure 2 Typical MDSC Trace for RTM6

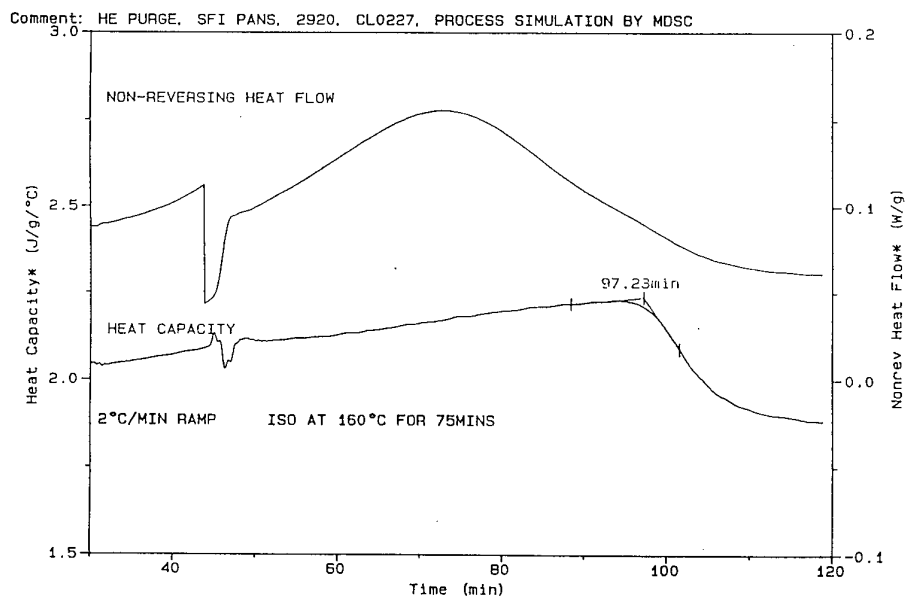


Figure 3 Schematic Diagram of Dielectric Instrumentation

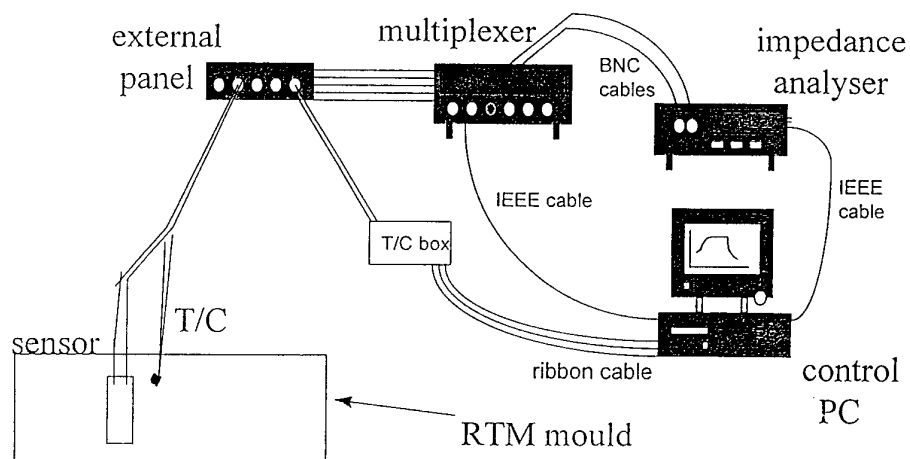
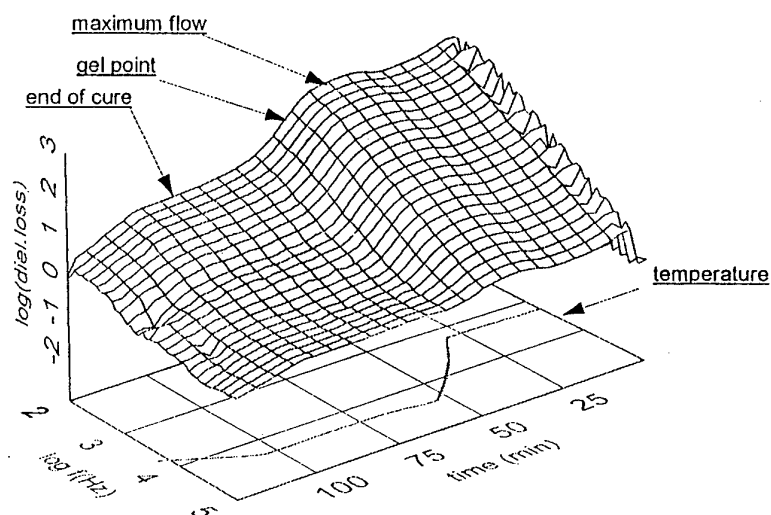
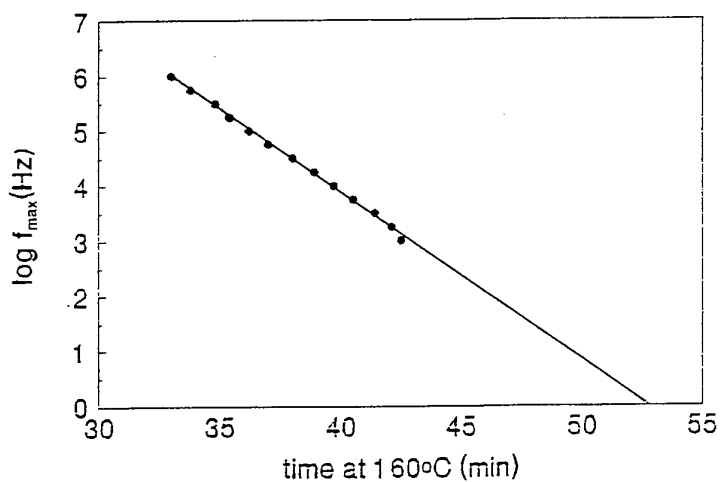
Figure 4 Log Dielectric Loss  $\epsilon''$  and log frequency vs time for RTM6Figure 5 Log frequency of  $\alpha$ -relaxation vs time for RTM6

Figure 6 2D Dielectric Response vs time For a Typical Autoclave Cure

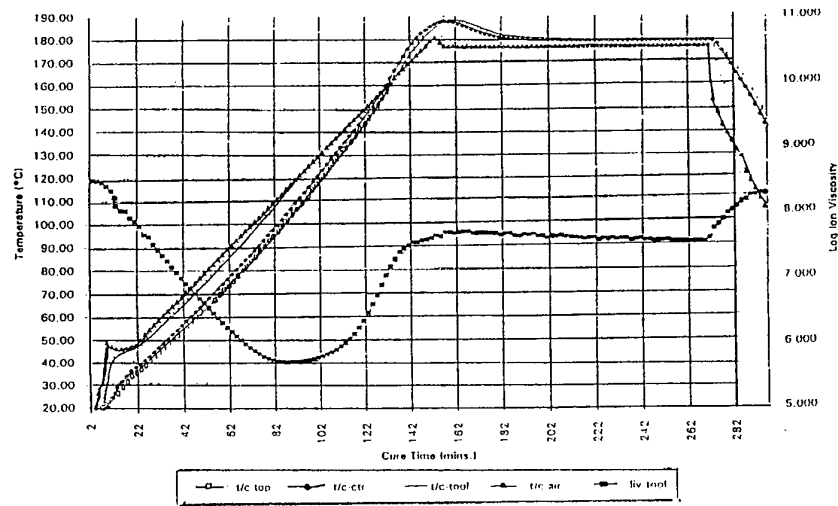


Figure 7 2D Dielectric Response vs Time for a 104 Ply Laminate of F934

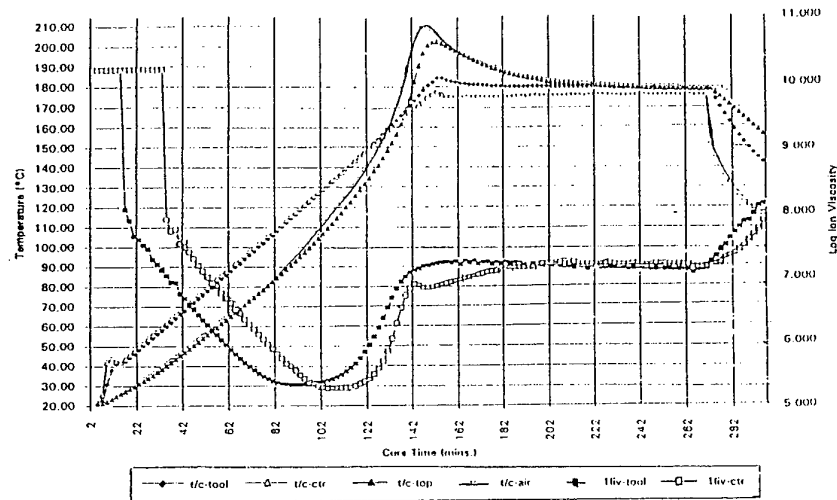


Figure 8 Schematic Diagram Showing The Location of Sensors in the RTM Tool

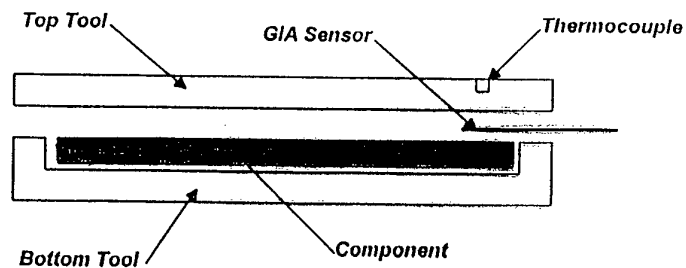


Figure 9 Typical Dielectric Response Trace For an RTM Cure

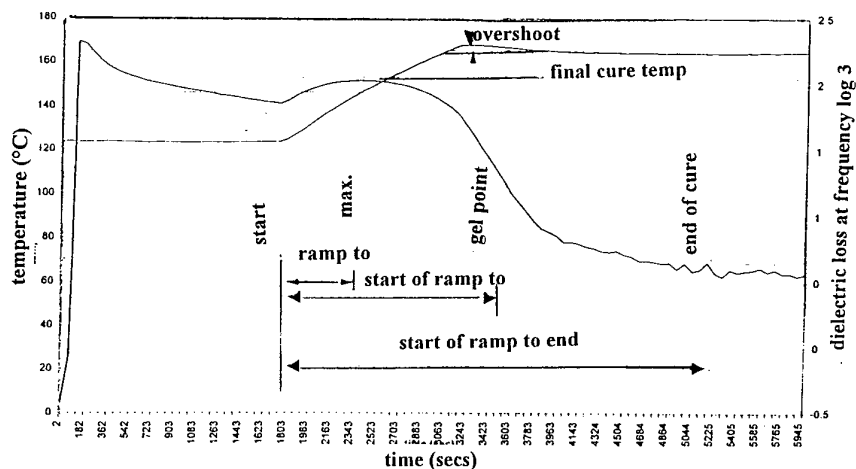


Figure 10 Schematic Diagram Representing the Modelling and Sensing Links in Full Process Modelling

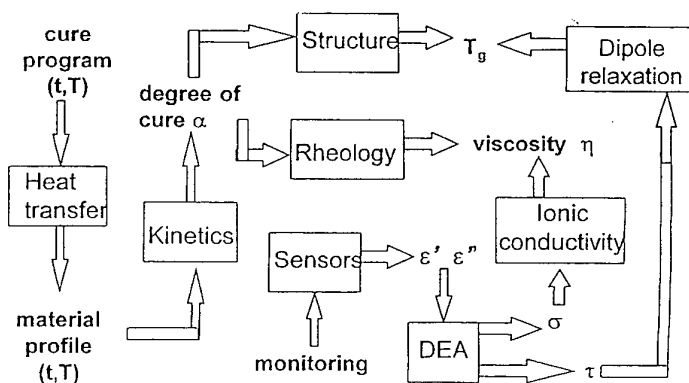
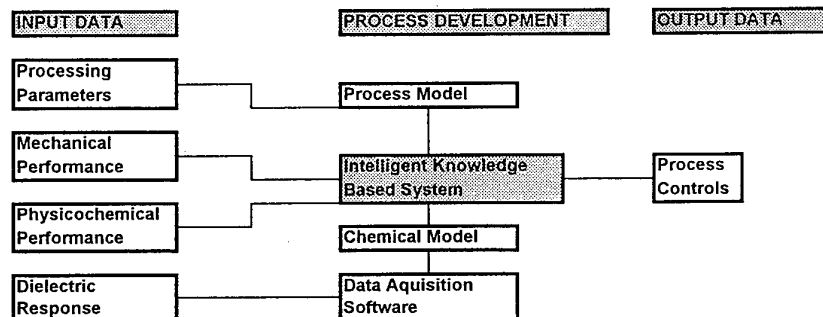


Figure 11 Schematic Diagram Representing a Full Intelligent Knowledge Based System



## Process Control of Deposition Profiles in the Manufacture of EB-PVD Thermal Barrier Coatings

J. R. Nicholls<sup>x</sup>, V. Pereira<sup>x</sup>, K. J. Lawson<sup>x</sup> and D. S. Rickerby<sup>\*</sup>

<sup>x</sup>Cranfield University, Cranfield, Bedford MK43 0AL, UK

<sup>\*</sup>Rolls Royce plc, Derby, UK

### ABSTRACT

For many applications of coatings it is often undesirable to have a uniform coating thickness around a component. Thermal barrier coatings on aerofoil components are a particular example where a uniform coating distribution around the blade or van would degrade aerodynamic performance. It is desirable therefore to limit the thickness of such coatings on the trailing edge of such components.

This paper describes the development of process control models capable of predicting both the deposition rate and column inclination during the deposition of EB-PVD thermal barrier coatings. Thus by programming the rate of rotation and absolute position of blades to be coated relative to the evaporation source it should be possible to predict coating geometries on complexed hardware.

### LIST OF SYMBOLS

d	deposition rate on the substrate inclined at an angle ( $\alpha$ ), defined by $h, \theta$ within the coating chamber.
$d_0$	deposition rate at a distance $h_0$ directly above the source, for a substrate with $\alpha = 0$ .
h	source to substrate separation
$h_0$	height of substrate plane, measured directly above the source
$\theta$	angular displacement of the substrate, measured relative to the normal to the source.

$\alpha$	inclination of the substrate to the line of vapour flux, measured normal to the substrate.
n	index defining the focus of the vapour flux from the evaporation source. A value of 0 is an omni directional evaporator.
D	separation of sources in a multi-source evaporator system.
x,y,z	orthogonal co-ordinates of the centroid of a substrate within the coating chamber, measure relative to the central source position.

### 1. INTRODUCTION

The drive to improve engine performance and fuel efficiency, while reducing emissions, has meant that the operating temperatures of the turbine section of aero-engines has increased significantly over the last 20 years. This has been achieved by novel material design, improved cooling technologies and better manufacturing methods [1]. The latest development in this drive for improved performance is to apply thermal barrier coatings to turbine aerofoil surfaces. Figure 1 illustrates this progressive materials and manufacturing technology development, together with the additional benefits offered by TBC coating aerofoils. Thus, thermal barrier coatings offer the potential of increasing turbine operating temperatures by between 70 and 150°C, without any increase in metal operating temperatures, or alternatively permits a reduction in the mass of cooling air required



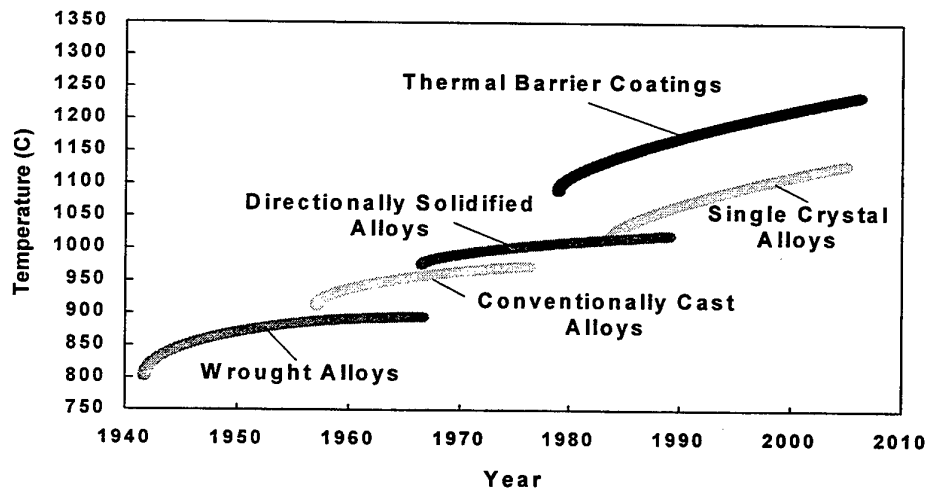


Figure 1 Increase in operational temperature of turbine components made possible by alloy, manufacturing technology and thermal barrier development [1]

while maintaining the turbines operating temperature giving improved specific fuel consumption, of some 0.25% [equivalent to an annual saving of the order of £6m for an airline operating a fleet of 747 or 777 aircraft [2]].

Thermal barrier coatings (TBC's) have been used in the gas turbine engine since the 1970's [3-5] to lower metal surface temperatures. These coatings, based on yttria partially stabilised zirconia (PYSZ), were deposited using thermal spray processing and have performed well in service, extending the lives of combustion chambers and annular platforms of high pressure nozzle guide vanes within the turbine section of the engine. Such thermal sprayed TBC systems have never successfully been applied to turbine aerofoils, due to their poor surface finish, high heat transfer coefficient, low erosion resistance and poor mechanical compliance. Success in coating turbine aerofoils has been achieved by adopting electron beam physical vapour deposition (EB-PVD) technology to coat these parts. Thermal

barrier coatings deposited by EB-PVD processes have a good surface finish [6], columnar microstructures with high strain compliance [6,7] and good resistance to erosion [6,8] and foreign object damage [8].

Table 1 compares the properties and performance of commercially produced thermally sprayed and EB-PVD deposited PYSZ thermal barrier coatings.

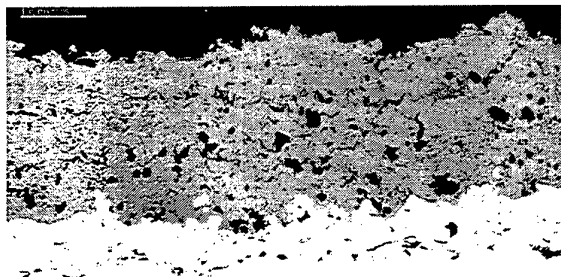
**Table 1 Properties of TBC's at Room Temperature**

Property/Characteristic	EB-PVD	Plasma Sprayed
Thermal Conductivity (W/mK)	1.5	0.8
Surface Roughness ( $\mu\text{m}$ )	1.0	10.0
Adhesive Strength (MPa)	400	20-40
Young's Modulus (GPa)	90	200
Erosion Rate (Normalised to PVD)	1	7

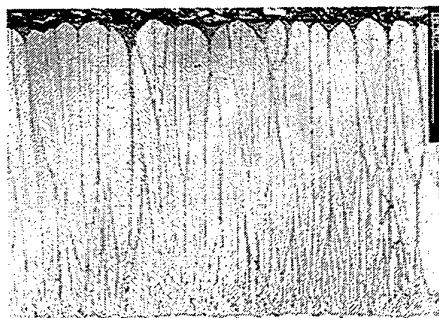
Unfortunately, the microstructure which gives the EB-PVD TBC system its high strain compliance and good erosion resistance leads to a relative high thermal conductivity when

compared to thermal sprayed coatings. Figure 2 provides a comparison between air plasma sprayed and EB-PVD coating morphologies. EB-PVD thermal barrier coatings have been used in production since 1989 [9].

From the foregoing it can be seen that thermal barrier coatings (TBC's) offer the potential to significantly reduce metal surface temperature,



a)



b)

Figure 2 Photomicrographs of a) a Plasma sprayed TBC coating and b) an EB-PVD TBC coating

to increase turbine entry temperatures, to provide improved specific fuel consumptions or any combination of these. However, for

many applications it is often undesirable to have a uniform coating thickness around a component. Thermal barrier coatings on aerofoil components are a particular example where a uniform coating distribution around the blade or vane would degrade aerodynamic performance. It is desirable to limit the thickness of such coatings on the trailing edge.

This paper describes the development of process control models capable of predicting both the deposition rate and column inclination during the deposition of EB-PVD thermal barrier coatings.

## 2. EB-PVD DEPOSITION OF THERMAL BARRIER COATINGS

Electron beam physical vapour deposition (EB-PVD) has been used to deposit TBC's which, because of their columnar microstructure (evident in the polished section, Figure 2b, and fracture micrograph Figure 3), exhibit very high levels of strain compliance. The columnar microstructure forms as a result of the atomistic processes involved in the nucleation and growth of the coating from the vapour phase.

The deposition of a thermal barrier coating involves the following process stages. Firstly, the component is coated with a 'bond coat'; this can be via a CVD route, e.g. a platinum aluminide bond coat, or via plasma spraying, electron beam physical vapour deposition, or electroplating to deposit an MCrAlY oxidation resistant overlay coating, where M is generally Ni, Co or a combination of these. The role of the bond coat is to grow a surface alumina layer, which acts to chemically bond the  $\text{ZrO}_2$ -8wt% $\text{Y}_2\text{O}_3$  thermal barrier coating to the metallic substrate.

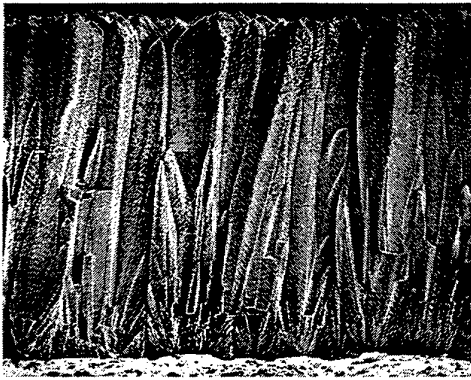


Figure 3) Fracture micrograph of an EB-PVD thermal barrier coating

The bond coated component is then prepared to an acceptable surface roughness, typically  $1.0\mu\text{m Ra}$  [2] with a peak to valley height of  $10\mu\text{m}$ . Deposition of the EB-PVD coating does not significantly alter this surface roughness, and therefore does not introduce an additional aerodynamic performance loss as observed for the rougher plasma sprayed counterparts [2].

Once bond coated and surface finished, the components are introduced into the vacuum deposition chamber to be coated with  $\text{ZrO}_2\text{-}8\%\text{Y}_2\text{O}_3$  ceramic. Figure 4 illustrates a schematic diagram of a commercial EB-PVD coater.

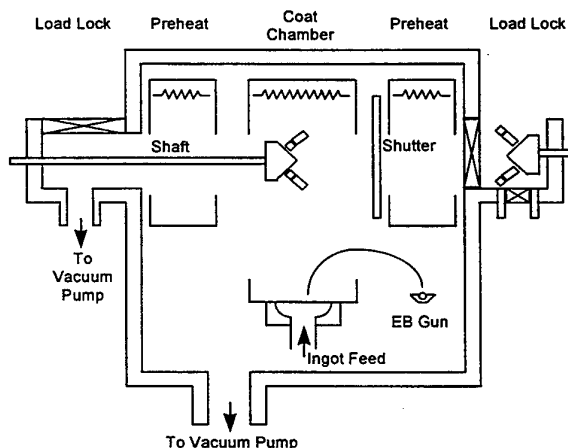


Figure 4 Schematic diagram of a commercial EB-PVD coater system

To maximise the throughput of coated parts, most commercial coaters utilise a load lock system. The EB-PVD coating cycle to deposit the ceramic involves the following steps:-

- 1) Load the components to be coated onto a manipulator, which allows at least two axis planetary motion of the component to be coated.
- 2) Pump the load lock chamber to vacuum and load the components to be coated into the pre-heater.
- 3) Heat the components to the deposition temperature, usually circa  $1000^\circ\text{C}$ , prior to loading in the main coater chamber.
- 4) Load into the main coater chamber and commence evaporation of the ceramic onto the component. The component to be coated is continuously rotated about its axis, which being moved, rotated or oscillated about a second axis. This ensures that all surfaces of the component are coated with ceramic. At the vacuum levels used within a commercial coater the vapour deposition of ceramic is effectively a 'line of sight' process. Thus this planetary motion is necessary to ensure all surfaces are adequately coated. Additional heating may be required to maintain the components being coated at the desired temperature.
- 5) Once coated the component is removed through the preheater and load lock system and the procedure is repeated for other components load via a second load lock. Systems with up to four load locks are commercially available to ensure a continual throughput of parts.

From the foregoing it is apparent that the performance of a thermal barrier coated aerofoil section, is critically dependent on the ceramic coating thickness, morphology and

surface roughness of the zirconia thermal barrier layer. Typical ceramic layer thicknesses are between 200-300 $\mu\text{m}$ , although a much thinner coating is required on the trailing edge for good aerodynamic performance.

Thus the ability to predict coating thickness, morphology, inclination and surface roughness both around a component, or from component to component is key to ensuring the reproducible manufacture of TBC coated hardware. The remainder of this paper address the development of a computer based process model, capable of predicting the thickness and inclination of the TBC microstructure on complexed geometry substrates, typical of aerofoil components.

### 3. MODELLING THE EB-PVD DEPOSITION OF ZIRCONIA CERAMIC

In the scientific literature, the deposition of thin films by Joule heating was proposed as early as 1887 [10], when Nahrwold used joule heating of platinum in vacuum to deposit thin metal films. Later studies by such well known scientists as Hertz, Knudsen and Langmuir researched the behaviour of such vapour streams, such that it is now widely accepted that the thickness distribution of a thermally evaporated coating, deposited from an ideal point source evaporator follows an inverse square law [11-13] governed by an equation of the form:-

$$\frac{d}{d_o} = \frac{h_o^2}{h^2} \cos^n \theta \cdot \cos \alpha \quad [1]$$

where  $d$  is the coating thickness at a distance ( $h$ ) from the vapour source,  $d_o$  is the thickness directly over the vapour flux at a distance ( $h_o$ ) from the source and  $\alpha$ ,  $\theta$  and  $n$  define the source to substrate geometry and the evaporation characteristics of the source. This idealised point source evaporator is illustrated

schematically in Figure 5, where the various nomenclatures used are annotated.

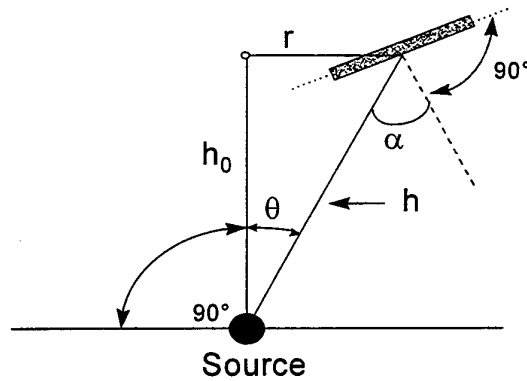


Figure 5 Schematic Representation of an Ideal Point Source Evaporator

In practice, a real evaporation source, typically a ceramic rod 3 to 5cm diameter with the diametrical surface molten, can be envisaged as multiple of point source evaporators, evaporating in parallel. Furthermore, during high rate deposition a virtual omni-directional source will be generated in the vapour cloud immediately above the source due to the localised high vapour pressure and atom-atom collisions within this vapour cloud. Thus the deposition rate at any point on a substrate (component) surface will follow a general equation of the form.

$$\frac{d}{d_o} = \sum_{j=1}^k A(j) \cdot \frac{h_{oj}^2}{h_j^2} \cos^{n(j)} \theta_j \cdot \cos \alpha_j \quad [2]$$

where  $\sum_{j=1}^k A(j) = 1$ . Thus the aggregate flux arriving at any point on a substrate surface, reflects the summation of the flux, from an array of 3-dimensional point sources, which model the molten surface and the evaporant plume directly above this rod source.

Values of  $\alpha$ ,  $\theta$ ,  $h$  and  $h_o$  are set by systems geometry, where as  $n(j)$  and  $A(j)$  are dependent on the performance of the evaporation source.

It is known that as the evaporation rate increases,  $n(j)$  increase. That is the evaporation process is more focused the higher the deposition rate. Equally  $n(j)$  may vary with angular displacement around the source, i.e. the source may have an assymetric deposition profile. Similarly changes in operating conditions, for example chamber pressure can modify both  $n(j)$  and  $A(j)$ . Hence the performance of the source depends on source geometry, deposition rate and the operating conditions within the coating chamber.

With the aim of predicting profiled thickness coatings, this early deposition theory has been re-examined and a computer based model developed capable of integrating the vapour flux from multiple source, both real and virtual, to predict the distribution of coating thickness on a component.

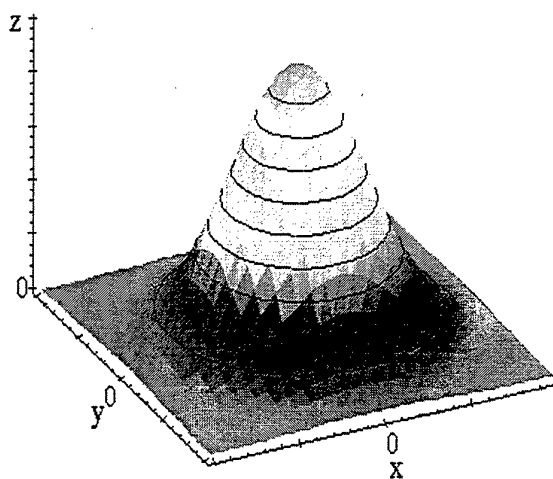
The rate of coating growth, and direction of growth, at any point on a component surface depends on integrating this complex vapour flux field from all sources, both virtual and real, onto an inclined surface element. A vectorial summation is used to predict both the coating thickness and its growth direction.

The coating surface is modelled using a triangular mesh, such that each surface element can be approximated as a flat plate of known geometry and orientation. The influence of substrate rotation about a component axis and the effect of varying the inclination of the component, or rotation about a second axis, can then be accommodated by moving this substrate element within the 3-dimensional coating space to match the expected substrate movement.

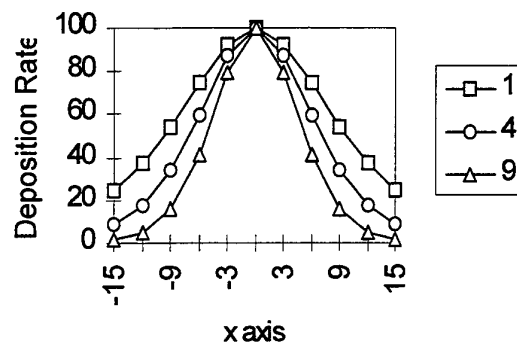
## 4. RESULTS AND DISCUSSION

### 4.1 Predicted Deposition Profiles for a Point-Source Evaporator

By solving the family of equations, implicit in equation 2 it is possible to predict the deposition profile expected for a classic point source evaporator. Results of this modelling are illustrated in Figure 6. The deposition profile exhibits the classic bell shaped curve with a peak rate of deposition directly above the source. It can be seen from Figure 6b that as the value for  $n$  (an index defining the source geometry) increases, the evaporant plume is more focused. The implication of this is that substrates have to be directly over the source, or be rotated through the evaporant flux if a uniform and acceptable deposition rate is to be achieved.



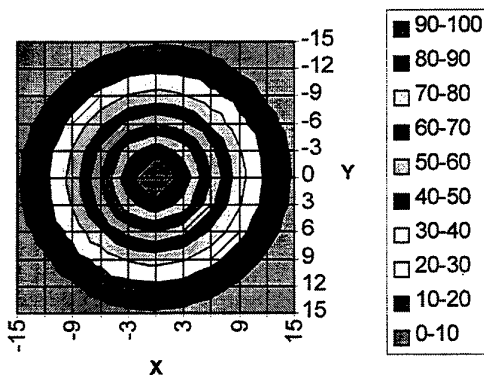
a) 3-dimensional surface for  $n = 4$

Effect of varying  $n$ 

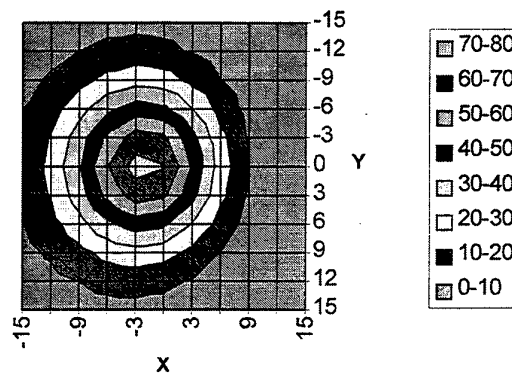
b) Characteristic bell shaped curve for  $n=1, 4$  and  $9$

Figure 6 Predicted deposition profiles for a point source evaporator

When an inclined substrate is held over such a vapour source, the peak deposition rate (maximum coating thickness) measured on the substrate is displaced from the centreline of the evaporant source. In addition, the maximum coating thickness measured on the substrate is reduced as the vapour flux arrives at an oblique incident vapour flux results in an assymetric coating thickness distribution on the substrate. This is illustrated in Figure 7.



a)  $\alpha = 0^\circ$



b)  $\alpha=45^\circ$

Figure 7 Contour plots of predicted deposition profiles for a flat, non inclined substrate ( $\alpha = 0^\circ$ ) with a substrate inclined at  $45^\circ$ .

This bell shaped evaporation profile and the assymetric distribution profile for inclined substrates is problematic when aiming to uniformly coat components. Three solutions are currently in use commercially, and often all three solutions are used in combination to achieve acceptable uniformity. Coating uniformity can be improved by:-

- 1) Moving the components to be coated through the primary plume of evaporation in such a manner that all parts of the component see the peak deposition condition for similar proportions of time in the deposition process.
- 2) Placing components remote but directly above the vapour source. This ensures the deposition cone angle is a minimum and therefore a maximum area has a deposition flux within acceptable limits, say  $\pm 10\%$ . The problem of this approach is that the rate of

deposition with separation distance varies as an inverse square law. Thus increasing the source to substrate distance by a factor of three will result in the deposition rate being reduced almost by a factor of 10, giving protracted

deposition times to achieve acceptable thicknesses.

3) The use of multiple sources, allows the area of uniform deposition to be increased by ensuring the evaporant plumes from each source overlap. This is illustrated in Figure 8.

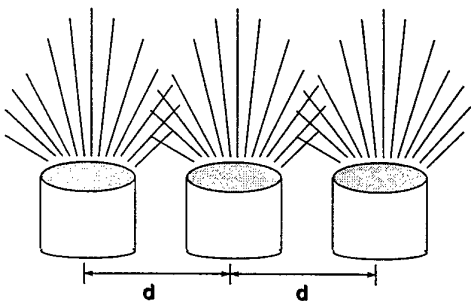
#### 4.2 Predicted Depositions Profiles from Multiple Point Source Evaporators

Figure 8a presents a schematic of a multiple source configuration, where three sources are separated by distance  $D$ .

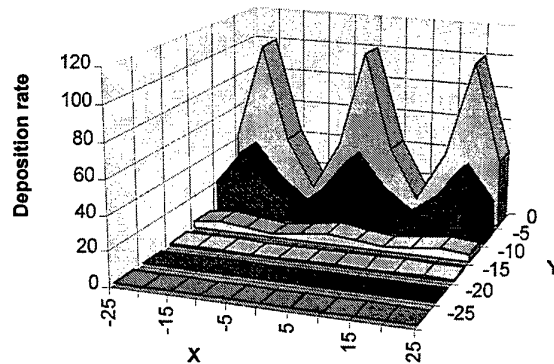
The critical parameter that controls uniformity under multiple source evaporation conditions is the relative separation of the source ( $D$ ) to the height of substrates above the plane of the sources ( $Z$ ).

Figure 8b illustrates the variations in deposition rate predicted when  $Z/D$  is equal to unity. Increasing the  $Z/D$  ratio to two (Figure 8c) gives a much more uniform deposition profile both directly above the source and oblique (offset from the centreline) to the three evaporation sources.

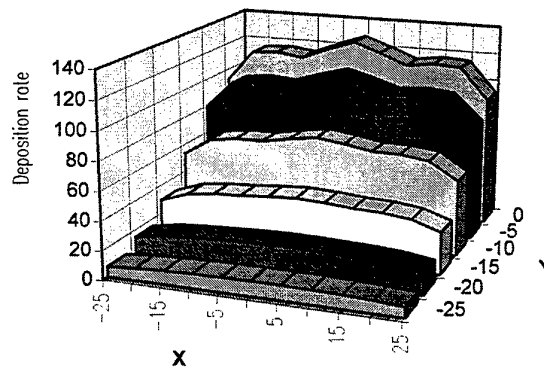
This approach allows much closer working distances, while still achieving uniform deposition, and permits greater component throughput, better yields and more simple planetary motion designs.



a) Schematic of source arrangement



b) Uniformity distribution of  $Z/D=1$



c) Uniformity distribution at  $Z/D=2$

Figure 8 Multiple Source Evaporation

#### 4.3 More Complex Point Source Geometries

The computer model allows more complex point source geometries to be investigated. It is possible to combine arrays of point sources to predict the evaporation behaviour of a large diameter ceramic ingots (termed wide sources). Wide source geometries up to 10cm diameter

have been modelled using either 6 or 13 point sources with good agreement between model predictions and measured evaporation profiles.

Equally, it is not necessary that each point source in a wide source configuration has identical evaporation characteristics. Thus it is possible to model assymetric evaporation behaviour, where due to the scanning pattern of the electron beam one part of the rod evaporation source behaves in a highly focused manner (say  $n=9$ ), while other areas give a more dispersed distribution of the vapour flux extremely wide, uniform vapour flux. (say  $n=1$ ).

One can also envisage models where each of these 'wide source' clusters are used as individual sources in a multiple source evaporation configuration to ensure an extremely wide, uniform vapour flux.

#### 4.4 Comparison of Predicted and Measured Deposition Profiles in a Laboratory EB-PVD Coater

To validate the predictive capability of this computerised evaporation model a number of deposition trials using a laboratory EB-PVD evaporator were compared with the predictions using this model.

The laboratory trials were undertaken in an EB-PVD box coater, with a 680mm cube working chamber.  $ZrO_2$ -8% $Y_2O_3$  was evaporated from source rods 38mm diameter onto substrates, which were heated to 1000°C. The chamber pressure was  $3 \times 10^{-3}$  mbar in an environment of Ar-10%  $O_2$ .

Deposition rates between 0.3 and 6  $\mu\text{m}/\text{min}$  were achieved depending on source to substrate distance, with substrates coated at 3 heights within the chamber, distributed with inclinations of 0, 30 and 60°. The fractograph illustrated in Figure 3 is typical of the coating microstructures obtained in these coating trials

for substrates directly above the evaporation source.

Figure 9 presents a comparison between the predicted and measured results. Agreement is exceedingly good,  $\pm 5\%$  over the range of deposition trials undertaken for the three working heights and three angles considered.

Within this box coater at Cranfield University, the evaporation source can be modelled using a point source evaporator with  $n=4.5$ , to an accuracy of  $\pm 5\%$ . Further, improvements were possible by assuming 'wide source' geometries but at the expense of computing time. A seven point wide source geometry gives high quality predictions for source rods up to 10cm diameter.

### Measured v. Predicted

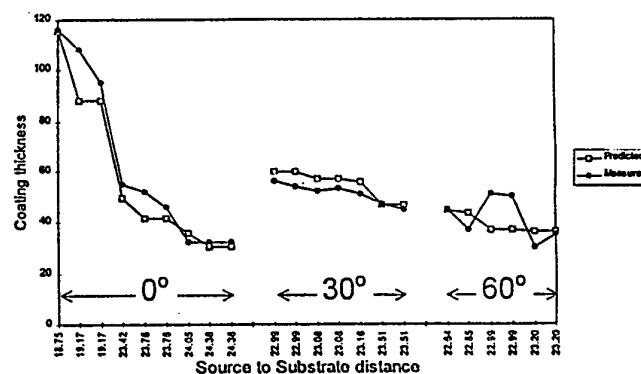


Figure 9 A comparison between measured and predicted deposition profiles

A measure of the 'goodness of fit' of these predictions is apparent from Figure 10. This figure plots a direct comparison between predicted and measured coating thicknesses irrespective of source to substrate separation or substrate inclination. The fit of the model to experiment is extremely good for the EB evaporation source used within the Cranfield coater when  $n=4.5$ . A perfect fit would be the diagonal straight line, included in Figure 10.



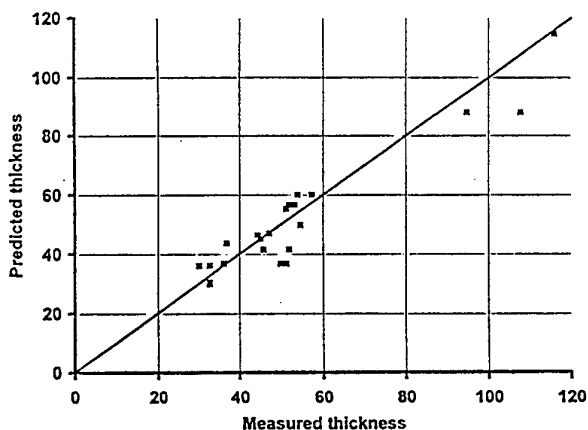


Figure 10 Scatter diagram demonstrating the 'goodness of fit' of the computer model predictions and experimental results

## 5.0 SUMMARY AND CONCLUSIONS

It has been shown possible, using computer methods and a model for an ideal point source evaporator, that one is able to model the rate of deposition, and hence coating thickness, on any substrate positioned, and inclined, within a coater chamber.

The model allows the characteristics of the evaporation source to be determined and permits the prediction of coating thicknesses, and column inclinations, for EB-PVD deposited ceramics on complex substrate geometries.

Ultimately it should be possible to predict the coating thickness profiles around aerofoil sections, as a function of the planetary motion of the component. Although, this has not been demonstrated yet.

Substrate complexity, does not invalidate the model assumptions, although calculations on very complexed geometries would be computer intensive.

One can foresee computer models similar to that proposed in this paper being used to design

mask geometries and component planetary motion, allowing the custom profiling of EB-PVD thermal barrier coatings onto aerofoil section to achieve optimal thermal resistance and good erosion behaviour without compromising the aerodynamic performance of the turbine blade or vane.

## ACKNOWLEDGEMENTS

The authors wish to thank EPSRC for financial support for this work, under the RoPA scheme. They also wish to thank the following organisations for support of work at Cranfield on the development of advanced thermal barrier coating systems: Rolls Royce plc, DERA, CEC.

## 8. REFERENCES

1. Driver D., Hall D. W. and Meetham G. W., in "The development of the gas turbine engines", Applied Science Publishers (London), 1981
2. Morrell P. and Rickerby D.S, "Advantages/Disadvantages of various TBC systems as perceived by the Engine Manufacturer, 85<sup>th</sup> Meeting of the Structural and Materials Panel, Aalborg, Denmark 15/16 Oct. 1997.
3. Brandon J. R., Taylor R. and Morrell P. "Microstructure, composition property, relationships in plasma-sprayed thermal barrier coatings", Surface and Coatings Technology, 50, (1992) 141.
4. Liebert C. H. et al, "Durability of zirconia thermal barrier coatings on air cooled turbine blades in cyclic jet engine operation", NASA TMX-3410 (1976).
5. Grisaffe S. J., "Thermal barrier coatings" NASA TMX-78848 (1978).

6. Rickerby D. S. and Morrell P., "Design and development of EB-PVD thermal barrier coatings for gas turbines" in "High Temperature Engineering" Institute of Materials, London UK (1997) to be published.
7. Strangman T. E. "Tailoring zirconia coatings for performance in a marine gas turbine environment" Journal of Engineering for Gas Turbines and Power, Vol. 112.
8. Nicholls J.R., Yaslier Y. and Rickerby D. S., "Erosion and foreign object damage of thermal barrier coatings" in 4<sup>th</sup> Int. Symp. on High Temperature Corrosion, Les Embiez, France, May 1996
9. Meier S. M. and Gupta D. K., "The evolution of thermal barrier coatings in gas turbine engines applications", Trans. ASME, 116, (1994), 250.
10. R. Nahrwold, cited in 'Deposition Technologies for Films and Coatings', Ed. R. F. Bunshah, Noyes Publications, New Jersey (1982) p83.
11. Massel L. I., and Glang R. 'Handbook of Thin Film Technology' McGraw-Hill (1970).
12. Vossen J. L., and Kern W., 'Thin Film Processes' Academic Press (1978).
13. R. F. Bunshah 'Deposition Technologies for Films and Coatings, Noyes Publications, New Jersey (1982).

# LASER HEATED OXIDE FIBER GROWTH USING MELT MODULATION TECHNIQUE

Ali Sayir,<sup>1,2</sup> Serene C. Farmer,<sup>1</sup> Pat Dickerson,<sup>2</sup> and Arnon Chait<sup>1</sup>

1 NASA Lewis Research Center, MS 106-5  
21000 Brookpark Road, Cleveland, OH 44135, USA

2 Case Western Reserve University, Cleveland, OH - USA

## **SUMMARY**

As a reinforcement for structural composites, single crystal alumina fibers offer low density, high modulus, and high creep resistance. In this study, the laser heated float zone approach was employed to grow c-axis  $\text{Al}_2\text{O}_3$  continuous fibers of high purity and high strength. A new melt modulation technique, laser scanning, avoids the formation of surface induced ripples and allows the growth of 50  $\mu\text{m}$  diameter sapphire fibers with strengths ( $\sim 7$  GPa) significantly greater than either commercially available fibers grown by the edge-defined film growth process ( $\sim 2$ -3 GPa) or laboratory fibers grown by stationary laser heating ( $\sim 5$  GPa). The present work suggests that surface striations are the predominant defects controlling the tensile strength of laser-scanned fibers at room temperature. Several possible mechanisms for inducing surface striations are systematically discussed for several oxide fiber compositions.

## **1 INTRODUCTION**

For reinforcement of high temperature structural composites, oxide-based fibers are particularly desirable because of their resistance to oxidative environments.<sup>1-3</sup>

However, polycrystalline oxide fibers based on alumina or mullite are limited to about 1200 °C due to creep and microstructural instabilities associated with grain growth. On the other hand, single crystal alumina, such as sapphire fibers, are mechanically and intrinsically stable to temperatures as high as 1500 °C.<sup>4-7</sup> Furthermore, sapphire has a low density (3.96 g/cm<sup>3</sup>) and a high modulus ( $\sim 450$  GPa) in the c-direction. Thus, c-axis single crystal sapphire fibers are an attractive candidate as a reinforcement for high temperature intermetallic and ceramic matrix composites.

Commercially available continuous sapphire fibers, such as Saphikon\* fiber, are currently made by the seeded drawing of molten alumina through a refractory capillary (Edge-Defined-Film-Fed-Growth; EFG-method).<sup>8,9</sup> Although the strength of these fibers ( $\sim 2$ -3 GPa) may be sufficient for some composite use, it would be desirable to have stronger sapphire fibers both at room and high temperature. However, the use of the EFG method to improve the tensile strength of the fibers suffers from a variety of problems. First, achieving high purity in the fibers is difficult due to corrosion of the crucible materials.<sup>9,10</sup> Second, opportunities for modifying the

---

\* Saphikon, Inc, NH 03055

fiber structural properties via dopants are limited because they generally exacerbate the corrosion problem. Third, fiber drawing rates, as well as the range of diameters, are limited because of the rate of heat dissipation at the growth interface.<sup>9-11</sup>

The limitations of the EFG-method can possibly be overcome with containerless growth via an externally heated float zone technique such as the laser heated floating zone (LHFZ) method. A significant advantage of the LHFZ method, with the free surface of the melt near the growth interface, is the avoidance of heterogeneous nucleation.<sup>12,13</sup> A characteristic of this technique is a free melt surface with a surface tension gradient that is a result of the temperature gradient along the free interface. A focused laser beam can produce small molten zones, which in turn allows the pulling of small diameter fibers.<sup>14-16</sup> The steep temperature gradients, easy embodiment of dopants in a containerless environment, and the capability of observing certain microscopic defects *in-situ* makes the LHFZ-technique favorable for producing stronger  $\text{Al}_2\text{O}_3$ -based fibers.<sup>17-19</sup> However, the LHFZ-technique does share some disadvantages with the EFG-method. These disadvantages are that volatile systems are difficult to grow and that processing related strains and cracking occur in large diameter fibers.

The objective of this work is to examine the effect of key LHFZ processing parameters on the growth of single crystal  $\text{Al}_2\text{O}_3$  fibers. The parameters examined were growth speed (pull-rate), heating technique and configuration, final fiber diameter and resultant diameter deviation along the fiber length. Both

stationary laser heating and a new laser scanning technique were applied to evaluate their effects on the quality of the fibers. A practical goal was to optimize parameters in order to obtain small diameter c-axis sapphire fibers with the highest strength possible. Thus, the effects of these parameters were evaluated by measurements of room temperature tensile strength and by SEM observations of the flaws controlling the fracture. The resulting morphologies and tensile strength values are compared with commercially available fibers produced by EFG. Possible mechanisms to explain results and achieve improved fibers are discussed.

## 2 EXPERIMENTAL

For the heating source, a coherent  $\text{CO}_2$ -laser beam<sup>#</sup> was used. The laser was split into two beams,  $180^\circ$  apart from each other. Each beam was then focused with zinc-selenide lenses to heat and form the molten zone at the top of a polycrystalline alumina source rod in the center of the processing chamber. The source rod can move vertically through the laser beam and its motion was computer-controlled. The maximum available laser power was 600 watts, but only a small fraction of this power was used because most of the radiation from a  $\text{CO}_2$ -laser (wavelength =  $10.6\ \mu\text{m}$ ) is absorbed by the alumina.<sup>20</sup> The molten zone temperature, which was measured in the infrared radiation region with an

---

<sup>#</sup> Model FH-1500, PRC CORP.,  
Landing, NJ 0785

infrared thermal monitor,<sup>+</sup> was used to control the laser power. However, absolute temperature was not measured because the emissivity of molten alumina is not known. For single crystal fiber growth, a seed crystal (c-axis sapphire) was lowered on the molten alumina until wetting occurred (Fig. 1). The growth direction was chosen to be the c-axis of sapphire (<0001> direction) since it offers the best mechanical properties.<sup>4,6,21-23</sup>

The controllable crystal growth parameters for the LHFZ method include the molten zone height, source to fiber diameter ratio, pull-rate, wetting angle,<sup>24-31</sup> and laser power distribution. For this study the molten zone height was kept constant at approximately one and one-half times the fiber diameter. At steady state, the source to fiber diameter ratio is inversely proportional to the square root of the feed rod to pull rod velocity ratio.<sup>16,19</sup> Adjusting the pull-rate of the crystal and feed-rate of the source material allows the growth of crystals with the required dimensions. The dimensions of a tapered seed fiber, where it joins the molten tip of the feed rod, are also important for obtaining the desired fiber cross-section (Figs. 1 and 2). The diameter of the molten zone or fiber was measured *in-situ* using a helium neon (He-Ne) laser shadow technique.<sup>§</sup> Feedback from the molten zone diameter measurement was used to control source rod and crystal (fiber) motion, thereby maintaining fairly

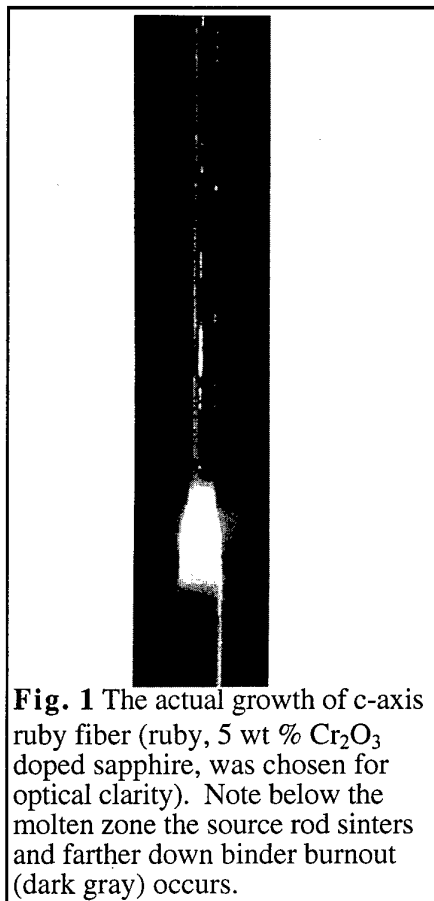


**Fig. 1** The actual growth of c-axis ruby fiber (ruby, 5 wt %  $\text{Cr}_2\text{O}_3$  doped sapphire, was chosen for optical clarity). Note below the molten zone the source rod sinters and farther down binder burnout (dark gray) occurs.

constant fiber diameters over more than 10 cm. All experiments were conducted in air. Neither the crystal nor the source rod was rotated.<sup>32-33</sup>

The meniscus shape at the tri-junction is characterized by the contact (wetting) angle  $\phi$  (Fig. 2), which is the angle between the tangent to the meniscus at the crystal-liquid-vapor tri-junction and the crystal growth axis.<sup>16,26-27</sup> When the crystal grows with a constant cross section, the external surface of the crystal is parallel to the growth axis (Fig. 2). A necessary condition for a constant cross-section is that the meniscus angle  $\phi$  is constant, in general approaching  $\phi_0$ , where  $\phi_0$  is assumed to be a material property for a given growth

<sup>+</sup> Model TM-2, Vanzetti Systems, Stoughton, MA 02072

<sup>§</sup> Model 500-01 Laser Mike Optical Micrometers, Techmet Co., Dayton, OH 45424

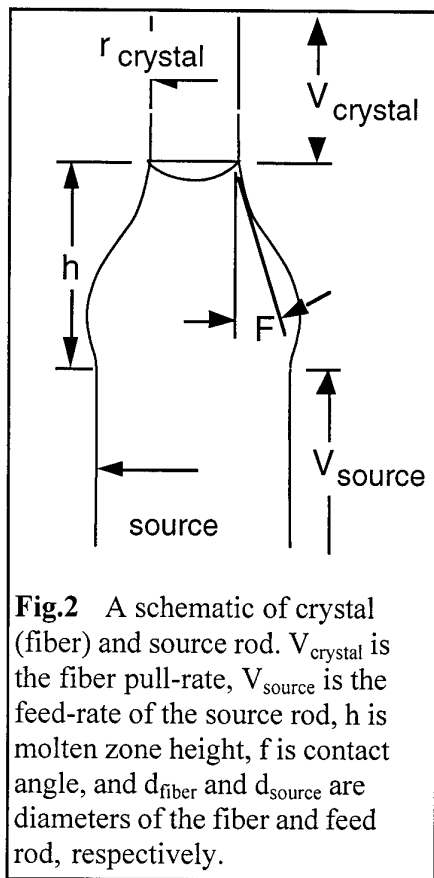


**Fig.2** A schematic of crystal (fiber) and source rod.  $V_{\text{crystal}}$  is the fiber pull-rate,  $V_{\text{source}}$  is the feed-rate of the source rod,  $h$  is molten zone height,  $f$  is contact angle, and  $d_{\text{fiber}}$  and  $d_{\text{source}}$  are diameters of the fiber and feed rod, respectively.

direction.<sup>34,35</sup> Furthermore, the value of  $\phi_0$  has been found to depend on the crystallographic orientation of the crystal surface along the periphery due to the anisotropy of the crystal-vapor interfacial free energy.<sup>31,34-35</sup> The crystal growth process was observed via a video camera. The wetting angle (Fig. 2) was measured from the video image. The apparatus and procedure used to make wetting angle measurements was essentially identical to those employed by Dreeben et. al.<sup>31</sup> in their study.

In previous work,<sup>20</sup> the laser beam was held stationary on the molten zone with a focused circular spot size of approximately 50 to 80  $\mu\text{m}$  and fiber diameters between 50 - 250  $\mu\text{m}$ . In this

study a new technique was used in which the focused laser beam was scanned across the molten zone (transverse to the fiber growth direction). Fibers with high tensile strength values were achieved when the turnover points of the laser beam were outside of the molten zone and the frequency of the scanning was above 20 Hertz. This technique was especially successful for very tight focusing conditions which allowed the growth of very small diameter fibers.

For preparation of the source rod, high purity (99.99% pure) polycrystalline alumina powder<sup>†</sup> was used. This powder was blended with 5 wt % binder<sup>®</sup> and glycerin was used as a plasticizer in a water based slurry. The slurry was then degassed overnight with a moderate vacuum ( $\sim 70 \times 10^3$  Pa) to achieve a high viscosity paste. This paste was extruded with a custom-made mini-extruder, i.e. a modified hypodermic syringe. The plastic syringe wall was replaced within high wear regions to avoid contamination. At least two extrusions were made to minimize porosity in the paste. The extruded source rod was normally 250  $\mu\text{m}$  in diameter and extruded lengths were 15 to 20 cm long. The rods were furnace dried in air at 200  $^{\circ}\text{C}$  for approximately 1 hour and placed in the LHFZ apparatus without any presintering.

The tensile strengths of the processed sapphire fibers were measured at room temperature in ambient air using a commercial load frame at a crosshead

<sup>†</sup> CERAC/Pure (325 mesh), Ceralox Corp., Tucson, AZ 08576

<sup>®</sup> Methocel 20-231, The Dow Chemical Company, Midland, MI 48674

speed of 0.125 cm/min. A test gauge length of 6 mm was used to increase the probability of retaining the primary fracture surfaces. In these tests, cardboard was used as fiber tabs to minimize bending stresses.<sup>20</sup> Each data point and its upper and lower limits represent the mean and plus or minus one standard deviation of 20 fibers respectively.

### 3. RESULTS

In the early part of this work, some fibers were produced with growth direction different than the c-axis. The tensile strength of these fibers were found to be independent of growth deviations from 1° to 7° from the <0001> axis. This is in agreement with the findings of previous researchers<sup>21,22</sup> and indicates that the room temperature tensile strength was determined from the size and random orientation of flaws rather than from the anisotropic character of the fracture toughness,  $K_{Ic}$ , of sapphire.<sup>22,23</sup> Nevertheless, the tensile strength values reported in the remainder of this work are for the fibers evaluated very close to the <0001> axis (within 2°).

The uniformity of the fiber cross-sectional dimensions along its length was found to have a profound effect on tensile strength. For stationary laser heating Fig. 3 shows the dependence of tensile strength on average fiber diameter deviation as measured along the length of fibers of nominally 100  $\mu\text{m}$  average diameter. The average meniscus angle,  $\phi$ , measured during these growth runs was  $15^\circ \pm 4^\circ$ . Generally, fibers pulled with a velocity ratio  $V_f/V_s$  (ratio of pull-rate of

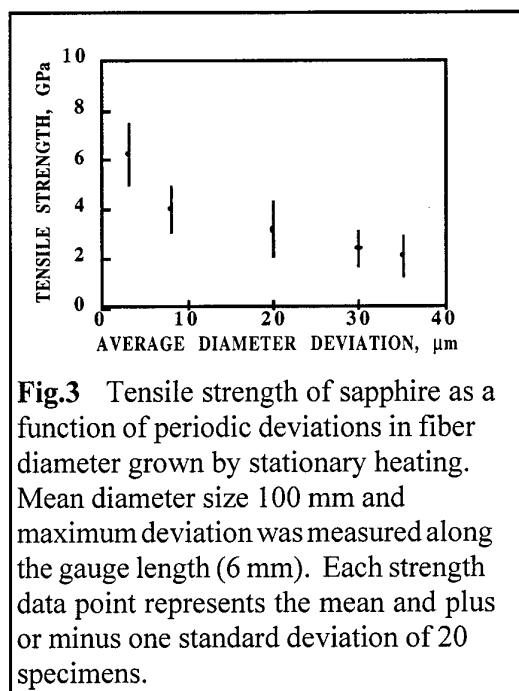


**Fig.3** Tensile strength of sapphire as a function of periodic deviations in fiber diameter grown by stationary heating. Mean diameter size 100  $\mu\text{m}$  and maximum deviation was measured along the gauge length (6 mm). Each strength data point represents the mean and plus or minus one standard deviation of 20 specimens.

the fiber to feed-rate of the source rod) of 9 or less had consistently smaller diameter deviations and higher tensile strengths than fibers pulled with higher ratios. Except for the results in Fig. 3, most fibers reported in the remainder of this work using stationary and scan heating had diameter deviations less than  $\pm 5 \mu\text{m}$  and less than  $\pm 3 \mu\text{m}$ .

The effect of the pull-rate on the tensile strength of fibers was also studied. In these studies, fiber diameter and the  $V_f/V_s$  ratio were held constant at 80  $\mu\text{m}$  and 5, respectively. Figure 4 shows that the fiber tensile strength decreased as the fiber pull-rate increased to 10 cm/h when stationary heating of the molten zone was used. However, the scan technique, in which the laser beam is scanned across the molten zone at a frequency of 20 Hz, allowed growth rates of 50 cm/h and did not cause a loss in fiber tensile strength from its slow growth rate level of 7 GPa.

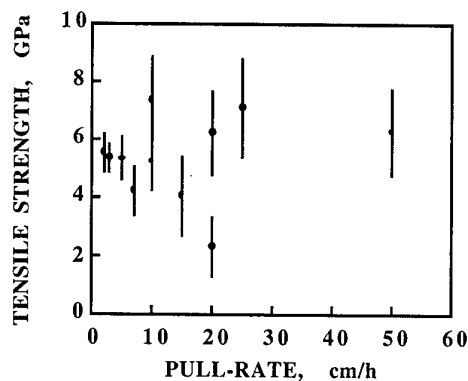


**Fig.4** Tensile strength of sapphire as function of the pull-rate of the fiber. These fibers were produced with 70 to 80  $\mu\text{m}$  diameter and velocity ratios of 9. The empty circles represent stationary heating and filled circles represent the scanning technique. Each data point represents the mean and plus or minus one standard deviation of 20 specimens.

Figure 5 depicts fiber surface morphologies corresponding to three different laser heating configurations. Figure 6a is the surface morphology of  $\langle 0001 \rangle$  direction grown fiber with stationary heating of a tightly focused laser beam. It reveals that there are two distinct surface features which are characteristic of the stationary LHFZ method. The first type are periodic and localized surface undulations which appear around the circumference. These are similar to the ripples left on a sandy beach and are therefore called "ripples".<sup>36-41</sup> The second type are periodic striations which extend around the fiber circumference and are parallel to the liquid-solid interface with a wavelength of 2 to 4  $\mu\text{m}$ . These striations are similar to surface waves (with very low amplitude) that were

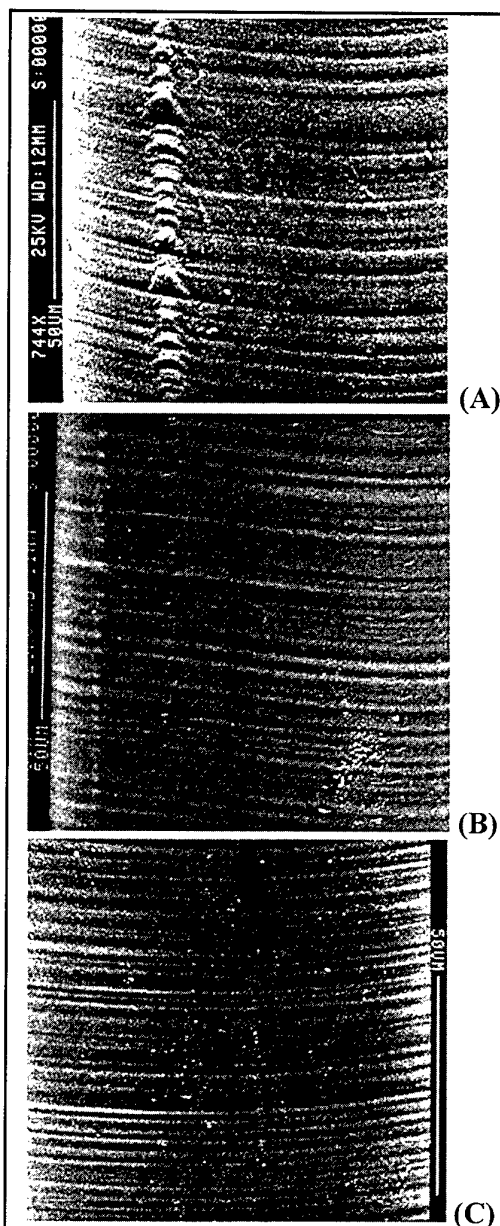


**Fig.5** SEM photographs of sapphire fiber surfaces. (A) stationary heating; (B) and (C) heating with the transverse scanning technique. Note that for the fiber shown in (B) the scan-length was within the molten zone whereas the fiber depicted in (C) had a scan-length outside of the molten zone.





**Fig. 6** SEM photograph of stationary heated fiber, showing laser induced ripples. Note that fracture originated from the ripples.

frozen during solidification. These two surface morphologies ("ripples" and "striations") differ from each other markedly. The "ripples" are highly localized and convex toward the liquid at the liquid-solid interface, whereas the striations encompass the entire fiber circumference and are parallel to the liquid-solid interface.

Figure 5b shows a photograph of a sapphire fiber grown with the scanning heating technique at which the scan-length was within the fiber diameter. In Fig. 5c the transverse scan-length was larger than the molten zone diameter. In the former case (Fig. 5b) the laser heat was concentrated at two points (the turnover points) where the laser scan has its maximum amplitude and thus this local area of the fiber was heated more than average. The latter (Fig. 5c) had the turnover points of the laser scan outside the molten zone and showed no indication of ripple formation. The latter scan configuration, with the elimination of ripple formation showed consistently

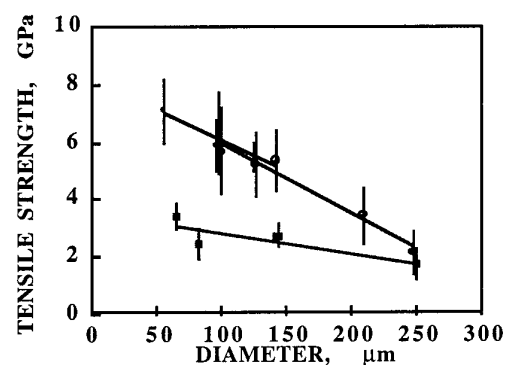


**Fig. 7** Tensile strength of sapphire as a function of the fiber diameter. Growth rate is 10 cm/h with velocity ratio of 9. The empty and filled circles represent the defocused stationary and focused scanning heating, respectively. EFG-grown fiber (Saphikon) is also reported for comparison (filled squares). Each data point represents the mean and plus or minus one standard deviation of 20 specimens. Solid lines represent least squares linear fitting of the empirical data using mean values.

higher tensile strength. This is especially important since almost all fibers, with very few exceptions, fractured from surface flaws (at room temperature). A typical fracture origin via a ripple surface flaw is depicted in Fig. 6.

Figure 7 shows the tensile strength of the LHFZ sapphire fibers as a function of final fiber diameter. The fiber pull-rate and velocity ratio were held constant at 10 cm/h and 9, respectively. The tensile strength of the fibers decreased monotonically with increasing fibers diameter. The tensile strength versus diameter characteristics of commercially available EFG sapphire (Saphikon) are also compared in Fig. 7 with LHFZ

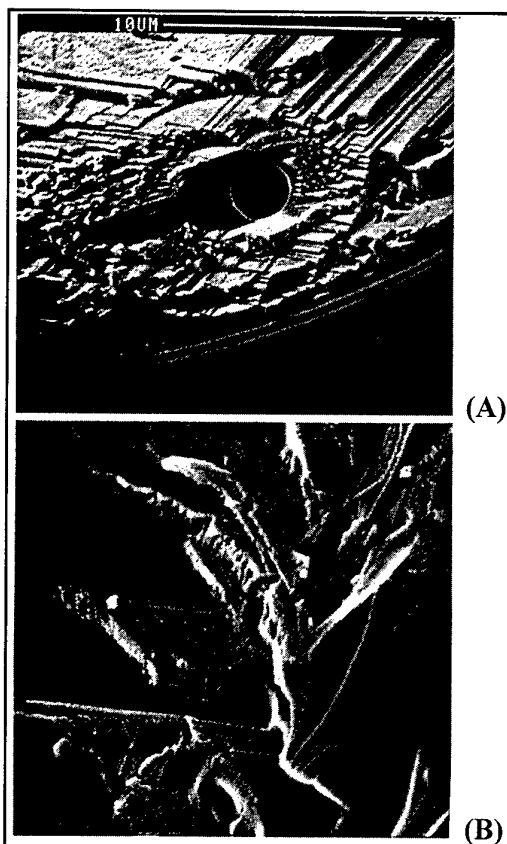


**Fig.8** SEM photographs of the LHFZ-grown (A) and EFG-grown fibers(B) showing the strength controlling internal flaw (void). Fracture from the internal voids was common for EFG-fibers. Less than 1 % of the LHFZ-fibers fractured from internal voids. Note the high magnification of the fracture origin showing typical fracture steps, which in this case were not directly related to the mist and hackle. (Field of view 20x20 $\mu$ m).

fibers. The tensile strength values of Saphikon fibers were considerably lower than LHFZ fibers. This may be due to a faster pulling rate and/or contamination from the crucibles. In contrast to the LHFZ fibers, the tensile strength of EFG fibers was not controlled by surface flaws but by processing related internal flaws (voids) as shown in Fig. 8

#### 4. DISCUSSION

There are two general results which emerge from this study when room temperature tensile strength is used as a measure of the effectiveness of LHFZ growth method. First, in contrast to the EFG fibers, the sapphire fibers grown under essentially all conditions examined here have higher tensile strengths. This improved tensile strength is related to the avoidance of internal voids, leaving only surface-related defects to control fracture of the LHFZ fibers. Second, surface flaws for the LHFZ are apparently related to three surface features that arise in the molten zone during laser processing and are then frozen into the solid fiber. These are gross diameter deviations along the fiber length, localized ripples that predominate during stationary and low amplitude scan heating, and periodic striations that occur more readily in laser grown fibers than in EFG. In the following paragraphs, possible mechanisms for the above surface phenomena are discussed with the purpose of suggesting processing methods for producing sapphire fibers with high and reproducible tensile strengths.

The diameter deviations and the tensile strength of the fibers may be closely related to the shape of the meniscus at the crystal-liquid-vapor tri-junction. The departure of the contact angle from its equilibrium value ( $\phi_0$ ) and therefore the long and short term diameter fluctuation was minimized by careful temperature control and most importantly by control of the diameter uniformity of the source rod. Diameter deviations, which were correlated to a decrease in fiber tensile strength (Fig.3),

# LASER HEATED OXIDE FIBER GROWTH USING MELT MODULATION TECHNIQUE

Ali Sayir,<sup>1,2</sup> Serene C. Farmer,<sup>1</sup> Pat Dickerson,<sup>2</sup> and Arnon Chait<sup>1</sup>

- 1 NASA Lewis Research Center, MS 106-5  
21000 Brookpark Road, Cleveland, OH 44135, USA
- 2 Case Western Reserve University, Cleveland, OH - USA

## SUMMARY

As a reinforcement for structural composites, single crystal alumina fibers offer low density, high modulus, and high creep resistance. In this study, the laser heated float zone approach was employed to grow c-axis  $\text{Al}_2\text{O}_3$  continuous fibers of high purity and high strength. A new melt modulation technique, laser scanning, avoids the formation of surface induced ripples and allows the growth of 50  $\mu\text{m}$  diameter sapphire fibers with strengths ( $\sim 7$  GPa) significantly greater than either commercially available fibers grown by the edge-defined film growth process ( $\sim 2$ -3 GPa) or laboratory fibers grown by stationary laser heating ( $\sim 5$  GPa). The present work suggests that surface striations are the predominant defects controlling the tensile strength of laser-scanned fibers at room temperature. Several possible mechanisms for inducing surface striations are systematically discussed for several oxide fiber compositions.

## 1 INTRODUCTION

For reinforcement of high temperature structural composites, oxide-based fibers are particularly desirable because of their resistance to oxidative environments.<sup>1-3</sup>

However, polycrystalline oxide fibers based on alumina or mullite are limited to about 1200 °C due to creep and microstructural instabilities associated with grain growth. On the other hand, single crystal alumina, such as sapphire fibers, are mechanically and intrinsically stable to temperatures as high as 1500 °C.<sup>4-7</sup> Furthermore, sapphire has a low density (3.96 g/cm<sup>3</sup>) and a high modulus ( $\sim 450$  GPa) in the c-direction. Thus, c-axis single crystal sapphire fibers are an attractive candidate as a reinforcement for high temperature intermetallic and ceramic matrix composites.

Commercially available continuous sapphire fibers, such as Saphikon\* fiber, are currently made by the seeded drawing of molten alumina through a refractory capillary (Edge-Defined-Film-Fed-Growth; EFG-method).<sup>8,9</sup> Although the strength of these fibers ( $\sim 2$ -3 GPa) may be sufficient for some composite use, it would be desirable to have stronger sapphire fibers both at room and high temperature. However, the use of the EFG method to improve the tensile strength of the fibers suffers from a variety of problems. First, achieving high purity in the fibers is difficult due to corrosion of the crucible materials.<sup>9,10</sup> Second, opportunities for modifying the

---

\* Saphikon, Inc, NH 03055

fiber structural properties via dopants are limited because they generally exacerbate the corrosion problem. Third, fiber drawing rates, as well as the range of diameters, are limited because of the rate of heat dissipation at the growth interface.<sup>9-11</sup>

The limitations of the EFG-method can possibly be overcome with containerless growth via an externally heated float zone technique such as the laser heated floating zone (LHFZ) method. A significant advantage of the LHFZ method, with the free surface of the melt near the growth interface, is the avoidance of heterogeneous nucleation.<sup>12,13</sup> A characteristic of this technique is a free melt surface with a surface tension gradient that is a result of the temperature gradient along the free interface. A focused laser beam can produce small molten zones, which in turn allows the pulling of small diameter fibers.<sup>14-16</sup> The steep temperature gradients, easy embodiment of dopants in a containerless environment, and the capability of observing certain microscopic defects *in-situ* makes the LHFZ-technique favorable for producing stronger  $\text{Al}_2\text{O}_3$ -based fibers.<sup>17-19</sup> However, the LHFZ-technique does share some disadvantages with the EFG-method. These disadvantages are that volatile systems are difficult to grow and that processing related strains and cracking occur in large diameter fibers.

The objective of this work is to examine the effect of key LHFZ processing parameters on the growth of single crystal  $\text{Al}_2\text{O}_3$  fibers. The parameters examined were growth speed (pull-rate), heating technique and configuration, final fiber diameter and resultant diameter deviation along the fiber length. Both

stationary laser heating and a new laser scanning technique were applied to evaluate their effects on the quality of the fibers. A practical goal was to optimize parameters in order to obtain small diameter c-axis sapphire fibers with the highest strength possible. Thus, the effects of these parameters were evaluated by measurements of room temperature tensile strength and by SEM observations of the flaws controlling the fracture. The resulting morphologies and tensile strength values are compared with commercially available fibers produced by EFG. Possible mechanisms to explain results and achieve improved fibers are discussed.

## 2 EXPERIMENTAL

For the heating source, a coherent  $\text{CO}_2$ -laser beam<sup>#</sup> was used. The laser was split into two beams,  $180^\circ$  apart from each other. Each beam was then focused with zinc-selenide lenses to heat and form the molten zone at the top of a polycrystalline alumina source rod in the center of the processing chamber. The source rod can move vertically through the laser beam and its motion was computer-controlled. The maximum available laser power was 600 watts, but only a small fraction of this power was used because most of the radiation from a  $\text{CO}_2$ -laser (wavelength =  $10.6 \mu\text{m}$ ) is absorbed by the alumina.<sup>20</sup> The molten zone temperature, which was measured in the infrared radiation region with an

---

<sup>#</sup> Model FH-1500, PRC CORP.,  
Landing, NJ 0785

infrared thermal monitor,<sup>+</sup> was used to control the laser power. However, absolute temperature was not measured because the emissivity of molten alumina is not known. For single crystal fiber growth, a seed crystal (c-axis sapphire) was lowered on the molten alumina until wetting occurred (Fig. 1). The growth direction was chosen to be the c-axis of sapphire (<0001> direction) since it offers the best mechanical properties.<sup>4,6,21-23</sup>

The controllable crystal growth parameters for the LHFZ method include the molten zone height, source to fiber diameter ratio, pull-rate, wetting angle,<sup>24-31</sup> and laser power distribution. For this study the molten zone height was kept constant at approximately one and one-half times the fiber diameter. At steady state, the source to fiber diameter ratio is inversely proportional to the square root of the feed rod to pull rod velocity ratio.<sup>16,19</sup> Adjusting the pull-rate of the crystal and feed-rate of the source material allows the growth of crystals with the required dimensions. The dimensions of a tapered seed fiber, where it joins the molten tip of the feed rod, are also important for obtaining the desired fiber cross-section (Figs. 1 and 2). The diameter of the molten zone or fiber was measured *in-situ* using a helium neon (He-Ne) laser shadow technique.<sup>§</sup> Feedback from the molten zone diameter measurement was used to control source rod and crystal (fiber) motion, thereby maintaining fairly

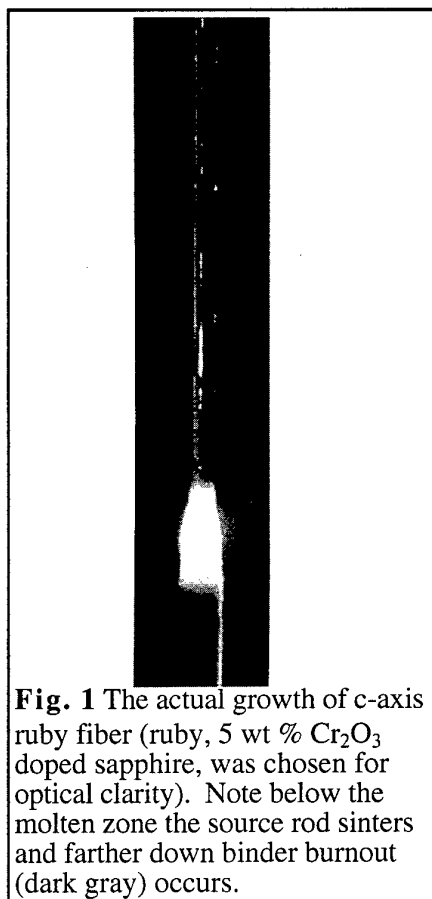


**Fig. 1** The actual growth of c-axis ruby fiber (ruby, 5 wt %  $\text{Cr}_2\text{O}_3$  doped sapphire, was chosen for optical clarity). Note below the molten zone the source rod sinters and farther down binder burnout (dark gray) occurs.

constant fiber diameters over more than 10 cm. All experiments were conducted in air. Neither the crystal nor the source rod was rotated.<sup>32-33</sup>

The meniscus shape at the tri-junction is characterized by the contact (wetting) angle  $\phi$  (Fig. 2), which is the angle between the tangent to the meniscus at the crystal-liquid-vapor tri-junction and the crystal growth axis.<sup>16,26-27</sup> When the crystal grows with a constant cross section, the external surface of the crystal is parallel to the growth axis (Fig. 2). A necessary condition for a constant cross-section is that the meniscus angle  $\phi$  is constant, in general approaching  $\phi_0$ , where  $\phi_0$  is assumed to be a material property for a given growth

<sup>+</sup> Model TM-2, Vanzetti Systems, Stoughton, MA 02072

<sup>§</sup> Model 500-01 Laser Mike Optical Micrometers, Techmet Co., Dayton, OH 45424

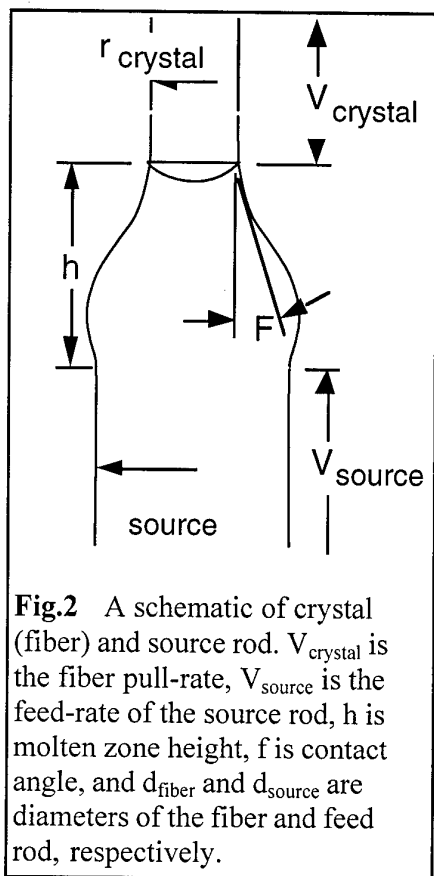


**Fig.2** A schematic of crystal (fiber) and source rod.  $V_{\text{crystal}}$  is the fiber pull-rate,  $V_{\text{source}}$  is the feed-rate of the source rod,  $h$  is molten zone height,  $f$  is contact angle, and  $d_{\text{fiber}}$  and  $d_{\text{source}}$  are diameters of the fiber and feed rod, respectively.

direction.<sup>34,35</sup> Furthermore, the value of  $\phi_0$  has been found to depend on the crystallographic orientation of the crystal surface along the periphery due to the anisotropy of the crystal-vapor interfacial free energy.<sup>31,34-35</sup> The crystal growth process was observed via a video camera. The wetting angle (Fig. 2) was measured from the video image. The apparatus and procedure used to make wetting angle measurements was essentially identical to those employed by Dreeben et. al.<sup>31</sup> in their study.

In previous work,<sup>20</sup> the laser beam was held stationary on the molten zone with a focused circular spot size of approximately 50 to 80  $\mu\text{m}$  and fiber diameters between 50 - 250  $\mu\text{m}$ . In this

study a new technique was used in which the focused laser beam was scanned across the molten zone (transverse to the fiber growth direction). Fibers with high tensile strength values were achieved when the turnover points of the laser beam were outside of the molten zone and the frequency of the scanning was above 20 Hertz. This technique was especially successful for very tight focusing conditions which allowed the growth of very small diameter fibers.

For preparation of the source rod, high purity (99.99% pure) polycrystalline alumina powder<sup>†</sup> was used. This powder was blended with 5 wt % binder<sup>®</sup> and glycerin was used as a plasticizer in a water based slurry. The slurry was then degassed overnight with a moderate vacuum ( $\sim 70 \times 10^3$  Pa) to achieve a high viscosity paste. This paste was extruded with a custom-made mini-extruder, i.e. a modified hypodermic syringe. The plastic syringe wall was replaced within high wear regions to avoid contamination. At least two extrusions were made to minimize porosity in the paste. The extruded source rod was normally 250  $\mu\text{m}$  in diameter and extruded lengths were 15 to 20 cm long. The rods were furnace dried in air at 200 °C for approximately 1 hour and placed in the LHFZ apparatus without any presintering.

The tensile strengths of the processed sapphire fibers were measured at room temperature in ambient air using a commercial load frame at a crosshead

<sup>†</sup> CERAC/Pure (325 mesh), Ceralox Corp., Tucson, AZ 08576

<sup>®</sup> Methocel 20-231, The Dow Chemical Company, Midland, MI 48674

speed of 0.125 cm/min. A test gauge length of 6 mm was used to increase the probability of retaining the primary fracture surfaces. In these tests, cardboard was used as fiber tabs to minimize bending stresses.<sup>20</sup> Each data point and its upper and lower limits represent the mean and plus or minus one standard deviation of 20 fibers respectively.

### 3. RESULTS

In the early part of this work, some fibers were produced with growth direction different than the *c*-axis. The tensile strength of these fibers were found to be independent of growth deviations from 1° to 7° from the <0001> axis. This is in agreement with the findings of previous researchers<sup>21,22</sup> and indicates that the room temperature tensile strength was determined from the size and random orientation of flaws rather than from the anisotropic character of the fracture toughness,  $K_{Ic}$ , of sapphire.<sup>22,23</sup> Nevertheless, the tensile strength values reported in the remainder of this work are for the fibers evaluated very close to the <0001> axis (within 2°).

The uniformity of the fiber cross-sectional dimensions along its length was found to have a profound effect on tensile strength. For stationary laser heating Fig. 3 shows the dependence of tensile strength on average fiber diameter deviation as measured along the length of fibers of nominally 100  $\mu\text{m}$  average diameter. The average meniscus angle,  $\phi$ , measured during these growth runs was  $15^\circ \pm 4^\circ$ . Generally, fibers pulled with a velocity ratio  $V_f/V_s$  (ratio of pull-rate of

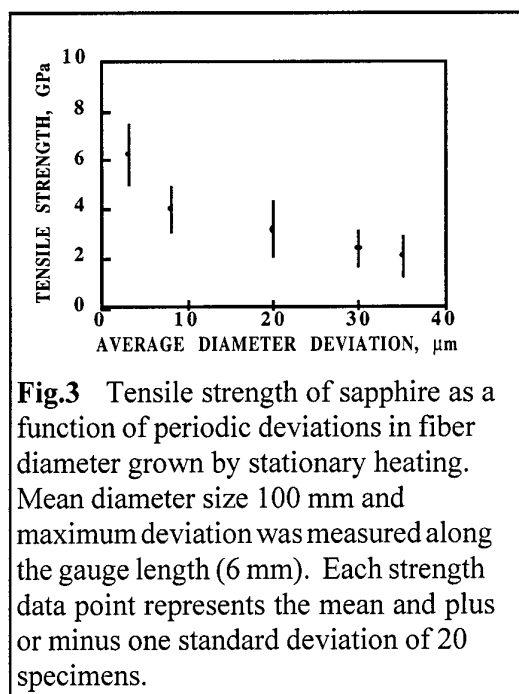


**Fig.3** Tensile strength of sapphire as a function of periodic deviations in fiber diameter grown by stationary heating. Mean diameter size 100  $\mu\text{m}$  and maximum deviation was measured along the gauge length (6 mm). Each strength data point represents the mean and plus or minus one standard deviation of 20 specimens.

the fiber to feed-rate of the source rod) of 9 or less had consistently smaller diameter deviations and higher tensile strengths than fibers pulled with higher ratios. Except for the results in Fig. 3, most fibers reported in the remainder of this work using stationary and scan heating had diameter deviations less than  $\pm 5 \mu\text{m}$  and less than  $\pm 3 \mu\text{m}$ .

The effect of the pull-rate on the tensile strength of fibers was also studied. In these studies, fiber diameter and the  $V_f/V_s$  ratio were held constant at 80  $\mu\text{m}$  and 5, respectively. Figure 4 shows that the fiber tensile strength decreased as the fiber pull-rate increased to 10 cm/h when stationary heating of the molten zone was used. However, the scan technique, in which the laser beam is scanned across the molten zone at a frequency of 20 Hz, allowed growth rates of 50 cm/h and did not cause a loss in fiber tensile strength from its slow growth rate level of 7 GPa.

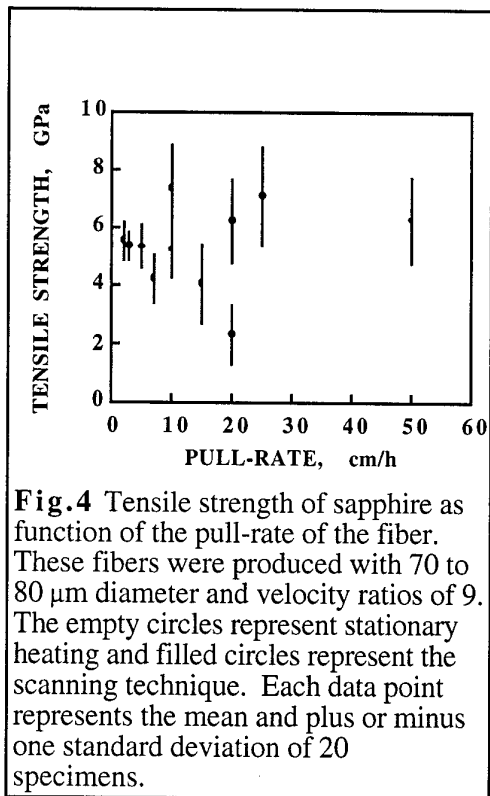
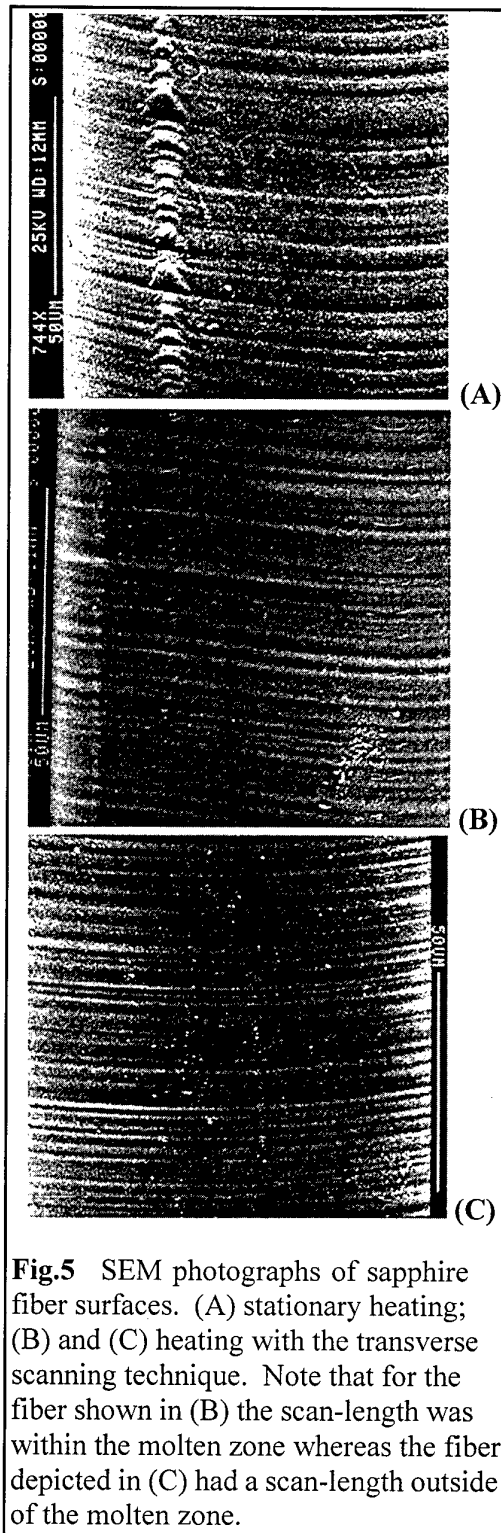


Figure 5 depicts fiber surface morphologies corresponding to three different laser heating configurations. Figure 6a is the surface morphology of  $\langle 0001 \rangle$  direction grown fiber with stationary heating of a tightly focused laser beam. It reveals that there are two distinct surface features which are characteristic of the stationary LHFZ method. The first type are periodic and localized surface undulations which appear around the circumference. These are similar to the ripples left on a sandy beach and are therefore called "ripples".<sup>36-41</sup> The second type are periodic striations which extend around the fiber circumference and are parallel to the liquid-solid interface with a wavelength of 2 to 4  $\mu\text{m}$ . These striations are similar to surface waves (with very low amplitude) that were







**Fig. 6** SEM photograph of stationary heated fiber, showing laser induced ripples. Note that fracture originated from the ripples.

frozen during solidification. These two surface morphologies ("ripples" and "striations") differ from each other markedly. The "ripples" are highly localized and convex toward the liquid at the liquid-solid interface, whereas the striations encompass the entire fiber circumference and are parallel to the liquid-solid interface.

Figure 5b shows a photograph of a sapphire fiber grown with the scanning heating technique at which the scan-length was within the fiber diameter. In Fig. 5c the transverse scan-length was larger than the molten zone diameter. In the former case (Fig. 5b) the laser heat was concentrated at two points (the turnover points) where the laser scan has its maximum amplitude and thus this local area of the fiber was heated more than average. The latter (Fig. 5c) had the turnover points of the laser scan outside the molten zone and showed no indication of ripple formation. The latter scan configuration, with the elimination of ripple formation showed consistently

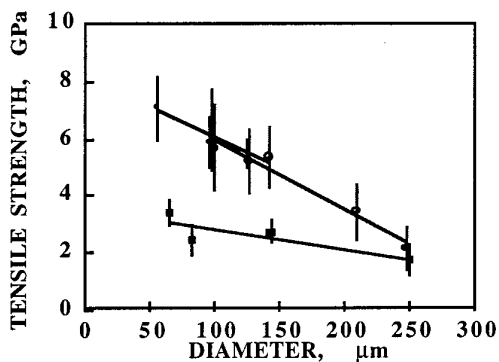


**Fig. 7** Tensile strength of sapphire as a function of the fiber diameter. Growth rate is 10 cm/h with velocity ratio of 9. The empty and filled circles represent the defocused stationary and focused scanning heating, respectively. EFG-grown fiber (Saphikon) is also reported for comparison (filled squares). Each data point represents the mean and plus or minus one standard deviation of 20 specimens. Solid lines represent least squares linear fitting of the empirical data using mean values.

higher tensile strength. This is especially important since almost all fibers, with very few exceptions, fractured from surface flaws (at room temperature). A typical fracture origin via a ripple surface flaw is depicted in Fig. 6.

Figure 7 shows the tensile strength of the LHFZ sapphire fibers as a function of final fiber diameter. The fiber pull-rate and velocity ratio were held constant at 10 cm/h and 9, respectively. The tensile strength of the fibers decreased monotonically with increasing fibers diameter. The tensile strength versus diameter characteristics of commercially available EFG sapphire (Saphikon) are also compared in Fig. 7 with LHFZ

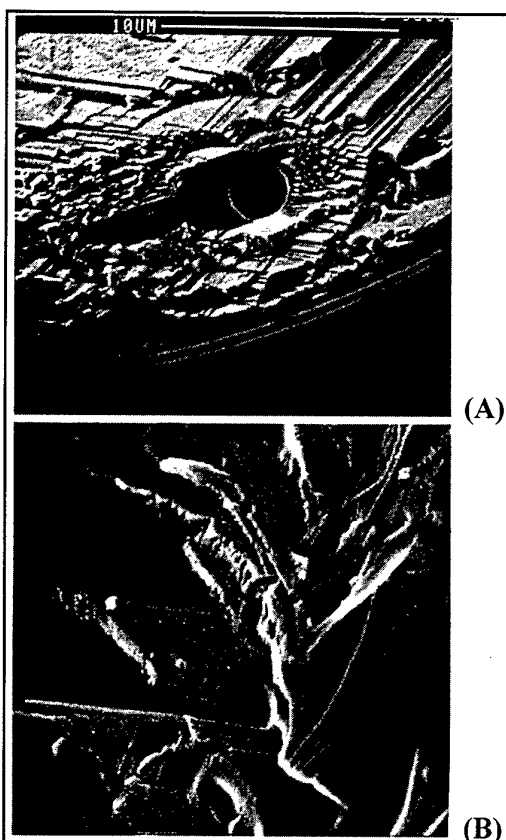


**Fig.8** SEM photographs of the LHFZ-grown (A) and EFG-grown fibers(B) showing the strength controlling internal flaw (void). Fracture from the internal voids was common for EFG-fibers. Less than 1 % of the LHFZ-fibers fractured from internal voids. Note the high magnification of the fracture origin showing typical fracture steps, which in this case were not directly related to the mist and hackle. (Field of view 20x20 $\mu$ m).

fibers. The tensile strength values of Saphikon fibers were considerably lower than LHFZ fibers. This may be due to a faster pulling rate and/or contamination from the crucibles. In contrast to the LHFZ fibers, the tensile strength of EFG fibers was not controlled by surface flaws but by processing related internal flaws (voids) as shown in Fig. 8

#### 4. DISCUSSION

There are two general results which emerge from this study when room temperature tensile strength is used as a measure of the effectiveness of LHFZ growth method. First, in contrast to the EFG fibers, the sapphire fibers grown under essentially all conditions examined here have higher tensile strengths. This improved tensile strength is related to the avoidance of internal voids, leaving only surface-related defects to control fracture of the LHFZ fibers. Second, surface flaws for the LHFZ are apparently related to three surface features that arise in the molten zone during laser processing and are then frozen into the solid fiber. These are gross diameter deviations along the fiber length, localized ripples that predominate during stationary and low amplitude scan heating, and periodic striations that occur more readily in laser grown fibers than in EFG. In the following paragraphs, possible mechanisms for the above surface phenomena are discussed with the purpose of suggesting processing methods for producing sapphire fibers with high and reproducible tensile strengths.

The diameter deviations and the tensile strength of the fibers may be closely related to the shape of the meniscus at the crystal-liquid-vapor tri-junction. The departure of the contact angle from its equilibrium value ( $\phi_0$ ) and therefore the long and short term diameter fluctuation was minimized by careful temperature control and most importantly by control of the diameter uniformity of the source rod. Diameter deviations, which were correlated to a decrease in fiber tensile strength (Fig.3),

are a result of the difference between the actual and equilibrium meniscus angle ( $\phi_0 - \phi$ ). This difference may also promote very small scale faceting. However, SEM characterization of the fibers grown in the  $\langle 0001 \rangle$  direction showed no visible faceting. The  $\{0001\}$  basal plane in sapphire is one of the low free energy planes, the other being the  $\{0112\}$  rhombohedral plane.<sup>21</sup> It was expected that the fiber diameter variations will presumably lead to growth twins at the solid-liquid interface providing an array of re-entrant corners that allow rapid freezing of larger diameter crystals with lower tensile strength. However, SEM and optical microscopic characterization of fracture surfaces failed to show twins. The tensile strength values reported here are very high. Therefore, expected twin sizes are beyond the resolution of SEM and may require TEM characterization.

The high strength results in Fig. 4 were achieved by a more uniform temperature distribution in the molten zone as a result of the scanning heating technique. Uniform growth temperature is a prerequisite for any crystal growth system. By using a scan amplitude greater than the zone width, the most important effect of the scanning technique was the minimization of laser damage caused by overheating at the scan velocity nodes (i.e., the turning point at the two extreme points of the scanning cycle). This damage took the form of local surface undulations. The avoidance of surface undulations ("ripples") was particularly important since fracture origins could easily be traced to this damage (Fig. 6). This was a dominant feature of stationary laser heating resulting from a large amount of energy absorbed in a short time and in a small

area. Using a defocused stationary laser beam, one can grow sapphire fibers which will not have ripple formation (Fig. 7). Fibers on the order of 100 to 150  $\mu\text{m}$  diameter showed high tensile strength of approximately 5 GPa (empty circles in Fig. 7). However, this technique with a defocused laser beam is limited to large diameter fibers ( $>100 \mu\text{m}$ ) since molten zone stability requirements<sup>24-27,42</sup> do not allow growth of small diameter fibers from a large molten zone.<sup>20</sup> In this work, this lower limit has been observed to be 100  $\mu\text{m}$ . Fig. 7 also depicts that the tensile strength of fibers decreases with increasing fiber diameter. The monotonic decrease in Fig. 7 with increasing fiber diameter was independent of the scanning or stationary heating technique. One possible explanation is the increased probability of finding weak strength controlling surface flaws due to the larger surface area of the large diameter fibers. Another possibility is that the large diameter fibers may have contained considerable internal stresses due to temperature gradients.<sup>16</sup> However, the calculation of the thermal field and the internal stress state (as discussed below and in Appendix A) does not justify the latter conjecture.

The calculation of the thermal field in the crystal requires the solution of the heat conduction equation together with the equation for thermal radiation transport. The latter transport is important for oxide fibers since they are semi-transparent to thermal radiation. A recent analytical solution of the coupled conduction-radiation equations (Appendix A) was applied to sapphire fibers in order to compute the axial and radial temperature fields in the crystal.<sup>43</sup> The principal findings are that the axial

temperature decays almost exponentially to the ambient temperature within approximately 2 cm of the liquid solid interface, with a weak dependency on the fiber diameter. The axial temperature gradient near the solidification interface is estimated to be about  $10^4$  °C/cm for a 100  $\mu\text{m}$  fiber, and about  $8.5 \times 10^4$  °C/cm for a fiber with 250  $\mu\text{m}$  diameter. From results shown in Appendix A, the axial temperature gradient is a weak function of the fiber radius. The axial stresses are temporal at temperatures above 1600 °C and can be estimated using viscoplastic models,<sup>44</sup> which include temporal evaluation of dislocations. However, room temperature tensile strength of these fibers is determined from minute surface flaws (e.g., ripples) and not from the dislocation activity.<sup>20,22</sup> These flaws are presumed to be the result of axial stresses at lower temperatures. With this in mind it is still notable that the increase in the axial stress with fiber diameter correlates well with the trends depicted in Fig. 7. The radial dependence of the thermal field is very weak, depending primarily on the convective cooling rate to the surroundings (Appendix A). The calculated total radial temperature drop is only about 0.1 °C, resulting in a radial temperature gradient of about 10 °C/cm.

The permanent impressions of the observed crests and troughs of the ripples along the fiber axis may be explained by a spatial enhancement of the laser energy on the surface of molten alumina.<sup>36-41</sup> That this damage was not propagated in the circumferential direction along the striations suggests the notion that the damage produced here is due to localized interaction of the electric-field (E-field) of the laser with the molten alumina. At a normal

incidence the quasistatic field is most intense along the fiber axis and perpendicular to the striations. As pointed out by Bloembergen,<sup>38</sup> there may exist intense local electric field enhancements within small surface defects such as, within the striations. The suggested model by Bloembergen<sup>38</sup> and Temple<sup>39</sup> might then explain the observed damage in Figs. 5a and 6. Their model suggests localized field enhancement within defects along the E-field which coincides with the axis of fibers in this work (perpendicular to the striations). This means that linearly polarized radiation incident upon striations will produce the largest perturbation whereas the perturbation goes to zero for defects running parallel to the incident polarization direction (along the striations which coincide with the circumferential direction of the molten zone).

The second type of surface defect, striations (Fig. 5), is seen for both the stationary and scanning laser heating configurations. These striations can not be the result of a local heating effect since laser heating has a gaussian distribution over 25 to 40  $\mu\text{m}$ ,<sup>14,42</sup> which is considerably larger than the typical periodicity of the observed striations (3 to 4  $\mu\text{m}$ ). Striations are periodic modifications to the fiber diameter; as such, they must be associated with a time periodicity of the contact angle. This periodicity may be traced to several possible origins. The first possibility is that the striations are caused by the puller mechanism, which is driven by a DC-servo motor. For such a mechanism to be the cause of the striations, their spatial wavelength must be proportional to the pulling rate. The striation wavelength was observed to be about 3

to 4  $\mu\text{m}$  and did not change when the pull-rate was increased from 1 to 50 cm/h. Furthermore, striations can not be a result of the pulling mechanisms since similar, but much shallower, striations were observed in EFG grown fibers which uses a conveyor belt type pulling mechanism without discrete steps. Nevertheless, pulling mechanisms produce disturbances and may provide inputs for other sources of striations which are discussed later.

Another possible source for striations is fluid instabilities within the molten zone. In the absence of forced flow due to fiber rotation, the flow inside the zone is driven primarily by two mechanisms. Gravity (bouyancy, natural) driven convection and surface tension driven convection must be considered. Natural convection in the zone will always occur in practice via an interaction between any horizontal radial temperature gradient in the melt with the vertical gravitational field.<sup>45</sup> Additionally, the top half of the zone (from the center to the solidification interface) is susceptible to Benard instability<sup>46</sup> when a hot fluid is placed below a cold fluid (this occurs since the temperature of the solidification front is colder than the temperature in the middle of the zone). If these flows are unstable, they may cause periodic fluctuations in the contact angle leading to striations. Rough estimates of the potential contribution from these mechanisms may be obtained by computing the relevant non-dimensional group, which in this case is defined as the Rayleigh number.<sup>46</sup> The appropriate characteristic length and temperature scales for the Rayleigh number for natural convection are the zone radius and radial temperature difference between the centerline and the

free surface. For a 100  $\mu\text{m}$  diameter fiber with a one degree temperature difference (representing an upper bound) the Rayleigh number is of order of  $10^{-7}$ . This means that natural convection should not play any significant role in the process. For Benard convection, the relevant characteristic length is the zone half height and the characteristic temperature difference is measured between the zone interior at the mid-height and the melting temperature. The Rayleigh number obtained for this case is of order of  $10^{-6}$  which is far below the Benard stability limit of 1708.<sup>46</sup> Therefore we exclude fluid instabilities originating from natural convection effects as the source of striations.

The axial temperature gradient along the free surface of the molten zone results in a gradient in surface tension. For most materials, including oxides, surface tension is lower at the hot (center) region than at the cold regions (melting and solidification fronts). This tangential stress gradient along the free surface results in so-called surface tension driven convection (Marangoni or thermocapillary convection). The effect of this flow on the thermal field is estimated by the value of the Marangoni number, defined as:

$$M_a \equiv - \frac{\delta\sigma}{\delta T} \Delta T L \eta^{-1} \alpha^{-1}$$

where  $M_a \equiv - \frac{\delta\sigma}{\delta T}$  is the surface tension derivative with respect to temperature,  $\Delta T$  is the characteristic tangential temperature difference across a distance  $L$ , and  $\eta$  and  $\alpha$  are the dynamic viscosity and thermal diffusivity, respectively. We estimate the temperature difference to be about 50 °C, over a half zone

distance of about 50  $\mu\text{m}$ . The Marangoni number is then about 10.

Velten, Schwabe and Scharman<sup>47</sup> provide insight as to the nature of the thermocapillary flows in liquid bridges, similar to the LHFZ and EFG processes. These authors have systematically studied the time periodic nature of instabilities of thermocapillary convection in cylindrical liquid bridges (i.e., captive drops between the top and bottom of vertically aligned cylinders held at different temperatures). They studied liquids with Prandtl numbers ( $\text{Pr} = \nu / \alpha$ ,  $\nu$  is the kinematic viscosity) of 1, 7, and 49, while molten alumina has a Prandtl number of about 10. From their studies, we expect the critical Marangoni number (when a steady laminar convection turns into a time periodic one), to be about  $10^3$  to  $10^4$ . Since this value is much larger than the estimated Ma-number in our case, we conclude that the surface tension driven convection in the zone is laminar and steady in time. From the definition of the surface tension Reynolds number,  $\text{Re}_\sigma$ , we can also compute an estimate for a characteristic velocity,  $U$ ,

$$\text{Re}_\sigma \equiv \frac{\text{Ma}}{\text{Pr}} = \frac{U L}{\nu}$$

This velocity is computed to be about 10 cm/s, which is in agreement with the value obtained from a full numerical simulation of the EFG process.<sup>48</sup> Since  $U \gg$  pull-rate, and because impurities typically possess very high Schmidt numbers ( $\text{Sc} = \nu / D$ ,  $D$  is species diffusivity) of order of  $10^2$ , one can expect a well mixed melt and a weak radial impurity segregation over the bulk of the fiber. The very near of the fiber edge may show other effects which may

be important for local segregation phenomena. The thermal field inside the melt may also be affected by convection to some degree, but only numerical simulations of the process may further elucidate the level of coupling between the flow and thermal fields. Furthermore, since the time periodicity of an unstable Marangoni flow should be independent of the pull-rate, one must expect a proportionality relationship between the pull-rate and the striations wavelength if they were to originate from such time periodic flows. Since their wavelength was found to be independent of the pull-rate, and because the estimated Ma was much below the critical Ma-number for the onset of melt oscillations, we conclude that the origin of the striations can not be attributed to time dependent melt oscillations.

Yet another possibility which may be considered is a capillary instability of a thin liquid (melt) film on a solid fiber. This type of instability is driven by surface tension which acts to minimize the free surface area. One might hypothesize a short thin melt film to exist near the vicinity of the triple point at the solidification front (where the solid, melt, and gas come into contact). Thin films are known to be unstable to capillary instabilities.<sup>49</sup> However, the estimated linearly unstable mode for this case (i.e. the infinitesimally small spatial mode predicted to grow fastest) is a long wave with characteristic wavelength of  $\lambda = 2\sqrt{2\pi} r$  ( $r$  is radius).<sup>50</sup> For a 50  $\mu\text{m}$  fiber the predicted wavelength is about 450  $\mu\text{m}$  which is two orders of magnitudes larger than the observed wavelength.

The last possible origin of the striations is linked to dynamic stability properties

of the molten zone. Liquids held by surface tension typically exhibit dynamic properties resembling the behavior of underdamped physical systems. For example, liquid drops excited by sudden motion tend to oscillate until viscous forces dampen the motion. In the LHFZ process, small modulations in the contact angle responsible for small diameter variations (striations) may then be the result of an oscillating free surface. In the absence of an external periodic force, such a system will oscillate at its own natural frequency following a perturbation, thereby always producing striations with a constant wavelength which will dampen in time. The molten zone natural frequency and damping characteristics are complex functions of its size, surface tension, and other thermophysical properties. To produce continuous striations, this mechanism must be continuously excited by perturbations containing a wide frequency range (e.g., periodic pulses provided through the DC-servo motor). A more complete description of the zone as a dynamic system is provided by considering the zone as a thermo-fluid system with free surfaces. In such models, the zone size and shape is uniquely determined by the combined conduction-convection heat transport and fluid motion equations.<sup>48,50</sup> While these models were formulated as steady state models (in a frame of reference moving at a constant pull rate), an explicit addition of the time dependent terms in the governing equations may indeed provide an answer to whether the zone, when viewed as a dynamic thermo-fluid system, is sensitive to small forcing modulations in the control parameters leading to sustained oscillations in contact angle. In addition to periodic pulses or variations in the pull-rate,

input power modulations should also be considered as potential sources. The study of such possibilities as a cause of striations is beyond the scope of this work and will be considered in a separate publication.

## **5. CONCLUSIONS**

Higher strength (6 to 7 GPa) sapphire fibers were produced in this study by a more uniform temperature distribution in the molten zone as a result of a new laser growth technique. This technique, laser scanning, avoided surface induced ripple formation which occurs during stationary heating and limits strength to 5 GPa. The scanning technique also allowed the rapid growth of high strength sapphire fibers with diameters near 50  $\mu\text{m}$ . These fibers displayed greater tensile strengths than those of commercially available EFG fibers ( $\sim 2\text{--}3$  GPa). The laser grown fibers fractured primarily from surface defects which are related to processing induced striations which extend around the fiber circumference. On the other hand, the strength controlling flaws in EFG fibers were internal voids. The avoidance of internal voids during laser processing could be attributed to slower growth rates, purer starting material, or to the containerless processing technique.

While possible mechanisms have been suggested to explain the results of this study, further studies are clearly required. First, a theoretical understanding of molten zone stability properties and its relation to striation formation should be pursued. Such an understanding may enable designers to optimize processing conditions. Initial analyses presented here suggest the

striations are the result of molten zone mechanical oscillations induced by processing related perturbations. Second, microscopic defects and their identification (e.g., micro facets and/or twins) via high resolution microscopy is needed to understand surface microstructure and improve the processing conditions. Nevertheless, the strength values reported here (6 to 7 GPa) are among the highest tensile strength values reported in the literature for continuous fibers and are considerable fractions (~20 %) of the theoretical strength value for sapphire (45 GPa). Finally, optimization of room temperature strength may or may not enhance high temperature behavior of sapphire fibers. Since these fibers should have their greatest technical significance at elevated temperatures, studies are needed to determine how the processing conditions and mechanisms discussed here affect fiber strength under conditions appropriate for processing and use in high temperature structural composites.

## 6. REFERENCES

1. A. G. Evans, "Perspective on the Development of High-Toughness Ceramics," *J. Am. Ceram. Soc.*, 73 (2) (1990) 187-193.
2. D. B. Marshall and J. E. Ritter, "Reliability of Advanced Structural Ceramics and Ceramic-Matrix Composites- A Review," *Am. Ceram. Soc. Bull.*, 66 (2) (1987) 309-317.
3. R. A. Signorelli and J. A. DiCarlo, "High Temperature Metal and Ceramic Matrix Composites," *J. Metals*, 37 (6) (1985) 41-42.
4. J. D. Snow and A. H. Heuer, "Slip Systems in  $Al_2O_3$ ," *J. Am. Ceram. Soc.*, 56 (3) (1973) 153-157.
5. B. J. Pletka, T. E. Mitchell, and A. H. Heuer, "Dislocation Structures in Sapphire Deformed by Basal Slip," *J. Am. Ceram. Soc.*, 57 (1974) 388-393.
6. R. F. Firestone and A. H. Heuer, "Creep Deformation of  $0^\circ$  Sapphire," *J. Am. Ceram. Soc.*, 59 (1-2) (1976) 24-29.
7. W. R. Cannon and T. G. Langdon, "Creep of Ceramics; Part 1 Mechanical Characteristics," *J. Mat. Sci.*, 18 (1983) 21-28.
8. B. Cockayne, "Developments in Melt-Grown Oxide Crystals," *J. Crystal Growth*, 34 (1968) 60-70.
9. J. T. A. Pollock, "Filamentary Sapphire; Part 1 Growth and Microstructural Characterization," *J. Mat. Sci.*, 7 (1972) 631-648.
10. K. Wada and K. Hoshikawa, "Growth and Characterization of Sapphire Ribbon Crystal," *J. Cryst. Growth*, 50 (1980) 151-154.
11. J. T. A. Pollock, "Filamentary Sapphire, Part 2 Fracture Strength in Tension," *J. Mat. Sci.*, 7 (1972) 649-653.
12. J. S. Haggerty, W. P. Menashi, and J. F. Wenckus, "Method for Forming Refractory Fibers by Laser Energy," U.S. Patent (3,944,640), March 16, 1976.
13. K. Eickoff and K. Guers, "Tiegelfreies Zonenschmelzen von Rubinkristallen Durch Aufheizen der Schmelzzone Mittels Laser," *J. Crystal. Growth*, 6 (1969) 21-23.
14. J. Mazumdar and W. M. Steen, "Heat Transfer Model for CW Laser Material Processing," *J. Appl. Phys.*, 51 (2) (1980) 941-947.
15. N. Kobayashi, "Power Required to form a Floating Zone and the Zone Shape," *J. Cryst. Growth*, 43 (1978) 417-420.



16. R. S. Feigelson, "Growth of Single Crystal Fibers," MRS Bull./Oct. (1988) 47-55.
17. K. M. Kim, "Microdefects in Small-Diameter Silicon Crystals Grown by the Pedestal Technique," J. Appl. Phys., 50 (2) (1979) 1135-1139.
18. M. Saifi, B. Dubois, E. M. Vogel, and F. A. Thiel, "Growth of Tetragonal BaTiO<sub>3</sub> Single Crystal Fibers," J. Mat. Res., 1 (3) (1986) 452-456.
19. R. S. Feigelson, "Pulling Optical Fibers," J. Cryst. Growth, 79 (1986) 669-680.
20. A. Sayir, J. B. Hurst, and S. Jones, "High Strength Single Crystal Alumina Fibers," in Proceedings of the 2nd Annual HITEMP Review (1989), NASA conference Publication 10039.
21. W. D. Scott, "Rhombohedral Twinning in Aluminum Oxide," in "Deformation of Ceramic Materials," eds. by R. C. Bradt and R. E. Tressler (1974) pp.151-167.
22. S. M. Wiederhorn, "Fracture of Sapphire," J. Am. Ceram. Soc., 52 (9) (1969) 485-491.
23. M. Iwasa and R. C. Bradt, "Fracture Toughness of Single-Crystal Alumina," in Advances in Ceramics; Vol.10 "Fracture and Properties of MgO and Al<sub>2</sub>O<sub>3</sub> Ceramics," ed. by W. D. Kingery (1979) pp.747-749.
24. E. Green, "Governing Equations for the Shapes of Molten Zones," J. Appl. Physics., 35 (4) (1964) 1297-1302.
25. L. B. Humphreys, J. A. Heminger, and G. W. Young, "Morphological Instability in a Float Zone," J. Cryst. Growth, 100 (1990) 31-50.
26. R. A. Brown, "Theory of Transport Processes in Single Crystal Growth from the Melt," AIChE Journal, 34 (6) (1988) 881-911.
27. S. R. Coriell, S. C. Hardy, and M. R. Cordes, "Stability of Liquid Zones," J. Colloid and Interface Sci., 60 (1) (1977) 126-132.
28. R. K. Sristava, P. A. Ramachandran, and M. P. Dudokovich, "Czochralski Growth of Crystals," J. Electrochem. Soc., 133 (5) (1986) 1009-1015.
29. A. L. Gentile and D. F. Elwell, "Crystal Growth," MRS Bull., 10 (1988) 23-60.
30. K. M. Kim, A. B. Dreben, and A. Schujko, "Maximum Stable Zone Length in Float-Zone Growth of Small Diameter Sapphire and Silicon Growth," J. Appl. Phys., 50 (6) 1979) 4472-4474.
31. A. B. Dreeben, K. M. Kim, and A. Schujko, "Measurement of Meniscus Angle in Laser Heated Float Zone Growth of Constant Diameter Sapphire Crystals," J. Cryst. Growth, 50 (1980) 126-132.
32. Y. Kamotani and J. Kim, "Effect of Zone Rotation in Oscillatory Thermocapillary Flow in Simulated Floating Zones," J. Cryst. Growth, 87 (1988) 62-68.
33. C. E. Chang and W. R. Wilcox, "Inhomogeneities due to Thermocapillary Flow in Floating Zone Melting," J. Cryst. Growth, 28 (1975) 8-14.
34. D. T. J. Hurle, "Control of Diameter in Czochralski and Related Crystal Growth Techniques," J. Cryst. Growth, 42 (1977) 473-482.
35. K. Tagaki and M. Ishi, "Crystal Growth of Sapphire Filaments by a Laser-Heated Floating Zone Technique," J. Mat. Sci., 12 (1977) 517-521.
36. S. E. Clark, N. C. Kerr and D. C. Emmony, "Anomalous Laser-Induced Periodic Surface Structures," J. Phys. D: Appl. Phys. 22 (1969) 527-534.

37. N. C. Kerr, B. A. Omar, S. E. Clark, and D. C. Emmony, "The Topography of Laser-Induced Ripple Structures," *J. Phys. D: Appl. Phys.* 23 (1990) 884-889.
38. N. Bloembergen, "Fundamentals of Laser-Solid Interactions," *AIP Conf. Proc.*, "Laser Solid Interactions in Laser Processing," Vol. 50, (1979) 1-9.
39. P. A. Temple and M. J. Soileau, "Polarization Charge Model for Laser-Induced Ripple Patterns in Dielectric Materials," *IEEE journal of Quantum Electronics*, QE-17, 10 (1981) 2067-2071.
40. N. C. Kerr, S. E. Clark, and D. C. Emmony, "High Resolution Imaging Studies into the Formation of Laser-Induced Periodic Surface Structures," *Appl. Optics*, 28 (17) (1989) 3718-3724.
41. N. R. Isenor, "CO<sub>2</sub> Laser-Produced Ripple Patterns on Ni<sub>x</sub>P<sub>1-x</sub> Surfaces," *Appl. Phys. Lett.*, 31 (3) (1977) 148-150.
42. M. Lax, "Temperature Rise Induced by a Laser Beam," *J. Appl. Physics*, 48 (9) (1977) 3919-3924.
43. S. A. Korpela, A. Chait, and M. Kassemi, "Heat Transfer in Fiber Formation," *Formation*, submitted to *J. Cryst. Growth* (1992).
44. C. T. Tsai, M. W. Yao, and A. Chait, "Prediction of Dislocation Generation During Bridgman Growth of GaAs Crystals," accepted for *J. Crystal Growth*.
45. V. S. Arpachi and P. S. Larsen, "Convection Heat Transfer," Prentice Hall, NJ, 1989.
46. P. G. Drazin and W. H. Reid, *Hydrodynamic Stability*, Cambridge University Press, NY, 1985.
47. R. Velten, D Schwabe, and A. Scharmann, "The Periodic Instability of Thermocapillary Convection in Cylindrical Liquid Bridges," *Phys. of Fluids A* 3 (2), (1991), 267 - 279.
48. G. W. Young and A. Chait, "Steady State Thermal Solutal Diffusion in a Float Zone," *J. Crystal Growth*, 96 (1989) 65-69.
49. E. Ballister, private communication, 1993.
50. A. L. Yarin, A. Oron, and P. Rosenau, "Capillary Instability of Thin Liquid Film on a Cylinder," *Phys. Fluids A* 5 (1) (1993) 91-98.

## APPENDIX A

The cooling of the semi-transparent sapphire fiber is controlled by the interplay between conduction and radiation heat transport modes. While the former is a diffusion process, the latter also implies an action-at-a-distance process in which heat energy can be transported to any volume element inside the fiber or directly to the outside. The equations which govern this combined process form a set of integro-differential equations which are nonlinear, non-local and are very difficult to solve. Using the differential approximation, Korpela et al.<sup>43</sup> have succeeded in formulating the governing differential equations and then solving them for the cooling of sapphire fibers grown from the melt. Their solution methodology uses an asymptotic analysis valid for small values of optical thickness, Biot number, Bi, (which measures the effect of convective cooling outside the fiber), and Peclet number (which measures the effect of pull-rate). In this Appendix we report only on certain findings from their study which are relevant to our work. The principal result of interest from their work is that

the axial temperature profile can be approximated as an exponential function which decays away from the solid melt interface

$$T(r, z) \sim \exp(-g z) \times J_0(\sqrt{2 \text{Bi}} r) \quad (\text{A1})$$

where  $g = f$  (pull-rate, optical and conduction properties, convection to outside) and  $J_0$  is the Bessel function of zeroth order. The axial temperature gradient at the interface ( $z=0$ ),  $\partial T(r, z) / \partial z$ , is controlled by the characteristic exponent  $g$ . The radial temperature field variation appears as a second order effect in the solution, since convection to the outside is represented by small parameter (Biot number). A series expansion of

$$J_0(\sqrt{2 \text{Bi}} r) = 1 + \text{Bi} r^2 + \dots \quad (\text{A2})$$

shows the radial temperature profile to be flat to a leading order, with a small parabolic variation along the radius. The radial temperature gradient at the interface,  $\partial T(r, z) / \partial z$ , is therefore linear in  $r$ , reaching a maximum at the fiber outer diameter. Due to smallness of the Biot number, the maximum radial gradient is very small in relation to the axial temperature gradient at the interface.

## SMART CURING OF COMPOSITE MATERIALS IN AUTOCLAVE

P. DUBLINEAU, J. CINQUIN

AEROSPATIALE  
CCR Louis Blériot  
12 Rue Pasteur, B.P. 76,  
92152 Suresnes Cedex, France

### 1 ABSTRACT

When fabricating structures made of fibre reinforced organic matrix composites careful attention must be paid to the manufacturing procedures.

The quality of the part may suffer and the cost may become excessive if improper manufacturing processes are used.

Therefore, the manufacturing process must be selected carefully to ensure that both the quality and the cost are acceptable. The major process variables which must be selected and controlled are the heat and pressure applied during autoclave curing of thermosetting matrix composites.

Although the aforementioned process variables can be chosen empirically, the empirical approach is undesirable and often impractical. Empirical, trial and error methods are expensive and time consuming, and do not ensure that the resulting processing conditions are optimum.

It is far more advantageous and convenient to establish the required process conditions and process variables either by the use of analytical models, or by expert systems.

AEROSPATIALE as developed software SCOOP -POLYM ® for modelling and simulation of cure processes of structures made of fibre reinforced organic matrix composites.

This presentation describes a computerised definition of optimise cure cycle to the simultaneous control of materials reaction behaviour and consolidation dynamics in autoclave.

General output of cure simulation is the optimum cure cycle used by the autoclave temperature controller.

This cycle takes in account :

- Part definition ( material, fibre, geometry)
- Polymerisation tools and environment
- Autoclave characteristic
- Autoclave loading (position of parts inside the autoclave)

In addition a dynamic control of the polymerisation could be made using dielectric sensors inside the composite part.

The real time control can be use as a feedback closed-loop control modification of autoclave power based on actual reaction behaviour of material.

Cure simulation and dynamic control of the autoclave process improve cured product quality and reduce fabrication cost by providing :

- Process optimisation
- Reduced process inconsistencies and product rejections
- Verification of process reaction behaviour kinetics
- Non destructive verification of cured properties
- Accurate, permanent process documentation
- Flexibility in adapting to new of modified process (material, tool...)

### 2 GENERAL PHYLOSOPHIE

The cure cycle optimisation software "POLYM" allows end users to define the more appropriate temperature cycle to apply to the autoclave. This software, design for industrial needs can be used in the case of multi parts polymerisation in the same time in the autoclave. For this simulation, the input of the software "POLYM" are :

- Materials data (thermal, physico-chemical, kinetics and rheology equations)
- Tooling and environment material data (thermal)
- Parts geometry and disposition in the autoclave
- Autoclave parameters (mainly the cartography of the thermal exchange coefficient in convection)

To manage this, the software is organised with :

- Data base integration (materials, tooling, parts, loading).
- A calculation module for thermal cycle optimisation based on the selection of critical point chosen automatically by the software depending of the parts and of the loading.
- Displaying the results, temperature profile, polymerisation ratio, viscosity, polymerisation speed versus time and position in the thickness of the part.

### 3 CURE CYCLE OPTIMISATION PRINCIPLE

Using the simulation process, we can obtain useful information to help to the design of the tooling, to help to the part disposition inside the autoclave and to define the optimum cure cycle. The questions to which a simulation software is very powerful are :

- Does the part could be processed with the proposed configuration ?
- Which thermal cycle do we have to use ?
- Which area could be critical in term of polymerisation ratio, exothermic...

The utilisation of such a software is based on the principles defined hereafter :

- The requirements we have to fulfil for a cure cycle definition are defined by temperatures limitation, degree of polymerisation, part homogeneity. These specifications have to be applied to the part, to the environment and to the heating machine (power limitation). These requirements could be for example a difference in the degree of polymerisation in all the points of the part not over a specified value during the gelification, or at the end of the polymerisation step. A mesh of the part could be define to verify that all the requirements are fulfil at any location of the part.

To save computing time, some critical points could be selected to avoid to make the cure cycle optimisation at any points of the mesh. The important parameter to select the critical points are the part thickness (e) and the transfer coefficient (h).

- The optimisation of the cure cycle is done only on the selected critical points. A simplified version could be used with only one parameter to optimise, the isothermal temperature of the gelification process. Other parameters such as the heating rate are imposed to the system.
- At the end, it is checked that all the points of the part fulfil the requirement. If it is not the case, we can remake the cure cycle optimisation including the point that did not fulfil the requirement as a critical point.

### 4 HOW DOES IT WORK

The software is organised with data base on the materials, the environmental products and on the parts. The part geometry could be define using the CAO files.

#### Material data base :

The material data base includes thermal and physico-chemical parameter of the material. Some requirements are added such as maximum difference temperature allowed on the part, maximum difference in the degree of conversion allowed on the part, definition of different isothermal temperatures needed by the material (gelification, polymerisation)

#### Tools data base :

The tools data base include the tool thermal characteristics.

#### Environmental products data base :

This data bas include the thermal characteristics of the upper and lower environment. These characteristics are obtained by global measurement including vacuum bag, peel ply...

#### Autoclave data base :

This data base includes all the thermal characteristics of the autoclave.

Two types of characterisation can be done.

A standard one. If the tooling is mainly 2D or quasi 2D, the convection coefficients do not depends on the position and on the number of tooling inside the autoclave. A global characterisation of the autoclave is enough.

A specific one. If the part is strongly 3D, this characterisation is related to one and only one part with one determined position in the hot air flow of the part.

The calculus is based on the resolution of a finite difference method of the heat equation with the chemical kinetic equation given the exothermic versus time, versus temperature and versus degree of polymerisation. The calculus is 1D in the thickness of the part. A specific subroutine allow to correlate the polymerisation evolution with the viscosity evolution and allow to predict the evolution of the viscosity versus time.

The critical points are chosen based on the thickness and on the convection coefficient of the global loading of the autoclave.

The curing cycle shape is a classical one that could be used easily with the autoclave under industrial conditions. It is made from isothermal segments with constant heating or cooling rates between these isothermal segments.

The requirements taken in account are :

- Temperature differences
- Difference in the degree of polymerisation
- Capability of the autoclave (maximum heating and cooling rates, maximum temperature suitable for the environment products and for the material of the part.

The cure cycle optimisation minimise the duration of the cure cycle taking in account all the requirements. The calculation is done for all the critical points.

The end user has the possibility to verify the local parameters at each point of the part.

## **5 RESULTS EXPLOITATION**

For the exploitation of the results, the end user can verify for a specific point of the part if the optimised cure cycle applied fulfil the requirement in terms of temperature, viscosity, degree of cure.

We can also have the information concerning minimum and maximum temperature, the maximum and minimum degree of cure, the maximum and minimum speed of polymerisation, the maximum and minimum of viscosity versus time for each critical points.

## **6 CONCLUSIONS**

The software described previously, allows the end user to determine the optimum cure cycle to apply to a part, taking in account the geometry of the part, the environment product, the position in the autoclave. For this we need to make a thermal characterisation of the autoclave to determine the thermal transfer coefficient. This characterisation could be a global one for the quasi 2D parts or a specific one for the 3D parts. The utilisation of such a software is an important tool for the cost manufacturing reduction because it allow the end user to cure simultaneously several parts in the same autoclave with a minimisation of the curing time. For future development, with the utilisation of dielectric sensors, we could also have a direct driving of the autoclave directly given in real time by the chemical state of the critical points in the part during the curing process to improve the homogeneity of the chemical reaction and of the temperature profil in the part.

## REPORT DOCUMENTATION PAGE

<b>1. Author's Reference</b>	<b>2. Originator's References</b>  RTO-MP-9 AC/323(AVT)/TP/5	<b>3. Further Reference</b>  ISBN 92-837-1004-5	<b>4. Security Classification of Document</b>  UNCLASSIFIED/ UNLIMITED		
<b>5. Originator</b> Research and Technology Organization North Atlantic Treaty Organization BP 25, 7 rue Ancelle, F-92201 Neuilly-sur-Seine Cedex, France					
<b>6. Title</b>  Intelligent Processing of High Performance Materials					
<b>7. Presented at/sponsored by</b> The Workshop of the RTO Applied Vehicle Technology Panel (organised by the former AGARD Structures and Materials Panel) held in Brussels, Belgium 13-14 May 1998.					
<b>8. Author(s)/Editor(s)</b>  Multiple			<b>9. Date</b>  November 1998		
<b>10. Author's/Editor's Address</b>  Multiple			<b>11. Pages</b>  164		
<b>12. Distribution Statement</b> There are no restrictions on the distribution of this document. Information about the availability of this and other RTO unclassified publications is given on the back cover.					
<b>13. Keywords/Descriptors</b> <table style="width: 100%; border: none;"> <tr> <td style="width: 50%; vertical-align: top;"> Composite materials Metals Processing Manufacturing Computerized simulation Polymers Process control Cost engineering Quality control </td> <td style="width: 50%; vertical-align: top;"> Metal matrix composites Titanium Steels Forging Intermetallics IPM (Intelligent Processing of Materials) Curing Lasers Melting </td> </tr> </table>				Composite materials Metals Processing Manufacturing Computerized simulation Polymers Process control Cost engineering Quality control	Metal matrix composites Titanium Steels Forging Intermetallics IPM (Intelligent Processing of Materials) Curing Lasers Melting
Composite materials Metals Processing Manufacturing Computerized simulation Polymers Process control Cost engineering Quality control	Metal matrix composites Titanium Steels Forging Intermetallics IPM (Intelligent Processing of Materials) Curing Lasers Melting				
<b>14. Abstract</b>  <p>Contains the papers presented at a Workshop on Intelligent Processing of High Performance Materials organised by the Applied Vehicle Technology Panel (AVT) of RTO, in Brussels, Belgium, 13-14 May 1998.</p> <p>The papers describe various aspects of intelligent processing, a methodology for simulating and controlling the processing and manufacture of materials, which is finding widespread application during the manufacture of functional electronic, photonic and composite materials as well as primary metals such as steel and aluminium.</p> <p>The papers are presented under the following headings:</p> <ul style="list-style-type: none"> <li>• Overview and analytical techniques</li> <li>• Metallic materials applications</li> <li>• Non-metallic materials applications</li> </ul>					



## RESEARCH AND TECHNOLOGY ORGANIZATION

BP 25 • 7 RUE ANCELLE

F-92201 NEUILLY-SUR-SEINE CEDEX • FRANCE

Télécopie 0(1)55.61.22.99 • Téléc 610 176

## DIFFUSION DES PUBLICATIONS

RTO NON CLASSIFIEES

L'Organisation pour la recherche et la technologie de l'OTAN (RTO), détient un stock limité de certaines de ses publications récentes, ainsi que de celles de l'ancien AGARD (Groupe consultatif pour la recherche et les réalisations aérospatiales de l'OTAN). Celles-ci pourront éventuellement être obtenues sous forme de copie papier. Pour de plus amples renseignements concernant l'achat de ces ouvrages, adressez-vous par lettre ou par télécopie à l'adresse indiquée ci-dessus. Veuillez ne pas téléphoner.

Des exemplaires supplémentaires peuvent parfois être obtenus auprès des centres nationaux de distribution indiqués ci-dessous. Si vous souhaitez recevoir toutes les publications de la RTO, ou simplement celles qui concernent certains Panels, vous pouvez demander d'être inclus sur la liste d'envoi de l'un de ces centres.

Les publications de la RTO et de l'AGARD sont en vente auprès des agences de vente indiquées ci-dessous, sous forme de photocopie ou de microfiche. Certains originaux peuvent également être obtenus auprès de CASI.

## CENTRES DE DIFFUSION NATIONAUX

## ALLEMAGNE

Fachinformationszentrum Karlsruhe  
D-76344 Eggenstein-Leopoldshafen 2

## BELGIQUE

Coordinateur RTO - VSL/RTO  
Etat-Major de la Force Aérienne  
Quartier Reine Elisabeth  
Rue d'Evere, B-1140 Bruxelles

## CANADA

Directeur - Gestion de l'information  
(Recherche et développement) - DRDGI 3  
Ministère de la Défense nationale  
Ottawa, Ontario K1A 0K2

## DANEMARK

Danish Defence Research Establishment  
Ryvangs Allé 1  
P.O. Box 2715  
DK-2100 Copenhagen Ø

## ESPAGNE

INTA (RTO/AGARD Publications)  
Carretera de Torrejón a Ajalvir, Pk.4  
28850 Torrejón de Ardoz - Madrid

## ETATS-UNIS

NASA Center for AeroSpace Information (CASI)  
Parkway Center, 7121 Standard Drive  
Hanover, MD 21076

## FRANCE

O.N.E.R.A. (Direction)  
29, Avenue de la Division Leclerc  
92322 Châtillon Cedex

## GRECE

Hellenic Air Force  
Air War College  
Scientific and Technical Library  
Dekelia Air Force Base  
Dekelia, Athens TGA 1010

## ISLANDE

Director of Aviation  
c/o Flugrad  
Reykjavik

## ITALIE

Aeronautica Militare  
Ufficio Stralcio RTO/AGARD  
Aeroporto Pratica di Mare  
00040 Pomezia (Roma)

## LUXEMBOURG

Voir Belgique

## NORVEGE

Norwegian Defence Research Establishment  
Attn: Biblioteket  
P.O. Box 25  
N-2007 Kjeller

## PAYS-BAS

RTO Coordination Office  
National Aerospace Laboratory NLR  
P.O. Box 90502  
1006 BM Amsterdam

## PORTUGAL

Estado Maior da Força Aérea  
SDFA - Centro de Documentação  
Alfragide  
P-2720 Amadora

## ROYAUME-UNI

Defence Research Information Centre  
Kentigern House  
65 Brown Street  
Glasgow G2 8EX

## TURQUIE

Millî Savunma Başkanlığı (MSB)  
ARGE Dairesi Başkanlığı (MSB)  
06650 Bakanlıklar - Ankara

## AGENCES DE VENTE

## NASA Center for AeroSpace Information (CASI)

Parkway Center  
7121 Standard Drive  
Hanover, MD 21076  
Etats-Unis

## The British Library Document Supply Centre

Boston Spa, Wetherby  
West Yorkshire LS23 7BQ  
Royaume-Uni

## Canada Institute for Scientific and Technical Information (CISTI)

National Research Council  
Document Delivery,  
Montreal Road, Building M-55  
Ottawa K1A 0S2  
Canada

Les demandes de documents RTO ou AGARD doivent comporter la dénomination "RTO" ou "AGARD" selon le cas, suivie du numéro de série (par exemple AGARD-AG-315). Des informations analogues, telles que le titre et la date de publication sont souhaitables. Des références bibliographiques complètes ainsi que des résumés des publications RTO et AGARD figurent dans les journaux suivants:

## Scientific and Technical Aerospace Reports (STAR)

STAR peut être consulté en ligne au localisateur de ressources uniformes (URL) suivant:  
<http://www.sti.nasa.gov/Pubs/star/Star.html>  
STAR est édité par CASI dans le cadre du programme NASA d'information scientifique et technique (STI)  
STI Program Office, MS 157A  
NASA Langley Research Center  
Hampton, Virginia 23681-0001  
Etats-Unis

## Government Reports Announcements &amp; Index (GRA&amp;I)

publié par le National Technical Information Service  
Springfield  
Virginia 2216  
Etats-Unis  
(accessible également en mode interactif dans la base de données bibliographiques en ligne du NTIS, et sur CD-ROM)







RESEARCH AND TECHNOLOGY ORGANIZATION

BP 25 • 7 RUE ANCELLE

F-92201 NEUILLY-SUR-SEINE CEDEX • FRANCE

Telefax 0(1)55.61.22.99 • Telex 610 176

DISTRIBUTION OF UNCLASSIFIED  
RTO PUBLICATIONS

NATO's Research and Technology Organization (RTO) holds limited quantities of some of its recent publications and those of the former AGARD (Advisory Group for Aerospace Research & Development of NATO), and these may be available for purchase in hard copy form. For more information, write or send a telefax to the address given above. **Please do not telephone.**

Further copies are sometimes available from the National Distribution Centres listed below. If you wish to receive all RTO publications, or just those relating to one or more specific RTO Panels, they may be willing to include you (or your organisation) in their distribution.

RTO and AGARD publications may be purchased from the Sales Agencies listed below, in photocopy or microfiche form. Original copies of some publications may be available from CASI.

## NATIONAL DISTRIBUTION CENTRES

## BELGIUM

Coordinateur RTO - VSL/RTO  
Etat-Major de la Force Aérienne  
Quartier Reine Elisabeth  
Rue d'Evere, B-1140 Bruxelles

## CANADA

Director Research & Development  
Information Management - DRDIM 3  
Dept of National Defence  
Ottawa, Ontario K1A 0K2

## DENMARK

Danish Defence Research Establishment  
Ryvangs Allé 1  
P.O. Box 2715  
DK-2100 Copenhagen Ø

## FRANCE

O.N.E.R.A. (Direction)  
29 Avenue de la Division Leclerc  
92322 Châtillon Cedex

## GERMANY

Fachinformationszentrum Karlsruhe  
D-76344 Eggenstein-Leopoldshafen 2

## GREECE

Hellenic Air Force  
Air War College  
Scientific and Technical Library  
Dekelia Air Force Base  
Dekelia, Athens TGA 1010

## ICELAND

Director of Aviation  
c/o Flugrad  
Reykjavik

## ITALY

Aeronautica Militare  
Ufficio Stralcio RTO/AGARD  
Aeroporto Pratica di Mare  
00040 Pomezia (Roma)

## LUXEMBOURG

See Belgium

## NETHERLANDS

RTO Coordination Office  
National Aerospace Laboratory, NLR  
P.O. Box 90502  
1006 BM Amsterdam

## NORWAY

Norwegian Defence Research Establishment  
Attn: Biblioteket  
P.O. Box 25  
N-2007 Kjeller

## PORTUGAL

Estado Maior da Força Aérea  
SDFA - Centro de Documentação  
Alfragide  
P-2720 Amadora

## SPAIN

INTA (RTO/AGARD Publications)  
Carretera de Torrejón a Ajalvir, Pk.4  
28850 Torrejón de Ardoz - Madrid

## TURKEY

Millî Savunma Başkanlığı (MSB)  
ARGE Dairesi Başkanlığı (MSB)  
06650 Bakanlıklar - Ankara

## UNITED KINGDOM

Defence Research Information Centre  
Kentigern House  
65 Brown Street  
Glasgow G2 8EX

## UNITED STATES

NASA Center for AeroSpace Information (CASI)  
Parkway Center, 7121 Standard Drive  
Hanover, MD 21076

## SALES AGENCIES

NASA Center for AeroSpace  
Information (CASI)

Parkway Center  
7121 Standard Drive  
Hanover, MD 21076  
United States

The British Library Document  
Supply Centre

Boston Spa, Wetherby  
West Yorkshire LS23 7BQ  
United Kingdom

Canada Institute for Scientific and  
Technical Information (CISTI)

National Research Council  
Document Delivery,  
Montreal Road, Building M-55  
Ottawa K1A 0S2  
Canada

Requests for RTO or AGARD documents should include the word 'RTO' or 'AGARD', as appropriate, followed by the serial number (for example AGARD-AG-315). Collateral information such as title and publication date is desirable. Full bibliographical references and abstracts of RTO and AGARD publications are given in the following journals:

## Scientific and Technical Aerospace Reports (STAR)

STAR is available on-line at the following uniform resource locator:

<http://www.sti.nasa.gov/Pubs/star/Star.html>

STAR is published by CASI for the NASA Scientific and Technical Information (STI) Program  
STI Program Office, MS 157A  
NASA Langley Research Center  
Hampton, Virginia 23681-0001  
United States

## Government Reports Announcements &amp; Index (GRA&amp;I)

published by the National Technical Information Service  
Springfield  
Virginia 22161  
United States  
(also available online in the NTIS Bibliographic Database or on CD-ROM)



Printed by Canada Communication Group Inc.

(A St. Joseph Corporation Company)

45 Sacré-Cœur Blvd., Hull (Québec), Canada K1A 0S7